

THE INTERACTION OF SOUND WITH TURBULENT FLOW

by

GEORGE PETER SUCCI

B.S., Massachusetts Institute of Technology  
(1973)

SUBMITTED IN PARTIAL FULFILLMENT  
OF THE REQUIREMENTS FOR THE  
DEGREE OF

DOCTOR OF PHILOSOPHY

at the

MASSACHUSETTS INSTITUTE OF TECHNOLOGY

JUNE, 1977

Signature of Author . . . . .  
Department of Physics, March 1977

Certified by . . . . .  
Thesis Supervisor

Accepted by . . . . .  
Chairman, Department of Physics Committee



THE INTERACTION OF SOUND WITH TURBULENT FLOW

by

GEORGE PETER SUCCI

Submitted to the Department of Physics on February 21, 1977 in partial fulfillment of the requirements for the Degree of Doctor of Philosophy.

ABSTRACT

Herein the generation of sound by subsonic turbulent air flow in cavities is studied. Two types of cavity modes are considered; the axial modes of a pipe open at both ends and the transverse modes of a rectangular duct. Experiments were performed to measure the acoustic spectra of the flow generated noise. A linear theoretical analysis, based on an isotropic model of the turbulent fluctuations, is developed to predict this spectra. Certain non linear phenomena (screech), due to the alteration of the source flow by the emitted sound, are identified. The necessary conditions for such instabilities examined.

Thesis Supervisor: K. U. Ingard

Title: Professor of Physics

## ACKNOWLEDGEMENTS

I greatly acknowledge the guidance of my advisor, Dr. Uno Ingard. His clear explanation of the physics of sound was essential to the task of completing the thesis. I also thank the doctoral thesis committee members, Dr. Bekefi and Dr. Dupree, for their interest and suggestions.

On the non technical side, much appreciation is due to my friend, Meg, who is the best of company when I am buried in work.

The thesis is dedicated to my father, who introduced me to experimental physics by granting me free access to his tool box. His unfailing patience in describing the inner works of our household encouraged me to think about the natural world.

## TABLE OF CONTENTS

	<u>Page</u>
ABSTRACT	2
ACKNOWLEDGEMENTS	3
LIST OF FIGURES	8
NOMENCLATURE	13
INTRODUCTION	20
1. FREE SPACE JET NOISE	23
1.1 Introduction	23
1.2 Turbulence as a Source of Sound	27
1.2.1 Review of Classical Acoustics	27
1.2.2 Derivation of Lighthill's Equation	29
1.2.3 Ribner's Equation	31
1.3 A Comparison of Three Calculations	34
1.3.1 Monopole Source, Frequency-domain Green's Function	34
1.3.2 Monopole Source, Time-domain Green's Function	39
1.3.3 Quadrupole Source, Time-domain Green's Function	43
1.3.4 Velocity Intensity and Total Power	48
1.4 Comments on the Turbulent Correlation	49
1.4.1 Choice of the Correlation	49
1.4.2 The Eighth Power Law	53
1.4.3 The Kolmogorov Inertial Subrange	55
1.4.4 Gaussian Correlation and the Relation Between the Turbulent and Acoustic Spectra	56
1.5 Summary	59
2. EXCITATION OF AXIAL PIPE MODES	62
2.1 Introduction	62
2.2 Experiment	64
2.2.1 Apparatus and Procedure	64
2.2.2 Variation With Pipe Length	66



TABLE OF CONTENTS (cont'd.)

	<u>Page</u>
2.2.3 Variation With Flow Speed	67
2.2.4 Variation With Microphone Placement	69
2.2.5 Effect of Liner	71
2.3 Theory	72
2.3.1 On Distinguishing Mean Flow Effects from Turbulent Fluctuations	72
2.3.2 The Green's Function	75
2.3.3 Analysis of the Pressure Reflection Coefficient	77
2.3.4 Transmission Out of the Ends of the Pipe	81
2.3.5 Effect of the Convective Derivative on the Source Term	85
2.3.6 Acoustic Field of a Point Source	89
2.3.7 Acoustic Field of a Distributed Source	90
2.3.8 The Upstream Acoustic Field	92
2.3.9 Numerical Comparison of Theory to Experiment	95
3. EXCITATION OF TRANSVERSE DUCT MODES	99
3.1 Introduction	99
3.2 Experiments	101
3.2.1 Apparatus and Procedures	101
3.2.2 Basic Effect	104
3.2.3 Spectra Variation With Jet Velocity and Diameter	105
3.2.4 Reduction by Strouhl Number	107
3.2.5 Separating Linear From Feedback Effects	110
3.2.6 Effect of Inlet Turbulence	112
3.2.7 Orifice Mounted on Axis	113
3.2.8 Upstream Versus Downstream Radiation	114
3.2.9 Effect of Microphone Placement	115

TABLE OF CONTENTS (cont'd.)

	<u>Page</u>
3.3 Theory	116
3.3.1 Duct Acoustics With Mean Flow	116
3.3.2 The Green's Function	121
3.3.3 Random Source Representation in a Duct	123
3.3.4 The Radiated Pressure	133
3.3.5 Gaussian Correlation and a Qualitative Analysis of the Low Frequency Spectra	137
3.3.6 Damping and the Smoothing of the High Frequency Spectra	139
3.3.7 Radiation Impedance and the Similarity of the High Frequency Duct Spectra to the Free Space Spectra	143
3.3.8 Velocity Power and Intensity	149
3.3.9 A Numeric Comparison of the Predicted to the Observed Low Frequency Spectra	152
4. SCREECH	155
4.1 Introduction	155
4.2 Orifice Screech	159
4.2.1 Orifice Screech: Apparatus and Procedure	159
4.2.2 Screech Dependence on the length to Diameter Ratio and Flow Speed	161
4.2.3 Similarity to Hole Tone	164
4.2.4 Perturbation of the Flow by Screens	165
4.2.5 A Kinematic Calculation of the Feed- back Frequency	167
4.2.6 Cavity Mode Excitation	170
4.3 Impingement Screech	177
4.3.1 Impingement Screech: Apparatus and Procedure	177
4.3.2 Free Jet Spectra From a Pipe and Orifice	178
4.3.3 Turbulent Sound Level Increase Due to the Obstruction of the Flow by a Flat Plate	180

TABLE OF CONTENTS (cont'd.)

	<u>Page</u>
4.3.4 Impingement Screech from a Tapered Orifice	181
4.3.5 Coupling of Impingement Screech to a Cavity Mode	184
4.3.6 Direct Comparison of Impingement Screech to Screech in Ducts	186
5. CONCLUSIONS AND RECOMMENDATIONS	188
APPENDIX: STABILITY ANALYSIS OF THE PERTURBED JET IN THE PRESENCE OF BOUNDARIES	196
A. 1 Introduction	196
A. 2 Problem Statement	197
A. 3 Integral Solution	199
A. 4 Comments on the Evaluation of the Integral	204
A. 5 Removing the Duct Wall	205
A. 6 Simplification to Two Dimensions	208
A. 7 Comments on the Application of the Theory to Screech	212
REFERENCES	217
FIGURES	225
BIOGRAPHICAL NOTE	292

LIST OF TABLES

TABLE

3.1 -- Table of Fourier Transforms	130
3.2 -- Table of Statistical Transform	131
4.1 -- Data for Screech Coupled to Cavity Modes	175
4.2 -- Normalized Data for Screech Coupled to Cavity Modes	176

LIST OF FIGURES

FIGURE	<u>Page</u>
1.1 -- Correlation contours for a free jet (Ref. 15).	225
1.2 -- Peak frequency of acoustic power spectra versus downstream distance (Ref.63 ).	226
1.3 -- Free space spectra fit by three independent isotropic correlation functions.	227
2.1 -- Acoustic spectra versus mean flow.	228
2.2 -- Apparatus used in axial mode study.	229
2.3 -- Frequency interval between axial modes versus pipe length.	230
2.4 -- Frequency interval between axial modes versus mean flow speed.	231
2.5 -- Comparison of inlet and exit pipe noise.	232
2.6 -- Inlet pressure reflection coefficient.	233
2.7 -- Exit pressure reflection coefficient.	234
2.8 -- Comparison of experimental and theoretical spectra at Mach .10.	235
2.9 -- Comparison of experimental and theoretical spectra at Mach .14.	236
2.10 -- Comparison of experimental and theoretical spectra at Mach .40.	237
2.11 -- Strouhl numbers used to compute the spectra.	238
2.12 -- Correlation time based on the Strouhl numbers.	239
2.13 -- Polar intensity plot for a 2" long pipe.	240
2.14 -- Polar intensity plot for a 4" long pipe.	241
2.15 -- Polar intensity plot for a 6" long pipe.	242

LIST OF FIGURES (cont'd.)

FIGURES	<u>Page</u>
2.16 -- Polar intensity plot for an 8" long pipe.	243
2.17 -- Polar intensity plot for a 10" long pipe.	244
2.18 -- Polar intensity plot for a 12" long pipe.	245
2.19 -- Polar intensity plot for a 14" long pipe.	246
2.20 -- Polar intensity plot for a 16" long pipe.	247
2.21 -- Polar intensity plot for an 18" long pipe.	248
3.1 -- Photo of experimental apparatus used to study the turbulent excitation of transverse modes in ducts.	249
3.2 -- Hot wire velocity calibration.	250
3.3 -- Photo of microphone holder used to detect the mode shape of the radiated sound.	251
3.4 -- Photo of orifice plates used to form air jets.	252
3.5 -- Photo of 60" pipe used to form air jet.	253
3.6 -- Comparison of low and high frequency spectra in a rectangular duct.	254
3.7 -- Low frequency spectra using a 1/4" diameter orifice plate.	255
3.8 -- Low frequency spectra using a 1/2" diameter orifice plate.	256
3.9 -- Low frequency spectra using a 1" diameter orifice plate.	257
3.10 -- High frequency spectra using a 1/4" diameter orifice plate.	258
3.11 -- High frequency spectra using a 1/2" diameter orifice plate.	259
3.12 -- High frequency spectra using a 1" diameter orifice plate.	260

LIST OF FIGURES (cont'd.)

FIGURES	<u>Page</u>
3.13 -- Reduction of low frequency spectra by Strouhl number. Here $f_s = \frac{.2V}{D} \approx 5.7$ KC.	261
3.14 -- Reduction of low frequency spectra by Strouhl number. Here $f_s = \frac{.2V}{D} \approx 2.5$ KC.	262
3.15 -- Reduction of high frequency spectra by Strouhl number. Here $f_s = \frac{.2V}{D} \approx 1.9$ KC.	263
3.16 -- Sound level versus mean flow for a 1/2" diameter orifice plate. Levels at first cutoff frequency (1.6 KC) are compared to those at a frequency between the first and second cutoff.	264
3.17 -- Sound level versus mean flow for a 1/2" diameter orifice plate. Two frequencies at which screech occurs are shown.	265
3.18 -- Low frequency spectra from an initially turbulent jet.	266
3.19 -- High frequency spectra from an initially turbulent jet.	267
3.20 -- Low frequency spectra observed when jet and duct axis are parallel.	268
3.21 -- Comparison of upstream and downstream radiated acoustic spectra.	269
3.22 -- Transverse variation of radiated sound at frequencies selected to show the mode shape.	270
3.23 -- Influence of mode shape on the detected spectra.	271
3.24 -- Radiation resistance of a simple source.	272
3.25 -- Comparison of theoretical and experimental spectra at Mach .6 for a 1/2" diameter orifice plate.	273

LIST OF FIGURES (cont'd.)

FIGURES	<u>Page</u>
4.1 -- Experimental apparatus used to generate screech.	274
4.2 -- Screech frequency versus flow speed for a 1/4" long orifice plate.	275
4.3 -- Screech frequency versus flow speed for a 1/2" long orifice plate.	276
4.4 -- Screech frequency versus flow speed for a 1" long orifice plate.	277
4.5 -- Summary of tests made to determine the length to diameter ratio necessary for screech.	278
4.6 -- Summary of tests made to determine the length to diameter ratio necessary for the modified hole tone.	279
4.7 -- Screech frequencies versus flow speed for the modified hole tone with a 5/8" inside diameter.	280
4.8 -- Screech frequency versus flow speed for the modified hole tone with a 4-11/32" inside diameter.	281
4.9 -- The suppression of orifice screech by screens.	282
4.10 -- Typical orifice screech spectra.	283
4.11 -- Screech spectra for the modified hole tone at Mach .33.	284
4.12 -- Screech spectra for the modified hole tone at Mach .34. All but the first peak are shown to coincide with cavity modes which have the indicated number of nodal diameters.	285
4.13 -- Experimental apparatus used to generate impingement screech.	286
4.14 -- Free space spectra from a 1/2" diameter orifice plate.	287
4.15 -- Free space spectra from a 60" long pipe with a 1/2" inside diameter.	288

LIST OF FIGURES (cont'd.)

FIGURES	<u>Page</u>
4.16 -- Increased sound level due to obstruction of the flow by a flat plate.	289
4.17 -- Impingement screech versus distance to plate.	290
4.18 -- Direct comparison of impingement screech to screech observed in a rectangular duct.	291



## NOMENCLATURE

SYMBOL	DESCRIPTION
a	Radius of cylinder, disk, or sphere
A	Cross sectional area
A	Pressure perturbation amplitude (Appendix)
b	Duct width
B	Radiated pressure amplitude
c	Speed of sound (3,4000 cm/sec)
$c_0$	Speed of sound in the quiescent air (Chapter 4)
$c_+$	Speed of sound in the quiescent air (Appendix)
$c_j$	Speed of sound in the jet (Chapter 4)
$c_-$	Speed of sound in the jet (Appendix)
$c_p$	Acoustic phase speed in a moving fluid... $c + V \cos\theta$
$c^-$	Normalized phase speed of a shear layer disturbance (Appendix) $\frac{\omega}{kc_+}$
d	Duct width
D	Pipe diameter
$D(\omega)$	Denominator in Green's function for an open ended pipe with flow
DB	Decibels
$\frac{D}{Dt}$	Convective derivative ... $\frac{\partial}{\partial t} + V_i \frac{\partial}{\partial X_i}$
f	Frequency
$f_n$	Frequency of $n^{\text{th}}$ harmonic
$f_s$	Strouhl Frequency
F	Frequency range
$\Delta F$	Interval between axial mode frequencies... $\frac{c(1-M)^2}{2(L+\delta_0+\delta_L)}$
G	Green's function
$H_n^1$	$n$ th order Hankel function of the first kind

NOMENCLATURE (cont'd.)

SYMBOL	DESCRIPTION
$i$	$\sqrt{-1}$
$I$	Acoustic intensity
$I_n$	$n$ th order modified Bessel function
$j_{n,s}$	$S^{\text{th}}$ root of first derivation of $J_n$
$J_n$	Bessel function of the first kind
$k$	Wavenumber ... $\frac{\omega}{c}$
$k_+$	Wavenumber for propagation in the direction of flow ... $\frac{\omega}{c(1+M)}$
$k_-$	Wavenumber for propagation opposite to the direction of flow ... $\frac{\omega}{c(1-M)}$
$k_{mn}$	Axial component of the wavenumber in a duct
$k_0$	Handa's $i\mu_0$ (Appendix)
$k_1$	Handa's $i\mu_-$ (Appendix)
kHz	Kilohertz
$K$	Wavenumber
$K_n$	$n^{\text{th}}$ order modified Bessel function
$\ell$	Point source location in a pipe
$L$	Pipe or orifice length
$m$	Integer
$m_0$	Unit mass of air
$M$	Mach number ... $\frac{V}{c}$
$n$	Integer
$N$	Integer
$p$	Total pressure
$p$	Acoustic pressure ... see Table of Fourier transforms on page 130.

NOMENCLATURE (cont'd.)

SYMBOL	DESCRIPTION
$\mathcal{P}$	Turbulent pressure
$q$	Monopole source strength in units of (volume/unit volume)/time
$q$	integer
$Q, Q(\omega)$	Designates the highest propagating mode at frequency $\omega$
$Q$	Total equivalent monopole source strength
$r$	Distance to observation point
$r_0$	Distance to source point
$R_0$	Pressure reflection coefficient at pipe inlet
$R_L$	Pressure reflection coefficient at pipe exit
$R$	Turbulent velocity correlation
$\mathcal{R}$	Turbulent pressure correlation ... see Table of Statistical transforms on pages 131 and 132.
$s$	Integer
$S$	Strouhl number
$S_\omega$	Monopole source strength in units of volume/time.
$t$	Time
$t', t''$	Retarded time
$T$	Time interval
$T$	Pressure transmission coefficient
$u$	Acoustic velocity
$u_{nw}$	Acoustic velocity normal to a duct wall in the region of zero mean flow
$u_{nf}$	Acoustic velocity normal to a duct wall in the region of mean flow
$u_0$	Velocity amplitude of a spherical source
$\mathbf{v}$	Total fluctuating velocity .. $v + u$
$v$	Turbulent velocity

NOMENCLATURE (cont'd.)

SYMBOL	DESCRIPTION
V	Mean velocity
w	Total velocity ... $V + v$ ... $V + v + u$
x	Observation point
$x_0$	Source point
y	Source point (Chapter 1)
(x, y, z)	Coordinates of the observation point
( $x_0, y_0, z_0$ )	Coordinates of the source point
z	Axial coordinate in a duct
Z	$ka \sin \theta$ (Chapter 2)
$\alpha$	Distance shift in the x direction in the correlation function
$\alpha$	Correlation length
$\alpha$	Ratio of convection velocity to mean velocity
$\beta$	Constant from boundary condition at wall (Appendix)
$\beta$	Distance shift in the y direction in the correlation function
$\beta_x, \beta_y$	Specific acoustic admittance
$\gamma$	Ratio of specific heats
$\gamma$	Distance shift in the z direction in the correlation function
$\delta$	Delta function
$\delta_0$	Inlet end correction for a open ended pipe with flow
$\delta_L$	Exit end correction for a open ended pipe with flow
$\epsilon$	Small quantity
$\tilde{\eta}$	Distance shift in the correlation function computed in the lab frame of reference
$\eta$	Shear layer displacement (Appendix)

NOMENCLATURE (cont'd.)

SYMBOLS	DESCRIPTION
$\lambda_{mn}$	Mode wavenumber in a hard wall duct
$\theta$	Angle between flow and observer
$\Theta$	Radiation resistance of a simple source in a duct.
$\lambda$	Wave length of sound
$\Lambda_{mn}$	Mean square amplitude of the cross duct mode
$\mu$	Coefficient of viscosity
$\mu_-$	$\sqrt{-\left \frac{(\Omega-KV)}{c_-}\right ^2 + k^2}$ (Appendix)
$\mu_+$	$\sqrt{-\left(\frac{\Omega}{c_+}\right)^2 + k^2}$ (Appendix)
$\nu$	Kinematic viscosity ... $\mu/\rho$
$\xi$	Distance shift in the correlation function computed in the jet frame of reference
$E$	Eddy volume
$\pi$	3.14159... ratio of circumference to diameter of a circle
$\Pi$	Radiated acoustic power
$\rho$	Total density ... $\rho_0 + \rho^0 + \rho$
$\rho_0$	Mean density
$\rho^0$	Turbulent density fluctuation
$\rho$	Acoustic density fluctuation
$\rho(k_x, k_y)$	Density of acoustic modes in a rectangular duct at the wave number $(k_x, k_y)$
$\frac{\sigma_{m\pi}}{b}$	Mode wavenumber in a second absorbing duct
$\frac{\sigma_{n\pi}}{d}$	Mode wavenumber in a sound absorbing duct
$\Sigma$	Summation symbol

NOMENCLATURE (cont'd.)

SYMBOL	DESCRIPTION
$\tau$	Time shift in the correlation function
$\varphi$	Axial angle in cylindrical coordinates
$\phi$	Phase of Fourier coefficient
$\psi$	Characteristic function for a cross duct mode
$\chi$	Coefficient of heat conduction
$\omega$	Angular frequency ... $2\pi f$
$\Omega$	Source volume
$\Omega$	Angular frequency (Appendix)
$\sigma$	Order of magnitude
< >	Average of N measurements
Re	Real part
SUB-SCRIPTS	
0	Pipe inlet
i	Incident wave
i, j	Tensor component
$\ell^+$	Acoustic wave upstream of the source point propagating in the direction of flow
$\ell^-$	Acoustic wave upstream of the source point propagating opposite to the direction of flow
L	Pipe exit
m, n	m, n <sup>th</sup> transverse mode in a duct
n	n <sup>th</sup> order
n	n <sup>th</sup> harmonic
o	Source point
q	q <sup>th</sup> transverse mode in a duct
r	Reflected wave
r <sup>+</sup>	Acoustic wave downstream of the source point propagating in the direction of flow
r <sup>-</sup>	Acoustic wave downstream of the source point propagating opposite to the direction of flow
s	Strouhl frequency
t	Transmitted wave
z	Axial component

NOMENCLATURE (cont'd.)

SUB-  
SCRIPT

DESCRIPTION

- + Propagation in the flow direction
- + Points outside the jet (Appendix)...  $r > R_j$
- Propagation opposite to the direction of flow
- Points inside the jet (Appendix) ...  $r < R_j$

SUPERSCRIPT

- ~ Vector
- ^ Unit vector
- Time average

## INTRODUCTION

In the now classical theory of sound from turbulent flow by Lighthill<sup>1, 2</sup> boundaries were not considered. Further, it was assumed that the turbulent flow field was not altered by sound emission.

For closed systems, such as cavities and waveguides, discrete modes may be excited. It is possible that the coupling between the flow field and acoustic modes is strong enough to alter the primary flow field. Under such conditions acoustically induced flow instabilities such as whistles occur. The objective of this thesis is to study the turbulent excitation of duct modes and the conditions for possible instabilities.

Chapter One reviews the theory of turbulent excitation of sound in free space. The induced acoustic field is calculated in three ways. The sound field is determined by time-domain Green's function technique for both Lighthill's<sup>1, 2</sup> quadrupole source model and Ribner's<sup>3, 4</sup> equivalent distribution of monopoles. The omission of turbulent shear interactions in an isotropic monopole model of the turbulence is demonstrated. The sound field is also determined by a frequency-domain Green's function technique for a monopole distribution. Time and frequency domain calculations yield identical results for the monopole source distribution. However, the frequency domain technique allows the analysis to be extended to



systems with boundaries in simple fashion.

Chapter Two examines the excitation of axial pipe modes by turbulent flow theoretically and experimentally. The experiment is performed by drawing air through a cylindrical pipe. The observations demonstrate that mode excitation diminishes as the flow speed increases. This is attributed to end losses which increase with flow speed. A Green's function, based on the measured pressure reflection coefficients, is used to predict the variation in spectra with flow.

Chapter Three demonstrates the excitation of transverse modes in pipes experimentally. Air is drawn through a small orifice into a rectangular duct. Pronounced asymmetric peaks are observed at the first few cutoff frequencies. The asymmetric nature of the peaks and relative spectral intensity are again explained by Green's function techniques. For high frequencies, where a large number of modes can propagate, the spectra resembles the free-space jet spectra. In this frequency range, the duct radiation impedance asymptotically approaches the free space impedance, hence the similar response to similar source distributions.

Chapter Four examines feedback instabilities, cases where the emitted sound field alters the jet flow itself. The chapter concentrates on screech tones of

circular orifices having length to diameter ratios between one half and two. The frequency dependence of the screech on Mach number and length is explained by a kinematic analysis of the feedback loop. It is further demonstrated that the frequency of the feedback instability must be approximately equal to that of an acoustic mode for screech to occur. Similar observations are presented with regard to air jets impinging on plates.

In conclusion two mechanisms exist whereby the acoustic energy from a turbulent jet can be concentrated at select frequencies. The first is the selective response of a medium with boundaries to a random source. The spectral line shape for such cases is accounted for by Green's function techniques. The second mechanism is the feedback instability which requires coupling of the jet flow to the acoustic field. Here the modification of the jet flow must be considered to determine the excitation frequencies.

It is recommended that future work be done on the screech instability. The influence of the acoustic cavity mode on the feedback instability should be examined in greater detail. In particular, the convection speed of jet column disturbances with and without adjacent resonators should be determined experimentally. Furthermore, the mechanism which limits the amplitude of the screech should be determined.

## 1. FREE SPACE JET NOISE

### 1.1 Introduction

Aerodynamic noise may be defined as that noise which is generated as a direct result of airflow without any part due to the vibrations of solid bodies.<sup>5</sup> The basic theory of aerodynamic sound generation and its application to noise radiated from turbulent jets was first given in two papers by Lighthill.<sup>1, 2</sup> He considers a fluctuating hydrodynamic flow covering a limited region surrounded by a large volume of fluid which is at rest, apart from the infinitesimal amplitude sound waves radiated by the turbulent flow. The exact equations governing the density perturbations in a turbulent, viscous, heat conducting fluid are compared with the approximate equations appropriate to an inviscid non heat conducting media at rest. The difference between the two sets of equations is treated as if it were an externally applied source field which is known if the flow is known.

The forcing terms fall into three groups: a Reynolds stress due to turbulent momentum convection, a term due to heat conduction and one due to viscous stresses. Not all terms contribute equally to the acoustic field, only the Reynolds stresses need be considered. It is a well established fact that in turbulent flow<sup>6, 7</sup> the ratio of inertial to viscous

stresses, the Reynolds number,  $\rho V D / \mu$ , is usually quite large, at least in most aero-acoustic applications. We, therefore, neglect viscosity. If we further assume that the flow emanates from a region of uniform temperature the effects of heat conduction ought to be the same order of magnitude as the viscous effects. This is providing the Prandtl number,  $\rho \mu / \chi$  is of order one, in air  $\rho \mu / \chi = .73$ . Our conclusion is that only the Reynolds stress contributes to the acoustic field. Lighthill further assumes that the turbulent flow is incompressible in the source region. To calculate the acoustic field one needs the statistical distribution of the Reynolds stresses

Ribner simplified the source field by observing that in low speed turbulence Lighthill's quadrupoles combine to behave as simple sources proportional to  $\frac{\partial^2 \rho}{\partial t^2}$ , where ' $\rho$ ' is the local pressure due to the turbulence. He observed that the effective volume of the fluid element in an unsteady flow fluctuates inversely as the local pressure. Part of this dilation is the sound source, the other part propagates the sound. From incompressibility it follows that the Reynolds stress is balanced by the spatial derivatives of the turbulent pressure field. The remaining unbalanced term is the second time derivative of the turbulent pressure. It is this term which

is the source of acoustic waves.

The simplification of source terms is essential if one is to make any progress in theory. A weak point of aeroacoustics is that it assumes the detailed structure of the turbulent field is known. This is not the case, either theoretically or experimentally.

Consider, for example, an experiment to determine the statistical distribution of the Reynolds stresses. To do this one measures the turbulent velocity fluctuations  $v_h v_l$  at  $(x, t)$  and  $v_i v_j$  at  $(x+\eta, t+\tau)$  where  $\eta$  and  $\tau$  are the spatial and temporal separation of the measurement. To evaluate the correlation one must carry out such measurements at all separations  $\eta$  and  $\tau$ , for all permutations of the indicies.

Ribner's analysis provides a basis for requiring only the properties of the scalar pressure field. The problem reduces to the measurement of  $\rho(x, t)$  and  $\rho(x+\eta, t+\tau)$  without additional permutation terms.

If Ribner's model is used, and the turbulent fluctuations are assumed to be isotropic, the sound from the interaction of turbulence with the mean shear is neglected. Lighthill calls this interaction the aerodynamic sounding board, Lilley<sup>8</sup> uses the phrase "shear noise" to distinguish it from the "self noise" of turbulence alone. In this thesis Ribner's model is used and

only the "self noise" is considered. To point out the omission, the sound fields from the source dilation model are here compared to that from the Reynolds stresses.<sup>10</sup> In both instances the time domain Green's function is used.

The technique of manipulating the scalar source terms with the frequency-domain Green's function is introduced first. The results are identical to those using time-domain techniques. The exercise is performed to elicit the assumptions implicit in the frequency domain calculation. One finds, for example, that the spatial Fourier transform represent first order retarded time effects. These points, are best demonstrated by comparison to the time-domain calculations.

Frequency domain techniques let one extend the theory to cases with boundaries. Such effects are considered by Ffowcs-Williams and Hawkings<sup>9</sup> and also by Curle<sup>10</sup> using time domain analysis. They use a free space Green's function. The extra terms in the integral expression due to not satisfying the boundary conditions must be simplified and interpreted. If, however, one works in the frequency-domain, the Green's function is comparatively simple. Differences in spectra between regions with and without boundaries are explained by differences in Green's function. That is, the medium responds differently to identical source functions

when boundaries are present.

With this in mind one simplifies a turbulent jet by assuming homogeneity and isotropy of the fluid fluctuations. One further specifies that the form of the correlation for such fluctuations is Gaussian. The predictions of such a distribution are compared to those of dimensional analysis and to experimental results. The same source correlation will be used to describe fluctuations in enclosed regions. This underscores the fact that a class of spectra variations can be attributed to variations in the response of the medium as opposed to changes in the turbulent sources.

## 1.2 Turbulence as a Source of Sound

### 1.2.1 Review of Classical Acoustics

Lighthill's<sup>1, 2, 7</sup> theory of turbulent noise is developed by analogy to classical linear acoustics. It is instructive, therefore, to review the solution to the acoustic response of a media with distributed volume sources  $q(\tilde{y}, t)$ . The linearized equations of mass and momentum conservation for an inviscid compressible fluid are

$$\frac{\partial \rho}{\partial t} + \rho_0 \frac{\partial U_i}{\partial x_i} = \rho_0 q \quad 1.1$$

$$\rho_0 \frac{\partial U_i}{\partial t} + \frac{\partial p}{\partial x_i} = 0 \quad 1.2$$

Here  $\rho$ ,  $p$ , and  $u_i$  are the acoustic density pressure and velocity perturbations;  $\rho_0$  is the average density. One further assumes adiabatic conditions

$$\Delta p = c^2 \Delta \rho \quad 1.3$$

Take the time derivative of Eq. 1.1 and subtract the divergence of Eq. 1.2 to find the forced wave equation

$$c^2 \nabla^2 \rho - \frac{\partial^2}{\partial t^2} \rho = -\rho_0 \frac{\partial q}{\partial t} \quad 1.4$$

Consider the associated equation for a point source. Let  $(\tilde{y}, t')$  be the source coordinates and  $(\tilde{x}, t)$  be the field coordinates. One needs the Green's function  $G(\tilde{x}, t | \tilde{y}, t')$  such that

$$c^2 \nabla^2 G - \frac{\partial^2 G}{\partial t^2} = -\delta(t - t') \delta(\tilde{y} - \tilde{x}) \quad 1.5$$

The solution is

$$G(\tilde{x}, t | \tilde{y}, t') = \frac{1}{4\pi c^2 |\tilde{x} - \tilde{y}|} \delta(t' - t + \frac{|\tilde{x} - \tilde{y}|}{c}) \quad 1.6$$

The solution to the acoustic field of a distributed source is then

$$\begin{aligned} \rho(\tilde{x}, t) &= \iiint_{\Omega} d\tilde{y} \int_{-T/2}^{+T/2} dt' G(\tilde{x}, t | \tilde{y}, t') \rho_0 \frac{\partial q(\tilde{y}, t')}{\partial t'} \\ &= \frac{\rho_0}{4\pi c^2} \iiint_{\Omega} \frac{1}{|\tilde{x} - \tilde{y}|} \frac{\partial q(\tilde{y}, t')}{\partial t'} \Big|_{t' = t - \frac{|\tilde{x} - \tilde{y}|}{c}} \end{aligned} \quad 1.7$$

where  $\Omega$  is a volume which contains the sources.



### 1.2.2 Derivation of Lighthill's Equations

This section reviews the acoustic analogy approach introduced by Lighthill.<sup>1, 2, 7</sup> He considers the sound radiated from a small region of fluctuating flow embedded in a large volume of fluid which is at rest. The equations governing the density perturbations in the real fluid are compared to those appropriate to a uniform media at rest, which coincide with the real fluid outside the region of turbulence. The difference between the two sets of equations will be considered as if it were the effect of an external source field, known if the flow is known, hence radiating sound according to the laws of linear acoustics.

Consider the complete Navier Stokes equations for fluid flow with no external sources. They are  
Mass Conservation

$$\frac{\partial \rho}{\partial t} + \frac{\partial \rho v_i}{\partial x_i} = 0 \quad 1.8$$

Momentum Conservation

$$\frac{\partial \rho v_i}{\partial t} + \frac{\partial \rho v_i v_j}{\partial x_j} = - \frac{\partial p_{ij}}{\partial x_j} \quad 1.9$$

Where  $\rho$ ,  $v$  and  $p$  are the total density velocity and pressure. In classical acoustics we assume particle velocities are small so that squares of time dependent terms are neglected.

In the analogy approach one compares the complete equations of motion (Eq. 1.8 and 1.9) to the linearized ones (Eq. 1.1 and 1.2) so as to group non linear terms on the right hand side of the wave equation. To do this rewrite the momentum equation as

$$\frac{\partial \rho v_i}{\partial t} + c^2 \frac{\partial \rho}{\partial x_i} = - \frac{\partial}{\partial x_j} (\rho v_i v_j + p_{ij} - c^2 \rho \delta_{ij}) \quad 1.10$$

Proceeding as in the linear case one has

$$\frac{\partial^2 \rho}{\partial t^2} - c^2 \nabla^2 \rho = \frac{\partial^2 T_{ij}}{\partial x_i \partial x_j} \quad 1.11$$

where

$$T_{ij} = \rho v_i v_j + (p_{ij} - p_{ij} \delta_{ij}) + (p_{ij} - c^2 \rho) \delta_{ij} \quad 1.12$$

The procedure yields a wave equation in which the non linear terms appear as source terms. An integral form is obtained by replacing  $\rho \frac{\partial q}{\partial t}$  in Eq. 1.7 with  $\frac{\partial^2}{\partial x_i \partial x_j} T_{ij}$ . As the complete Navier-Stokes equations have not been solved in differential form one will encounter similar difficulties in the integral form. It is necessary to simply  $T_{ij}$ .

$T_{ij}$  is composed of three parts. The first,  $\rho v_i v_j$ , represents the convection of momentum  $\rho v_i$  at velocity  $v_j$ . At low flow speeds it is reasonable to replace  $\rho$  by the average density  $\rho_0$ . One further neglects the acoustic component of the fluctuating

velocities  $v_i$  and  $v_j$ , these velocities are assumed to be due only to turbulence. The second term,  $(P_{ij} - P_{ij} \delta_{ij})$  represents the viscous contribution to the stress tensor. For high Reynolds numbers this term is negligible, compared to  $\rho_0 v_i v_j$ . The third term,  $(\rho - \rho_0) \delta_{ij}$ , represents the effect of heat conduction, i.e., the departure from the adiabatic pressure density relation in Eq. 1.3. For Prandtl numbers  $\mathcal{O}(1)$  this contribution is the same as the viscous one, and therefore negligible. The solution is

$$\rho = \iiint_{-2}^{2} d^3\gamma \int_{-T/2}^{T/2} dt' G(\vec{x}, t | \vec{\gamma}, t') \frac{\partial^2}{\partial \gamma_i \partial \gamma_j} \rho_0 v_i v_j \quad 1.13$$

Where  $\rho$  is the acoustic density fluctuation and  $v_i v_j$  the turbulent velocity perturbations. An interesting approach was used by Kraichnan<sup>11</sup> and later by Mawardi.<sup>12</sup> They point out that Lighthill's equation is an integral equation for the unknown density  $(\rho - \rho_0)$ , assuming the medium is inviscid and non heat conducting. If  $v_i v_j$  are assumed to be independent of density Eq. 1.13 results as the first approximation in an iterative solution.

### 1.2.3 Ribner's Equation

Ribner<sup>3</sup> reduces the source field to an equivalent distribution of monopoles. He starts with Eq. 1.11, ignores heat conduction and viscosity, and explores the

consequences of the approximate incompressibility of the turbulence. The key to the analysis is to assume the perturbation in the pressure consists of two parts; the pseudosound 'p' generates the sound, the acoustic pressure 'p' propagates the sound. He restates Eq. 1.11

as

$$\frac{1}{c^2} \frac{\partial^2 (\rho + p)}{\partial t^2} - \frac{\partial^2 (\rho + p)}{\partial x_i^2} = \frac{\partial^2 (\rho_0 v_i v_j)}{\partial x_i \partial x_j} - \frac{\partial^2 (\rho - \rho_0) v_i v_j}{\partial x_i \partial x_j} \quad 1.14$$

For an incompressible fluid

$$-\frac{\partial^2 \rho}{\partial x_i^2} = \frac{\partial^2 (\rho_0 v_i v_j)}{\partial x_i \partial x_j} \quad 1.15$$

That is, the pressure gradients balance the Reynolds stress. Subtracting Eq. 1.15 from Eq. 1.14 gives

$$\frac{1}{c^2} \frac{\partial^2 \rho}{\partial t^2} - \frac{\partial^2 \rho}{\partial x_i^2} = \frac{1}{c^2} \frac{\partial^2 \rho}{\partial t^2} \quad 1.16$$

where he neglects  $\frac{1}{c^2} \frac{\partial^2 (\rho - \rho_0) v_i v_j}{\partial x_i \partial x_j}$ . For low speed turbulence, e.g., jets up to moderate speeds,  $\rho - \rho_0 \approx \rho$  within the turbulence and the neglected term is much less than  $\left| \frac{1}{c^2} \frac{\partial^2 \rho}{\partial t^2} \right|$ . Mawardi,<sup>12</sup> in a separate analysis, shows that this term is  $\mathcal{O}(M^4)$  and therefore small compared to  $\rho$ , which is  $\mathcal{O}(M^2)$ , for subsonic flow.

Ribner offers the following interpretation of Eq. 1.16.

"For acoustic purposes we replace the turbulent

flow by an equivalent acoustic media at rest containing the appropriate dilations. For such a medium

$$\rho_0 \text{ dilation rate} = - \frac{\partial}{\partial t} \rho$$

where  $\rho_0$  is the mean value of the local density  $\rho$ . On a certain understanding ... either side of this equation has the same local sound generating effect as a fluctuating source of matter injected at the rate  $\rho_0 \dot{\rho} \approx - \frac{\partial \rho}{\partial t}$ . But it is the time rate of  $\rho_0 \dot{\rho}$  that constitutes the effective acoustic source strength ... the result is

$$\text{effective source strength } \rho_0 \frac{\partial \dot{\rho}}{\partial t} = - \frac{\partial^2 \rho}{\partial t^2} \approx - \frac{1}{c^2} \frac{\partial^2 p}{\partial t^2} //$$

Here the notation is changed to conform to present usage,

$\rho$  is the density fluctuation associated with turbulent pressure fluctuations .

The separation of the pressure field into two parts needs additional comment. The concept of the pseudosound was introduced by Blokhintsev.<sup>13</sup> The pseudosound field dominates within and near the turbulent region. It decays, however, as  $|X|^{-3}$  whereas the acoustic pressure decays as  $|X|^{-1}$ . Consequently, the acoustic pressure dominates in the far field. Two other differences exist that allow one to separate  $p$  from  $p$ . First, is the relation of pressure to velocity. The fluctuating turbulent pressure ' $p$ ' is proportional to the square of the turbulent velocity fluctuation

( $p \approx \rho_0 V^2$ ) whereas the acoustic pressure 'p' is directly proportional to the acoustic velocity fluctuation ( $p = \rho_0 cu$ ). Turbulent pressure fluctuations are convected only in the direction of the mean flow at approximately the average flow speeds. Acoustic waves travel in all directions with speeds equal to  $c + V \cos \theta$ , where  $\theta$  is the angle between the vector to the observation point and the direction of mean flow. In summary, the pseudosound field has the characteristics of a pressure field in an incompressible flow, being dominated by inertial rather than compressional effects.

### 1.3 A Comparison of Three Calculations

#### 1.3.1 Monopole Source, Frequency-Domain Green's Function

The acoustic field of a turbulent jet is calculated here using a frequency-domain Green's function. Morse and Ingard<sup>14</sup> (Chapter 7.1) consider the sound radiated from a random distribution of volume sources. The source term they consider is proportional to a first time derivative. Ribner's<sup>3</sup> work indicates that the source term should be proportional to a second time derivative; the extra derivative will give an additional factor of  $\omega^2$  in the intensity. The results of Morse and Ingard are correct for a distribution of volume sources, however, the monopole source characteristics of turbulent jets are different from this simple model, to see this compare Eq. 1.4 to Eq. 1.16.

The appropriate modifications are introduced in this section.

The procedure is to first discuss the representation of random sources, then relate this representation to the calculated acoustic field. The source field can only be described in statistical fashion. On the other hand, the instantaneous acoustic field depends on the instantaneous distribution of the sources. The structure of the wave equation embodies this fact in requiring an instantaneous description of the source field. The theoretical task is to reduce all formulas to those which only require statistical information.

Mathematically, one computes the instantaneous acoustic pressure from a complete description of the source. The statistical properties are extracted by computing the magnitude of the Fourier pressure amplitude. It is shown later that the amplitude of the Fourier spectra is proportional to the Fourier transform of the source correlation, the most often used description of random fields.

The technique has its analogue in laboratory procedure. The microphone detects the instantaneous value of the acoustic field. The signal is then Fourier analyzed and averaged to provide a record of the statistical behavior of the acoustic field. Hence, the parallel in

in deducing average properties from a instantaneous ones.

One first discusses the representations of a source  $\rho(\tilde{y}, t)$ . One can equivalently describe its time behavior at point  $\tilde{y}$  by its Fourier transform

$$\rho(\omega, \tilde{y}) = \frac{1}{2\pi} \int_{-T/2}^{T/2} dt \rho(\tilde{y}, t) e^{i\omega t} \quad 1.17$$

To extend the description to spatial variables one takes the multiple Fourier transform

$$\rho(\omega, \tilde{k}) = \frac{1}{16\pi^4} \int_{-T/2}^{T/2} dt \iiint_{\Omega} d^3\gamma \rho(\tilde{y}, t) e^{i\omega t - i\tilde{k}\cdot\tilde{y}} \quad 1.18$$

where the space integration is over the source volume  $\Omega$ .

Now consider the statistical time behavior of the source at point  $\tilde{y}$ . Continuity requires a measurement at one instant be closely related to a measurement made at the next instant. As the time interval between two successive observations increases one expects the measurements to be less and less related to one another. These expectations are quantified by considering the relation between two observations separated by an interval  $\tau$  for all times  $t$ . Taking the average of the product of these two observations yields the source correlation

$$R(\tilde{y}, \tau) = \lim_{T \rightarrow \infty} \frac{1}{T} \int_{-T/2}^{T/2} dt \rho(\tilde{y}, t) \rho(\tilde{y}, t + \tau) \quad 1.19$$

The value of  $R$  at  $\tau = 0$  is the time average source strength.



To extend this function to spatial coordinates consider a similar set of measurements between two points separated by a distance  $\eta$ .

$$R(\tilde{y}, \tilde{\eta}, \tau) = \lim_{T \rightarrow \infty} \frac{1}{T} \int_{-T/2}^{T/2} dt \rho(\tilde{y}, t) \rho(\tilde{y} + \tilde{\eta}, t + \tau) \quad 1.20$$

If the source is homogeneous it is independent of uniform translations of the coordinate system. One defines, for homogeneous systems,

$$R(\tilde{\eta}, \tau) = \lim_{\substack{T \rightarrow \infty \\ \Omega \rightarrow \infty}} \frac{1}{T\Omega} \int_{-T/2}^{T/2} dt \iiint_{\Omega} d^3\tilde{y} \rho(\tilde{y}, t) \rho(\tilde{y} + \tilde{\eta}, t + \tau) \quad 1.21$$

If there is mean flow the turbulent pattern will be convected at some finite speed. With flow  $R(\tilde{\eta}, \tau)$  will not be peaked at  $\tilde{\eta} = 0$ , this is because an eddy located at  $\tilde{y}$  at  $t = 0$  has moved a distance  $\tilde{v}\tau$  by the time  $t = \tau$ . One compensates for the convection by defining the correlation in the system  $\xi = \eta - \tilde{v}\tau$ .

$$R(\xi, \tau) = R(\eta - \tilde{v}\tau, \tau) \quad 1.22$$

Again, consider the point  $\hat{y}$ . Since the descriptions  $R(\tau)$  and  $\rho(\omega)$  are derived from the same source function  $\rho(t)$  one expects the two to be related. Following Morse and Ingard<sup>14</sup> (Chapter 1.3) one computes the Fourier transform of  $R$ .

$$\begin{aligned}
\frac{1}{2\pi} \int_{-\infty}^{\infty} d\tau \rho(\tau) e^{i\omega\tau} &= \frac{1}{2\pi T} \int_{-T/2}^{T/2} d\tau e^{i\omega\tau} \int_{-T/2}^{T/2} dt \rho(t) \rho(t+\tau) \\
&= \frac{1}{2\pi T} \int_{-T/2}^{T/2} dt \rho(t) e^{-i\omega t} \int_{t-T/2}^{t+T/2} d\nu \rho(\nu) e^{i\omega\nu} \\
&= \frac{2\pi}{T} |\rho(\omega)|^2
\end{aligned} \tag{1.23}$$

The Fourier transform of the auto-correlation function over time  $T$  is  $\frac{2\pi}{T}$  times the spectra amplitude  $|\rho(\omega)|^2$  of  $\rho(t)$ .

The extension to spatial coordinates yields

$$\frac{16\pi^4}{\Omega T} |\rho(\omega, \tilde{k})|^2 = \frac{1}{16\pi^4} \int_{-T/2}^{T/2} d\tau \iiint_{\Omega} d^3\eta \rho(\eta, \tau) e^{i\omega\tau - i\tilde{k}\cdot\tilde{\eta}} \tag{1.24}$$

A shift to the system  $\tilde{\xi}$  in the frame of the jet flow, gives

$$\frac{16\pi^4}{\Omega T} |\rho(\omega, \tilde{k})|^2 = \frac{1}{16\pi^4} \int_{-T/2}^{T/2} d\tau \iiint_{\Omega} d^3\xi \rho(\xi, \tau) e^{i\omega(1-M\cos\theta)\tau - i\tilde{k}\cdot\tilde{\xi}} \tag{1.25}$$

where  $M$  is the Mach number and  $\theta$  the angle between the observer and mean flow.

One can now compute the pressure radiated from a stochastic distribution of monopoles via frequency-domain techniques. Start with the forced wave equation, Eq. 1.16. Take the Fourier transform to find

$$\left(\frac{\omega}{c}\right)^2 p(\omega, \tilde{x}) + \nabla^2 p(\omega, \tilde{x}) = \left(\frac{\omega}{c}\right)^2 \rho(\omega, \tilde{x}) \tag{1.26}$$

The Green's function for the Helmholtz equation is

$$G_{\omega}(\tilde{x}|\tilde{y}) = \frac{e^{i k |\tilde{x} - \tilde{y}|}}{4 \pi |\tilde{x} - \tilde{y}|} \quad k = \frac{\omega}{c} \quad 1.27$$

from which one finds

$$\begin{aligned} p(\omega, \tilde{x}) &= \iiint_{\Omega} d^3 \gamma \frac{e^{i k |\tilde{x} - \tilde{\gamma}|}}{4 \pi |\tilde{x} - \tilde{\gamma}|} \left(\frac{\omega}{c}\right)^2 \rho(\omega, \tilde{\gamma}) \\ &\approx \frac{e^{i k x}}{4 \pi x} \left(\frac{\omega}{c}\right)^2 \iiint_{\Omega} d^3 \tilde{\gamma} e^{-i \tilde{k} \cdot \tilde{\gamma}} \rho(\omega, \tilde{\gamma}) \\ &= \frac{e^{i k x}}{4 \pi x} \left(\frac{\omega}{c}\right)^2 (2\pi)^3 \rho(\omega, \tilde{k}) \end{aligned} \quad 1.28$$

where

$$\tilde{k} = \hat{x} k$$

Now compute the magnitude of  $p(\omega, \tilde{x})$  to find

$$|p(\omega, \tilde{x})|^2 = \left(\frac{\omega}{c}\right)^4 \left(\frac{1}{4 \pi x}\right)^2 (2\pi)^6 |\rho(\omega, k)|^2 \quad 1.29$$

However,  $|\rho(\omega, \tilde{k})|^2$  is proportional to the multiple Fourier transform of the autocorrelation  $\mathcal{R}$  of  $\rho$ , by Eq. 1.24 we have

$$|p(\omega, x)|^2 = \left(\frac{\omega}{c}\right)^4 \left(\frac{1}{4 \pi x}\right)^2 \frac{T_{\Omega}}{4 \pi^2} \int_{-T/2}^{T/2} d\tau \iiint_{\Omega} d^3 \eta \mathcal{R}(\eta, \tau) e^{i \omega \tau - i \tilde{k} \cdot \tilde{\eta}} \quad 1.30$$

Transforming to  $\xi$  coordinates by Eq. 1.25 gives

$$|p(\omega, x)|^2 = \left(\frac{\omega}{c}\right)^4 \left(\frac{1}{4 \pi x}\right)^2 \frac{T_{\Omega}}{4 \pi^2} \int_{-T/2}^{T/2} d\tau \iiint_{\Omega} d^3 \xi \mathcal{R}(\xi, \tau) e^{i \omega (1 - M \cos \theta) \tau - i \tilde{k} \cdot \tilde{\xi}} \quad 1.31$$

### 1.3.2 Monopole Source, Time Domain Green's Function

The radiated pressure is here calculated for the same monopole source field, this time using a time-

domain Green's function. The radiated acoustic pressure  $p$ , which is a solution to Eq. 1.16, is determined by the Green's function Eq. 1.6, note that  $G$  is multiplied by  $c^2$  since we are calculating the pressure and not the density.

$$p(\tilde{x}, t) = \int_{-T/2}^{T/2} dt' \iiint_{\Omega} d^3\gamma G(\tilde{x}, t | \tilde{\gamma}, t') \frac{1}{c^2} \frac{\partial^2}{\partial t'^2} \rho(\tilde{\gamma}, t') \quad 1.32$$

$$\text{where } t' = t - \frac{|\tilde{x} - \tilde{\gamma}|}{c} \approx \frac{1}{4\pi x c^2} \iiint_{\Omega} d^3\gamma \frac{\partial^2}{\partial t'^2} \rho(\tilde{\gamma}, t')$$

Here the distance  $\frac{1}{|\tilde{x} - \tilde{\gamma}|}$  is approximated by  $\frac{1}{x}$ ,  $t'$  is the retarded time. Now compute the covariance of  $p$

$$\begin{aligned} p(\tilde{x}, \tau) &= \overline{p(\tilde{x}, t) p(\tilde{x}, t + \tau)} \\ &= \frac{1}{(4\pi x)^2} \frac{1}{c^4} \overline{\iiint_{\Omega} d^3\gamma' \iiint_{\Omega} d^3\gamma'' \frac{\partial^2}{\partial t'^2} \rho(\tilde{\gamma}', t') \frac{\partial^2}{\partial t''^2} \rho(\tilde{\gamma}'', t'' + \tau)} \end{aligned} \quad 1.33$$

$$\text{where } t' = t - \frac{|\tilde{x} - \tilde{\gamma}'|}{c}$$

$$t'' = t - \frac{|\tilde{x} - \tilde{\gamma}''|}{c}$$

Here bars indicate time averages and primes indicate source coordinates.

To proceed one uses the relations given in Goldstein<sup>6</sup> (Chapter 2)

$$\overline{\frac{\partial^2}{\partial t^2} \rho(t) \frac{\partial^2}{\partial t^2} \rho(t + \tau)} = \frac{\partial^4}{\partial \tau^4} \overline{\rho(t) \rho(t + \tau)} \quad 1.34$$

$$\overline{\rho(t+\tau_0)\rho(t+\tau_0+\tau)} = \overline{\rho(t)\rho(t+\tau)} \quad 1.35$$

Eq. 1.34 relates time derivatives to derivatives in the correlation interval  $\tau$ . Eq. 1.35 states that the correlation of a stochastic function is independent of uniform time translations. Substituting  $\tau_0 = \frac{|\tilde{x}-\tilde{y}'|}{c}$  gives

$$\rho(\tilde{x}, \tau) = \frac{1}{(4\pi x)^2} \frac{1}{c^4} \int \dots \int d^3 r' d^3 r'' \frac{\partial^4}{\partial \tau^4} \overline{\rho(\tilde{y}', \tau) \rho(\tilde{y}'', t + \tau + \frac{\tilde{x} \cdot \tilde{\eta}}{c})} \quad 1.36$$

where one approximates

$$\frac{|\tilde{x}-\tilde{y}'|}{c} - \frac{|\tilde{x}-\tilde{y}''|}{c} \approx \frac{\tilde{x}}{x} \cdot \frac{(\tilde{y}'' - \tilde{y}')}{c} = \frac{\hat{x} \cdot \tilde{\eta}}{c} \quad 1.37$$

Here  $\tilde{\eta}$  is the separation vector  $(\tilde{y}'' - \tilde{y}')$ . One now introduces the average position  $\tilde{r}_0 = \frac{\tilde{y}' + \tilde{y}''}{2}$ . The Jacobian of the transform from  $(\tilde{y}', \tilde{y}'')$  to  $(\tilde{r}_0, \tilde{\eta})$  is unity. Hence

$$\rho(\tilde{x}, \tau) = \frac{1}{(4\pi x)^2} \frac{1}{c^4} \int \dots \int d^3 r_0 d^3 \eta \frac{\partial^4}{\partial \tau^4} \overline{\mathcal{R}(\tilde{r}_0, \tilde{\eta}, \tau + \frac{\hat{x} \cdot \tilde{\eta}}{c})} \quad 1.38$$

where, as before,

$$\mathcal{R}(\tilde{r}_0, \tilde{\eta}, \tau) = \overline{\rho(\tilde{r}_0, t) \rho(\tilde{r}_0 + \tilde{\eta}, t + \tau)} \quad 1.39$$

To find the spectral density compute the Fourier trans-

$$\begin{aligned} \text{form of } p(x, \tau) \\ \frac{2\pi}{T} |\rho(\omega, \tilde{x})|^2 &= \frac{1}{2\pi} \int_{-T/2}^{T/2} d\tau e^{i\omega\tau} p(\tilde{x}, \tau) \\ &= \frac{1}{2\pi} \frac{1}{(4\pi x)^2} \left(\frac{\omega}{c}\right)^4 \int \dots \int d^3 r_0 d^3 \eta \overline{\mathcal{R}(\tilde{r}_0, \tilde{\eta}, \tau)} e^{i\omega\tau - i\hat{k} \cdot \tilde{\eta}} \end{aligned} \quad 1.40$$

Where the following identities have been used

$$\int e^{i\omega\tau} \frac{\partial^4}{\partial \tau^4} \rho(\tau) d\tau = \omega^4 \int e^{i\omega\tau} \rho(\tau) d\tau \quad 1.41$$

$$\int e^{i\omega\tau} \rho\left(\tau + \frac{\hat{x} \cdot \hat{n}}{c}\right) d\tau = \int e^{i\omega(\tau - \hat{x} \cdot \hat{n}/c)} \rho(\tau) d\tau \quad 1.42$$

If the source is homogeneous the integral over  $r_0$  yields the source volume  $\Omega$ . Thus,

$$|p(\omega, \hat{x})|^2 = \left(\frac{\omega}{c}\right)^4 \frac{1}{(4\pi x)^2} \frac{T\Omega}{4\pi^2} \int_{-T/2}^{T/2} d\tau \iiint d^3\eta \rho(\eta, \tau) C^{i\omega\tau - i\hat{k} \cdot \tilde{\eta}} \quad 1.43$$

Transferring to the  $\xi$  coordinate system

$$|p(\omega, \hat{x})|^2 = \left(\frac{\omega}{c}\right)^4 \frac{1}{(4\pi x)^2} \frac{T\Omega}{4\pi^2} \int_{-T/2}^{T/2} d\tau \iiint d^3\xi \rho(\xi, \tau) C^{i\omega(-M \cos \theta) - i\hat{k} \cdot \tilde{\xi}} \quad 1.44$$

Inspection shows Eqs. 1.30 and 1.31 are identical to Eqs. 1.43 and 1.44, as was to be demonstrated.

Note that the spatial Fourier transform has its origin in the first order retarded time effects, (see Eq. 1.42). The question "what is the spectral density of the source?" can now be assured without ambiguity. The answer is to consider only the temporal variations at a point.

The answer depends on whether the spectra is computed in the  $\tilde{\xi}$  or  $\tilde{\eta}$  system. It has been shown that the Fourier amplitude spectra of the source is proportional to the Fourier transform of the source correlation  $\mathcal{R}$  (Eq. 1.22). However,  $\mathcal{R}$  depends on the frame

in which it is measured. For moving eddies the turbulent fluctuations seen by a fixed observer will appear much more rapid because of the convection of the random spatial pattern of the turbulence with the flow. The rapid convection of the fluctuations cause the time variation seen by an observer moving with the flow to be much slower than those seen by a fixed observer. In a moving frame the correlation at a point will decay much more slowly.

Figure 1.1 is taken from measurements of the second order time delay correlation carried out by Davies, Fisher, and Barratt.<sup>15</sup> The spacing between lines parallel to the  $\tau$  axis is a measure of the correlation  $\tau$ , the smaller the spacing, the shorter the interval of correlation. The diagram indicates that measurements made in the frame of the jet flow are correlated for longer intervals than those made in a stationary frame.

Note that these considerations do not modify the radiated pressure spectra. Variations in  $R$  from the  $\xi$  to  $\tilde{\eta}$  systems are compensated for by the appearance of the  $(1 - M \cos \theta)$  term in the exponential.

### 1.3.3 Quadrupole Source, Time Domain Green's Function

Now consider the radiated pressure from a stochastic distribution of Reynolds stresses. Here only the major steps in calculating the spectra are

outlined, the reader is referred to the literature<sup>1, 6, 16</sup> for more detailed accounts. The point is Eq. 1.51 which demonstrates that the radiated field has its origin in two mechanisms, turbulence alone and turbulent shear interactions. Eq. 1.13 is the starting point of this analysis. As the observer is in the far-field, where the laws of classical acoustics apply,  $\rho$  can be replaced by  $\frac{p}{c^2}$  to yield

$$p(\tilde{x}, t) = \frac{1}{4\pi} \iiint_{\Omega} d^3\gamma \frac{1}{|\tilde{x} - \tilde{\gamma}|} \frac{\partial^2}{\partial x_i \partial x_j} T_{ij}(\tilde{\gamma}, t') \quad 1.45$$

where

$$T_{ij} = \rho_0 v_i v_j$$

Here  $t'$  is the retarded time,  $\tilde{\gamma}$  the source point and  $\tilde{x}$  the observation point. Twice applying the divergence theorem together with a decay of  $T_{ij}$  faster than  $\frac{1}{y}$  allows a change to differentiation in the observer's coordinates.

$$p(\tilde{x}, t) = \frac{1}{4\pi} \frac{\partial^2}{\partial x_i \partial x_j} \iiint_{\Omega} d^3\gamma \frac{1}{|\tilde{x} - \tilde{\gamma}|} T_{ij}(\tilde{\gamma}, t') \quad 1.46$$

Differentiating and neglecting terms  $\mathcal{O}(x^{-2})$  gives

$$p(\tilde{x}, t) = \frac{1}{4\pi} \frac{x_i x_i}{c^2 x^2} \iiint_{\Omega} d^3\gamma \frac{\partial^2}{\partial t^2} T_{ij}(\tilde{\gamma}, t') \quad 1.47$$

where we have approximated

$$x_i - \gamma_i \approx x_i \quad \frac{1}{|\tilde{x} - \tilde{\gamma}|} \approx \frac{1}{x}$$

Eq. 1.47 implies that if the source is stochastic so is



the radiated pressure field. Now compute the correlation of  $p$  to find

$$\begin{aligned} \rho(\tilde{x}, \tau) &= \overline{p(\tilde{x}, t) p(\tilde{x}, t+\tau)} \\ &= \frac{1}{(4\pi x)^2} \frac{1}{c^4} \frac{x_i x_j x_k x_l}{x^4} \int \dots \int d^3 \gamma' d^3 \gamma'' \frac{\partial^4}{\partial \tau'^4} \overline{T_{ij}(\tilde{\gamma}', t') T_{kl}(\tilde{\gamma}'', t''+\tau)} \end{aligned} \quad 1.48$$

where we have used the identity given in Eq. 1.34. Again, noting the cross correlation of a stationary function is independent of time translation (see Eq. 1.35) and switching to the coordinates  $(\tilde{r}_0, \tilde{\eta})$  (see paragraph following Eq. 1.37) gives

$$\rho(\tilde{x}, \tau) = \frac{1}{(4\pi x)^2} \frac{1}{c^4} \frac{x_i x_j x_k x_l}{x^4} \int \dots \int d^3 r_0 d^3 \eta \frac{\partial^4}{\partial \tau^4} \overline{T_{ij}(\tilde{r}_0, t) T_{kl}(\tilde{r}_0 + \tilde{\eta}, t + \tau + \frac{\tilde{x} \cdot \hat{\eta}}{c})} \quad 1.49$$

The flow is now separated into a mean part  $V$  and a fluctuating part  $v$ . Contracting over the indicies<sup>16, 17</sup> and assuming homogeneous isotropic turbulence gives

$$\rho(x, \tau) = \frac{1}{(4\pi x)^2} \frac{1}{c^4} \int \dots \int d^3 r d^3 \eta \frac{\partial^4}{\partial \tau^4} \left[ \rho_0 v_i'^2 \rho_0 v_i''^2 + 2(\cos^4 \theta + \cos^2 \theta) \mathcal{V}^{-2} \frac{\rho_0 v_i' \rho_0 v_i''}{\rho_0 v_i' \rho_0 v_i''} \right] \quad 1.50$$

where the prime and double prime indicate

$$v_i' = v_i(\tilde{r}_0, t)$$

$$v_i'' = v_i(\tilde{r}_0 + \tilde{\eta}, t + \tau + \tilde{x} \cdot \hat{\eta}/c)$$

The first term in Eq. 1.50 is due to turbulence alone and the second to turbulent shear interactions. To get

the spectral density one computes the Fourier transform of  $p(x, \tau)$  to find

$$|p(\omega, \tilde{x})|^2 = \left(\frac{\omega}{c}\right)^4 \frac{1}{(4\pi x)^2} \frac{T}{4\pi^2} \int \dots \int d^3 r_0 d^3 \eta e^{i\omega\tau - i\tilde{k} \cdot \tilde{\eta}} \left[ R_{1111}(\tilde{\eta}, \tau) + 2(\cos^4 \theta + \cos^2 \theta) V^{-2} R_{11}(\eta, \tau) \right] \quad 1.51$$

where

$$R_{1111}(\tilde{\eta}, \tau) = \overline{\rho_0 v_1^2(\tilde{r}_0, t) \rho_0 v_1^2(\tilde{r}_0 + \tilde{\eta}, t + \tau)}$$

$$R_{11}(\eta, \tau) = \overline{\rho_0 v_1(\tilde{r}_0, t) \rho_0 v_1(\tilde{r}_0 + \tilde{\eta}, t + \tau)}$$

Transforming to moving coordinates  $\xi$  gives

$$|p(\omega, \tilde{x})|^2 = \left(\frac{\omega}{c}\right)^4 \frac{1}{(4\pi x)^2} \frac{T}{4\pi^2} \int \dots \int d^3 r_0 d^3 \xi e^{i\omega(1 - M \cos \theta)\tau - i\tilde{k} \cdot \tilde{\xi}} \left[ R_{1111}(\xi, \tau) + 2(\cos^4 \theta + \cos^2 \theta) V^{-2} R_{11}(\xi, \tau) \right] \quad 1.52$$

Inspection reveals the similarity of Eqs. 1.51

and 1.52 to Eqs. 1.43 and 1.44 and also to Eqs. 1.30 and

1.31. The first terms are identical if the quadrupole

covariance  $R_{1111}$  is replaced by the pressure covariance

$\mathcal{P}$ . In effect,  $\rho_0 v_1^2$  is replaced with the pressure  $\mathcal{P}$ .

This is physically consistent since Bernoulli's equation

requires that incompressible pressure fluctuations be

equal to  $\frac{\rho_0 V^2}{2}$ .

The second term is the "shear noise" that origin-

ated in the turbulent shear interactions. By assuming a

specific model for the correlations  $R_{1111}$  and  $R_{11}$

Ribner shows that the contribution to the time average

intensity is approximately equal. The shear noise

modifies the angular distribution by  $\cos^4 \theta + \cos^2 \theta$ . Ribner further points out that the self noise peak is shifted to a frequency above the shear noise peak by a factor of  $\sqrt{2}$ . For example, if  $R_{11} \propto e^{-(\omega_0 \tau)^2}$  one expects  $R_{1111} \propto e^{-2(\omega_0 \tau)^2}$  which gives the factor of  $\sqrt{2}$ . This point is important in that the emphasis in the thesis has been to collate the results with a single correlation function. Such attempts consistently fail to account for low and high frequency regimes simultaneously. If the low frequency results are in agreement with the data, the high frequency spectra will disagree and vice versa.

Experiments<sup>18, 19</sup> reveal that there is an additional angular dependence due to the refraction of sound through the shear layer. All these calculations assume that once the sound is generated it travels through a medium at rest. This is not so, especially for sources near the centerline of the jet. Sound emitted from this region has to travel through the velocity gradients that separate the center of the jet from the ambient atmosphere. The complete solution to refraction through axisymmetric shear layers in three dimensions is, as yet, unsolved. Results are available in two dimensions for refraction through one<sup>20</sup> and two<sup>21</sup> shear layers.

### 1.3.4 Velocity Intensity and Total Power

Three separate methods have been used to calculate  $|p(\omega, \tilde{x})|^2$ . This quantity was chosen for discussion as it is the one measured in the laboratory with the microphone and spectrum analyzer. However, it is not the only quantity of interest. Other acoustical quantities are often required, which are here derived from the Fourier amplitude spectra.

The radial acoustic intensity at frequency

$$f = \frac{\omega}{2\pi} \text{ is}$$

$$I(\omega, \tilde{x}) = \frac{\text{Re} [p(\omega, \tilde{x}) e^{-i\omega t}] \text{Re} [\hat{x} \cdot \tilde{U}(\omega, \tilde{x}) e^{-i\omega t}]}{4} \quad 1.53$$

$$= \frac{1}{4} [\rho(\omega, \tilde{x}) \tilde{U}(\omega, \tilde{x})^* + \rho(\omega, x)^* \tilde{U}(\omega, x)] \cdot \hat{x}$$

In the far field the velocity is radial and equal to the pressure divided by the free space impedance  $\rho_0 c$ . Hence,

$$I(\omega, \tilde{x}) = \frac{1}{2} \frac{|p(\omega, \tilde{x})|^2}{\rho_0 c} \quad 1.54$$

Integrating over a sphere of radius  $x$  gives the power radiated at frequency  $\frac{\omega}{2\pi}$ .

$$\Pi(\omega) = \iint_A I(\omega, \tilde{x}) dA \approx 4\pi x^2 \frac{|p(\omega, x)|^2}{2 \rho_0 c} \quad 1.55$$

The approximation becomes exact if the radiation is isotropic.

One can also construct the time average

intensity at  $\tilde{x}$  by converting a time integral into a frequency one. In the far field

$$I(\tilde{x}) = \frac{1}{\rho_0 c T} \int_{-T/2}^{T/2} |p(\tilde{x}, t)|^2 dt$$

$$= \frac{2\pi}{\rho_0 c T} \int_{-\infty}^{\infty} |p(\omega, \tilde{x})|^2 d\omega$$
1.56

The total time average power is the

$$\Pi = \iint_A I(\tilde{x}) dA \approx 4\pi x^2 \frac{2\pi}{\rho_0 c T} \int_{-\infty}^{\infty} |p(\omega, \tilde{x})|^2 d\omega$$
1.57

Where again the approximation is exact if the radiation is isotropic.

#### 1.4 Comments on the Turbulent Correlation

##### 1.4.1 Choice of the Correlation Function

The crucial quantity in determining sound radiated from turbulence is the space time correlation within the turbulent jet. It is known for homogeneous turbulent processes that the velocity fluctuations are near Gaussian. Townsend's<sup>22, 23</sup> investigation of the homogeneous turbulence behind wire mesh screens has established that the velocity correlations in space are near Gaussian. Furthermore, it has been established that the velocity fluctuations at a single point are Gaussian to within experimental error.

The data on the free jet demonstrate the situation is considerably more complex. Figure 1.2 shows the

development of a round initially laminar subsonic jet from a nozzle of diameter  $D$ . The annular region about the jet becomes turbulent and spreads linearly outward and inward. This region of turbulence progressively diminishes the laminar, or potential, core until it is completely obliterated four to six diameters downstream.

Lilley<sup>15</sup> has organized the data on round jets with a view towards acoustic applications. One result is that the turbulent intensity varies radially as a universal function of  $(r - D/2)/\alpha$ . Here  $\alpha$  is the scale of variation and  $r$  the distance from the jet axis. Recent work by Uberoi and Singh<sup>24</sup> on two dimensional jets at 45 diameters in the fully developed region, show that such intensity variations may be measurement errors due to time averaging. The usual measurements are made by time averaging data from probes fixed in space, Singh records the temperature fluctuations by shooting a probe across the jet at high speeds. Each record was shifted to have a common center and averaged. The resulting profiles showed mean square fluctuations which are quite flat, indicating homogeneous intensity profiles. By averaging the records without this adjustment they were able to reproduce the two humped curve in agreement with stationary probes. This indicates that the jet itself is well mixed, but swings from side to side. A

stationary probe will randomly measure ambient and jet conditions thereby recording an apparent fluctuation where there are none.

Aside from intensity variations, there is also the problem of scale variations along the length of the jet. Lassiter<sup>25</sup> has demonstrated that both the longitudinal and radial scales were found to increase with the axial distance. Goldstein and Rosenbaum<sup>17</sup> have developed a theory for the axisymmetric jet which can deal with such variations. Roughly speaking, the jet is sliced perpendicular to its axis into a series of disks, each of which radiates independently.

Ribner<sup>63</sup> has explored the experimental consequences of such variations. He correlates the velocity fluctuation at various axial positions in the jet with the radiated pressure at a point in the far field. He deduces that different portions of the jet contribute to different frequency regions in the emitted spectra (Fig. 1.2). In particular, he finds that the high frequency sound is generated near the nozzle and the low frequency sound downstream. Such observations are consistent with the scale changes observed by Lassiter.<sup>25</sup>

Despite marked departures from isotropy in real jets, simple isotropic models have been used with

some success in accounting for the observed behavior of jets. Gaussian correlation, in particular, is used in view of the fact that it accounts for the structure of homogeneous turbulence. Recall that the measurements of Davies<sup>15</sup> et al have confirmed that the turbulent fluctuations are convected with the flow. This indicates that only in the moving frame,  $\xi$ , do the space and time functions separate into a product of two functions. Let  $\alpha$  be the length scale and  $\omega_0$  be the inverse of the time scale. In the frame moving with the jet speed  $V$

$$R(\xi, \tau) = \frac{1}{\rho^2 c} \left\{ (\omega_0 \tau)^2 + \frac{\xi_x^2 + \xi_y^2 + \xi_z^2}{\alpha^2} \right\} \quad 1.58$$

in the lab frame

$$R(\eta, \tau) = \frac{1}{\rho^2 c} \left\{ (\omega_0 \tau)^2 + \frac{(\eta_x + V\tau)^2 + \eta_y^2 + \eta_z^2}{\alpha^2} \right\} \quad 1.59$$

For low subsonic speeds ( $V \approx 0$ ) the two are identical.

Ribner<sup>3</sup> has used the form given in Eq. 1.59 to account for the directionality observed in the intensity measurements due to convection. Meecham<sup>26</sup> uses the same functional form to account for the high frequency sound spectrum in terms of an integral over the turbulent energy spectrum. Incidentally, Ribner works with a simple monopole model whereas Meecham works from Lighthill's quadrupole model.



Simple isotropic turbulence with the Gaussian spacetime correlation is assumed throughout this thesis. Such assumptions allow quantitative calculations of the Fourier spectra to be made which will then be directly compared to the data. These assumptions will enable one to account for the spectra in limited frequency bands. Detailed agreement both above and below the Strouhl peak is not possible due to real variations in the jet turbulence.

#### 1.4.2 The Eighth Power Law

Using only dimensional arguments Lighthill showed that total acoustic power should vary as the eighth power of the mean velocity. These arguments are reproduced here for future reference.

Recall that the power is the integral of the radiated intensity over a surface enclosing the source (Eq. 1.57). The far field intensity is the time averaged pressure divided by  $\rho_0 c$  (Eq. 1.56). The mean square pressure is the value of the pressure covariance at  $\tau = 0$ . One further assumes that the source is isotropic. Substitution of Eq. 1.50 into Eq. 1.57 yields

$$\mathcal{P} = \frac{1}{4\pi} \frac{\rho_0}{c^5} \int \dots \int d^3 r_0 d^3 \eta \frac{24}{\partial \tau^4} \overline{V_i'{}^2 V_i''{}^2} \quad 1.60$$

Let  $D$  be the jet diameter. The intergration over  $r_0$  yields the source volume  $\Omega$  which is approximately  $D^3$ .

The time derivative  $\frac{\partial}{\partial \tau}$  is proportional to a characteristic frequency. It is known from experiment that the jet noise peaks at a frequency  $f_s \approx .2 \frac{V}{D}$ , this characteristic value is known as the Strouhl frequency. The ratio of the observed peak frequency to the value  $\frac{V}{D}$  is the Strouhl number, which is approximately constant over a wide range of Reynolds numbers, flow speeds and jet diameters. This allows one to set  $\frac{\partial}{\partial \tau} \approx \frac{V}{D}$ . The turbulent velocity  $v$  increases monotonically with the mean flow and is approximately  $.1V$ . Substituting these values into Eq. 1.60 gives

$$\pi \approx \frac{\rho_0 V^8 D^2}{C^5} \quad 1.61$$

Olsen<sup>27</sup> et al. and von Gierke<sup>28</sup> have collated the experiment on model jets and aircraft jets. They find good agreement for subsonic flow. Supersonic<sup>29</sup> data indicates departures from the eighth power law, in this regime the power goes approximately as the third power of velocity. One can easily see this if one recalls that the mechanical power in the jet is  $\frac{\rho_0 V^3 D^2}{2}$ . The efficiency predicted by the eighth power law is the ratio of acoustic to total power, which is  $M^5$ . This can only hold for low velocities, at some point the acoustic power must be reduced, less it exceed the mechanical power of the jet.

### 1.4.3 The Kolmogorov Inertial Subrange

Now consider the spectral distribution of acoustic energy from a dimensional standpoint. The jet velocity and diameter are not sufficient scales, as these combine to give only a single characteristic frequency. To get frequency variations one must scale the equations to the eddy size  $\eta$  and the power per unit mass  $\epsilon$ .

In the turbulent region the particular form of the driving mechanism that maintains the turbulence must influence its structure, at least for those eddies whose size is comparable to the driving mechanism. These large eddies transmit their energy to the smaller eddies via non linear coupling, eventually the energy is dissipated as heat in the microscale eddies. Kolmogorov postulates that there is a range of eddy sizes, termed the inertial subrange, for which the statistical properties are supposed to be independent of both the driving mechanism and the viscosity. The size of the eddies in this range is smaller than the size  $D$  of the large eddies and larger than the size  $d \approx \frac{\nu}{\epsilon^{1/3}}$  of the heat dissipating eddies.

Morse and Ingard<sup>14</sup> (Chapter 11.4) have calculated the acoustic spectra implied by such considerations. They use a Lighthill model neglecting turbulent shear

interactions, retarded time effects, and convection by the mean flow. Under this set of restrictions they find

$$\pi(\omega) \propto \frac{1}{4\pi x^2} \rho_0 c^2 M^{10.5} \frac{1}{(kD)^{3.5}} \quad \omega \gg \frac{CM}{L} \quad 1.62$$

valid for frequencies greater than the Strouhal frequency.

Two factors emerge. First the spectral intensity increases as a high power of the velocity, here given as 10.5. Second the intensity, at a given velocity, falls off as a  $\omega^{-3.5}$ .

This yields a 10.5 DB drop in spectral amplitude per octave. That is

$$\frac{\Delta SPL}{\text{octave}} = 10 \log \frac{\pi(2\omega)}{\pi(\omega)} \approx -10.5 \text{ DB} \quad 1.63$$

#### 1.4.4 Gaussian Correlation and the Relation Between the Turbulent and Acoustic Spectra

Some implications of Gaussian correlation using Ribner's model are worked out here. For simplification attention is restricted to low subsonic speeds. It is further assumed that the source volume is small enough so what the correlation distance can be set to zero. This is equivalent to neglecting retarded times. For a more detailed discription including the effects of convection and finite spatial correlation see Ribner's<sup>4</sup> account. In this limit

$$R(\vec{r}, \tau) = \rho^2 \equiv S(\vec{r}) e^{-(\omega_0 \tau)^2} \quad 1.64$$

where  $\Xi$  is the effective source volume (note  $\delta$  has dimensions of  $L^{-3}$ ). The spectral energy distribution of the turbulence is the Fourier transform of  $\mathcal{R}$

$$\frac{2\pi}{T} |\rho(\omega, 0)|^2 = \frac{\overline{\rho^2} \Xi}{2\sqrt{\pi} \omega_0} e^{-\left(\frac{\omega}{2\omega_0}\right)^2} \quad 1.65$$

The energy is maximum at zero and falls off monotonically as the angular frequency  $\omega$  increases. This is a direct consequence of the form of the correlation, as the Fourier transform of a Gaussian function is Gaussian. Note that experiments on turbulence behind grids show the energy peaked at some non-zero frequency, which implies that some error is introduced by the present approximation. The error is not too large if the peak frequency is approximately zero.

To compute the radiated acoustic pressure spectra one carries out the integration indicated in Eq. 1.30 to find

$$\frac{2\pi}{T} |\rho(\omega, x)|^2 = \left(\frac{\omega}{c}\right)^4 \frac{1}{(4\pi x)^2} \frac{\overline{\rho^2} \Xi}{2\sqrt{\pi} \omega_0} e^{-\left(\frac{\omega}{2\omega_0}\right)^2} \quad 1.66$$

Note that the ratio of acoustic to turbulent amplitude goes as the fourth power of  $\omega$

$$\frac{|\rho(\omega, x)|^2}{|\rho(\omega, 0)|^2} \propto \omega^4 \quad 1.67$$

This factor implies that the radiative efficiency increases as the fourth power of the frequency. This

has the effect of shifting the acoustic intensity maximum to  $\omega = 2^{3/2}\omega_0$ . Eq. 1.66 implies a spectra that behaves qualitatively as free space jet noise. That is the level increases with frequency to a maximum and then falls off as the frequency is increased further. Dimensionally one requires  $\omega_0 \approx \frac{V}{D}$ . The frequency regime in which Kolmogorov's assumptions should apply coincide with the region of frequencies greater than  $\omega_0$  deduced from Gaussian correlation. They are in qualitative agreement in that both predict a decrease in level with increasing frequency. However, the Gaussian model does not give the simple power law that was deduced before.

Figure 1.3 compares the spectra predicted in Eq. 1.66 to that detected from a free jet. The microphone was located at  $90^\circ$  to the jet axis so as to minimize turbulent shear and convection effects. The plots were generated for three characteristic values of  $\omega_0$  and the amplitudes shifted to coincide the low, middle, and high portions of the frequency plot. The figure indicates that an isotropic description of the jet fails to account for all the details of the observed spectra. In particular, a function that accounts for the high frequency end cannot also account for the low frequency sound. Discrepancies of this

form will occur in our evaluation of the spectra for systems with boundaries. However, it will always be possible to get close agreement for limited portions of the spectra.

To calculate the total power one first evaluates the time average intensity at point  $\tilde{x}$  (Eq. 1.56) and then integrates over the surface of a sphere of radius  $x$  (Eq. 1.57) to find

$$\begin{aligned} \pi &= \iint_A dA \int_{-\infty}^{\infty} d\omega \frac{2\pi}{\rho_0 c T} |p(\omega, x)|^2 \\ &= \frac{3}{4\pi} \frac{\Omega \Xi \omega_0^4}{\rho_0 c^5} \overline{p_0^2} \end{aligned} \quad 1.68$$

One can now use dimensional analysis to evaluate this expression. The spectra maximum occurs at the Strouhl frequency, which is given approximately by  $\omega_0 \approx \frac{V}{D}$ . The pressure fluctuations  $p$  are proportional to the square of the turbulent velocity fluctuations. Recalling that the turbulent velocity fluctuations are proportional to the mean gives  $p \propto \beta V^2$ . Letting  $\Xi$  and  $\Omega$  scale as the cube of the jet diameter  $D^3$  gives

$$\pi \propto \frac{\rho_0 V^8 D^2}{c^5} \quad 1.69$$

The eighth power law is then equivalently deduced from a monopole or quadrupole source field.

### 1.5 Summary

Chapter One serves as an introduction to

Lighthill's acoustic analogy analysis of turbulent jet noise. Ribner's reduction of the source field to an equivalent monopole distribution is presented.

The statistical properties of the radiated acoustic field were calculated in three separate fashions. The first concerned the prediction of sound from a monopole source distribution via frequency-domain analysis. The results are identical to the same analysis using time-domain techniques. The parallel development clarifies certain details of the calculation. The third calculation proceeded from the quadrupole source field via time domain techniques. By comparison one finds that the isotropic monopole model neglects turbulent shear interactions. Aside from this the predictions are identical.

To proceed one needs the source correlation, i.e., a statistical description of the turbulent fluctuations. Observations on homogeneous turbulence have indicated that an isotropic Gaussian distribution is appropriate. The results of such an assumption are compared to those of dimensional analysis and found to be in qualitative agreement. The drawback is that turbulent inhomogeneities cannot be accounted for, this limits comparison of data and theory to limited portions of the spectra. However, such a model enables one to make numerical predictions



for systems with boundaries and will be used in  
Chapters Two and Three.

## 2. EXCITATION OF AXIAL PIPE MODES

### 2.1 Introduction

Now consider the effect of boundary conditions on the spectra of sound emitted by turbulence. Herein the flow excitation of an axial pipe of uniform cross section  $A$  and length  $L$  is examined. The problem is reduced to one dimension, the boundary conditions are the reflection coefficients at the ends.

In the most elementary treatment of the plane wave eigenmodes of an open ended pipe it is assumed that the ends are pressure nodes. Hence, the pipe resonates at frequencies  $f_n = \frac{nc}{2L}$ . With mean flow, one must account for the difference in phase speed for a wave travelling with the flow,  $c_p = c(1+M)$ , and against the flow,  $c_p = c(1-M)$ . With flow the pipe eigenmodes are  $f_n = \frac{nc(1-M^2)}{2L}$ . The acoustic response of the pipe to an oscillating source will be greatest when the source frequency equals an eigenfrequency.

The ends of the pipe, however, are not perfect reflectors of the incident intensity. There is always some portion of the incident wave that radiates out the end. Ingard and Singhal<sup>30</sup> have demonstrated that the departure from perfect reflection increases with flow. This implies that the eigenmodes are damped by the sound radiated out of the ends of the

pipe. The response of a pipe at its eigenfrequencies diminishes with increasing flow.

Herein the response of the pipe to the turbulence in the air flow itself is investigated. A cylindrical pipe was connected to a plenum chamber and then to a pump (Fig. 2.2). The mean flow was varied from Mach 0.0 to Mach 0.5. A microphone, placed several diameters in front of the inlet, detected the resulting acoustic field. The signal was then spectrum analyzed, an average of 256 spectra was computed by a separate device, at each flow speed, and then plotted.

One observes that at low flow speeds the pressure spectra varies periodically with frequency, with peaks at the eigenfrequencies. As the flow speed increases the peaks at the eigenfrequencies are no longer there, the pressure spectra resembles the smooth variation with frequency seen in free space jet noise (Fig. 2.1). The results are consistent with the observed behavior of the reflection coefficients.

In the theoretical section, Ingard's<sup>31</sup> construction of a Green's function from the empirical pressure reflection coefficients is presented. The response of a pipe to a turbulent field with Gaussian correlation is predicted with this Green's function. This model accounts for the observed changes in spectra with flow.

## 2.2 Experiment

### 2.2.1 Apparatus and Procedure

The experimental apparatus is shown schematically in Fig. 2.2. A small cylindrical pipe was connected to a pump through a plenum chamber. The pressure in the plenum was lowered so as to draw air through the pipe at flow speeds to to Mach .5. The mass flux was monitored by a calibrated orifice downstream of the plenum.

A microphone was placed several diameters in front of the inlet at an angle  $\theta$  to the pipe axis. The signal was amplified and spectrum analyzed in the zero to ten kilocycle range. A second microphone, connected to a sound level meter, was used to evaluate the C weighted intensity as a function of the angle. Additional measurements were made with the microphone in the chamber. The discussion will concentrate, however, on the upstream measurements.

Consider the placement of the microphone. In the chamber, the acoustic wave from the pipe must first pass through the exit jet, where it is refracted, before it reaches the microphone. Apart from this, the turbulent noise from the exit jet completely masks the pipe noise, which makes detection of the pipe modes impossible. If the microphone were mounted in

the pipe in addition to the acoustic wave it would detect the turbulent pressure fluctuations in the mean flow. The acoustic pressure also depends on the axial position of the microphone. If it was located at a node for a given mode the pressure amplitude at this frequency is not detected. The problem is further complicated by the fact that the node location depends on the flow speed since the effective length depends on the mean flow. The final option is to mount the microphone in front of the inlet. This has its own problems, the pressure spectra is multiplied by  $\omega^2$  due to the radiation impedance of free space. In addition, there is some dependence on the angle  $\theta$  due to the finite size of the inlet. However, the transfer function for these effects is independent of the Mach number, it is this condition that motivates measurements in front of the inlet.

The upper limit on flow speed of Mach .5 is due to the vena contracta. The flow entering the pipe contracts to an area six-tenths the pipe cross section. The mass flux is maximum when the flow speed at the contraction is sonic. The mass flux in the pipe is identical to that in the vena contraction, hence the velocity in the pipe is about six-tenths that in the contraction. This means the maximum flow speed in the pipe is approximately half the speed of sound.

### 2.2.2 Variation with Pipe Length

Herein it is established that it is the axial modes of the pipe which are excited. In the simplest model of a pipe open at both ends the wavelength of the fundamental is twice the pipe length. It follows that the fundamental frequency is inversely proportional to the pipe length, since  $f = \frac{c}{L}$ . Since overtones are harmonics the frequency interval between modes is equal to the fundamental and should therefore show the same dependence on length.

If one accounts for variations with flow speed and phase changes at the ends the frequency of the  $n^{\text{th}}$  mode is given by

$$f_n = \frac{\eta c (1 - M^2)}{2(L + \delta_o + \delta_L)} \quad 2.1$$

Where  $\delta_o$  and  $\delta_L$  are the end corrections which give the phase shifts  $\phi = \pi + \frac{2k\delta}{1 - M^2}$ . Ingard and Singhal find  $\delta_o \approx \delta_L \approx .3D(1 - M^2)$ . It follows that the interval between peaks is given by

$$\Delta f = f_i = \frac{c}{2L \left[ \frac{1}{1 - M^2} + .6 \frac{D}{L} \right]} \quad 2.2$$

To check this prediction a 1" diameter pipe was examined for lengths from 2" to 18" in 2" increments.

The flow speed in the pipe was held at a constant value of Mach .14. With the exception of 2" pipe the data agrees

with the prediction in Eq. 2.2. The 2" case is an example of orifice screech which is discussed in Chapter Four. The length test demonstrates it is the axial modes which are excited (Fig. 2.3).

### 2.2.3 Variation With Flow Speed

There is an additional way to check for axial modes. That is to monitor the variation in frequency with mean flow. The prediction is that the fundamental frequency is reduced as the flow speed increases. This result can be understood if one recalls that the sound is convected with the mean flow. The time for a wave to travel downstream is  $\frac{L}{c+V}$  and back upstream is  $\frac{L}{c-V}$ . The frequency is inversely proportional to the period to complete such a cycle and is given by  $f_1 = \frac{c}{2L} (1-M^2)$ .

To check this variation, spectra were obtained for a 1/2" inner diameter pipe 12" long with a 1/16" wall. The microphone was 2" in front of the inlet. The pressure drop across the pipe was set and the spectra plotted from zero to ten kilohertz. The flow speed was determined from the pressure drop and from a calibrated orifice downstream. Figure 2.1 is an example of spectra taken with this setup. Pronounced excitation only occurs for flow speeds up to Mach .3, the fundamental varies approximately 10% in this range. As the

observed bandwidth is about 50% of the fundamental frequency some comment on data reduction is advisable.

The experimenter has two options to determine variations with flow. One is to study the location of the fundamental,  $f_1$ , and the other is to measure the spacing between peaks,  $\Delta f$ . In a frequency analysis the minimum error is the channel width of the analyzer, in these experiments this is always  $\frac{1}{200}$  of the maximum frequency. Graphically, this is approximately the line width of the pen. Assume one chooses to locate the fundamental. The frequency range is set to 1,000 Hz and the instrument resolution is 5 Hz. However, the resonant peak has a finite bandwidth which is approximately one half the separation between modes. The resonant peak, or center, is extremely difficult to determine.

Now assume that the average spacing between peaks is studied. The frequency range is set to 10,000 Hz and the instrument resolution is 50 Hz. However, a large number of modes are now in evidence and the average spacing can be determined with great accuracy. If  $n$  modes are excited in a range  $F$  the spacing is simply  $\Delta f = \frac{F}{n}$ . So long as a large number of modes are evident the measurement is quite accurate. If, however, the flow speed is above Mach .3 the modes are overdamped and neither method



is adequate.

Figure 2.4 presents an analysis of  $\Delta f$  versus mean flow. The error bars are set to 50 Hz, i.e., the resolution of the spectrum analyzer. At low flow speeds it is clear that the accuracy is much better than this. Only at high flow speeds, where the modes are heavily damped, does the error approach the resolution limit. The frequency shifts are clearly those predicted in Eq. 2.2. Hence, the second test establishes the fact that it is the axial pipe modes which are excited.

Given the fact that the axial modes are excited one now has at his disposal an independent means of measuring the flow speed. This is to measure the interval between modes and calculate what flow speed is necessary to produce this interval. The flow speed determined in this fashion agrees with that determined by the pressure drop to  $\pm$  Mach .05. The acoustic calibration of flow speed is used in Figure 2.1. The data in Figure 2.4 is based on flow speeds calculated from the pressure drop across the inlet, and there is no circular reasoning used in the evaluation of the shifts with flow speed.

#### 2.2.4 Variation with Microphone Placement

This section establishes the acoustic field for different microphone locations. A cylindrical pipe

of 1" inner diameter and 1/16" walls was used. Pipe lengths from 2" to 18" in 2" increments at flow speeds of Mach .07, .11 and .14 were investigated. Acoustic spectra were taken at 0°, 45° and 90° to the pipe axis 12" from the inlet.

With the exception of the 2" pipe, the excitation of axial modes was evident for the entire range explored. In addition to spectra, intensity measurements were taken at 10° increments from 0° to 90°, (Figure 2.13 to 2.21). Again, excepting the 2" length the variation is smooth and approximately independent of angle. There is some decrease in level, approximately 2DB, as the microphone travels from a maximum at 0° to a minimum at 90°. This may be suppression of the high frequencies by interference effects due to the finite size of the inlet.

In addition spectra measurements were made with the microphone in the plenum chamber. No mode excitation was observed. The spectra in the chamber is dominated by the exit jet noise. Figure 2.5 plots the C weighted SPL for a microphone in the chamber versus one on axis in front of the inlet. Before comparing plots the increase in level due to chamber reverberation must be determined. The screech data from the 2" pipe provides this calibration as the screech level far exceeds any

turbulent noise at the inlet or exit. At Mach .14 the screech is greatest, the level in the chamber exceeds that outside by 10DB. One concludes that, all other things being equal, chamber measurements should exceed exterior measurements by 10DB. However, the observed level changes for 4" to 18" pipes are approximately 30DB. This can only be accounted for by noting the sound from the exit jet dominates the acoustic field in the chamber.

Of interest is the fact that the sound level, for 4" to 18" pipes, is independent of length. If boundary layer turbulence along the pipe walls was the sound source, the level would increase with length. It does not, therefore the spectra is determined by inlet and exit conditions. This implies that in a study of self noise of duct liners great care must be taken to separate end effects from sound generated in pipes.

#### 2.2.5 Effect of Liners

This experiment considers the effect of an absorbent liner on the spectra. A 1-1/2" inner diameter pipe was lined with a 1/4" thick blanket of Scott acoustic foam. Lengths from 2" to 18" in 2" increments were examined for velocities from Mach .07 to .20. For lengths greater than 6" no evidence of mode excitation occurred. For lengths below 6" only the first or second mode was detected, and these were severely damped.

The behavior is expected, the longer the path length the greater the acoustic damping. No increase in level due to liner roughness was observed.

### 2.3 Theory

#### 2.3.1 On Distinguishing Mean Flow Effects From Turbulent Fluctuations

Consider the complete mass and momentum equations for an inviscid non heat conducting compressible fluid.

These are

Mass Conservation

$$\frac{\partial \rho}{\partial t} + \frac{\partial \rho w_j}{\partial x_j} = 0 \quad 2.3$$

Momentum Conservation

$$\frac{\partial \rho w_i}{\partial t} + \frac{\partial \rho w_i w_j}{\partial x_j} + \frac{\partial p}{\partial x_i} = 0 \quad 2.4$$

Where  $w_i$  is the total fluid velocity. One must separate the velocity fluctuations from the mean flow velocity  $V_1$ .

Thus set

$$v_i = w_i - V_1 \delta_{i1}$$

First transform the mass equation to find

$$\left[ \frac{\partial}{\partial t} + V_1 \frac{\partial}{\partial x_1} \right] \rho + \frac{\partial \rho v_j}{\partial x_j} = 0 \quad 2.5$$

Before making a similar substitution in the momentum equation one first transforms it to a more suitable form.

Subtract  $w_i$  times Eq. 2.3 from Eq. 2.4 to get the

momentum equation

$$\rho \left[ \frac{\partial}{\partial t} + w_j \frac{\partial}{\partial x_j} \right] w_i + \frac{\partial p}{\partial x_i} = 0 \quad 2.6$$

Eq. 2.6 is the more familiar expression used in fluid mechanics. Substituting  $v_i + v_1$  for  $w_i$  one finds

$$\rho \left[ \frac{\partial}{\partial t} + v_1 \frac{\partial}{\partial x_1} \right] v_i + \rho v_j \frac{\partial}{\partial x_j} v_i + \frac{\partial p}{\partial x_i} = 0 \quad 2.7$$

Add  $v_1$  times Eq. 2.5 to Eq. 2.7 to find

$$\left[ \frac{\partial}{\partial t} + v_1 \frac{\partial}{\partial x_1} \right] \rho v_i + \frac{\partial}{\partial x_j} \rho v_i v_j + \frac{\partial p}{\partial x_i} = 0 \quad 2.8$$

Eqs. 2.5 and 2.8 are the exact mass and momentum equations written in a form that separates the constant mean flow  $v_1$  from the velocity fluctuation  $v_i$ . To get the wave equation multiply Eq. 2.5 by the convective derivative  $\frac{\partial}{\partial t} + v_1 \frac{\partial}{\partial x_1}$  and subtract the result from the gradient,  $\frac{\partial}{\partial x_i}$ , of Eq. 2.8. This gives

$$\left[ \frac{\partial}{\partial t} + v_1 \frac{\partial}{\partial x_1} \right] \rho - \frac{\partial^2}{\partial x_i^2} p = \frac{\partial^2}{\partial x_i \partial x_j} \rho v_i v_j \quad 2.9$$

Assuming an adiabatic pressure density relation gives

$$\frac{1}{c^2} \frac{D^2}{Dt^2} p - \nabla^2 p = \frac{\partial^2}{\partial x_i \partial x_j} \rho v_i v_j \quad 2.10$$

where

$$\frac{D}{Dt} = \frac{\partial}{\partial t} + v_1 \frac{\partial}{\partial x_1}$$

Assume that the acoustic portion of the Reynolds stresses negligible, i.e.,  $v_i v_j = (v_i + u_i)(v_j + u_j) \approx v_i v_j$ .

If the turbulent fluctuations are approximately incompressible we have

$$-\nabla^2 \rho = \frac{\partial^2}{\partial x_i \partial x_j} \rho_0 v_i v_j \quad 2.11$$

which we have used  $\rho = p + \rho$ . Using the same approximation as in Eq. 1.16 one finds

$$\frac{1}{c^2} \frac{D^2}{Dt^2} p - \nabla^2 p = -\frac{1}{c^2} \frac{D^2}{Dt^2} \rho \quad 2.12$$

To reduce the problem to one dimension take the average over the cross section. One finds

$$\frac{1}{c^2} \frac{D^2}{Dt^2} P_{AVG} - \frac{\partial^2}{\partial x^2} P_{AVG} = -\frac{1}{c^2} \frac{D^2}{Dt^2} \rho_{AVG} \quad 2.13$$

where  $P_{AVG} = \frac{1}{A} \iint \rho \, dy \, dz$

$$\rho_{AVG} = \frac{1}{A} \iint \rho \, dy \, dz \quad 2.14$$

Taking the Fourier transform gives

$$(1 - M^2) \frac{\partial^2}{\partial x^2} p(\omega, x) + 2i k M \frac{\partial}{\partial x} p(\omega, x) + k^2 p(\omega, x) = -\left(k + i M \frac{\partial}{\partial x}\right)^2 \rho(\omega, x) \quad 2.15$$

where

$$p(\omega, x) = \frac{1}{2\pi} \int_{-\infty}^{\infty} dt P_{AVG} e^{i\omega t} \quad 2.16$$

$$\rho(\omega, x) = \frac{1}{2\pi} \int_{-\infty}^{\infty} dt \rho_{AVG} e^{i\omega t}$$

### 2.3.2 The Green's Function

The linear acoustic response of an open-ended pipe is given by the Green's function. This will be constructed here from the empirical pressure reflection coefficients at the ends following Ingard's<sup>31</sup> procedure.

A coordinate system is used such that the inlet is at  $x = 0$  and the exit at  $x = L$ . The boundary conditions are the pressure reflection coefficients  $R_0$  and  $R_L$ . It is assumed that these are given for all values of the mean flow.

Consider a harmonic source of unit strength located at  $x = x_0$ . The pressure field induced by this source is the Green's function  $G_\omega(x|x_0)$  which solves

$$(1 - M^2) \frac{\partial^2 G}{\partial x^2} + 2i k M \frac{\partial G}{\partial x} + k^2 G = -\delta(x - x_0) \quad 2.17$$

To develop the Green's function one specifies the acoustic field to the right and left of the source point (subscript  $r$  and  $l$ ) as the sum of a wave propagating with (subscript  $+$ ) and against (subscript  $-$ ) the mean flow.

$$\begin{aligned} G_\omega &= p_{e-} e^{-ik_-x} + p_{e+} e^{+ik_+x} & 0 < x < x_0 \\ G_\omega &= p_{r-} e^{-ik_-x} + p_{r+} e^{+ik_+x} & x_0 < x < L \end{aligned} \quad 2.18$$

where

$$k_{\pm} = \frac{\omega}{c(1 \pm M)}$$

One needs four restrictions to determine the coefficients  $p_{r-}$ ,  $p_{r+}$ ,  $p_{l-}$ , and  $p_{l+}$  uniquely.

Continuity of pressure at the point  $x_0$  gives

$$p_{e-} e^{-ik_- x_0} + p_{e+} e^{+ik_+ x_0} = p_{r-} e^{-ik_- x_0} + p_{r+} e^{+ik_+ x_0} \quad 2.19$$

To find the second restriction integrate Eq. 2.17 over a small region  $\epsilon$  about the source point  $x_0$ . The value of the right hand side is  $-1$ . Let  $\epsilon$  go to zero and assume continuity at  $x = x_0$ , only the first term on the left hand side contributes. Dividing by  $1-M^2$  gives the magnitude of the discontinuity in slope.

$$\begin{aligned} & -ik_- p_{r-} e^{-ik_- x_0} + ik_+ p_{r+} e^{+ik_+ x_0} = \\ & = -ik_- p_{e-} e^{-ik_- x_0} + ik_+ p_{e+} e^{+ik_+ x_0} - \frac{1}{1-M^2} \end{aligned} \quad 2.20$$

The third and fourth restrictions come from the pressure reflection coefficients  $R_0$  and  $R_L$ . Care is needed as to which wave is the incident one. At the inlet it is the wave travelling against the flow; at the exit, it is the wave travelling with the flow. Hence

$$p_{e+} = R_0 p_{e-} \quad 2.21$$

$$p_{r-} = R_L e^{i(k_+ + k_-)L} p_{r+} \quad 2.22$$

Solving Eqs. 2.19 to 2.22 for the incident wave coefficients at the ends gives

$$p_{e-} = \frac{1}{-2ik D(\omega)} \left[ e^{+ik_+ x_0} + R_L e^{i(k_+ + k_-)L} e^{-ik_+ x_0} \right] \quad 2.23$$

$$p_{r+} = \frac{1}{-2ik D(\omega)} \left[ e^{-ik_+ x_0} + R_0 e^{+ik_- x_0} \right] \quad 2.24$$



where

$$D(\omega) = 1 - R_o R_L e^{i(k_+ + k_-)L} \quad 2.25$$

Substituting Eqs. 2.21 and 2.22 into Eq. 2.18 gives

$$G_\omega = p_L \left[ e^{-i k_- x} + R_o e^{+i k_+ x} \right] \quad x < x_o \quad 2.26$$

$$G_\omega = p_{r+} \left[ e^{+i k_+ x} + R_L e^{i(k_+ + k_-)L} e^{-i k_- x} \right] \quad x > x_o$$

Substituting Eqs. 2.23 and 2.24 into Eq. 2.26 gives

$$G_\omega(x | x_o) = \frac{e^{i k_+(x-x_o)}}{-2i k D(\omega)} \left[ 1 + R_L e^{i(k_+ + k_-)(L-x)} \right] \left[ 1 + R_o e^{i(k_+ + k_-)x_o} \right] \quad x > x_o \quad 2.27$$

$$= \frac{e^{-i k_-(x-x_o)}}{-2i k D(\omega)} \left[ 1 + R_L e^{i(k_+ + k_-)(L-x_o)} \right] \left[ 1 + R_o e^{i(k_+ + k_-)x} \right] \quad x < x_o \quad 2.27$$

Which is identical to the expression published by Ingard

and Singhal.<sup>30</sup> The problem was worked in detail so as to identify the incident wave at either end. The discrepancy between perfect and measured reflection will be attributed to radiation losses out the ends. One can then deduce the magnitude of the transmission coefficients from the intensity difference between the incident and reflected wave.

### 2.3.3 Analysis of the Pressure Reflection Coefficients

Consider the pressure reflection coefficients in a pipe with flow. To clarify their influence the fundamental pipe mode will be constructed first through

simple arguments. We will then consider the effects of mean flow.

In the most elementary treatment of the axial modes of a straight pipe with no flow it is assumed that the ends are pressure nodes, so that the wavelength of the  $n^{\text{th}}$  mode is  $\frac{2L}{n}$ . The frequency of oscillation is then  $f_n = \frac{nc}{2L}$ .

If the ends are pressure nodes then one finds

$$p_i + p_r = 0$$

which implies

$$\frac{p_r}{p_i} = -1 = R_o \quad 2.28$$

at the inlet. An identical expression is found at the exit. Here the subscripts  $i$  and  $r$  indicate the incident and reflected wave respectively.

The condition is identical to the requirement that the intensity of the incident wave equal that of the reflected wave

$$\frac{|p_i|^2}{\rho_0 c} = \frac{|p_r|^2}{\rho_0 c}$$

which implies

$$\frac{|p_i|}{|p_r|} = 1 = |R_o| \quad 2.29$$

Identical results are obtained at the exit. At zero flow the condition of a pressure node implies perfect intensity reflection. If one allows for phase shifts, the ends are no longer pressure nodes. However, so long as the

magnitude of the pressure reflection coefficient is unity the ends are perfect reflectors of the incident intensity.

The condition that the incident intensity be completely reflected will be used to derive pressure reflection coefficients for a lossless pipe with flow. The flow makes the medium anisotropic as the phase speed depends on the direction of propagation. Moreover, the intensity expression is anisotropic.<sup>31</sup> For propagation with the flow  $I_+ = \frac{|P_+|^2}{\rho_0 c} (1+M)^2$ , for propagation against the flow  $I_- = \frac{|P_-|^2}{\rho_0 c} (1-M)^2$ . If one now requires the reflected intensity equal the incident one finds

at the inlet

$$\frac{|P_i|^2}{\rho_0 c} (1-M)^2 = \frac{|P_r|^2}{\rho_0 c} (1+M)^2$$

which implies

$$\frac{|P_r|}{|P_i|} = \frac{1-M}{1+M} = |R_o| \quad 2.30$$

Similar requirement at the exit gives

$$\frac{|P_r|}{|P_i|} = \frac{1+M}{1-M} = |R_L| \quad 2.31$$

The measurements of Ingard and Singhal<sup>30</sup> show that

$$|R_o| \approx \left[ \frac{1-M}{1+M} \right]^{1.33} \quad R_o = |R_o| e^{i\left(\pi + \frac{2k\delta_o}{1-M^2}\right)} \quad 2.32$$

$$|R_L| \approx 1 \quad R_L = |R_L| e^{i\left(\pi + \frac{2k\delta_L}{1-M^2}\right)} \quad 2.33$$

Figures 2.6 and 2.7 compare the measured coefficients (Eqs. 2.32 and 2.33) to those of a lossless duct (Eqs. 2.30 and 2.31). The measurements extend only up to Mach .5. It is clear that the discrepancy between perfect and measured reflection increases with the flow speed. That is, as the flow increases so do the losses.

Their measurements show that the end corrections  $\delta_o$  and  $\delta_L$  are approximately equal to  $.3D(1-M^2)$ . That is, the effective length of the pipe depends on flow. The importance of these measurements is that they can be substituted into the Green's function to give the actual response of ducts. The measured reflection coefficients will be used to account for the decreased mode excitation with increasing flow.

It is of some interest to note that the reflection coefficient at the upstream end can be derived assuming the duct inlet is a one dimensional nozzle in which the fluid is accelerated from rest to the mean speed  $V$ . If one considers the limit as the nozzle length is much less than the wavelength, the nozzle can be described as a set of boundary conditions at the inlet. Marble<sup>32</sup> has considered the acoustic response of quasi-steady nozzles. The solution may be found by matching stagnation temperature, mass flow, and entropy across the nozzle. The application to pipe

flow was pointed out in Bohn and Zukoski's<sup>33</sup> discussion of the measured inlet pressure reflection coefficient. They find, by the circuitous route of Marble's calculations, the expression in Eq. 2.30.

Cummings<sup>34</sup> has considered the reflection coefficient at the exit. He also uses a quasi-steady model. One point brought out is that the air leaving the exit retains the form of a circular jet for some diameters downstream and that this must be accounted for in the analysis of the exit reflection. This is in marked contrast to the inlet where one assumes the flow accelerates from zero in a negligible distance.

#### 2.3.4 Transmission Out of the Ends of the Pipe

Consider the sound transmitted out of the ends of the pipe. The calculation is done in two steps. The first quantity one needs is the pressure just outside the ends of the pipe. This follows from an energy balance assuming all losses are due to radiation. The second step is to replace the fields just outside the ends by an equivalent distribution of monopoles. From this distribution one calculates the radiation into free space.

In the first step one must account for the asymmetry in flow conditions in the intensity expressions.

Just before the inlet the mean flow is zero, the acceleration of the fluid takes place in the vena contracta. The intensity in this region is  $\frac{|p_d|^2}{\rho_0 c}$ . Just after the exit the mean flow is approximately the same as in the duct. The deceleration of the fluid takes place over a comparatively long distance, on the order of five jet diameters. The intensity in this region is then  $\frac{|p_d|^2}{\rho_0 c} (1 + M)^2$

Close to the end the pressure is approximately uniform across a disk of the same diameter as the pipe. Moreover, one may assume the acoustic velocity is approximately parallel to the pipe axis. Under these conditions one may calculate the transmitted intensity from a one dimensional model. At the inlet one assumes

$$\begin{aligned}
 I_t &= I_i - I_r \\
 \frac{|p_t|^2}{\rho_0 c} &= \frac{|p_d|^2}{\rho_0 c} (1 - M)^2 - \frac{|p_d|^2}{\rho_0 c} (1 + M)^2 \\
 T_{inlet} \frac{|p_t|}{|p_i|} &= \left[ (1 - M)^2 - |R_d|^2 (1 + M)^2 \right]^{1/2} \qquad 2.34
 \end{aligned}$$

Again, assuming all losses are radiative one finds at the exit

$$\begin{aligned}
 I_t &= I_i - I_r \\
 (1 + M)^2 \frac{|p_d|^2}{\rho_0 c} &= \frac{|p_d|^2}{\rho_0 c} (1 + M)^2 - |p_d|^2 (1 - M)^2 \\
 T_{exit} \frac{|p_t|}{|p_i|} &= \frac{\left[ (1 + M)^2 - |R_d|^2 (1 - M)^2 \right]^{1/2}}{(1 + M)} \qquad 2.35
 \end{aligned}$$

where  $T_{inlet}$  and  $T_{exit}$  are the magnitudes of the inlet and exit pressure transmission coefficients.

Consider the second step in the calculation which describes the propagation from the immediate vicinity of the inlet into free space. Outside the inlet the medium is uniform and at rest, hence the resulting pressure field is transmitted according to the laws of classical acoustics. At the exit the field is embedded in the center of a cylindrical jet with large velocity gradients at the shear layer. One expects refraction due to these shear layers, and possible channeling of the sound in the aerodynamic duct formed by the velocity gradients (ref. 14, Chapter 11).

Consider the inlet first. As a first approximation one can model the end conditions as a distribution of volume sources. Let the average acoustic velocity be  $U_0 e^{-i\omega t}$  and uniform in a direction parallel to the tube axis. Then the strength of an equivalent volume source is  $S_\omega$  equal to  $U_0 A$  or  $S_\omega$  equal to  $\frac{|p_t| A}{\rho_0 c}$ . If one distributes the source over the duct cross section  $A$  the source strength per unit area  $S'_\omega$  is then  $\frac{|p_t|}{\rho_0 c}$ . The model is by Morse<sup>35</sup> to calculate the radiation from a piston in a plane wall. One finds the free space acoustic pressure  $p(\omega, \tilde{r})$  is

$$\begin{aligned}
p(\omega, \tilde{r}) &= i k \rho_0 c \iint_A dA S'_\omega \frac{e^{i \tilde{k} \cdot (\tilde{r} - \tilde{r}_0)}}{4\pi r} \\
&\approx -i k \rho_0 c \frac{e^{i k r}}{4\pi r} S'_\omega \int_0^a r_0 dr_0 \int_0^{2\pi} d\phi e^{-i k r_0 \sin \theta \cos \phi} \\
&= -i k \rho_0 c \frac{e^{i k r}}{4\pi r} S'_\omega 2\pi \int_0^a r_0 dr_0 J_0(k r_0 \sin \theta) \\
&= -i k \rho_0 c \frac{e^{i k r}}{4\pi r} S'_\omega \pi a^2 \frac{2 J_1(k a \sin \theta)}{k a \sin \theta}
\end{aligned}$$

Hence

$$|p(\omega, r)| = \frac{k a^2}{4 r} |p_t| \left| \frac{2 J_1(k a \sin \theta)}{k a \sin \theta} \right| \quad 2.36$$

where  $a$  is the pipe radius and  $\theta$  the angle that  $\tilde{r}$  makes with the pipe axis.  $|p_t|$  is given in Eq. 2.34. Let  $T_{SPACE}$  be the transmission coefficient from the inlet to the point  $(r, \theta)$ .

$$\begin{aligned}
T_{SPACE} &= \frac{|p(\omega, \tilde{r})|}{|p_t|} = \frac{k A}{4\pi r} \left| \frac{2 J_1(z)}{z} \right| \\
&= \frac{k A}{4\pi r} \left| 1 - \frac{z^2}{8} + \frac{z^4}{132} \right| \quad 2.37
\end{aligned}$$

where  $z = k a \sin \theta$ . The approximation<sup>36</sup> holds in the limit as the wavelength is much larger than the duct radius. This is the case since this Chapter considers frequencies below the first cutoff. The first term in the expansion predicts uniform radiation. The second term predicts a decrease in radiated pressure with increasing angle and frequency. This suppression of high frequencies may



account for the decrease in level with angle observed in Figures 2.13 to 2.20.

Consider the problem of sound transmission from the exit. One can start by modeling the acoustic field in the immediate vicinity of the exit by an equivalent point source. One must then account for the refraction of sound through the velocity gradients in the jet. Experimental work is available for the single frequency point source in air jets (Atvars<sup>18</sup> et al and Grande<sup>19</sup>). The theoretical problem is solved in two dimensions for one shear layer by Gottlieb<sup>20</sup> and for two shear layers by Grahm and Grahm.<sup>21</sup> Since experiment indicates that the exit jet spectra completely dominates the acoustic field of the pipe the analysis will not be carried out.

### 2.3.5 Effect of the Convective Derivative on the Source Term

Herein the acoustic field in a pipe due to a distribution of pressure sources is calculated. The turbulent source term is given in Eq. 2.15 as

$$- \left( k + i M \frac{\partial}{\partial x_0} \right)^2 p(\omega, x_0) \quad 2.38$$

The formal solution to the forced wave equation is

$$p(\omega, x) = \int_0^L dx_0 G_\omega(x|x_0) \left( k + i M \frac{\partial}{\partial x_0} \right)^2 p(\omega, x_0) \quad 2.39$$

where G is defined in Eq. 2.26.

To get an expression that can be interpreted it is necessary to have the convective derivative operate on the Green's function. This is done by expanding the term

$$\left(k + iM \frac{\partial}{\partial x_0}\right)^2 = k^2 + 2i k M \frac{\partial}{\partial x_0} - M^2 \frac{\partial^2}{\partial x_0^2} \quad 2.40$$

and differentiating by parts. To simplify the resulting expression assume that the turbulent sources are contained entirely within the pipe and are sufficiently far from the ends so that  $p$  and  $\frac{\partial p}{\partial x_0}$  may be set to zero at the inlet and exit. Further assume that the observation point is located outside the source region. Under these restrictions the radiated field is

$$p(\omega, x) = \int_0^L dx_0 p(\omega, x_0) \left(k - iM \frac{\partial}{\partial x_0}\right)^2 G_\omega(x|x_0) \quad 2.41$$

If the source contribution from the ends is significant, or if the observation point is in the source volume, then Eq. 2.41 is incomplete and the other terms resulting from differentiating by parts must be considered.

To calculate the field radiated out of the pipe it is necessary to find the magnitude of the incident pressure wave at the inlet. Here all sources are located downstream from the observation point, hence  $G_\omega(x|x_0)$  for  $x < x_0$  is to be used (Eq. 2.26). This is given as

$$G_{\omega}(x|x_0) = p_{e-}(x_0) e^{-ik_-x} + p_{e-}(x_0) R_0 e^{ik_+x} \quad 2.42$$

The Green's function is composed of two waves, one travelling with the flow and the other against the flow. The incident pressure wave at the origin travels against the flow and is proportional to  $e^{-ik_-x}$ . Substituting  $G$  into Eq. 2.41 and selecting the incident pressure wave,  $p_i(\omega, x)|_{x=0}$ , gives

$$\begin{aligned} p_i(\omega, 0) &= \int_0^L dx_0 \rho(\omega, x_0) \left( k - iM \frac{\partial}{\partial x_0} \right)^2 p_{e-}(x_0) \\ &= \frac{1}{-2ikD(\omega)} \int_0^L dx_0 \rho(\omega, x_0) \left( k - iM \frac{\partial}{\partial x_0} \right)^2 \\ &\quad \left\{ e^{ik_-x_0} + R_L e^{i(k_++k_-)L} e^{-ik_+x_0} \right\} \\ &= \frac{1}{-2ikD(\omega)} \left\{ (k + Mk_-)^2 \int_0^L dx_0 e^{+ik_-x_0} \rho(\omega, x_0) \right. \\ &\quad \left. + R_L e^{i(k_++k_-)L} (k - Mk_-)^2 \int_0^L dx_0 \rho(\omega, x_0) e^{-ik_+x_0} \right\} \quad 2.43 \end{aligned}$$

To interpret this expression note that the spatial Fourier expansion of  $\rho(\omega, x_0)$  is given by

$$\begin{aligned} \rho(\omega, x_0) &= \frac{1}{2\pi} \int_{-\infty}^{\infty} dx_0 \rho(\omega, x_0) e^{\mp ik_{\pm} x_0} \\ &= \frac{1}{2\pi} \int_0^L dx_0 \rho(\omega, x_0) e^{\mp ik_{\pm} x_0} \quad 2.44 \end{aligned}$$

The limits of integration are changed by noting  $\rho$  is zero outside the pipe. The spatial transform is given in the set of travelling waves  $e^{\pm i k_x x}$  since the Green's function is expressed in this set. Had the Green's function been expanded in the set of standing waves  $\sin \frac{n\pi x}{L}$  the standing wave expansion of  $\rho$  would have to be used. Expressing Eq. 2.44 in terms of  $\rho(\omega, k_{\pm})$  gives

$$\rho_i(\omega, 0) = \frac{i\pi k}{D(\omega)} \left\{ \frac{1}{(1-M)^2} \rho(\omega, k_-) + \frac{R_L e^{i(k_+ + k_-)L}}{(1+M)^2} \rho(\omega, k_+) \right\} \quad 2.45$$

The incident pressure field is composed of two parts, which are interpreted as follows. The first is proportional to  $\rho(\omega, k_-)$ . This is due to sound waves that travel directly to the inlet from the source. Only that portion of the turbulence that has a wave number  $k_- = \frac{\omega}{c(1-M)}$  contributes. That is, that portion of the source distribution whose wavenumber satisfies the dispersion relation for propagation upstream contributes. The second term is due to sound waves that initially travel downstream but are reflected off the exit. If there was no reflection at the exit, i.e., if  $R_L$  equals zero, this term would not exist. This interpretation is supported by the fact that only the portion  $\rho(\omega, k_+)$  of the turbulence contributes. That is only disturbances whose wavenumber satisfies the dispersion relation for

propagation downstream,  $k_+ = \frac{\omega}{c(1+M)}$  contribute to this term.

### 2.3.6 Acoustic Field of a Point Source

Consider a source whose dimensions are much less than the wavelength of sound generated. In this limit it can be modeled as a single point source

$$p(\omega, x_0) = p(\omega) D \delta(x - \ell) \quad 2.46$$

where  $\ell$  is the location of the equivalent source and  $D$  the effective length of the source (note the  $\delta$  function has units of  $L^{-1}$ ). Taking the transform indicated in Eq. 2.44 and substituting into Eq. 2.45 gives

$$p_i(\omega, 0) = \frac{p(\omega) i\pi k D}{D(\omega)} \left\{ \frac{1}{(1-M)^2} e^{+ik\ell} + \frac{1}{(1+M)^2} R_L e^{i(k_++k_-)L} e^{-ik_+\ell} \right\} \quad 2.47$$

From which one finds the magnitude

$$|p_i(\omega, 0)|^2 = \frac{|p(\omega)|^2 \pi^2 k^2 D^2}{|D(\omega)|^2} \left\{ \frac{1}{(1-M)^4} + \frac{1}{(1+M)^4} |R_L|^2 - \frac{2|R_L|}{(1-M^2)^2} \cos(k_++k_-)(L+\delta_L-\ell) \right\} \quad 2.48$$

The cosine term in the expression arises from interference effects, which are possible only because the source location  $\ell$  is specified. If one lets  $\ell$  vary over the length of the pipe and computes the average value of  $|p_i(\omega, 0)|^2$  this term drops out whereas the others remain the same.

Computing this average one finds

$$\langle |p_i(\omega, 0)|^2 \rangle = \frac{1}{L} \int_0^L dl |p_i(\omega, 0)|_l^2$$

$$= \frac{|\rho(\omega)|^2 \pi^2 k^2 D^2}{|\rho(\omega)|^2} \left\{ \frac{1}{(1-M)^4} + \frac{1}{(1+M)^4} |R_L|^2 \right\} \quad 2.49$$

We can define a transfer coefficient

$$T_{DUCT}^2 = \frac{\langle |p_i(\omega, 0)|^2 \rangle}{|\rho(\omega)|^2} \quad 2.50$$

Note that averaging over all source positions has removed all dependence on  $l$ . The magnitude of the generated acoustic wave depends only on the Fourier amplitude of the source field, which can be derived from a statistical description of the time variations of the source strength. The location of the source  $l$  has its counterpart, in distributed sources, in the phases of the Fourier coefficients of the source. The neglect of such phases is equivalent to the neglect of interference effects.

### 2.3.7 Acoustic Field of a Distributed Source

Consider the acoustic field of a distributed source. Let the Fourier coefficient of the source be given by

$$\rho(\omega, k_{\pm}) = |\rho(\omega, k_{\pm})| e^{i\phi_{\pm}} \quad 2.51$$

where  $\phi_{\pm}$  is the phase of the coefficient. Substituting into Eq. 2.45 and computing the amplitude gives the incident pressure amplitude

$$|p_i(\omega, 0)|^2 = \frac{\pi^2 k^2}{|D(\omega)|^2} \left\{ \frac{|p(\omega, k_-)|^2}{(1-M)^4} + \frac{|p(\omega, k_+)|^2}{(1+M)^4} |R_L|^2 - |p(\omega, k_-)| |p(\omega, k_+)| \frac{2|R_L|}{(1-M^2)^2} \cos[(k_+ + k_-)(L + \delta) + (\phi_- - \phi_+)] \right\} \quad 2.52$$

Note the similarity of Eq. 2.52 to Eq. 2.48.

The interference term due to localization of a point source has been replaced by the phase term  $(\phi_- - \phi_+)$ . The expression, as it stands, cannot predict the sound field of a random source, because only amplitudes and not phases can be deduced from the correlation function.

Consider the average of  $N$  measurements of the incident pressure and assume the value of the phases to be random, one finds

$$\begin{aligned} \langle |p_i(\omega, 0)|^2 \rangle &= \frac{1}{N} \sum_{n=1}^N |p_i(\omega, 0)|_n^2 \\ &= \frac{\pi^2 k^2}{|D(\omega)|^2} \left\{ \frac{|p(\omega, k_-)|^2}{(1-M)^4} + \frac{|p(\omega, k_+)|^2}{(1+M)^4} |R_L|^2 \right\} \quad 2.53 \end{aligned}$$

The result is equivalent to taking the average over all source locations.

To understand the effect of averaging consider a point source that moves in a random fashion in the duct. Let the time needed to compute a Fourier analysis at the inlet be smaller than the time it takes for the position  $\ell$  to change significantly. Any single analysis will contain interference effects due to the approximate localization of the source. An average of  $N$  such

measurements would have the cosine term contribute randomly and therefore tend toward zero.

Consider the Fourier analysis of the field due to a distributed source. Any single analysis depends on the precise distribution in time and space of the sources, hence it will include interference effects. If the average of  $N$  measurements is taken these interference effects contribute randomly and therefore tend toward zero.

One may ask which expression to use, i.e., Eq. 2.49 or 2.53. The answer depends on the extent of information concerning the source. To use the model of a distributed source requires statistical information concerning the distribution in both time and space.

Information concerning turbulent fields in short pipes is limited and the approximation of a random point source is more appropriate. Eq. 2.49 only requires that one specify the correlation in time and will therefore be used.

#### 2.3.8 The Upstream Acoustic Field

The transfer coefficients  $T$  are now used to predict the acoustic spectra in front of the inlet. The various calculations are tied together so as to derive the acoustic spectra outside the pipe from the turbulent



source spectra inside the pipe. Only the correlation in time will be assumed. In effect, one considers the average field from a collection of random point sources. From Eqs. 2.50, 2.37 and 2.34 one finds

$$\langle |p(\omega, \tilde{r})|^2 \rangle = T_{\text{SPACE}}^2 T_{\text{INLET}}^2 T_{\text{DUCT}}^2 |p(\omega)|^2 \quad 2.54$$

Assume that the source is described by a Gaussian correlation in time

$$R(\tau) = \overline{p^2} e^{-(\omega_0 \tau)^2} \quad 2.55$$

Taking the Fourier transform yields the source spectra

$$|p(\omega)|^2 = \frac{\sqrt{\pi}}{\omega_0} \overline{p^2} e^{-\left(\frac{\omega}{2\omega_0}\right)^2} \quad 2.56$$

To concentrate on the spectral line shape, separate the frequency dependent terms in Eq. 2.54 from those which determine the average amplitude to get

$$\langle |p(\omega, r)|^2 \rangle \propto \left| \frac{2 J_1\left(\frac{\omega a \sin \theta}{c}\right)}{\frac{\omega a \sin \theta}{c}} \right| \frac{\omega^4}{|D(\omega)|^4} e^{-\left(\frac{\omega}{2\omega_0}\right)^2} \quad 2.57$$

$$\xrightarrow{\theta \rightarrow 0} \frac{\omega^4}{|D(\omega)|^2} e^{-\left(\frac{\omega}{2\omega_0}\right)^2}$$

If the microphone is on the pipe axis  $\theta = 0$  and the last line is exact. The exponential term comes from the source distribution. A factor of  $\omega^2$  comes from the radiation impedance of free space and a second factor of  $\omega^2$  from this second time derivative in the source term. The  $|D(\omega)|^2$  in the denominator comes from the

response characteristic of the duct (Eq. 2.25), it depends on the flow speed through the reflection coefficients. It is this term that is responsible for the periodic amplitude variations observed in Figure 2.1.

Explicitly

$$|D(\omega)|^2 = 1 - 2 |R_o| |R_L| \cos \left\{ \frac{2 \left( \frac{\omega}{c} \right) (L + \delta_o + \delta_L)}{1 - M^2} \right\} + |R_o|^2 |R_L|^2 \quad 2.58$$

The duct response is maximum at frequencies where  $|D(\omega)|^2$  is minimum. This occurs at frequencies where the cosine term is equal to one. That is when

$$f_n = \frac{\omega_n}{2\pi} = \frac{nc(1 - M^2)}{2(L + \delta_o + \delta_L)} \quad 2.59$$

If the product  $|R_o| |R_L|$  was equal to one, then  $|D(\omega)|^2$  equals zero at  $\omega_n$ . Hence the duct response is infinite. This occurs if the ends are perfect reflectors of the incident intensity, i.e. if

$$|R_o| |R_L| = \frac{1 - M}{1 + M} \frac{1 + M}{1 - M} = 1 \quad 2.60$$

However, the measurement of Ingard and Singhal<sup>30</sup> have shown that

$$|R_o| |R_L| = .95 \left( \frac{1 - M}{1 + M} \right)^{1.33} < 1 \quad 2.61$$

As the flow speed increases, the product  $|R_o| |R_L|$  decreases, consequently  $|D(\omega)|^2$  varies less and the acoustic spectra smooths out. That is, the eigenmodes are damped.

### 2.3.9 Numerical Comparison of Theory to Experiment

Herein the observed spectra is fit by the expression in Eq. 2.57. All mean intensity information is lumped into a proportionality constant,  $B$ , which is a function of the flow speed and the distance of the microphone from the inlet. The data is fit by adjusting  $B$  and  $\omega_0$ .

Figures 2.8 to 2.10 compare the theoretical spectra to that observed in experiment. All of the qualitative features are accounted for. First, it is clear that the spectral line shape agrees with that observed. Second, the amplitude peaks at the resonant frequencies are damped at the higher flow speeds. Finally, the average rise and fall of the amplitude with frequency is the same as is observed.

It should be noted that at high frequencies the theoretical amplitudes match the observations. At low frequencies the data exceeds the theoretical levels. The same effect was observed in fitting the free space spectra with an isotropic turbulent model. The inhomogeneities of the turbulence must be accounted for to fit both the high and low frequency ends of the spectra.

Moreover, at low speeds, the theoretical resonant peaks are greater than those observed. This

discrepancy is due to non-radiative damping such as turbulent and visco thermal losses. At high flow speeds the predicted and observed resonant peaks agree. At these velocities, radiative damping is the dominant loss mechanism and the model, based only on end losses, is more accurate.

It is also possible that some modification of the exit reflection coefficient may be necessary at low flow speeds. The empirical coefficients given by Ingard and Singhal<sup>30</sup> are used throughout (Eqs. 2.32 and 2.33). At zero flow the two reflection coefficients should agree, however, they give  $|R_O| = 1$  whereas  $|R_L| = .95$ . They indicate that  $|R_L|$  is an average for all frequency ranges and flow speeds, at best, a good approximation. Such discrepancies do indicate that a more detailed study of the exit reflection coefficient is in order. In particular, if one substitutes the value .95 for  $|R_L|$  at low flow speeds greater radiative damping would occur. This would bring the theory in better agreement with the observations.

In Figure 2.11 the Strouhl numbers that were used to fit the data are plotted. This fit was done on a computer using a least squares procedure. Here, one assumes that the correlation frequency  $\omega_c$  is related to the Strouhl frequency  $f_s$  as

$$\begin{aligned}
\omega_0 &= 2\pi f_s \\
&= 2\pi S \frac{V_{JET}}{D_{JET}} \\
&= 2\pi S \frac{V_{DPIPE} / .6}{\sqrt{.6} D_{PIPE}}
\end{aligned}
\tag{2.62}$$

Here the inlet turbulence is assumed to be the major noise source. The Strouhl numbers are based on the velocity and diameter at the narrowest point of the vena contracta. The numbers obtained range from a high of .68 to a low of .16. This is well within the range observed in free space spectra. Strouhl numbers based on pipe diameters and velocity are 2.15 times larger than those based on the inlet jet.

The scatter of Strouhl numbers is large, and some additional comment is necessary. If  $\omega_c$  is the correlation frequency then the correlation time is given by

$$\tau = \frac{2\pi}{\omega_c} = \frac{D_{JET}}{V_{JET} S}
\tag{2.63}$$

Such a calculation (Figure 2.12) gives a correlation time that varies from a high of .5 milliseconds at low flow speeds, to a low of .2 milliseconds when the inlet is choked. The near constancy of the correlation time indicates why the Strouhl number varies inversely with the flow speed.

A discussion of the amplitude  $\beta$  is premature as several untested assumptions were made in determining

how sound is transmitted out of the ends. For example, it has been assumed that the departure from perfect intensity reflection is due solely to radiative damping. Any non-radiative losses at the ends would alter the transmission coefficients and obscure the interpretation of  $\beta$ . Suffice to say that the change in amplitude serves only to move the pattern of spectral variation by a constant factor and does not alter the relative line shape.

### 3. EXCITATION OF TRANSVERSE DUCT MODES

#### 3.1 Introduction

In the present section the aerodynamic excitation of high order acoustic modes in a rectangular duct by a turbulent jet is explored. The nature of the duct response in the vicinity of an eigenfrequency and the range of frequencies is determined for which the qualitative behavior of the acoustic response of a duct differs from free space.

Sound can be transmitted in a duct in more than one mode. As the frequency of the source is increased beyond mode cutoff, a new mode is available for the radiation of sound down the duct. The response of the duct to a sound source is greatest when the source frequency is equal to an eigenfrequency. Random sources, such as turbulent jets, contain all frequencies. One expects that the detected pressure spectra will show peaks at the eigenmodes.

Herein, the pressure response of a duct to an enclosed air jet was measured in two frequency bands: 0 to 5 kHz and 0 to 25 kHz. The jet noise source in these experiments was produced by drawing air through an orifice, on which various orifice sizes, flow rates, and orifice locations were used.

One observes that the pressure spectra does exhibit asymmetric singularities (pressure spikes) at frequencies equal to the cutoff frequencies for the first few higher order duct modes. As yet the discontinuous nature of the radiated pressure field from a random source has not been demonstrated by any published experimental data. One of the aims of this chapter is to demonstrate such peaks in the pressure spectrum exist. One accounts for these spikes theoretically by considering the response of the duct to a turbulent field with Gaussian correlation. This model accounts for the variations in spectra at the eigenmodes.

In a frequency range in which a large number of modes can propagate the spectra smooths out, i.e., the duct spectra resemble the free space jet spectra. To account for this, one notes that the asymptotic limit of the duct radiation impedance is the free space impedance. This implies that the linear response of a duct to a turbulent source should be identical to the free space response to the same source in the high frequency limit. This accounts for the observed spectra.

Pressure spikes termed impingement screech have been observed, in certain instances, in the high frequency limit. These will be identified, in Chapter 4, as nonlinear feedback oscillations that occur when an air



jet impinges on a wall. They depend on the alteration of the jet structure by the emitted sound. Phenomena in which the field reacts back on the source cannot be accounted for without considering the variations produced in the jet, and are not considered in this chapter.

### 3.2 Experiment

#### 3.2.1 Apparatus and Procedure

In principal, the apparatus is a rectangular duct with a small hole in its side. One end is fitted to a suction device which lowers the pressure in the duct. The air drawn through the hole develops turbulent fluctuations which generate the sound. This sound is detected by a microphone mounted flush to the duct wall. The signal is then spectrum analyzed, and then the average of 256 analyses computed and plotted.

The rectangular duct has inner dimensions of  $1\frac{1}{2}$ " by 4". A nonreflective acoustic termination is placed at its end. This is fashioned from a triangular wedge of acoustic fiberglass. The first 56" of the duct is the test section. The top and bottom are fitted with eight detachable plates (Fig. 3.1). These plates are used to mount microphones, orifices and pressure taps as needed.

The next 72" is an acoustic muffler consisting of two strips of acoustic foam mounted on the sides of

the duct. The muffler reduces any noise generated by the suction apparatus. The transmission loss exceeds 40 DB above 1 kHz and exceeds 20 DB above 250 Hertz.

Fixed to the end of this section is a pipe which leads to the suction apparatus. A cutoff valve connects the apparatus to the main exhaust facility, a pneumatically operated butterfly valve modulates the mass flux. Additional flow resistors were used to control the mass flux. These were blocks of acoustic foam placed in front of a wire screen in the duct.

A hot wire anemometer was used to calibrate the flow speed. To calibrate the probe, a  $\frac{1}{2}$ " diameter orifice plate was mounted at the end of the duct, as shown in Fig. 2.1. The mass flux through the orifice is calculated from the pressure drop across it<sup>37</sup> (Eq. 4.1). Continuity of mass flux, plus the ratio of jet-to-duct cross-section, gives the flow speed in the duct. The probe cannot be mounted in the jet since hot wire measurements are inaccurate at near sonic speeds, hence the mounting of the probe in the low velocity mean duct flow.

The orifice plates were then mounted on the side. The velocity versus pressure drop was calculated as before. Comparison of anemometer readings from this data to standard axial mounts showed no substantial deviations (Fig. 3.2).

One quarter inch B+K microphones were used to detect the acoustic field. The protective cover which shields the microphone membrane was removed so as to provide a smooth surface to the flow. The microphone was mounted in a test plate with the membrane flush to the surface of the plate. Recall that transverse modes are characterized by their variation in a plane normal to the duct axis. To detect such modes, the microphone must be at a pressure antinode. In rectangular ducts, the corners are pressure antinodes for all modes. Two plates with the microphone mounted at the corner were made. A third plate was machined to allow transverse variation of the microphone (Fig. 3.3). The plate has a double row of  $\frac{1}{4}$ " holes spaced by  $\frac{1}{2}$ " from center to center. The second row is staggered behind the first to provide  $\frac{1}{4}$ " increments in microphone location. The holes are stopped with aluminum plugs when the microphone is not in place.

Circular orifice plates of  $\frac{1}{4}$ ",  $\frac{1}{2}$ " and 1" diameter were machined from  $\frac{1}{8}$ " thick aluminum plate (Fig. 3.4). The orifices are tapered so as to present a sharp edge to the in-coming flow. Tapering is necessary to avoid orifice screech when the thickness to diameter is between  $\frac{1}{2}$  and 2. The plates were mounted on the side of the duct so that the jet enters perpendicular to the duct axis. A fourth plate,  $\frac{1}{2}$ " diameter, was mounted to let

the air enter parallel to the duct axis. It was this plate that was used for the velocity calibration (Fig. 3.1). Finally, a 60" pipe,  $\frac{1}{2}$ " inner diameter, was mounted on a plate (Fig. 3.5).

The electric apparatus consists of a microphone power supply, a spectrum analyzer, a spectrum averager, and an x-y plotter.

### 3.2.2 Basic Experiment

In the experiment an orifice plate is mounted in the center of the test section. The pressure in the duct is reduced and air drawn through the orifice. The air jet impinges on the opposite wall. The turbulent fluctuations in the air jet act as the sound source. The acoustic signal is analyzed in two frequency ranges, termed low (0 to 5 kHz) and high (0 to 25 kHz) (Fig. 3.6).

The low frequency range spans the first four transverse duct modes. In this limit the frequency separation between modes is greater than their bandwidth when excited by a random source. Inspection of Fig. 3.6 shows that just beyond each mode cutoff the sound level increases abruptly. Of particular interest is the asymmetric shape of the curves which characterizes the excitation of transverse modes. Recall that such modes propagate only if the frequency is above a certain cutoff.

The duct pressure response to excitation of a given mode is zero below its cutoff frequency  $\omega_n$ , infinite at the cutoff frequency, and proportional to  $\frac{1}{\omega^2 - \omega_n^2}$  above cutoff (see section 3.3.1). The infinite response is in the ideal case of infinite source impedance and zero damping. Real fluid effects limit the response to approximately 10 DB. Nonetheless, the asymmetric shape is still evident.

In the high frequency range the spectra resembles the free space jet spectra (Fig. 3.6 ). Below five kilohertz the level jumps at the cross modes are still evident. Above five kilohertz the spectra smooths out. One can show that the radiation impedance in the high frequency limit asymptotically approaches the free space impedance, hence the similarity. Two physical effects are responsible for the smoothing of the curve. First, the damping limits the level jump at cutoff. Second, a new mode cuts on before the level shift from the previous mode has subsided. The influence of the neighboring modes overlap so as to make the contribution of any given mode small, in this range.

### 3.2.3 Spectra Variation with Jet Velocity and Diameter

Herein the effects of flow speed and orifice diameter are investigated. Since the flow rate in the duct is much smaller than that of the jet, the duct

response should remain approximately independent of flow speed. Aside from level shifts due to increased turbulence, the spectra should be similar. Three orifice diameters,  $\frac{1}{4}$ ",  $\frac{1}{2}$ ", and 1", were tested for jet flow speeds up to Mach 1. Representative spectra are presented for each of these cases.

The low frequency spectra are presented in Figs. 3.7, 3.8, and 3.9. Level jumps at the first three cutoff frequencies are observed for all flow speeds. Moreover, the characteristic asymmetric shape of the peak is observed in all cases. The sound level rises monotonically with velocity as expected. The intensity at the high frequency end appears to increase at a faster rate than the low frequency intensity in these plots. Recall that, in free space, the spectra peaks at a Strouhl frequency approximately equal to  $\frac{.2V}{D}$ . As the velocity increases, the intensity shifts toward the higher frequencies. Hence the observed level increases at low frequencies should be smaller than those at high frequencies.

The high frequency spectra are presented in Figs. 3.10, 3.11, and 3.12. Here the average response of the duct is most evident. Aside from screech tones, the spectra increases with flow in a manner similar to free space spectra. Dotted lines, indicating average

behavior, are drawn at low and high velocities in Figs. 3.10 and 3.11. As before, the sound level increases monotonically with velocity. Moreover, the peak of the average behavior increases with flow speed approximately as the Strouhl frequency. These observations are consistent with the low frequency behavior.

Certain spectral anomalies, termed screech peaks are sometimes observed above Mach .6. These peaks are nonlinear effects which are due to the coupling of the jet flow to the acoustic waves produced. One indicator of a separate mechanism is the line shape. Screech peaks are symmetric about their maximum, the duct response is asymmetric and peaked at a cutoff frequency.

#### 3.2.4 Reduction by Strouhl Number

It is oftentimes useful to establish scaling laws for data reduction. In aeroacoustics the Lighthill eighth power law, and its extension by von Gierke<sup>38</sup> to spectral analysis (see section 4.3.2) has been found useful. The basis for data reduction is the proposition that the spectral intensity is maximum at a frequency given by  $f_s = \frac{.2V}{D}$ , where V and D are the jet velocity and diameter. The point is that spectra should be similar for experiments with similar Strouhl numbers.

Such a comparison is made here. Figs. 3.13 and 3.14 present the spectra with the same Strouhl frequency

(5.7 kHz and 2.5 kHz ) for the low frequency regime. Fig. 3.15 compares two orifices of similar Strouhl frequency (1.9 kHz ) in the high frequency regime. From the figures it is clear that the spectral shape reduces according to Strouhl number.

One exception is of note, the line shape below the first cutoff. In each case (Figs. 3.13 and 3.14) the orifice with the lower jet velocity exhibits a decay in level as the frequency increases from zero to the first cutoff. The orifice with the greater velocity exhibits levels approximately independent of frequency. Such behavior may indicate the dominance of sources other than sound from the jet turbulence at low jet speeds. One possibility is the wall turbulence in the duct.

One item of note is that the overall level increases with increasing velocity. Let us assume that the radiated power in the duct is proportional to  $V_D^8$  as is the case for free jets. If the spectra shape is identical, the power per unit frequency should increase in the same fashion. The level ratio between orifices of different diameters but similar Strouhl numbers is given by



$$\begin{aligned} \Delta SPL &= 10 \log \frac{V_1^8 D_1^2}{V_0^8 D_0^2} \\ &= 10 \log \frac{\left(\frac{V_1}{D_1}\right)^8 D_1^{10}}{\left(\frac{V_0}{D_0}\right)^8 D_0^{10}} \end{aligned}$$

3.1

$$= 100 \log \frac{D_1}{D_0}$$

where  $D_1$  and  $D_0$  are the orifice diameters. The ratio is independent of velocity for orifices with identical Strouhl numbers. If the diameter is doubled, the level should increase by 30 DB. To check this, the average separation between lines was computed, in the frequency band indicated, for Figs. 3.13, 3.14, and 3.15. One finds

Figs.	$D_0$	$D_1$	$f_s$ kHz	Range kHz	$\Delta SPL$
3.13	$\frac{1}{4}$ "	$\frac{1}{2}$ "	5.7	2 → 5	26
3.14	$\frac{1}{2}$ "	1"	2.5	2 → 5	35
3.15	$\frac{1}{2}$ "	1"	1.9	5 → 15	30

The result holds for the high frequency spectra where the duct response is identical to the free space response. The scale is only approximate for the low

frequency spectra. In this range the turbulent sound field is especially sensitive to variations in the jet velocity and diameter. The error for a 10% deviation of the Strouhal number gives an uncertainty of  $10 \log \left( \frac{f_{s1}}{f_{s0}} \right)^8 \approx \pm 3.4$  DB, or a net error of 6.8 DB. The observed deviations are 4 and 5 DB. This suggests that the dimensional scaling laws do apply to the ducts, even in the low frequency region.

### 3.2.5 Separating Linear from Feedback Effects

Certain peaks in the spectra were identified as nonlinear effects. These were termed screech peaks. They were distinguished from the linear duct response at cutoff by their symmetric line shape. Herein the two effects are separated by plotting amplitude variations versus flow speeds.

In the linear response of the duct the sound pressure level is proportional to the turbulent intensity. Since the turbulent intensity increases monotonically with flow speed, it follows that the level should also increase monotonically.

A nonlinear effect depends on the interaction of the jet flow with the acoustic wave it produces. Such interactions depend strongly on the jet flow speed. Screech instabilities only occur for certain flow speeds. One finds that the sound level no longer increases monotonically with flow speed.

To show the linear character of the duct response at the cutoff frequency, the behavior of the first transverse mode ( $f = 1.6$  kHz) is studied in detail (Fig. 3.16). Its behavior is compared to the amplitude dependence on flow speed for a point ( $f = 2.5$  kHz) between the first and second cutoff frequencies. This comparison is done for a  $\frac{1}{2}$ " diameter orifice mounted on the side of the duct. One finds that both frequencies have the same variation in amplitude with flow speed. The only difference is that the level at the first cutoff is 7 DB higher than the level between modes. That the intensity follows the same power law indicates the response of the duct at cutoff is independent of velocity.

Of note is the fact that the amplitude increases as the sixth power of velocity. At first this seems to contradict the result of the previous section. This is not so. The Strouhl frequency increases with flow speed for an orifice of fixed diameter. In Fig. 3.16 the Strouhl frequency varies from a low of 2.7 kHz at Mach .5 to a high of 5.4 K.C. at Mach 1.0. The  $\gamma^8 D^2$  law holds only for experiments with similar Strouhl numbers.

In Fig. 3.17 two frequencies identified as screech peaks are investigated; these are at 9.1 kHz and 13.0 kHz. The amplitude does not vary monotonically with velocity. In particular, the level seems to peak at

Mach .7 and .8 and then fall off. Such variations with flow speed identify the screech as a separate, nonlinear effect.

### 3.2.6 Effect of Inlet Turbulence

Herein the effect of inlet turbulence on spectral line shape is determined. The spectral line shape should be independent of variations in inlet flow conditions since it is dominated by the duct response. Contrast the simple orifice to the flow from a long pipe. The flow entering the duct from a sharp edged orifice is laminar; it does not become turbulent until points further downstream. The flow from a long pipe, on the other hand, is fully turbulent. For comparison to the orifice data the flow was drawn into the duct from a 60" pipe of  $\frac{1}{2}$ " inner diameter (Fig. 3.5).

The low frequency spectral dependence on flow speed is presented in Fig. 3.18. The line shape is similar to that observed for orifices. In particular, the asymmetric shape of the peak at cutoff is evident for all flow speeds.

The high frequency spectral dependence on flow speed is presented in Fig. 3.19. Again the line shape is similar to that observed for orifices. In particular, the spectra resembles the free space spectra in this range. Absent from this figure is evidence of screech peaks. In

section 4.3.5 one screech peak is shown to occur at sufficiently high flow velocities.

Of note is the periodic ripples superimposed on the low frequency plot in Fig. 3.18. The spacing between these ripples is 112.5 Hertz. This corresponds to a cavity length  $L = \frac{c}{2\Delta F} = 60"$ . The ripples represent the excitation of the axial pipe modes. The response of the pipe is superimposed on the duct response.

### 3.2.7 Orifice Mounted on Axis

Herein the orifice was placed so that the air jet entered parallel to the duct axis. The acoustic foam wedge was removed from the upstream end and a  $\frac{1}{2}$ " orifice plate was mounted in its place (Fig. 3.1).

Acoustic spectra versus velocity in the low frequency range are presented in Fig. 3.20. Again, one observes asymmetric peaks at cutoff frequencies for all flow speeds. The effect, however, is not as pronounced as it is for side-mounted orifices. This is due to masking of the acoustic wave by the convected turbulence. The hard-walled orifice plate in the plane of the duct cross-section also influences the spectra. To circumvent these effects, the orifice was mounted on the duct side. The microphone could be mounted upstream in a region of zero mean flow.

The change of location introduces impingement screech. This screech occurs only if the air jet strikes an opposing wall. No screech was observed for the orifice mounted on axis.

### 3.2.8 Upstream versus Downstream Radiation

With the exception of the orifice mounted on axis all spectra were taken with the microphone located upstream. In this region, apart from some recirculation, there is negligible convected turbulence to mask the acoustic wave. In addition, the duct response is independent of jet velocity as the mean flow is zero. Conditions downstream of the orifice should be similar since the flow speed in the duct is small.

Two microphones were used to check this, one upstream and the other downstream. The flow speed was set, and both upstream and downstream spectra were plotted on the same graph. The only error introduced by such procedure is the difference in microphone response, which is approximately 0.8 DB.

The spectra at Mach .25 and 1.0 for a  $\frac{1}{2}$ " orifice are compared in Fig. 3.21. The response at the low flow speed is approximately identical. At high flow speeds a periodic variation of level with frequency is observed downstream, but not upstream. Aside from these variations the response is identical. The microphone was placed

upstream to avoid these flow-induced effects which obscure the interpretation of the spectra.

### 3.2.9 Effect of Microphone Placement

The point of this experiment is to emphasize that the duct response is due to the excitation of the transverse modes. It also demonstrates the influence of microphone placement on the detected spectra. The microphone holder shown in Fig. 3.3 was placed upstream from a  $\frac{1}{2}$ " orifice. The flow speed was set and level changes with changes in the transverse microphone position noted. Three frequencies were selected for detail inspection.

Frequency kHz	Propagating Modes	Cutoff Frequency kHz	Dominant Mode Shape	Nodes
1.0	(0,0)	0	1	0
1.8	(0,0) (1,0)	1.67	$\cos \frac{\pi x}{d}$	0 1
3.5	(0,0) (1,0) (2,0)	3.35	$\cos \frac{2\pi x}{d}$	0 1 2

Above a cutoff frequency all lower modes still propagate. However, the duct response is greatest at a given mode near its cutoff. Hence the detected pressure variations should be dominated by the transverse variations of that mode.

Fig. 3.22 indicates this variation. At 1 kHz only the plane wave propagates, the pressure is uniform across the duct cross section. At 1.8 kHz the first antisymmetric mode dominates, hence the node at the center of the duct. At 3.5 kHz the first symmetric mode dominates, hence the observation of two nodes.

The pressure waves in the various modes are additive. If the microphone is placed at an antinode for a mode, this mode will not be detected. This effect is demonstrated for the first antisymmetric mode (Fig. 3.23). The center of the duct is a node for this mode, hence its influence is not detected. In particular, the peak at the first cutoff is unobserved. For this reason all other experiments were done with the microphone at the corner.

### 3.3 Theory

#### 3.3.1 Duct Acoustics with Mean Flow

Consider a rectangular duct of width  $d$  and height  $b$ . Assume there is uniform mean flow throughout the duct. The linearized wave equation for a harmonic acoustic pressure perturbation of angular frequency  $\omega$  is

$$\left\{ (1 - M^2) \frac{\partial^2}{\partial z^2} + 2i \frac{\omega M}{c} \frac{\partial}{\partial z} + \left( \frac{\omega}{c} \right)^2 + \frac{\partial^2}{\partial x^2} + \frac{\partial^2}{\partial y^2} \right\} p = 0 \quad 3.2$$

where the  $z$  direction lies along the duct axis (see Eq. 2.12 and set  $\varphi$  equal to zero).



Mungar<sup>39</sup> has pointed out that the boundary condition at the walls must be re-examined if flow is present. There can be no mean flow parallel to the duct wall due to the action of viscosity. Morse and Ingard<sup>14</sup> have shown such effects can be modeled as viscous attenuation terms for infinitesimal acoustic velocities parallel to the wall. However, in the presence of mean flow one must assume an infinitesimal region of fluid near the walls in which the mean flow speed is zero. The fluid in the duct is assumed to slip past this region.

When there is relative motion between the fluid and the walls, continuity of displacement must be used in place of continuity of velocity. The normal acoustic velocity  $U_{nf}$  in the fluid is

$$U_{nf} = \frac{D}{Dt} \xi_{nf} = (-i\omega + iV k_z) \xi_{nf} \quad 3.3$$

where  $\xi_{nf}$  is the particle displacement normal to the walls in the moving fluid. The wall velocity  $U_{nw}$  in the stationary fluid near the walls is obtained from the normal particle displacement  $\xi_{nw}$  at the wall by

$$U_{nw} = \frac{\partial}{\partial t} \xi_{nw} = -i\omega \xi_{nw} \quad 3.4$$

Continuity of particle displacement gives

$$\xi_{nw} = \xi_{nf}$$

or

$$\frac{U_{nw}}{-i\omega} = \frac{U_{nf}}{-i\omega + iV k_z}$$

3.5

In the absence of slip continuity of displacement and normal velocity are equal. Now use the condition that the particle displacement at the walls is zero, i.e. the fluid cannot penetrate the hard-walled duct. From Eq. 3.4 it is clear that  $U_{nw}$  is zero. The momentum equation relates pressure gradients in the moving fluid to particle velocities

$$\rho_0 \frac{D}{Dt} U_{nf} = -\frac{\partial p}{\partial n}$$

or

$$\rho_0 (-i\omega + iV k_z)^2 \xi_{nf} = -\frac{\partial p}{\partial n}$$

3.6

Substituting Eq. 3.5 into Eq. 3.6 and requiring  $U_{nw}$  equal to zero gives

$$\frac{\rho_0 (-i\omega + iV k_z)^2}{-i\omega} U_{nw} = -\frac{\partial p}{\partial n}$$

or, by Eq. 3.4 with  $\xi_{nw} = 0$ ,

$$0 = - \frac{\partial p}{\partial n} \quad 3.7$$

The ordinary Neumann Condition on the pressure field at the walls still holds.

Locate the origin of the coordinate system at a corner of the duct. The walls are located at  $x=0, b$  and  $y=0, d$ . A set of solutions satisfy the wave equation

$$p_{mn} = \psi_{mn}(x, y) e^{i k_{mn} z} \quad 3.8$$

where

$$\psi_{mn} = \cos \frac{m\pi x}{b} \cos \frac{n\pi y}{d}$$

$$k_{mn} = \frac{\pm \sqrt{k^2 - (1-M^2)k_{mn}^2} - Mk}{1-M^2}$$

$$k_{mn}^2 = \left(\frac{m\pi}{b}\right)^2 + \left(\frac{n\pi}{d}\right)^2 \quad k = \left(\frac{\omega}{c}\right)$$

Each  $\psi_{mn}$  represents a pressure field, or mode, in the duct which satisfies both the wave equation and the boundary conditions. The field is, in general, a linear combination of the modes  $\psi_{mn}$ .

Note that the transverse portion  $\psi_{mn}(x,y)$  of the modes is orthogonal. Thus

$$\int_0^b dx \int_0^d dy \psi_{mn}(x,y) \psi_{pq}(x,y) = \delta_{mp} \delta_{nq} \Lambda_{mn} bd \quad 3.9$$

where  $bd$  is cross section of the duct and  $\Lambda_{mn}$  the average value of  $\psi_{mn}^2$ .

$$\Lambda_{mn} = \begin{cases} 1 & \text{both } m=0 \text{ and } n=0; \text{ either} \\ \frac{1}{2} & \text{ } m=0 \text{ or } n=0 \text{ but not both;} \\ \frac{1}{4} & \text{ } m \neq 0 \text{ and } n \neq 0. \end{cases}$$

It will be convenient to replace the double index  $m,n$  by the single index  $n$ . To do so, arrange the modes in order of increasing  $\mathcal{H}_{mn}$ .

For a wave to propagate in the  $m,n^{\text{th}}$  mode,  $k_{mn}$ , the wave number in the axial direction, must be real. Given the angular frequency  $\omega$ ,  $k_{mn}$  is real only if

$$\left(\frac{\omega}{c}\right)^2 > \mathcal{H}_{mn}^2 (1-M^2)$$

or

$$\omega > \omega_{mn} (1-M^2)$$

3.10

where

$$\omega_{mn} = c \mathcal{H}_{mn}$$

For any frequency  $\omega$  there are only a finite number of propagating modes.

### 3.3.2 The Green's Function

If the sound generator is a simple harmonic source at point  $(x_0, y_0, z_0)$ , the resulting acoustic disturbance is the Green's function  $G_\omega(\tilde{r}|\tilde{r}_0)$ . Such a function solves the forced wave equation

$$\left[ (1-M^2) \frac{\partial^2}{\partial z^2} + \frac{2i\omega M}{c} \frac{\partial}{\partial z} + \left(\frac{\omega}{c}\right)^2 + \frac{\partial^2}{\partial x^2} + \frac{\partial^2}{\partial y^2} \right] G = \delta(x-x_0) \delta(y-y_0) \delta(z-z_0) \quad 3.11$$

where  $G$  must satisfy the boundary condition in Eq. 3.7.

$G$  can be expanded in a series of eigenfunctions  $\psi_{mn}$ .

For an infinite duct the acoustic waves propagate away from the source point. Thus

$$\begin{aligned} G &= \sum_n A_{n-} \psi_n(x, y) e^{i k_{n-} |z-z_0|} & z < z_0 \\ G &= \sum_n A_{n+} \psi_n(x, y) e^{i k_{n+} |z-z_0|} & z > z_0 \end{aligned} \quad 3.12$$

where

$$k_{n\pm} = \frac{\sqrt{k^2 - (1-M^2) \lambda_n^2}}{1-M^2} = \frac{M k}{1-M^2}$$

Insertion of the expansion into the wave equation. Eq. 3.11, then multiplying by  $\psi_n^*$  and integrating over the cross section  $bd$  gives a set of equations

$$\left[ (1-M^2) \frac{\partial^2}{\partial z^2} + 2i k M \frac{\partial}{\partial z} + (k^2 - \kappa_n^2) \right] A_{n\pm} e^{i k_{n\pm} |z-z_0|} = \frac{-\psi_n(x_0, y_0)}{bd \mathcal{L}_n} \delta(z-z_0) \quad 3.13$$

Integrating from  $z_0 - \epsilon$  to  $z_0 + \epsilon$  gives the magnitude of the discontinuity in the derivative with respect to  $z$  at the source point

$$(1-M^2) (i k_{n+} A_{n+} + i k_{n-} A_{n-}) = \frac{-\psi_n(x_0, y_0)}{bd \mathcal{L}_n} \quad 3.14$$

Continuity of the pressure requires

$$A_{n+} = A_{n-} \quad 3.15$$

One has, dropping the subscript  $\pm$  on the  $A_n$ 's,

$$A_n = \frac{i \psi_n(x_0, y_0)}{(k_{n+} + k_{n-}) bd \mathcal{L}_n} \quad 3.16$$

In the limit of zero flow this reduces to

$$A_n = \frac{i \psi_n(x_0, y_0)}{2 k_n b d \mathcal{L}_n}$$

which can be found in Morse and Ingard<sup>14</sup> (Chapter 9).

The Green's function is

$$G = \sum_n \frac{i \psi_n(x, y) \psi_n(x_0, y_0) e^{i k_{n\pm} |z - z_0|}}{(k_{n+} + k_{n-}) b d \mathcal{L}_n} \quad 3.17$$

where the + sign holds for  $z > z_0$  and the - sign for  $z < z_0$  on the term in the exponential.

### 3.3.3 Random Source Representation in a Duct

Consider the representation of a random source in a duct. The issue is sufficiently complex to warrant a separate discussion. The description is done in steps. First comes a review of the correlation in time, next space correlation along the duct axis, then the space correlation in the plane of the duct cross section. Finally, the full space time correlation is presented as the union of the above. A number of transforms are introduced; to keep track of these the results are summarized in tables 31 and 32. On the right hand side is a note on dimensions which provides a useful check on the formulas.

Consider a region of turbulent pressure fluctuations  $p$  inside a rectangular duct ( $0 < x < b$ ,  $0 < y < d$ ) with rigid walls. Let the fluctuations be confined to a region  $-L/2 < z < L/2$ . To construct a measure of the temporal variations of the source at point  $\tilde{r}_0$ , one proceeds as in free space.

$$p(\tilde{r}_0, \omega) = \frac{1}{2\pi} \int_{-\infty}^{\infty} dt p(\tilde{r}_0, t) e^{i\omega t} \quad 3.18$$

$$p(\tilde{r}_0, t) = \int_{-\infty}^{\infty} d\omega p(\tilde{r}_0, \omega) e^{-i\omega t} \quad 3.19$$

Similarly, the correlation is

$$R(\tilde{r}_0, \tau) = \frac{1}{T} \int_{-T/2}^{T/2} dt p(\tilde{r}_0, t) p(\tilde{r}_0, t+\tau) \\ = \int_{-\infty}^{\infty} d\omega R(\tilde{r}_0, \omega) e^{-i\omega \tau} \quad 3.20$$

$$R(\tilde{r}_0, \omega) = \frac{1}{2\pi} \int_{-\infty}^{\infty} d\tau R(\tilde{r}_0, \tau) e^{i\omega \tau} \\ = \frac{2\pi}{T} |p(\tilde{r}_0, \omega)| \quad 3.21$$



See Eq. 1.23 for a proof of Eq. 3.21. If the source is homogeneous, one can drop the source point  $\tilde{r}_0$  in the description of  $\mathcal{R}$ .

Now consider a measure of the spatial variation along the duct axis. Again, one proceeds as in free space. The Fourier transform is

$$\rho(k) = \frac{1}{2\pi} \int_{-\infty}^{\infty} dz \rho(z) e^{-ikz} \quad 3.22$$

$$\rho(z) = \int_{-\infty}^{\infty} dk \rho(k) e^{ikz} \quad 3.23$$

Similarly, the correlation is

$$\begin{aligned} \mathcal{R}(r) &= \frac{1}{L} \int_{-L/2}^{L/2} dz \rho(z) \rho(z+r) \\ &= \int_{-\infty}^{\infty} dk \mathcal{R}(k) e^{ikr} \end{aligned} \quad 3.24$$

$$\begin{aligned} \mathcal{R}(k) &= \frac{1}{2\pi} \int_{-\infty}^{\infty} dr \mathcal{R}(r) e^{-ikr} \\ &= \frac{2\pi}{L} |\rho(k)|^2 \end{aligned} \quad 3.25$$

Now consider a measure of the spatial variation for points separated in the plane of cross section of the duct. If one defines

$$R(\alpha, \beta) = \frac{1}{bd} \int_0^b dx \int_0^d dy \rho(x, y) \rho(x+\alpha, y+\beta) \quad 3.26$$

as the pressure correlation for simultaneous measurements separated by  $\alpha$  and  $\beta$ , one must decide what values to use for  $\rho$  when  $x+\alpha$  exceeds  $b$  or  $y+\beta$  exceeds  $d$ .

One possibility is that  $\rho$  is zero outside the source region, as was the case for axial pipe modes (Eq. 2.44). In this case, however, computational difficulties are encountered when the source correlation is related to the radiated pressure. In particular, it is impossible to expand the source in the duct eigenfunctions if the source strength is assumed to be zero outside the walls. Here it is more convenient to consider the walls as reflectors and to consider  $\rho$  outside the duct to be the mirror image of the distribution inside. Following Morse and Ingard<sup>14</sup> (Chapter 9), one expands the source in the eigenfunctions of cross section and limits attention to points inside the duct. The Fourier transform is

$$\rho(x, y) = \sum_{mn} P_{mn} \psi_{mn}(x, y) \quad 3.27$$

$$P_{mn} = \frac{1}{bd \Lambda_{mn}} \int_0^b dx \int_0^d dy \rho(x, y) \psi_{mn}(x, y) \quad 3.28$$

Similarly the correlation is

$$R(\alpha, \beta) = \sum_{mn} R_{mn} \psi_{mn}(\alpha, \beta) \quad 3.29$$

$$\begin{aligned} R_{mn} &= \frac{1}{\Lambda_{mn} bd} \int_0^b d\alpha \int_0^d d\beta R(\alpha, \beta) \psi_{mn}(\alpha, \beta) \\ &= \Lambda_{mn} |P_{mn}|^2 \end{aligned} \quad 3.30$$

To get Eq. 3.30, substitute the Fourier expansion of  $\rho$  (Eq. 3.27) into Eq. 3.26. Substitute the resulting expression for  $R(\alpha, \beta)$  into line 1 of Eq. 3.30. Then recall

$$\begin{aligned} \psi_{mn}(x+\alpha, y+\beta) &= \cos \frac{m\pi}{b}(x+\alpha) \cos \frac{n\pi}{d}(y+\beta) \\ &= \left\{ \frac{\cos \frac{m\pi x}{b} \cos \frac{m\pi \alpha}{b} - \sin \frac{m\pi x}{b} \sin \frac{m\pi \alpha}{b} \right\} \\ &\quad \left\{ \frac{\cos \frac{n\pi y}{d} \cos \frac{n\pi \beta}{d} - \sin \frac{n\pi y}{d} \sin \frac{n\pi \beta}{d} \right\} \end{aligned}$$

The result follows from the orthogonality of the sines and cosines.

Since the walls are rigid the pressure fluctuations will be periodic in the wave numbers  $k_x = \frac{\pi}{b}$  and  $k_y = \frac{\pi}{d}$ . Similar assumptions are made when the displacement of a violin string of length  $L$  is expanded in a series  $\sin \frac{n\pi x}{L}$ . If one looks closely at the series and asks what displacement is predicted for  $x$  outside the end points, one finds the displacement periodic in  $k_x = \frac{\pi}{L}$ .

The description of arbitrary space time variations is the union of the above transforms. Thus the Fourier transform is

$$P(\vec{r}_0, t) = \sum_{m,n} \int_{-\infty}^{\infty} dk \int_{-\infty}^{\infty} d\omega P_{mn}(\omega, k) e^{-i\omega t + i k z} \quad 3.31$$

$$P_{mn}(\omega, k) = \frac{1}{\mathcal{L}_{mn} b d 4\pi^2} \int_0^b dx \int_0^d dy \int_{-\infty}^{\infty} dz \int_{-\infty}^{\infty} dt \Psi_{mn}(x, y) P(\vec{r}_0, t) e^{i\omega t - i k z} \quad 3.32$$

Similarly, the correlation is

$$\begin{aligned} R(\vec{r}, \tau) &= \frac{1}{b d L T} \int_0^b dx \int_0^d dy \int_{-L/2}^{L/2} dz \int_{-T/2}^{T/2} dt P(x, y, z, t) P(x+\alpha, y+\beta, z+\gamma, t+\tau) \\ &= \sum_{m,n} \int_{-\infty}^{\infty} dk \int_{-\infty}^{\infty} d\omega R_{mn}(\omega, k) \Psi_{mn}(\alpha, \beta) e^{-i\omega \tau + i k \gamma} \end{aligned} \quad 3.33$$

$$R_{mn}(\omega, k) = \frac{1}{\Lambda_{mn} b d 4\pi^2} \int_0^b d\alpha \int_0^d d\beta \int_{-\infty}^{\infty} d\gamma \int_{-\infty}^{\infty} d\tau R(\tilde{\eta}, \tau) \Psi_{mn}(\alpha, \beta) e^{i\omega\tau - i k \gamma}$$

$$= \frac{4\pi^2}{LT} \Lambda_{mn} |P_{mn}(\omega, k)|^2$$

3.34

where

$$\tilde{\eta} = \alpha \hat{x} + \beta \hat{y} + \gamma \hat{z}$$

For each mode  $m, n$  at frequency  $\omega$  all values of  $k$  are needed for the source description. One may well ask why this is so since the wave equation demands

$k = k_{mn} = \sqrt{\left(\frac{\omega}{c}\right)^2 - \left(\frac{m\pi}{b}\right)^2 - \left(\frac{n\pi}{d}\right)^2}$ . The answer is that one can choose any variation whatsoever in the source distribution. When it comes time to find the radiated pressure, only those values of  $k = k_{mn}$  will contribute.

Consider, for example, the simple case of a point source oscillating at frequency  $\omega_0$  in a narrow tube. Only the plane wave propagates. The complete spatial Fourier description of the source requires all values of  $k$ , since its location is given by a delta function. The radiated pressure, however, only contains the wave number  $k_0 = \frac{\omega_0}{c}$ . The point is, only in the radiation field are  $\omega$  and  $k$  connected; in the source all variations are possible.

TABLE 3.1  
TABLE OF FOURIER TRANSFORMS

Transform	Dimension
-----------	-----------

Time variation at a point

$$P(\omega) = \frac{1}{2\pi} \int_{-\infty}^{+\infty} dt e^{i\omega t} P(t) \quad [P^T]$$

$$P(t) = \int_{-\infty}^{+\infty} d\omega e^{-i\omega t} P(\omega) \quad [P]$$

Space variation in duct cross section

$$P_{mn} = \frac{1}{bd\Lambda_{mn}} \int_0^b dx \int_0^d dy \psi_{mn}(x,y) P(x,y) \quad [P]$$

$$P(x,y) = \sum_{mn} P_{mn} \psi_{mn}(x,y) \quad [P]$$

Space variation along duct axis

$$P(k) = \frac{1}{2\pi} \int_{-\infty}^{+\infty} dz e^{-ikz} P(z) \quad [P^L]$$

$$P(z) = \int_{-\infty}^{+\infty} dk e^{ikz} P(k) \quad [P]$$

Arbitrary space time variation

$$P_{mn}(\omega, k) = \frac{1}{\Lambda_{mn} bd 4\pi^2} \int_0^b dx \int_0^d dy \int_{-\infty}^{+\infty} dz \int_{-\infty}^{+\infty} dt \psi_{mn}(x,y) P(\tilde{r}, t) e^{i\omega t - ikz} \quad [P^{TL}]$$

$$P(\tilde{r}, t) = \sum_{mn} \int_{-\infty}^{+\infty} dk \int_{-\infty}^{+\infty} d\omega P_{mn}(\omega, k) e^{-i\omega t + ikz} \quad [P]$$

TABLE 3.2  
TABLE OF STATISTICAL TRANSFORMS

Transform	Dimension
Time variation at a point	
$\mathcal{R}(\tau) = \frac{1}{T} \int_{-T/2}^{T/2} dt \rho(t) \rho(t+\tau)$ $= \int_{-\infty}^{\infty} d\omega \mathcal{R}(\omega) e^{-i\omega\tau}$ $= \frac{2\pi}{T} \int_{-\infty}^{\infty} d\omega  \rho(\omega) ^2 e^{-i\omega\tau}$	$[\rho^2]$
$\mathcal{R}(\omega) = \frac{1}{2\pi} \int_{-\infty}^{\infty} d\tau \mathcal{R}(\tau) e^{i\omega\tau}$ $= \frac{2\pi}{T}  \rho(\omega) ^2$	$[\rho^2 T]$
Space variation in duct cross section	
$\mathcal{R}(\alpha, \beta) = \frac{1}{bd} \int_0^b dx \int_0^d dy \rho(x, y) \rho(x+\alpha, y+\beta)$ $= \sum_{mn} \mathcal{R}_{mn} \psi_{mn}(\alpha, \beta)$ $\sum_{mn} \Lambda_{mn}  \rho_{mn} ^2 \psi_{mn}(\alpha, \beta)$	$[\rho^2]$
$\mathcal{R}_{mn} = \frac{1}{\Lambda_{mn} bd} \int_0^b d\alpha \int_0^d d\beta \psi_{mn}(\alpha, \beta) \mathcal{R}(\alpha, \beta)$ $= \sum_{mn}  \rho_{mn} ^2 \Lambda_{mn}$	$[\rho^2]$

Transform

Dimension

Space variation along duct axis

$$R(\gamma) = \frac{1}{L} \int_{-L/2}^{L/2} dz \rho(z) \rho(z+\gamma) \quad [\rho^2]$$

$$= \int_{-\infty}^{\infty} dk R(k) e^{ik\gamma}$$

$$= \frac{2\pi}{L} \int_{-\infty}^{\infty} dk |\rho(k)|^2 e^{ik\gamma}$$

$$R(k) = \frac{1}{2\pi} \int_{-\infty}^{\infty} d\gamma R(\gamma) e^{ik\gamma} \quad [\rho^2 L]$$

$$= \frac{2\pi}{L} |\rho(k)|^2$$

Arbitrary space time variation

$$R(\tilde{\eta}, \tau) = \frac{1}{bdLT} \int_0^b dx \int_0^d dy \int_{-L/2}^{L/2} dz \int_{-T/2}^{T/2} dt \rho(x, y, z, t) \rho(x+\alpha, y+\beta, z+\gamma, t+\tau) \quad [\rho^2]$$

$$= \sum_{mn} \int_{-\infty}^{\infty} dk \int_{-\infty}^{\infty} d\omega R_{mn}(\omega, k) \psi_{mn}(\alpha, \beta) e^{-i\omega\tau + ik\gamma}$$

$$= \sum_{mn} \int_{-\infty}^{\infty} dk \int_{-\infty}^{\infty} d\omega \frac{4\pi^2}{LT} \mathcal{L}_{mn} |\rho_{mn}(\omega, k)|^2 \psi_{mn}(\alpha, \beta) e^{-i\omega\tau + ik\gamma}$$

$$R_{mn}(\omega, k) = \frac{1}{\mathcal{L}_{mn} bd 4\pi^2} \int_0^b d\alpha \int_0^d d\beta \int_{-\infty}^{\infty} d\gamma \int_{-\infty}^{\infty} dt R(\tilde{\eta}, \tau) \psi_{mn}(\alpha, \beta) e^{i\omega\tau - ik\gamma}$$

$$= \frac{4\pi^2}{LT} \mathcal{L}_{mn} |\rho_{mn}(\omega, k)|^2 \quad [\rho^2 TL]$$



### 3.3.4 The Radiated Pressure

Consider the acoustic radiation from a region of turbulent pressure fluctuations inside a rectangular duct. Assume the flow in the duct is small enough so that its effects on the duct modes can be neglected.

The radiated pressure is

$$\begin{aligned}
 p(\omega, \tilde{r}) &= k^2 \iiint_{\Omega} d^3 r_0 G_{\omega}(\tilde{r} | \tilde{r}_0) p(\omega, \tilde{r}_0) \\
 &= \frac{i k^2}{2bd} \sum_{q=0}^{Q(\omega)} \frac{\psi_q(x, y)}{\mathcal{L}_q k_q} e^{i k_q z} \iiint_{\Omega} d^3 r_0 p(\omega, \tilde{r}_0) \psi_q(x_0, y_0) e^{-i k_q z_0}
 \end{aligned}
 \tag{3.35}$$

The approximation is in truncating the expression for  $G$  at the last propagating mode. Here  $Q(\omega)$  denotes the mode whose cutoff frequency is closest to the source frequency  $\omega$ . Note the double index  $m, n$  has been replaced by the single index  $q$ .

Inspection of Eq. 3.35 shows that the integral over the source volume  $\Omega$  gives a term proportional to the multiple Fourier transform of  $\varphi$  (Eq. 3.32). Thus

$$\begin{aligned}
 p(\omega, \tilde{r}) &= i 2 \pi^2 k^2 \sum_{q=0}^{Q(\omega)} \frac{\rho_q(\omega, k_q) \psi_q(x, y) e^{i k_q z}}{k_q} \\
 &= i 2 \pi^2 k^2 \sum_{q=0}^Q \frac{\rho_q \psi_q}{k_q} e^{i(k_q z + \phi_q)}
 \end{aligned}
 \tag{3.36}$$

where we have shortened the notation to

$$Q = Q(\omega)$$

$$\Psi_q = \Psi_q(x, y)$$

$$P_q = |P_q(\omega, k_q)|$$

$$\phi_q = \text{ARG} [P_q(\omega, k_q)]$$

Compute the magnitude of the radiated pressure to find

$$\begin{aligned} |p(\omega, \tilde{r})|^2 &= p(\omega, \tilde{r}) p(\omega, \tilde{r})^* \\ &= 4\pi^* k^4 \left\{ \sum_{q=0}^Q \frac{P_q^2 \Psi_q^2}{k_q^2} \right. \\ &\quad \left. + 2 \sum_{q=0}^{Q-1} \sum_{s=q+1}^Q \frac{P_q P_s \Psi_q \Psi_s \cos[(k_q - k_s)z + (\phi_q - \phi_s)]}{k_q k_s} \right\} \end{aligned}$$

3.37

The expression for the radiated pressure depends on both the magnitude and the phase of the turbulent pressure. This phase dependence does not appear in the expression for the radiated power in the axial direction. The power at frequency  $\omega$  is proportional to the integral over the cross section of  $|p(\omega, r)|^2$ . The integration over the cross terms is zero by the orthogonality of the  $\psi$ 's.

In the laboratory, however, one can get reproducible point measurements independent of the axial coordinate  $z$  if the average of a large number of spectra is taken. No integration of measurements over the duct cross section is needed. The implication is that the phases  $\phi_q$  are random and therefore contribute nothing to the average.

Consider the average of  $N$  spectra.

$$\begin{aligned}
 \langle |p(\omega, \tilde{r})|^2 \rangle &= \frac{1}{N} \sum_{n=1}^N |p(\omega, \tilde{r})|_n^2 \\
 &= \frac{4\pi^4 k^4}{N} \sum_{n=1}^N \left\{ \sum_{q=0}^Q \frac{P_q^2 \psi_q^2}{k_q^2} \right. \\
 &\quad \left. + 2 \sum_{q=0}^{Q-1} \sum_{s=q+1}^Q \frac{P_q P_s}{k_q k_s} \psi_q \psi_s \cos[(k_q - k_s)z + (\phi_q - \phi_s)] \right\} \\
 &= 4\pi^4 k^4 \sum_{q=0}^Q \frac{P_q^2 \psi_q^2}{k_q^2}
 \end{aligned}$$

3.38

Where it is assumed that the  $n^{\text{th}}$  measurement  $(\phi_q - \phi_s)_n$  is random and therefore the second term is zero for large  $N$ . The expression for the average magnitude of the radiated pressure depends only on the magnitude of the

source pressure spectra. Eq. 3.34 shows that this quantity is proportional to the multiple Fourier transform of the source correlation. Hence

$$\begin{aligned}
 \langle p(\omega, \vec{r})^2 \rangle &= LT \pi^2 k^4 \sum_{q=0}^Q \frac{R_{mn}(\omega, k_q) \psi_q^2}{k_q^2} \\
 &= \frac{LT k^4}{4bd} \sum_{q=0}^Q \frac{\psi_q^2}{k_q^2 \Lambda_q^2} \int_0^b d\alpha \int_0^d d\beta \int_{-\infty}^{+\infty} d\gamma \int_{-\infty}^{+\infty} d\tau R(\vec{\eta}, \tau) \psi_q(\alpha, \beta) e^{i\omega\tau - ik_q\gamma}
 \end{aligned}$$

3.39

One may ask why it is necessary to use such averages in ducts and not free space. In a duct there are a number of modes in which sound can propagate; in free space there is only one mode. Each mode in a duct propagates at a different phase speed. This generates interference effects which depend on the distance from a source, even in the case of a single point source with random fluctuations in time. Such interference effects depend on the coherence of the source. If the source fluctuations are random, these interference effects will tend to zero for an average over many measurements. Hence the radiated pressure will no longer depend on the distance from the source.

### 3.3.5 Gaussian Correlation and a Qualitative Analysis of the Low Frequency Spectra

Eq. 3.39 provides the basis for interpreting the observed spectra. In accordance with previous work, the radiated pressure from an isotropic Gaussian distribution of sources is determined. Let the correlation length be  $a$  and the correlation time  $\frac{1}{\omega_0}$ . Thus

$$R(\tilde{\eta}, \tau) = \frac{1}{\rho^2} e^{-\left[ (\omega_0 \tau)^2 - \frac{\alpha^2 + \beta^2 + \gamma^2}{a^2} \right]} \quad 3.40$$

One computes  $R_{mn}(\omega, k)$  by performing the integrals indicated in Eq. 3.34. These are given separately

$$\int_{-\infty}^{\infty} d\tau e^{-\omega_0 \tau^2 + i \omega \tau} = \frac{\sqrt{\pi}}{\omega_0} e^{-\left(\frac{\omega}{2\omega_0}\right)^2}$$

$$\int_{-\infty}^{\infty} d\gamma e^{-\left(\frac{\gamma}{a}\right)^2 + i k_{mn} \gamma} = \sqrt{\pi} a e^{-\left(\frac{k_{mn} a}{2}\right)^2}$$

$$\int_0^b d\alpha \cos \frac{m\pi \alpha}{b} e^{-\left(\frac{\alpha}{a}\right)^2} \approx \frac{\sqrt{\pi} a}{2} e^{-\left(\frac{m\pi a}{b}\right)^2}$$

$$\int_0^d d\beta \cos \frac{n\pi \beta}{d} e^{-\left(\frac{\beta}{a}\right)^2} \approx \frac{\sqrt{\pi} a}{2} e^{-\left(\frac{n\pi a}{d}\right)^2}$$

The approximations in the last two lines come from taking the upper limit as  $\infty$ ; these hold only if  $a \ll b$  and  $a \ll d$ . Combining these results gives

$$R_{mn}(\omega, k_{mn}) = \frac{\overline{p^2}}{16 L_{mn} b d} \frac{a^3}{\omega} e^{-\frac{1}{4} \omega^2 \left[ \frac{1}{\omega_0^2} + \left( \frac{a}{c} \right)^2 \right]} \quad 3.41$$

Note that the mode number does not appear in the exponent.

This is because

$$\left( \frac{k_{mn} a}{2} \right)^2 + \left( \frac{m \pi a}{b} \right)^2 + \left( \frac{n \pi a}{d} \right)^2 = \left( \frac{\omega a}{2c} \right)^2$$

If Eq. 3.41 is substituted into Eq. 3.39, the radiated pressure is

$$\langle |p(\omega, r)|^2 \rangle = \frac{\overline{p^2} a^3 L T \pi^2}{16 b d \omega} k^4 e^{-\frac{1}{4} \omega^2 \left[ \frac{1}{\omega_0^2} + \left( \frac{a}{c} \right)^2 \right]} \sum_{q=0}^{Q(\omega)} \frac{\psi_q^2(x, r)}{L_q k_q^2} \quad 3.42$$

Of particular interest is the dependence on  $\frac{1}{k_q^2} = \left[ \left( \frac{\omega}{c} \right)^2 - \lambda_q^2 \right]^{-1}$  in the summation. As the frequency is increased above an eigenfrequency, a new term is added to the sum. At precisely this frequency  $k_q$  is equal to zero, which gives a pole in the pressure response.

As the frequency is increased above the eigenfrequency, the contribution of this term diminishes and approaches  $k^{-2}$  asymptotically. These poles have their origin in the Green's function, i.e., the duct response, and not on the turbulent field. Further, note the asymmetric nature of this contribution. For  $\omega < \omega_q$  the sum terminates before this mode contributes. For  $\omega > \omega_q$  the mode propagates and is included in the summation. Hence the asymmetry of the peaks in the low frequency spectra (Figs. 3.7, 3.8, 3.9, 3.18 and 3.20).

Further note the dependence of  $\psi_q$  on the observer's coordinates. If the microphone is at a node,  $\psi_q$  equals zero, and the mode is not detected. This feature is demonstrated experimentally in Fig. 3.23. With the microphone in the center, the (1,0) mode is not detected. The behavior is further demonstrated in Fig. 3.22 by altering the transverse position of the microphone.

### 3.3.6 Damping and the Smoothing of the High Frequency Spectra

Herein the theoretical infinite peaks at the cutoff frequencies is corrected. To remedy the situation, one postulates some damping of the modes. This can be done in a formal manner by assuming a uniform specific acoustic admittance at the walls. Thus the Neumann boundary conditions for zero mean flow

$$\left. \frac{\partial p}{\partial x} \right|_{x=0,b} = 0$$

$$\left. \frac{\partial p}{\partial y} \right|_{y=0,d} = 0$$

are replaced by

$$\left. \frac{\partial p}{\partial x} \right|_{x=0,b} = \pm i k \beta_x p$$

$$\left. \frac{\partial p}{\partial y} \right|_{y=0,d} = \pm i k \beta_y p$$

3.43

This change introduces a damping of the acoustic waves; see Morse and Ingard<sup>14</sup> (Chapter 9). In working such a problem, the difficulty arises in that the eigenfunctions are no longer orthogonal to their complex conjugates<sup>40</sup>. To expand the Green's function in such a set becomes quite tedious. Recall, however, that the poles are due to  $k_q^2 \rightarrow 0$  as the cutoff frequency is approached. It will be assumed that the damping is so small that the wave functions and eigenfrequencies are given sufficiently accurately by the undamped values. The only modification by damping is assumed to be in the wave number  $k_q$ . Such assumptions are common to the treatment of similar problems in room acoustics.<sup>41</sup> The argument is that damping modifies the response only in the vicinity of an eigenfrequency, i.e., at a pole.

Consider the modified boundary conditions given in Eq. 3.43. The addition of damping gives



$$k_{mn}^2 = k^2 - \left(\frac{\pi \bar{v}_m}{b}\right)^2 - \left(\frac{\pi \bar{v}_n}{d}\right)^2$$

where, in the limit of small  $\beta$

$$\frac{\pi \bar{v}_m}{b} \approx \frac{m\pi}{b} - \frac{2i\beta_x k}{\pi m} \quad m > 0$$

$$\frac{\pi \bar{v}_n}{d} \approx \frac{n\pi}{d} - \frac{2i\beta_y k}{\pi n} \quad n > 0$$

Hence

$$k_{mn}^2 \approx k_{mn}^{\circ 2} - 2i k \left( \frac{\epsilon_m \beta_x}{b} + \frac{\epsilon_n \beta_y}{d} \right)$$

$$k_{mn}^{\circ 2} = \left(\frac{\omega}{c}\right)^2 - \left(\frac{m\pi}{b}\right)^2 - \left(\frac{n\pi}{d}\right)^2 \quad 3.44$$

The  $\frac{\pi \bar{v}_m}{b}$ ,  $\frac{\pi \bar{v}_n}{d}$  reduce to the mode wave numbers  $\mathcal{A}_{mn}^{\circ}$ , plus a correction factor. One then has

$$|k_{mn}|^2 \approx \begin{cases} k_{mn}^{\circ 2} & k^2 \neq \left(\frac{m\pi}{b}\right)^2 + \left(\frac{n\pi}{d}\right)^2 \\ 4 k^2 \left| \frac{\epsilon_m \beta_x}{b} + \frac{\epsilon_n \beta_y}{d} \right|^2 & k^2 \approx \left(\frac{m\pi}{b}\right)^2 + \left(\frac{n\pi}{d}\right)^2 \end{cases}$$

3.45

$$\epsilon_m = \begin{cases} 1 & m=0 \\ 2 & m>0 \end{cases}$$

That is, at the eigenfrequency the magnitude of the wave number  $k_{mn}$  is now nonzero. This implies that the singularities at the cutoff frequencies have been removed from the theory.

Numeric calculations based on visco-thermal damping have been done. The results for the first mode show that the predicted level changes exceed those observed. Such work suggests that the radiative damping may be the dominant loss mechanism.<sup>42</sup>

To determine the influence of damping on the high frequency spectra, consider the radiated pressure at frequencies just above and below the cutoff frequency  $\omega_Q$ . Consider the change in radiated pressure normalized to the pressure at a frequency just below the cutoff.

$$\frac{\Delta p}{p} = \left\{ \frac{\langle |p(\omega_Q + \epsilon)|^2 \rangle - \langle |p(\omega_Q - \epsilon)|^2 \rangle}{\langle |p(\omega_Q - \epsilon)|^2 \rangle} \right\}$$

$$= \left\{ \frac{\Lambda_Q k_Q^2(\omega_Q + \epsilon)}{\sum_{q=0}^{Q-1} \Lambda_q k_q^2(\omega_Q - \epsilon)} \right\} \quad \begin{array}{l} \text{since } k_q(\omega_Q + \epsilon) \approx k_q(\omega_Q - \epsilon) \\ \text{if } q < Q \text{ and } \epsilon \ll 1 \end{array}$$

$$= \left\{ \frac{\Lambda_Q k_Q^2(\omega_Q + \epsilon)}{(Q-1) k^2} \right\} \quad \begin{array}{l} \text{since } k_q(\omega_Q - \epsilon) \approx k \\ \text{if } \omega_Q \gg \omega_q \end{array}$$

$$= \lim_{Q \rightarrow \infty} 0 \quad \text{if } k_Q(\omega_Q) \text{ finite} \quad 3.46$$

The approximation is in substituting the asymptotic limit of  $k_q$  for the sum in the denominator. This substitution is correct if  $Q$  is large. If  $k_Q$  is finite, it is clear that the pressure change approaches zero as  $\frac{1}{Q}$ , where  $Q$  is the number of propagating modes. Note that the limit is correct only if  $k_Q$  is nonzero at the cutoff, as is the case when there is damping.

The conclusion is the change in radiated pressure when a new mode propagates is small compared to the contribution from all other modes if there are a large number of propagating modes. In this fashion, the assumption of finite damping accounts for the smoothing of the spectra in the high frequency limit. This collates with the observed spectra under a variety of conditions (Figs. 3.10, 3.11, 3.12 and 3.19).

### 3.3.7 Radiation Impedance and the Similarity of the High Frequency Duct Spectra to Free Space Spectra<sup>†</sup>

The damping argument (Eq. 3.46) states that the spectra smooths out in the high frequency limit. It can be shown that the spectra is identical to the free space spectra in the high frequency limit. Morse and Ingard<sup>14</sup> have shown this is true for a simple volume source.

---

<sup>†</sup>The author is indebted to Dr. Rice of NASA Lewis for suggesting the use of averaging techniques in duct acoustics.

Herein the analysis is extended to radiation from a turbulent source. In the model of Morse and Ingard the volume source  $q$  is replaced by a small sphere of radius  $a$  whose surface oscillates with velocity amplitude  $U_0$ . To connect the analysis to turbulent flow, note that the source term  $S_\omega$ , of Morse and Ingard, has the units of volume per unit time. Here the source term  $q$  has the units volume per unit volume per time. Inspecting the mass continuity equation, Eq. 1.1, shows that  $\rho_0 S_\omega$  is equivalent to  $m_0 q$ , where  $m_0$  is a unit mass. Further, note that  $q$  can be replaced by an equivalent turbulent dilation  $\frac{k \rho}{\rho_0 c}$  (section 1.2.3). This follows from Ribner's analysis presented in Chapter 1. Thus

$$4\pi a^2 U_0 = S_\omega = \frac{m_0 q}{\rho_0} = \frac{m_0 k \rho}{\rho_0^2 c} \quad 3.47$$

where  $a$  is the radius of the simple spherical volume source.

A check on dimensions shows that the units are correct. The only important difference is the factor  $k$  in the equivalent turbulent source. This comes from the appearance of a second time derivative, in place of a single time derivative for turbulent fields.

The key to the analysis is to examine the asymptotic limit of the radiation impedance. The

impedance is the ratio of the net force on the surface of the sphere to the surface velocity  $U_0$ . The real portion of the impedance,  $\Theta$ , is a measure of the magnitude of the radiated pressure. Morse and Ingard<sup>14</sup> have shown this is (Ref. 14, p. 502, Eq. 9.2.12)

$$\Theta = \rho_0 c \frac{8\pi^2 a^4}{bd} \sum_{m,n} \frac{k}{k_{mn}} \frac{\psi_{mn}^2(x_0, y_0)}{\mathcal{L}_{mn}} \quad 3.48$$

where  $(x_0, y_0, 0)$  is the coordinate of the equivalent spherical source (Fig. 3.24). They state, without proof, "if we average out the narrow peaks, the curve approaches the value  $\rho_0 c (4\pi a^2) k^2 a^2$ , which is the radiation resistance of the source in free space" (Ref. 14, p. 503). A proof is provided here.

For a nonlocalized source it is appropriate to consider the average value of  $\Theta$  for all source points  $(x_0, y_0)$ .

$$\begin{aligned} \Theta' &= \frac{1}{bd} \int_0^b dx_0 \int_0^d dy_0 \Theta(x_0, y_0) \\ &= \rho_0 c \frac{8\pi^2 a^4}{bd} \sum_{m,n}^{MN} \frac{k}{k_{mn}} \end{aligned} \quad 3.49$$

To evaluate  $\Theta'$  in the limit of large  $M, N$ , the double sum is replaced an integral. The discrete values  $\frac{m\pi}{b}$  and  $\frac{n\pi}{d}$

are replaced by the continuum values  $k_x$  and  $k_y$ . Thus

$$\begin{aligned} \frac{k_o}{k_{mn}} &= \left[ 1 - \left( \frac{m\pi}{k_o b} \right)^2 - \left( \frac{n\pi}{k_o d} \right)^2 \right]^{-1/2} \\ &\rightarrow \left[ 1 - \left( \frac{k_x}{k_o} \right)^2 - \left( \frac{k_y}{k_o} \right)^2 \right]^{-1/2} \\ &= \left[ 1 - \left( \frac{k}{k_o} \right)^2 \right]^{-1/2} \end{aligned} \quad 3.50$$

where  $k_o$  is the wave number of the source which oscillates at frequency  $\omega_o$ . The sum is broken into three parts

$$\sum_{mn} \frac{k}{k_{mn}} = \left\{ \begin{array}{l} \sum_{m,0}^{M,0} \frac{k_o}{k_{m0}} \rightarrow \int_0^{k_o} \rho(k_x, 0) \frac{k_o}{k_{m0}} dk_x \\ \sum_{m,n}^{MN} \frac{k_o}{k_{mn}} \rightarrow \int_0^{k_o} dk_x \int_0^{(k_o^2 - k_x^2)^{1/2}} dk_y \rho(k_x, k_y) \frac{k_o}{k_{mn}} \\ \sum_{0,n}^{0,N} \frac{k_o}{k_{0n}} \rightarrow \int_0^{k_o} \rho(0, k_y) \frac{k_o}{k_{0n}} dk_y \end{array} \right. \quad 3.51$$

The first and last sum are for modes with transverse variations only in the x or only in the y direction. The

middle sum indicates modes that have both x and y variations. The density terms indicate the number of new modes added per unit increase in wave number at the wave number  $(k_x, k_y)$ . For a rectangular geometry these densities are constant. They are

$$\rho(k_x, 0) = \frac{b}{\pi}$$

$$\rho(k_x, k_y) = \frac{bd}{\pi^2} \quad 3.52$$

$$\rho(0, k_y) = \frac{d}{\pi}$$

Integrating using the values given in Eq. 3.52 yields

$$\sum_{m,0}^{M,0} \frac{k_0}{k_{m0}} \approx \frac{k_0 b}{2}$$

$$\sum_{m,n}^{M,N} \frac{k_0}{k_{mn}} \approx k_0^2 \frac{bd}{2\pi} \quad 3.53$$

$$\sum_{0,n}^{0,N} \frac{k_0}{k_{0n}} \approx \frac{k_0 d}{2}$$

Substituting back into Eq. 3.49 gives

$$\Theta' \simeq \rho_0 c \frac{8\pi^2 a^4}{bd} \left\{ \frac{k_o^2 bd}{2\pi} + \frac{k_o(b+d)}{2} \right\}$$

$$\simeq \rho_0 c 4\pi a^2 k_o^2 a^2 + \mathcal{O}\left(\frac{b+d}{k_o}\right) \quad 3.54$$

Which was to be proven. The procedure is identical to that used to predict the high frequency behavior of rooms. Close inspection of Eq. 3.54 shows that  $bd$  is the area of the duct cross section and  $2(b+d)$  is the circumference. By analogy to room acoustics, one can generalize

$$\Theta' \simeq \rho_0 c \frac{8\pi^2 a^4}{A} \left\{ \frac{k_o^2 A}{2\pi} + \frac{k_o L}{4} \right\} \quad 3.55$$

for ducts of arbitrary cross section.  $A$  is the cross sectional area and  $L$  the length of the perimeter.

Since the radiation impedance of a duct is the same as that of free space, in the high frequency limit, the duct response should be similar to the free space response. The same source distribution should yield similar spectra. Hence the explanation for the high frequency behavior observed in Figs. 3.10, 3.11, 3.12 and 3.19. The arguments concerning finite damping showed that



the spectra should smooth out in this limit. The averaging procedure demonstrates that the duct response is identical to the free space response.

### 3.3.8 Velocity, Power and Intensity

Now consider other acoustical quantities. The situation in a duct is quite different from free space. In free space, assuming source isotropy, the intensity power and velocity could be deduced from a single pressure measurement in the far field. The relations between acoustic quantities is much more complicated in a duct if transverse modes are excited. A single point measurement is not sufficient to determine the other parameters. If, however, the pressure measurement is made at a common antinode for all the excited modes, then a maximum value can be established for the intensity and power.

Let the pressure field be given by Eq. 3.36

$$p(\omega, \tilde{r}) = i 2\pi^2 k^2 \sum_{q=0}^Q \frac{P_q \psi_q}{k_q} e^{i(k_q z + \phi_q)} \quad 3.56$$

It follows that the velocity in the z direction is

$$U_z(\omega, \tilde{r}) = \frac{i 2\pi^2 k}{\rho_0 c} \sum_{q=0}^Q P_q \psi_q e^{i(k_q z + \phi_q)} \quad 3.57$$

where  $U_z$  follows from the momentum equation  $\rho_0 \frac{\partial}{\partial t} U_z = - \frac{\partial p}{\partial z}$ .

The intensity in the  $z$  direction at frequency  $\omega$  is

$$\begin{aligned}
 I_z(\omega, \tilde{r}) &= \frac{1}{4} \left[ p(\omega, \tilde{r}) U_z(\omega, \tilde{r})^* + p(\omega, \tilde{r})^* U_z(\omega, \tilde{r}) \right] \\
 &= \frac{2\pi^4 k^3}{\rho_0 c} \left\{ \sum_{q=0}^Q \frac{P_q^2 \psi_q^2}{k_q} \right. \\
 &\quad \left. + 2 \sum_{q=0}^{Q-1} \sum_{s=q+1}^Q \frac{P_q P_s \psi_q \psi_s}{k_q} \cos[(k_q - k_s)z + (\phi_q - \phi_s)] \right\}
 \end{aligned}$$

3.58

Using the random phase assumption to compute the average of  $N$  measurements gives

$$\langle I_z(\omega, \tilde{r}) \rangle = \frac{2\pi^4 k^3}{\rho_0 c} \sum_{q=0}^Q \frac{P_q^2 \psi_q^2}{k_q}$$

3.59

The power radiated in the  $+z$  direction at frequency  $\omega$  is obtained by integrating over the duct cross section

$$\begin{aligned}
 \Pi_z(\omega) &= \int_0^b dx \int_0^d dy I_z(\omega, \tilde{r}) \\
 &= \frac{2\pi^4 k^3 b d}{\rho_0 c} \sum_{q=0}^Q \frac{P_q^2 \Lambda_q}{k_q}
 \end{aligned}$$

3.60

To establish a relation between these exact quantities and a single pressure measurement, first recall Eq. 3.38

$$\langle |p(\omega, \tilde{r})|^2 \rangle = 4\pi^4 k^3 \sum_{q=0}^Q \frac{k}{k_q} \frac{P_q^2 \psi_q^2}{k_q} \quad 3.61$$

It follows from the definitions of  $k_q$  and  $\Lambda_q$  that

$$\Lambda_q \leq 1 \quad \frac{k}{k_q} \geq 1 \quad 3.62$$

If the microphone is placed at a corner,  $\psi_q$  is identically 1 for all  $q$ . The inequalities in Eq. 3.62 then show

$$\frac{1}{2\rho_0 c} \langle |p(\omega, r)|^2 \rangle \Big|_{\text{corner}} \geq \langle I_z(\omega, \tilde{r}) \rangle \Big|_{\text{for all } \tilde{r}}$$

and

$$\frac{bd}{2\rho_0 c} \langle |p(\omega, r)|^2 \rangle \Big|_{\text{corner}} \geq \pi_z(\omega) \quad 3.63$$

In engineering problems the maximum values are often the quantities that are needed. The inequalities of Eq. 3.63 demonstrate that an upper limit on the radiated power and intensity can be established from a single measurement.

### 3.3.9 A Numeric Comparison of Predicted to the Observed Low Frequency Spectra

Consider the spectra predicted in Eq. 3.42. Examine the prediction for a  $\frac{1}{2}$ " orifice mounted on the side of a  $1\frac{1}{2}$ " by 4" rectangular duct. The duct height and width is then equal to

$$b = 8 D \qquad d = 3 D \qquad 3.64$$

where  $D$  is the jet diameter. For numerical comparison, let the inverse of the correlation time,  $\omega_0$ , be given by the Strouhl frequency

$$\omega_0 = 2\pi f_s = 2\pi \left( .25 \frac{V}{D} \right) = \frac{\pi}{2} \frac{MC}{D} \qquad 3.65$$

Choose a velocity so that the contribution of space and time correlation is approximately equal; that is

$$\frac{D}{C} \approx \frac{1}{\omega_0}$$

$$M \approx \frac{2}{\pi} \approx .63 \qquad 3.66$$

Here the correlation length is assumed to be equal to the jet diameter. Substituting these values into Eq. 3.42 gives

$$\langle p(\omega, r)^2 \rangle = B x^4 e^{-\frac{1}{2} x^2} \sum_{mn}^{MN} \frac{\psi_{mn}^2(x, \gamma)}{L_{mn} \left[ x^2 - \left(\frac{m\pi}{8}\right)^2 - \left(\frac{n\pi}{3}\right)^2 \right]}$$

3.67

where

$$x = \frac{\omega}{\omega_0}$$

All information concerning the absolute level is absorbed into B.

In Fig. 3.25 a comparison of Eq. 3.67 is made to the observed spectra for a  $\frac{1}{2}$ " orifice with mean flow speed Mach .61. The qualitative features of the curve are in agreement with the prediction. First, the asymmetric shape of the peaks is predicted quite accurately. In fact, the spectra levels are accurate to  $\pm 2$  DB for frequencies above the first cutoff. This is quite good considering only dimensional arguments are used to fit the data. It should be noted that the parameter B was chosen so that predicted and observed spectra lie close to one another. This does not affect the curve shape at the peaks, which is the point of interest.

The most glaring disparity is for frequencies below the first cutoff. As was the case for free space, an isotropic model of the source fluctuations can only

account for limited portions of the spectra. A complete analysis requires that the inhomogeneities of the turbulent field be accounted for. This discrepancy does not detract from the main point. The spectral line shape can be explained through a linear analysis of the duct response. The asymmetric peaks have their origin in the selective response of the duct to a source near a cutoff frequency. No alteration of the turbulent spectra needs to be assumed.

## 4. SCREECH

### 4.1 Introduction

In these studies of flow-generated sound several instances where the sound field departed from that predicted by linear models were observed. Until now it was assumed that the aerodynamic sources in the fluid could be given without reference to the acoustic field that they produce. This assumption must be abandoned if one is to account for the screech anomalies. In such cases the acoustic pressure reacts back on the flow field so as to produce a coupled, or feedback, oscillation.

Previously it was assumed that the jet fluctuations which produce the sound are random and could be statistically described by a Gaussian correlation. This method is not adequate for screech. There exist collective modes of oscillation of the jet that are different than the random turbulent fluctuations. It is these modes which are important in feedback. In a feedback loop a perturbation of the jet results in an amplifying fluctuation of the flow. The fluctuation breaks into ring vortices which are convected downstream. When these vortices encounter some obstruction or discontinuity, they produce an acoustic wave. This travels back to the origin of the jet and perturbs it, thereby closing the feedback loop.

The whistling teapot is a common example of just such an effect<sup>43</sup>. In escaping from the teapot, the vapour passes through two concentric circular orifices spaced a short distance apart. The first orifice serves to form a jet. This jet passes through the second orifice and, if the flow speed is right, a discrete tone is generated. In the absence of a second orifice one hears only the broadband hiss which typifies sound emission from model jets.

Two similar instabilities have occurred in these studies. The first was observed in the excitation of axial pipe modes. Intense pure tone oscillations occurred for pipe lengths which were short compared to the pipe diameter. This is shown here to occur for cylindrical orifices having length-to-diameter ratios between one half and two.

The second instability was observed in the turbulent excitation of transverse modes in ducts. Intense pure tone oscillations occurred if the flow speed was right. These are here shown to be those due to a jet impinging on a flat plate.

Anderson<sup>44</sup> studied the orifice tone extensively. He explores the conditions for the excitation of pure tones by airflow through a sharp-edged cylindrical orifice. Here separation of the flow from the upstream edge allows for shear layer oscillations and thereby orifice



screech. His results are presented in nondimensional form as Strouhl number versus Reynolds number. Heller<sup>45</sup> also observed such tones occurred for length-to-diameter ratios between one half and two.

This investigation of orifice screech presents the results in plots of frequency versus flow speed to facilitate the kinematic analysis of the problem. In particular, one can account for the observed screech frequencies by careful analysis of the feedback loop. One assumes that disturbances of the jet at the inlet are propagated downstream<sup>46</sup>. At the exit the sudden expansion of orifice diameter generates an acoustic wave. This propagates upstream and perturbs the jet at the inlet. The fundamental screech frequency is inversely proportional to the period required to transverse such a cycle. Overtones are assumed to be integral multiples of the fundamental.

It is further shown that screech occurs only if the frequency is approximately that of an axial acoustic mode. This is seen by noting the screech tones occur near the intersection of a screech mode with the axial pipe frequency. Suitable alterations of the geometry are then explored to show coupling with the radial acoustic modes.

The second instability was observed in the excitation of transverse modes in ducts. These were the

narrow band peaks which occurred at certain flow speeds. Analysis of level versus jet velocity showed that these were nonlinear effects.

Recall the screech occurred in configurations where the air jet impinged on the opposite duct wall. Pure tone oscillations have been observed when a subsonic jet impinges on a wall. The impingement couples the air jet to the acoustic field.

Powell and Unfried<sup>47,48</sup> observed a similar effect in the study of edge tones. In their work a jet from a rectangular slot impinges on a triangular wedge located downstream. In the classical edge tone experiments the wedge angle is acute. However, these experimenters varied the angle to  $180^\circ$ , i.e., a flat plate. They observed screech in this setup.

Wagner<sup>49</sup>, and later Neuwerth<sup>50</sup>, investigate the free subsonic circular jet impinging on a flat plate. Screech occurs at Mach numbers greater than .6 and nozzle-to-plate separations less than 6 jet diameters. They observe that periodic shedding of ring vortices at the jet boundary can be induced by an acoustic wave either inside or outside the jet. To minimize the influence of acoustic modes, Neuwerth lined all surfaces with sound proofing material. In this fashion he isolates the effect of the wave travelling inside the jet column.

Herein such modes are shown to occur in the presence of an acoustic mode. A free jet exists from an orifice in a flat plate and impinges on a second plate. The separation is the same as is the duct experiment. The screech frequencies produced here are the same as those observed in the duct. These frequencies are approximately those of the acoustic mode between two flat plates.

In a separate experiment the change in frequency by the presence of an acoustic resonator is demonstrated. First, an air jet from a long pipe is set to impinge on a flat pipe, and the screech tone is noted. Next, a cavity is formed by fitting a plate snugly over the pipe exit. The screech frequency is observed to shift to that of the acoustic cavity.

## 4.2 Orifice Screech

### 4.2.1 Orifice Screech: Apparatus and Procedure

Herein the generation of pure tones caused by drawing air through circular orifices of small length-to-diameter (L/D) ratio is described. The phenomena is characterized by intense pure tone oscillations termed "orifice screech." The apparatus differs from that used to determine the axial mode excitation of pipes in that the L/D ratio is small. Roughly speaking, orifice screech is observed for holes in plates, whereas the axial modes are observed in long pipes. The critical parameter is the

length-to-diameter ratio and not whether the entrance is a flat plate or a pipe (Fig. 4.1).

The apparatus is a flat plate fixed to a cylindrical plenum chamber, 15" in diameter by 30" long. The plenum was damped by two flat boards of fiberglass sound absorber. At the center of the plate a small circular hole was drilled, typically  $\frac{1}{2}$ " diameter. The plenum was evacuated to a pressure below atmospheric and air drawn through the orifice. The flow-generated sound was detected with a microphone, and the signal was spectrum analyzed. The microphone was mounted in the ambient air outside the plenum.

The apparatus differs from Anderson's<sup>44</sup> in one important feature. He uses a compressor system. The plenum is raised to a pressure higher than atmospheric, and air is forced through the orifice. He finds it necessary to place a stainless steel screen  $\frac{1}{2}$ " in front of the orifice plate to "stabilize" the flow. All air is passed through the screen before entering the orifice. The precaution is necessary since upstream disturbances generated in the compressor plumbing are forced through the orifice. In the present setup, air enters from the quiescent atmosphere and such precautions are unnecessary.

As the flow velocity increases, the jet tones appear quite suddenly. As the velocity of the flow

increases further, the amplitude decreases gradually, finally merging into the broadband turbulent noise. There is a mid-range between "onset" and "offset" in which the amplitude is insensitive to velocity changes. A typical spectra from a  $L = \frac{1}{2}$ ",  $D = \frac{1}{2}$ " orifice is presented (Fig. 4.10). The extremely narrow peaks distinguish screech from broadband turbulent-generated sound. The difference is noted quite easily by ear. Turbulent noise is perceived as a hiss, whereas orifice screech is a shrill piercing whistle.

#### 4.2.2 Screech Dependence on the Length-to-Diameter Ratio and Flow Speed

Herein the range in which screech occurs is established. The orifice is a  $\frac{1}{2}$ " diameter hole drilled in an aluminum plate of thickness  $\frac{1}{8}$ ",  $\frac{1}{4}$ ",  $\frac{1}{2}$ ", 1", and 2". The flow speed was varied from zero to Mach 1.0 in each case. Screech was observed for the  $\frac{1}{4}$ ",  $\frac{1}{2}$ ", and 1" thicknesses it did not occur for the  $\frac{1}{8}$ " or 2" plate (Fig. 4.5). The tones were observed in a range of flow speeds from Mach .25 to Mach .85. The flow speed was calculated from the pressure drop across the orifice by the isentropic nozzle approximation<sup>37</sup>

$$M = \frac{V}{C_0} = \sqrt{\frac{2}{\gamma-1} \left[ 1 - \left( \frac{P_T}{P_A} \right)^{\frac{\gamma-1}{\gamma}} \right]}$$

4.1

where

$V$  velocity in the air jet  
 $c_o$  speed of sound in the quiescent air  
 $\gamma$  ratio of specific heats  
 $P_T$  pressure in the plenum  
 $P_A$  upstream atmospheric pressure

The results on the  $(L/D)$  necessary for screech confirm the observations of Heller<sup>45</sup>.

It is especially important that the inlet edge of the orifice be sharp for maximum efficiency in the production of tones. If one does so little as to place a pencil point near the inlet, the tones are suppressed. This is not true for the exit; here wide variations in the geometry can be tolerated.

The importance of a sharp inlet motivates several aspects of the study. The flow separates from the walls of the orifice at the leading edge. It then contracts to approximately .6 of the inlet area forming a jet surrounded by an annulus of quiescent air between the jet and the walls. Such a well-defined symmetric system can support collective modes of oscillation which propagate down the jet column. These begin as perturbations in the jet diameter and develop into ring vortices. Such vortices have been observed in both orifice screech<sup>51</sup> and impingement screech.<sup>49,50</sup>

A qualitative explanation of the absence of screech tones for large  $L/D$  can be given. Recall that the viscous forces induce the jet to expand back to the walls of the pipe. If the length is short enough, the flow never reattaches to the walls. If the length is long enough, the flow reattaches, and the propagation of the ring vortices is perturbed. The mean flow portion of the feedback loop is broken, and screech does not occur.

Figs. 4.2, 4.3, and 4.4 plot the screech frequency versus mean flow speed. The circles are the observed points, the solid line is the theoretical feedback frequency, Eq. 4.4, and the dotted line the axial pipe mode, Eq. 4.6. In all cases the screech frequency increases with the flow speed. If a series of tones are detected at a given flow speed, their frequencies are related as the ratio of integers. In all cases the data is clustered about the intersection of the feedback frequency with the axial mode frequency.

To emphasize the clustering, consider the  $\frac{1}{4}$ " data (Fig. 4.2). For low speed the data lies along the path of the feedback instability. At Mach .62 the frequency jumps by 3 kHz. This can be explained if one assumes some interaction between the feedback mode and the axial pipe modes. The jump signifies a change in coupling from the first to the second axial mode.

#### 4.2.3 Similarity to Hole Tone

If orifice screech is similar to the hole tone, one expects that the critical features are determined by the diameter and separation between inlet and exit. To check this feature, two thin orifice plates were constructed. These were separated by a short length of pipe with an inner diameter larger than the orifice diameter.

The orifice plates were fashioned out of  $\frac{1}{16}$ " thick sheet of aluminum. In each plate a  $45^\circ$  tapered hole was drilled to form a  $\frac{1}{2}$ " diameter hole so as to fashion a sharp edge. In the first test, the separation between edges was set to  $\frac{1}{2}$ ". Two pipe diameters were studied,  $\frac{5}{8}$ " and  $4\frac{11}{32}$ ".

Fig. 4.7 is a plot of the screech data observed for the  $\frac{5}{8}$ " inner diameter separator. Superimposed on the graph is the trace of the feedback and axial frequencies used for the  $\frac{1}{2}$ "  $\times$   $\frac{1}{2}$ " orifice (Fig. 4.3). The data from this experiment follows the same trend as that observed for the simple orifice of similar length and diameter.

Fig. 4.8 is a plot of the screech data observed for the  $4\frac{11}{32}$ " inner diameter separator. Superimposed on the graph is the trace of the feedback frequency used for the  $\frac{1}{2}$ "  $\times$   $\frac{1}{2}$ " orifice. Besides the axial modes, there are now radial cavity modes whose frequencies are below 20 kHz. Two pronounced cases of radial mode excitation are



indicated by triangles in place of circles for the data points. There are too many radial modes below 20 kHz to plot with any clarity on the graph. However, the excitation of such modes, for the down pointing triangles, is verified in section 4.2.6. Note that the data points approximately follow the feedback frequency. The relations, however, are considerably more complex than that of observed for the  $\frac{5}{8}$ " inner diameter separator.

In the next experiment the L/D bounds on screech are determined for the  $\frac{5}{8}$ " inner diameter separator. The geometry is identical to that presented in Fig. 4.7, except for the separation between edges. The plate separation was set at 0",  $\frac{1}{4}$ ",  $\frac{1}{2}$ ", 1" and 2". The ratio of orifice diameter-to-plate separation in which screech was observed is the same as that of a simple orifice. To see this, compare Figs. 4.5 and 4.6.

#### 4.2.4 Perturbation of the Flow by Screens

Herein it is shown that the unimpeded propagation of disturbances down the jet column play an essential role in the production of screech tones. It was once thought that the perturbation of the jet shear layer at the inlet drives the axial acoustic mode. In such a model, only the inlet flow conditions are critical. This model is incorrect, as it is demonstrated here.

To settle the question, one needs to perturb the jet downstream without any perturbation of the axial mode. This is done with a wire screen placed in the center of the orifice. A jet passing through the screen becomes turbulent, whereas the axial mode is undisturbed. Consider the first axial acoustic mode. The center of the orifice is at a velocity node, a screen placed at this point has negligible effect on the acoustic fluctuations in the orifice. Hence only the jet is perturbed.

Two  $\frac{3}{8}$ " diameter holes were drilled in a  $\frac{1}{2}$ " plexiglass plate. The rear side of one hole was then drilled to a slightly larger diameter so as to allow a wire screen to be mounted in the center. The screen was held in place by an annular plexiglass plug with a  $\frac{3}{8}$ " inner diameter. The only difference between the two orifices is the screen at the center. The screen was composed of 5 mil wire with 30 strands per inch. This gives approximately 70% open area.

Air was drawn through the unmodified orifice and screech was observed. Next, air was drawn through the screened orifice. No screech occurred for any flow speed up to Mach 1.0. One concludes that the continuity of the jet column is an essential part of orifice screech.

A screen flush to the inlet inhibits screech for the same reason. The inlet flow is turbulent and collective modes of oscillation on the jet are suppressed.

The screech is suppressed if the screen is placed flush to the exit. This experiment must be done carefully. If the screen bows slightly past the exit wall, screech occurs.

For a summary of these observations, see Fig. 4.9.

#### 4.2.5 A Kinematic Calculation of the Feedback Frequency

Covert and Bilanin<sup>52</sup> have studied a similar screech mechanism caused by air flow past a rectangular cutout in a flat surface. They extend an analysis proposed by Rossiter.<sup>53</sup> The central point is that the flow separates from the surface at the leading edge of the cutout, thereby forming an unstable shear layer. Any perturbation of the shear layer travels downstream towards the trailing edge. The interaction at the trailing edge generates an acoustic wave that propagates upstream to force the shear layer. The feedback cycle is then completed.

A similar mechanism exists for orifice screech. The air separates from the surface at the inlet to form a cylindrical jet with a well-defined shear layer. Any disturbance at the inlet propagates down the jet as a displacement of the shear layer which then develops into ring vortices. When these vortices reach the trailing edge, they generate an acoustic pulse. This pulse

travels back upstream to force the shear layer at the inlet, thereby forming a feedback loop.

Assume that the phase shifts of such disturbances are zero at the inlet and exit. Let  $t_H$  be the time it takes for a disturbance of the jet to reach the exit

$$t_H = \frac{L}{\alpha V} \quad 4.2$$

where  $\alpha$  is the ratio of the convection speed of such disturbances to the mean jet speed  $V$ ;  $L$  is the length, i.e. thickness of the orifice.

Let  $t_A$  be the time it takes for the resulting acoustic pulse to reach the inlet. There are two paths, one through the quiescent annulus, the other through the jet column.

In the annulus the phase speed is  $c$ , in the jet it is  $c - V$ . Hence, the characteristic acoustic time is

$$t_{A1} = \frac{L}{c} \quad t_{A2} = \frac{L}{c - V} \quad 4.3$$

The feedback frequency is inversely proportional to the period to complete the cycle

$$f_i = \frac{1}{t_{A1} + t_H} = \frac{c}{L} \frac{\alpha M}{1 + \alpha M} \quad 4.4$$

$$f_2 = \frac{1}{t_{A2} + t_H} = \frac{c}{L} \frac{\alpha M (1-M)}{1 + (\alpha - 1) M} \quad 4.5$$

In the experiment the points lie along the path given by Eq. 4.4 and only these curves are presented. That is, the acoustic feedback through the annulus accounts for the observed frequencies. Overtones are assumed to be integral multiples of the fundamental. The convection speed was set at six tenths the mean flow speed ( $\alpha = .6$ ).

Consider the behavior of the axial pipe frequencies with flow. The fundamental is

$$f_A = \frac{c}{2L} \frac{1}{\left[ \frac{1}{1-M^2} + .6 \frac{D}{L} \right]} \quad 4.6$$

It has been observed that for screech excitation to occur the feedback frequency  $f_1$  must be approximately that of the axial pipe mode. Consider the interaction of the  $n^{\text{th}}$  feedback mode with the  $q^{\text{th}}$  axial acoustic mode. Setting the two frequencies equal yields a cubic equation in the Mach number.

$$n f_1 = q f_A$$

gives

$$M^3 \alpha \left[ 1 - \frac{n}{q} \frac{1.2 D}{L} \right] + M^2 + M \alpha \left[ \frac{n}{q} \left( 2 + 1.2 \frac{D}{L} \right) - 1 \right] - 1 = 0 \quad 4.7$$

The real valued solution to Eq. 4.7 for  $0 \leq M \leq 1$  gives the Mach number about which the screech is centered. The intersection of the solid and dotted lines in Figs. 4.2, 4.3 and 4.4 represent a graphical solution to Eq. 4.7 for selected values of  $\frac{D}{L}$  with  $\alpha = .6$ . The cubic equation can be solved exactly. Care must be taken since the equation reduces to a quadratic when  $\frac{D}{L} = \frac{q}{1.2 n}$ .

Some comment on the choice of convective velocity is in order. The most compelling argument is the experimental evidence of Wagner and Neuwerth.<sup>49,50</sup> Through schlieren photography they determine the propagation speed of the ring vortices to be approximately six tenths the mean flow speed. Anderson<sup>51</sup> finds the value of  $\alpha = .53$  in a similar study. Analytic calculations by Handa<sup>54</sup> and Bilanin<sup>55</sup> predict that the phase speed of a shear layer disturbance propagates at <sup>approximately</sup> half the mean flow speed.

This can be explained qualitatively by considering a vortex sheet at the jet boundary. Imagine these vortices to be solid rollers whose bottoms move, without slip, at the jet velocity and whose tops roll, without

slip, on the quiescent air. The center of mass of these rollers will then move a half the jet velocity.

#### 4.2.6 Cavity Mode Excitation

The screech studies of thin orifice plates separated by a 4  $\frac{1}{2}$ " cylinder (Fig. 4.8) demonstrated the excitation of additional tones. These are due to the coupling of the feedback instability to the cylinder modes. This is demonstrated by examining one velocity in great detail.

The case under review is represented in Fig. 4.8 as triangles that point down, i.e., at Mach .34. The excited modes have nodal lines that lie along the radii. These divide the cylinder into a set of "pie slice" regions. Only those modes with an odd number of nodes are excited; these are called the antisymmetric modes.

First, one establishes that the phenomena is a screech instability. In Fig. 4.10 the spectra for a simple orifice is presented. In Fig. 4.11 the spectra of the hole tone at Mach .33 is presented. The similarity in line shape and the magnitude of the fundamental, in comparison to the harmonics, shows that the screech mechanism is similar. At Mach .34, only 5 mm Hg larger pressure drop, the cavity modes are excited (Fig. 4.12). The feedback frequency should increase about 3% in a shift of flow speed from Mach .33 to Mach .34 (Eq. 4.4). This slight

shift is enough to make the screech tones coincident with the third, seventh and eleventh antisymmetric cylinder mode.

Consider the modes of oscillation of a disk of air bound by a hard walled cylinder of radius  $R_0$ . The pressure field inside the cylinder is the sum of the natural modes.

$$p(r, \theta) = p_{ns} J_n(k_{ns} r) e^{in\theta} \quad 4.8$$

Where  $J_n$  is the Bessel function of the first kind. The walls impose the boundary condition

$$\left. \frac{\partial p(r, \theta)}{\partial r} \right|_{r=R_0} = 0 \quad 4.9$$

hence

where

$$k_{ns} R_0 = j'_{ns} \quad J'_n(j'_{ns}) = 0 \quad 4.10$$

Thus the natural frequencies are

$$f_{ns} = j'_{ns} \frac{c}{2\pi R_0} \quad 4.11$$

The prime on  $J$  signifies differentiation with respect to its argument. The notation follows Abramowitz and Stegun<sup>36</sup>. One needs the values  $j'_{n,1}$  for odd  $n$  up to



17. For values greater than  $n = 8$  tables are not easily found, and it proved necessary to calculate the roots  $j'_{n,1}$  by computer.

Let the radius  $R_0 = 5.54$  cm, the speed of sound  $C = 34,000 \frac{\text{cm}}{\text{sec}}$  and the length  $L = 1.27$  cm. To place the predicted screech notes at the observed values, it is necessary to assume  $\alpha = .547$ . An equivalent change would be to lower the Mach number to nine tenths its nominal value of .34 and keep  $\alpha = .6$ . Table 4.1 presents a numerical comparison of the observed frequencies of excitation to those given by Eq. 4.11.

Based on the ratio of observed-to-calculated frequencies, it is clear that all but the first peak coincide with the antisymmetric cavity modes. There is, however, a numerical discrepancy that increases with increasing frequency. At the last observed peak the difference is 250 Hz. The error in the frequency measurement is approximately 100 Hertz, hence the difference cannot be attributed to experimental error in the frequency measurement.

One possibility is that the radial frequencies are altered by the presence of the air jet in the center. An accurate calculation should include this modification. Another possibility is that the error lies in the value of  $\frac{C}{2\pi R_0}$ . The ratio of the observed-to-calculated

frequencies is correct to 2%. A 2% error in the radius  $R_0$ , approximately 1 mm, would then account for the discrepancy.

The data can be reduced in a manner independent of  $\frac{c}{2\pi R_0}$ . This is to consider the ratio of the screech tones to the screech tone of maximum amplitude, observed at 4.2 kilocycles. If Eq. 4.11 is correct, this ratio should be given as  $\frac{j'_{n,1}}{j'_{3,1}}$ . Table 4.2 presents the data reduced in this fashion. The numbers agree in absolute value within an error of .05.

Only the first peak differs significantly. Inspection of Table 4.1 shows the observed peaks are separated, on the average, by 2.1 kilohertz. It is most probable that the first peak is the difference tone due to the interaction of the excited modes with their nearest neighbors. All the other peaks are clearly due to the excitation of the antisymmetric cavity modes.

It is instructive to recall that this entire section is devoted to the screech behavior at a single velocity. A complete analysis of the data given in Fig. 4.8 requires a similar study at each velocity. Such a task is beyond the scope of this chapter. One point that comes out is that the screech depends, in some fashion, on the distance of the wall from the jet column. This effect is incorporated into an analysis of the shear layer stability of a jet and is presented in the appendix.

TABLE 4.1

Data for Screech Coupled to Cavity Modes

$n,s$	$j'_{n,s}$	Screech Frequency Eq. 4.4 kHz	Cavity Frequency Eq. 4.11 kHz	Observed Frequency Fig.4.12 kHz	$\frac{f_{\text{observed}}}{f_{\text{calculated}}}$
1,1	1.84		1.80	2.1	1.17
3,1	4.20	4.20	4.12	4.2	1.02
5,1	6.42		6.30	6.3	1.00
7,1	8.58	8.40	8.42	8.4	1.00
9,1	10.71		10.51	10.6	1.01
11,1	12.83	12.59	12.59	12.7	1.01
13,1	14.93		14.65	14.7	1.00
15,1	17.02	(16.79)	16.70	16.8	1.01
17,1	19.11		18.75	19.0	1.01

This table demonstrates the coupling of screech to the radial acoustic modes.

TABLE 4.2

Normalized Data for Screech Coupled to Cavity Modes

$n, s$	screech harmonic	$\frac{j'_{n,1}}{j'_{3,1}}$	$\frac{f_{n,1} \text{ observed}}{f_{3,1} \text{ observed}}$	$\frac{\text{calculated ratio}}{\text{observed ratio}}$
1,1		.44	.50	.88
3,1	1	1.00	1.00	1.00
5,1		1.53	1.50	1.02
7,1	2	2.04	2.00	1.02
9,1		2.55	2.52	1.01
11,1	3	3.05	3.02	1.01
13,1		3.55	3.50	1.01
15,1	4	4.05	4.00	1.01
17,1		4.55	4.52	1.01

### 4.3 Impingement Screech

#### 4.3.1 Impingement Screech, Apparatus and Procedure

A screech mode was also observed in the experiments on the excitation of transverse modes in ducts. It was shown that the initial peaks in the observed spectra were due to the selective response of the duct at its cutoff frequency. Further, it was proved that the spectra should smooth out in the high frequency limit, i.e., when a large number of modes can propagate. However, intense pure tones were observed in this frequency regime at flow velocities above Mach .6. These are here identified as a feedback instability, termed impingement screech, due to the obstruction of the air jet by the opposing wall of the duct.

Wagner<sup>49</sup> has shown that a jet incident on a flat plate screeches. This occurs only if the plate is less than 6 diameters from the jet nozzle, and if the Mach number is greater than .6. He collated the acoustic frequency with the shedding of ring vortices on the jet column. He concludes that the screech is due to "feedback between the flow and the pressure field generated by it." Neuwerth<sup>50</sup> later extended the work to include screech at supersonic velocities.

The nozzle they used is not quite the same as the orifice plate or pipe used in the duct experiments

(Figs. 3.4 and 3.5). Their apparatus was a converging nozzle followed by a short length of pipe (Fig. 4.13). Herein it is shown that impingement screech occurs using an orifice plate and a 60" pipe. That is, the slight variations of inlet conditions in the duct experiments from Wagner's nozzle do not suppress impingement screech.

The apparatus used here is a plenum chamber 60" long and 12" wide. At the exit the chamber converges to a diameter of 4". A  $\frac{1}{2}$ " thick orifice plate with a hole tapered to 45° to a  $\frac{1}{2}$ " diameter was attached to this end. In the second experiment a 60" pipe with a  $\frac{1}{2}$ " inner diameter was fixed to a plate that was, in turn, secured to the chamber exit. A square flat plate, 4" on a side, was placed in the air jet at various distances from the exit. The plenum pressure is raised to force air out at a constant rate.

Before investigating the screech, some data on the turbulent-generated noise is taken. A qualitative presentation is given so as to provide spectra for comparison to the turbulent excitation of cavities.

#### 4.3.2 Free Jet Spectra from Pipes and Orifices

The variation in free space spectra with jet flow speed is given here. This is done to demonstrate that the qualitative spectra of free jets is the same for both a long pipe and an orifice. For a more detailed analysis

the reader is referred to von Gierke's<sup>38</sup> studies. He shows that the spectra can be scaled by introducing the dimensionless frequency

$$\frac{f D}{V} \frac{c_j}{c_o} \quad 4.12$$

and the power

$$10 \log \left[ \frac{1}{\rho_o A} \frac{dW}{df} \frac{V}{D} \frac{c_o}{c_j} \right] \quad 4.13$$

where

- $c_j$  sound speed in the jet
- $c_o$  sound speed in the quiescent air
- $\frac{dW}{df}$  spectrum of acoustic power output from the jet
- $D$  jet diameter

The difference between  $c_j$  and  $c_o$  accounts for the temperature differences between the jet and free space.

The spectra presented here was measured 24" from the jet axis in the plane of the exit nozzle. Fig. 4.14 presents the data for a jet from a tapered orifice. Fig. 4.15 presents the data for a jet from a 60" pipe. The shape of the spectra is the same in both cases. Observe that the level increases monotonically with jet flow speed.

The point is that the qualitative features are not altered by the initial level of turbulence. Air from a tapered orifice is laminar at the exit. The turbulence is caused by the mass entrainment at the jet boundary. The air jet from a long pipe is turbulent at the exit. The level, of course, is altered by mass entrainment at the jet boundaries. The differences at the exit do not alter the character of the emitted acoustic spectra. These observations reinforce those made in the study of turbulent sources in ducts. In the duct, the spectral line shape was similar for both the orifice and pipe jets.

#### 4.3.3 Turbulent Sound Level Increase due to the Obstruction of the Flow by a Flat Plate

The increased broadband noise due to obstructing the flow is demonstrated. First, the sound generated by an air jet from a tapered orifice is measured. Next a flat plate is placed in the air jet and the sound is measured again. Here the distance of the plate from the orifice is great enough, 9 jet diameters, so that screech does not occur.

In Fig. 4.16 the spectral sound intensity for this experiment is given. At the same flow speed, the jet incident on the plate is much louder than the free jet. Actual shifts range from 7 to 12 DB depending on the frequency. The line shape of the spectra is unchanged. This



indicates that the mechanism for sound generation is similar in both the free jet and the obstructed jet.

This is not the case if the plate is within 6 jet diameters of the orifice. In such cases screech occurs at selected flow speeds. The resulting spectra shows intense narrow band peaks at the screech frequencies. These peaks have the same shape as those observed in the high frequency duct spectra (Figs. 3.10, 3.11 and 3.12).

There are, of course, quantitative differences in the generated sound when the flow is obstructed. These differences are of secondary importance in establishing the mechanism for sound generation. One must first separate the linear effects from the feedback effects before addressing the more quantitative aspects of the study. It is with this intent that the arguments concerning spectral line shape are presented. For a more detailed study of the sound generated by air jets on flat plates, we refer the reader to the work of Olsen, Miles and Dorsh.<sup>62</sup>

#### 4.3.4 Impingement Screech from a Tapered Orifice

Here we reproduce impingement screech, observed by Wagner<sup>49</sup> and Neuwerth<sup>50</sup>, using a jet from a tapered orifice impinging on a flat plate. The apparatus is shown in the middle diagram of Fig. 4.13. The pressure drop across the plate was set at a ratio of .60 which gives a

flow speed of Mach .83 (Eq. 4.1). The separation between orifice and plate was altered at constant flow speed.

The orifice is mounted with its flat side toward the compressor. The direction of air flow through the orifice is the same as in the duct experiment. The orifice plate is  $\frac{1}{4}$ " thick, and the hole tapers at  $45^\circ$  to the nominal diameter of  $\frac{1}{2}$ ", such orifices do not screech by themselves. The separation "x" is measured from the inner surface to the obstructing wall.

Screech was observed for separations from  $\frac{1}{16}$ " to  $2\frac{1}{2}$ ", i.e., from .88 to 5 jet diameters. For separations greater than 5 jet diameters no screech is observed. This result agrees with Wagner<sup>49</sup> and Neuwerth's<sup>50</sup> observation that the obstructing plate must be less than 6 diameters from the nozzle.

In Fig. 4.17 the observed screech frequencies are plotted against the inverse of the plate separation. If the screech is associated with an axial acoustic mode parallel to the jet, the frequency should scale as  $\frac{1}{x}$ ; i.e., the data points should lie along straight lines. This happens; however, the screech frequencies are only approximately equal to the cavity frequencies  $\frac{nc}{2x}$ . In fact, two screech modes appear. All other frequencies can be interpreted as harmonics or difference tones based on these two modes, which have been arbitrarily labeled  $F_A$  and  $F_B$ .

Examine the implication of the separation range to interpret the screech observed in ducts. Recall that in the duct experiment the orifice plates were mounted so that the distance between the jet inlet and the opposing wall was  $1\frac{5}{8}$ ". This separation is the sum of the duct height,  $1\frac{1}{2}$ ", and the plate thickness  $\frac{1}{8}$ ". The orifice plates had diameters of  $\frac{1}{4}$ ",  $\frac{1}{2}$ " and 1". All of these screeched. Clearly the  $\frac{1}{2}$ " and 1" orifice are in the separation range established by Wagner<sup>49</sup>. However, the  $\frac{1}{4}$ " orifice is located  $6\frac{1}{2}$  jet diameters from the opposing wall, i.e., just outside the separation limit for screech to occur in free space.

One can account for this if Wagner's<sup>49</sup> explanation of the separation limit is examined. For screech to occur the plate must be inserted in the laminar core of the jet. In free space the core extends from 5 to 6 diameters from the exit. In an enclosed space the core persists for longer distances. Consider the flow field of an ideally expanded jet in free space. At the exit the turbulence is zero and the streamlines parallel over the entire jet diameter, apart from the boundary layer. Downstream the region of no turbulence tapers off to 0 at 5 to 6 jet diameters. As this occurs, the mean diameter of the jet gets larger (Fig. 1.2).

What happens is that the shear layer accelerates the air surrounding the jet. Consequently, instabilities

in the process of mass entrainment have caused the turbulent regime to grow. If the laminar core is to be reduced in this fashion, an unimpeded entrainment air by the shear layer is essential. In a closed space such as a duct the walls impede the flow of mass into the jet. Consequently, the laminar core lasts for larger distances. The screech of the  $\frac{1}{4}$ " orifice occurs at such a large separation from the plate because the length of its laminar core is longer in a duct.

#### 4.3.5 Coupling of Impingement Screech to Cavity Mode

Neuwerth<sup>50</sup> and Wagner<sup>49</sup> show that screech occurs without any influence from adjacent acoustic cavities. It was shown earlier that the orifice screech instability can be altered by the influence of an adjacent acoustic resonator. Herein such coupling is demonstrated for impingement screech.

Screech was observed, in one instance, when air entered the rectangular duct from a 60" pipe. This occurred at a duct to atmospheric pressure ratio of .45 with a screech frequency equal to 9.1 kHz.

An attempt to reproduce this result was made using the apparatus diagramed at the bottom of fig. 4.13. Here the jet exits from the pipe onto the flat plate; no other reflecting surfaces are nearby, hence

there are no adjacent acoustic resonators. Screech was observed at

$\frac{P_{\text{atmospheric}}}{P_{\text{plenum}}}$	Frequency kHz
.44	11.0
.45	11.0
.47	12.2
.48	12.3

The pressure drop is about the same as that in the duct, but the frequency is off by at least 2 kHz.

To remedy the frequency disparity, a second plate was fit snugly over the end of the pipe. In this manner an acoustic resonator is formed between the nozzle and impingement plate. The distance between plates is  $1\frac{1}{2}$ ", hence the cavity modes are at 4.46, 8.92, 13.39 and 17.85 kilocycles. The observed screech frequencies occurred at

$\frac{P_{\text{atmosphere}}}{P_{\text{plenum}}}$	Frequency kHz
.44	9.00 18.00
.45	9.00 18.00
.48	8.85 17.65
.50	8.70 ---

That is, the screech was shifted to a frequency coincident with the second and fourth cavity modes. These correspond to a standing pressure wave whose wavelength is equal to, and one half, the separation between plates. In addition, one finds that the observed screech frequencies are coincident with that frequency observed in the duct.

#### 4.3.6 Direct Comparison of Impingement Screech to Screech in Ducts

Herein a direct comparison of impingement screech is made to screech seen in the duct experiments. In the duct, the separation between the inlet and the opposite wall was  $1 \frac{5}{8}$ ". The same separation between the exit and impingement plate was set in a test using the apparatus diagramed in the middle of Fig. 4.13. The flow speed was varied and the resulting screech frequencies were measured. As in the duct, the screech only occurred for flow speeds greater than Mach .5.

In Fig. 4.18 the screech frequency is plotted as a function of flow speed. Data from both the duct and compressor test is presented. From the figure it is evident that the data in one experiment compliments that in the other. That is, the screech occurs at approximately the same flow speeds and frequencies.

The solid lines represent the first four acoustic modes for two plates separated by  $1 \frac{1}{2}$ ". The

observed screech frequencies are clustered about these lines. Such a comparison is only approximate, as the data of the previous section has shown that the frequency still depends somewhat on the flow speed.

## 5. CONCLUSIONS AND RECOMMENDATIONS

Herein the generation of sound by turbulent flow in cavities is examined. Two types of cavities are considered: the axial modes of a pipe open at both ends, and the transverse modes of a rectangular duct. Experiments are performed to measure the acoustic spectra of the flow-generated noise. A linear theoretical analysis, based on an isotropic model of the turbulent fluctuations, is developed to predict this spectra. Certain nonlinear phenomena, due to the alteration of the source flow by the emitted sound, are identified. The conditions necessary for such instabilities are examined.

To introduce the linear procedure, calculations are carried out for a turbulent source in free space. Here some of the limitations of the model are discussed. One assumes a finite volume of turbulent fluid. An isotropic pattern of noise sources is created continuously at one face of the volume and is convected at a finite velocity to the downstream face where it disappears. Implicit in this description is a neglect of turbulent shear and refraction effects.

To make the comparison between alternate procedures explicit, detailed calculations were carried out. The results derived from Lighthill's<sup>1,2</sup> quadrupole model using time domain techniques are given in Eqs. 1.51 and



1.52. Similar results are derived from Ribner's equivalent distribution of monopoles, again using time domain analysis (Eqs. 1.43 and 1.44). Ribner's model is used again, this time using frequency domain analysis to derive the spectra of the radiated pressure (Eqs. 1.30 and 1.31). Frequency and time domain techniques give precisely the same answer for Ribner's source model. Aside from the turbulent shear interaction, these are the same results as one gets from Lighthill's model. This is providing Ribner's turbulent pressure sources  $q$  are assumed identical to the local turbulent kinetic energy fluctuations  $\rho_0 v^2$ .

An interesting extension of this analogy would be to assume a second distribution of monopoles whose strength is proportional to  $\rho_0 Vv$ , where  $V$  is the mean flow speed and  $v$  the fluctuating velocity. This would, in some fashion, account for the turbulent shear effects. However, care must be taken to introduce the angular dependence  $2(\cos^4 \theta + \cos^2 \theta)$ , where  $\theta$  is the angle between the observer and the direction of flow. It is recommended that theoretical studies be continued to establish this analogy.

Another problem that needs further work is the inhomogeneities in the turbulent field. Ribner<sup>63</sup> has already used the variation in characteristic scales of the turbulence to collate data on the free space spectra.

He observes that a single correlation function cannot account for the entire spectra. Nonetheless, limited portions of the spectra can be described assuming a single correlation function. Here attention is placed on the mid and high frequencies. It is recommended that the minimum number of separate correlation functions needed to account for the observed spectra be established.

In the second chapter an experimental study of the turbulent excitation of axial pipe modes is given. Such effects have been reported before<sup>30,56</sup>, but were not conclusively identified. Identification is accomplished by showing that the interval between modes depends on flow speed and length precisely as an axial mode (Figs. 2.3 and 2.4). Previous observations concerning diminished mode excitation at high flow speeds are confirmed here.

To account for these observations in detail, a frequency domain analysis of sound generation by isotropic turbulence in pipes is developed. To carry the analysis to a point where only a statistical description of the turbulence is required, it proves necessary to introduce a random phase assumption. It is demonstrated that the influence of the Fourier phase coefficient is identical to localization of the source (Eqs. 2.48 and 2.52). Thus, neglecting phase terms is equivalent to averaging over all possible source positions. Sound generation from the ends

of the pipe can then be predicted from a statistical description of the source field (Eq. 2.54). Direct comparison to the experimental results (Figs. 2.8, 2.9 and 2.10) demonstrates that radiative damping accounts for the diminished excitation at high flow speeds.

It was assumed that the losses at the ends are purely radiative. From this assumption the transmission coefficients out the pipe ends can be derived from the measured pressure reflection coefficients. It may be that some other loss mechanism acts at the ends. This will alter the transmission coefficient. It is recommended that an experimental study of the transmission coefficient be performed. It is further recommended that the behavior of the exit pressure reflection coefficient be examined in greater detail to account for some small discrepancies.

In the third chapter an experimental study of the turbulent excitation of the transverse modes in ducts is presented. Two effects are established. The first is that the level of radiated sound increases in discrete jumps at the first few cutoff frequencies. For frequencies slightly greater than the nearby cutoff, the level decreases smoothly. The asymmetric shape of these curves is predicted using frequency domain techniques (Eq. 3.38). Again it proved necessary to introduce a random phase assumption to carry the calculations to completion.

In the ideal case the level jumps should be infinite at the cutoff frequencies. Damping requires that these jumps be finite as is indicated in Eq. 3.45. However, visco-thermal damping alone cannot predict the magnitude of the observed jumps. It is recommended that the mechanism that limits these level shifts be established. In particular, the approximation that the acoustic contribution to the Reynolds stress is negligible is not valid when the predicted acoustic velocities are infinite.

The second effect established by these experiments is that the spectra smooths out at frequencies where a large number of modes can propagate. In fact, the spectra strongly resembles the spectra of sound generated by turbulence in free space. To understand the smoothing, recall that damping effects make the peak height finite. At frequencies of large modal density a new mode cuts on before the sound level has diminished from the level jump at the previous cutoff frequency. This overlap of peaks causes the curve to smooth out. A quantitative analysis based on this idea is given in Eq. 3.46.

The problem can also be approached by calculating the average radiative resistance of the duct. In the high frequency limit the radiative resistance

approaches that in free space. Herein, this concept is applied to the interpretation of acoustic spectra in rectangular ducts. An extension of the limit to ducts of arbitrary shape is given in Eq. 3.55. In short, the duct spectra is similar to the free space spectra since the duct and free space response are approximately the same in this limit.

In the experimental phase two anomalies occurred that are identified as nonlinear effects. Orifice screech occurred in pipes having small length-to-diameter ratios. Impingement screech occurred in ducts when the air jet impinged on a nearby wall. Further experiments were performed to establish the conditions necessary for such instabilities. It is shown that the emitted acoustic field reacts back on the jet so as to alter the primary flow field. A kinematic analysis of orifice screech proved adequate to predict the frequency dependence on length and flow speed (Eq. 4.4). Further it was demonstrated experimentally that the feedback cycle is unstable only if the feedback frequency is approximately that of an adjacent axial acoustic mode. From this observation one can predict the velocities and frequencies at which the feedback cycle is most likely to be unstable and thereby produce "screech" (Eq. 4.7).

It is further observed that variations in geometry that produce additional acoustic modes can markedly alter the screech frequencies. In the appendix the shear layer instability of a circular jet subject to an acoustic perturbation in the presence of boundaries is derived. The dispersion relation for such a disturbance is deduced (Eq. A28), and its limiting forms are presented (Eqs. A35, A39, A42 and A43). Phase speed calculations of the shear layer instability indicate that the coupling of feedback to the resonator may be through the spatial gradients. That is to say, if a resonator is present, all spatial variations are dominated by the characteristic wavenumber of the resonator. The influence of such coupling is to alter the phase speed of the shear disturbance (Eqs. A48 and A49). Preliminary experimental observations are in qualitative agreement with this result. It is recommended that a quantitative experimental study be initiated to see how the phase speed is changed when a resonator is present. It is further recommended that one establish whether or not the phase speed is adequately described by linear analysis.

In summary, a study of flow-generated sound in cavities has been performed. For linear effects, a detailed prediction of spectral line shape of the radiated sound is possible. For nonlinear effects, some important

aspects of how sound couples to the flow that generates  
it are established.

APPENDIX: STABILITY ANALYSIS OF THE PERTURBED JET IN THE PRESENCE OF BOUNDARIES

A.1 Introduction

The collective oscillations of the jet play an essential role in screech instabilities. It is therefore useful to calculate the motion of the jet subject to an acoustic perturbation. Herein the linear analysis of a forced jet surrounded by a quiescent annular region bound, in turn, by a hard-walled duct is presented. The theory is developed to the point where a rather complex dispersion relation must be solved. Rather than solve the equation numerically, several limiting cases are presented. These correspond to a free circular jet, a two-dimensional shear layer in the vicinity of a hard wall, and a free two-dimensional shear layer. The solutions of the linear equations in these limits have been given by Tam<sup>57</sup>, Sedel'nikov<sup>58</sup>, Handa<sup>54</sup>, Covert and Bilanin<sup>52</sup>, and Miles<sup>59</sup>.

One should first establish what portion of the acoustic pulse couples to the shear layer. Three possibilities exist, the particle displacement, the particle velocity, and the pressure perturbation. Chanaund and Powell<sup>43</sup> demonstrate that the pressure perturbation forces the shear layer. They force a circular jet from an orifice with an acoustic wave from a loudspeaker. This was



done in the study of the hole tone, where a second orifice plate is mounted downstream. They find:

With the sound from the speaker (located on the jet axis) disturbing the jet, the flow pattern was observed to be symmetric and similar to that found with the plate and no speaker. The speaker was then moved to a position perpendicular to the jet axis, and again a symmetric pattern resulted! Since the acoustic wavelength was much greater than the nozzle diameter, the particle motion lateral to the jet must have been in phase across the jet diameter and so, if the jet were appreciably sensitive to the motion, some asymmetry of the disturbances, at least, should have occurred. Since they did not, it appears that the axisymmetric jet is predominantly pressure sensitive.

In an acoustic wave the particle velocity and displacement are parallel to the direction of propagation. The acoustic pressure, being a scalar field, has no such directionality. With the loudspeaker downstream, the propagation direction is parallel to the jet. With the loudspeaker perpendicular to the axis, the propagation direction is perpendicular to the jet. If the jet were sensitive to either the acoustic displacement or velocity, some changes should have occurred by changing the direction of the incident acoustic wave. Since no changes were observed, one concludes that the acoustic pressure forces the jet.

#### A.2 Problem Statement

Consider the perturbation of a compressible, inviscid, cylindrical jet in the vicinity of a rigid

boundary. Let the jet and the boundary be coaxially symmetric and have radii  $R_j$  and  $R_o$ . Assume the mean velocity  $\tilde{V} = V \hat{z}$  is uniform for all  $r < R_j$  and zero for all  $r > R_j$ . Here the jet axis lies along the  $z$  axis, and  $r$  is the radial distance from this axis. Let the shear layer at  $R_j$  be driven by a localized pressure disturbance at  $z = 0$ . Assuming isentropic conditions gives

$$\nabla^2 p_- = \frac{1}{c_-^2} \frac{D^2}{Dt^2} p_- \quad r < R_j \quad A1$$

$$\nabla^2 p_+ = \frac{1}{c_+^2} \frac{\partial^2}{\partial t^2} p_+ \quad r > R_j \quad A2$$

where the "-" subscript refers to points in the jet and the "+" to points outside the jet. Here

$$\frac{D}{Dt} = \frac{\partial}{\partial t} + V \frac{\partial}{\partial z}$$

Let the shear layer displacement from the equilibrium position  $R_j$  be labelled  $\eta(R_j, t)$ . Momentum conservation requires that the radial particle acceleration be equal to the radial pressure gradient at the shear layer. Thus

$$\rho_- \frac{D^2}{Dt^2} \eta = -\frac{\partial p}{\partial r} \quad r = R_j \quad A3$$

$$\rho_+ \frac{\partial^2 \eta}{\partial t^2} = - \frac{\partial p_+}{\partial r} \quad r = R_j \quad \text{A4}$$

On the jet axis the pressure must be finite,  
hence

$$\rho_- < \infty \quad r = 0 \quad \text{A5}$$

The hard wall demands that the radial particle velocity be zero at  $r = R_0$ . Equivalently

$$\frac{\partial p_+}{\partial r} = 0 \quad r = R_0 \quad \text{A6}$$

Continuity of pressure at the shear interface requires

$$p_+ = p_- + A \delta(z) e^{i(n\varphi - \omega t)} \quad r = R_j \quad \text{A7}$$

where  $A \delta(z) e^{i(n\varphi - \omega t)}$  is the acoustic forcing term at the inlet.

### A.3 Integral Solution

To solve Eqs. A1 to A7, introduce the Fourier Laplace transform. This procedure is identical to Tam's analysis of the free jet. Thus

$$P_{\pm}' = \int_0^{\infty} dz \int_{-\infty}^{\infty} dt \quad p_{\pm} e^{-i(Kz - \Omega t)} \quad \text{A8}$$

$$\eta' = \int_0^{\infty} dz \int_{-\infty}^{\infty} dt \eta e^{-i(\kappa z - \Omega t)} \quad \text{A9}$$

whose inverse transforms are

$$\rho_{\pm} = \frac{1}{4\pi^2} \int_{-\infty+i\epsilon}^{\infty+i\epsilon} d\kappa \int_{-\infty}^{\infty} d\Omega \rho'_{\pm} e^{i(\kappa z - \Omega t)} \quad \text{A10}$$

$$\eta = \frac{1}{4\pi^2} \int_{-\infty+i\epsilon}^{\infty+i\epsilon} d\kappa \int_{-\infty}^{\infty} d\Omega \eta' e^{i(\kappa z - \Omega t)} \quad \text{A11}$$

Transforming Eqs. A1 and A2, assuming initial conditions are zero, gives

$$\nabla_t^2 \rho'_- = \left\{ -\left[ \frac{\Omega - \kappa V}{C_-} \right]^2 + \kappa^2 \right\} \rho'_- = \mu_-^2 \rho'_- \quad \text{A12}$$

$$\nabla_t^2 \rho'_+ = \left\{ -\left[ \frac{\Omega}{C_+} \right]^2 + \kappa^2 \right\} \rho'_+ = \mu_+^2 \rho'_+ \quad \text{A13}$$

where  $\mu_-^2$  and  $\mu_+^2$  are the quantities in curly brackets, { }, in A12 and A13 and

$$\nabla_t^2 = \frac{\partial^2}{\partial r^2} + \frac{1}{r} \frac{\partial}{\partial r} + \frac{1}{r^2} \frac{\partial^2}{\partial \phi^2}$$

Continuing the transforms of Eqs. A3 to A7 gives

$$\frac{1}{\xi_-} \frac{\partial}{\partial r} p_-' = (\Omega - \kappa V)^2 \eta' \quad r = R_j \quad \text{A14}$$

$$\frac{1}{\xi_+} \frac{\partial}{\partial r} p_+' = \Omega^2 \eta' \quad r = R_j \quad \text{A15}$$

$$p_-' < \infty \quad r = 0 \quad \text{A16}$$

$$\frac{\partial p_+'}{\partial r} = 0 \quad r = R_0 \quad \text{A17}$$

$$p_+' = p_-' + \frac{i A e^{i n \phi}}{\Omega - \omega} \quad r = R_j \quad \text{A18}$$

To solve A12 and A13, assume  $p_{\pm}' = p_{\pm}'(r) e^{i n \phi}$  which gives

$$\frac{1}{r} \frac{\partial}{\partial r} r \frac{\partial}{\partial r} p_{\pm}'(r) - \frac{n^2}{r^2} p_{\pm}'(r) = \mu_{\pm}^2 p_{\pm}'(r)$$

or

$$r \frac{\partial}{\partial r} r \frac{\partial}{\partial r} p_{\pm}'(r) - \left\{ (\mu_{\pm} r)^2 + n^2 \right\} p_{\pm}'(r) = 0 \quad \text{A19}$$

The solution to A19 is the  $n^{\text{th}}$  modified Bessel functions of the argument  $x = r \mu_{\pm}$ , where the + or - holds for  $r > R_j$  or  $r < R_j$ . Eqs. A14 through A19 are the boundary conditions the solution must satisfy. Explicitly one has

$$p_{-n}'(r) = A \left| I_n(\mu_- r) + \alpha \frac{K_n(\mu_- r)}{\pi} \right| \quad r < R_j \quad \text{A20}$$

$$p_{+n}'(r) = B \left| \beta I_n(\mu_+ r) + \frac{K_n(\mu_+ r)}{\pi} \right| \quad r > R_j \quad \text{A21}$$

where A, B,  $\alpha$  and  $\beta$  are numerical constants to be determined by the boundary conditions. The factor  $\frac{1}{\pi}$  has been used to facilitate the expansions in the limiting cases. The notation of Abramowitz and Stegun<sup>36</sup> is used for the Bessel functions.

That the pressure be finite at the origin (Eq. A16) requires  $\alpha = 0$ . The hard wall (Eq. A16) requires

$$\beta = - \frac{1}{\pi} \left. \frac{K_n'(x)}{I_n'(x)} \right|_{x = \mu_+ R_0} \quad \text{A22}$$

where the prime signifies differentiation with respect to the argument  $x$ . Substituting A20 and A21 into A14 and A15 gives

$$\left\{ \frac{\mu_-}{\beta_- (\Omega - \kappa V)^2} \frac{I_n'(x)}{I_n(x)} \right\}_{x = \mu_- R_j} p_{-n}'(R_j) e^{\ln \phi} = \eta' \quad \text{A23}$$

$$\left\{ \frac{\mu_+}{\beta_+ \Omega^2} \frac{\beta I_n'(x) + \frac{1}{\pi} K_n'(x)}{\beta I_n(x) + \frac{1}{\pi} K_n(x)} \right\}_{x = \mu_+ R_j} p_{+n}'(R_j) e^{\ln \phi} = \eta' \quad \text{A24}$$

Eliminating the pressure by Eq. A18 from A23 and A24

gives

$$\eta' = \frac{-i A e^{i n \varphi}}{(\Omega - \omega) \Delta(\kappa, \Omega)} \quad \text{A25}$$

where

$$\Delta(\kappa, \Omega) = \frac{\rho_+ \Omega^2}{\mu_+} \frac{\beta I_n(x) + \frac{1}{\pi} K_n(x)}{\beta I_n'(x) + \frac{1}{\pi} K_n'(x)} \Big|_{x=\mu_+ R_j} - \frac{\rho_- (\Omega - \kappa V)^2}{\mu_-} \frac{I_n(x)}{I_n'(x)} \Big|_{x=\mu_- R_j} \quad \text{A26}$$

Assume that both the jet and annulus have equal specific heat ratios and that unperturbed static pressures in the jet and annulus are equal. From the identity  $c = \sqrt{\frac{\gamma P}{\rho}}$  it follows

$$\rho_+ c_+^2 = \rho_- c_-^2 \quad \text{A27}$$

which implies

$$\Delta(\kappa, \Omega) = \rho_+ c_+^2 \left\{ - \frac{\mu_+^2 - \kappa^2}{\mu_+} \frac{\beta I_n(x) + \frac{1}{\pi} K_n(x)}{\beta I_n'(x) + \frac{1}{\pi} K_n'(x)} \Big|_{x=\mu_+ R_j} + \frac{\mu_-^2 - \kappa^2}{\mu_-} \frac{I_n(x)}{I_n'(x)} \Big|_{x=\mu_- R_j} \right\} \quad \text{A28}$$

The solution for the shear layer displacement

is

$$\eta = \frac{-i A C e^{i n \varphi}}{4 \pi^2} \int_{-\infty}^{\infty} d\Omega \int_{-\infty + i\epsilon}^{\infty + i\epsilon} d\kappa \frac{e^{i(\kappa Z - \Omega t)}}{(\Omega - \omega) \Delta(\kappa, \Omega)} \quad \text{A29}$$

The general form of the amplifying solution is

$$\eta \propto e^{i(kz - \omega t)}$$

where  $\omega$  is the frequency of the acoustic perturbation, and  $k$  is the solution to the dispersion relation  $\Delta(k, \omega) = 0$ .

#### A.4 Comments on the Evaluation of the Integral

The integral given in A29 is, in general, quite difficult to solve. The customary approach is via the theorem of residues. It is essential, therefore, to locate the roots of the dispersion relation  $\Delta(k, \omega) = 0$ . A detailed analysis of the evaluation in the limit of a two-dimensional free shear layer is provided by Miles.<sup>59</sup> Bilanin and Covert<sup>52</sup> have solved the dispersion relation numerically for a two-dimensional shear layer located near a hard wall. Similar numerical solutions for the free vibrations of a supersonic cylindrical jet given by Sedel'nikov<sup>58</sup> and Handa<sup>54</sup>. Tam<sup>57</sup> has demonstrated that so long as the radius of such a jet is large compared to the wavelength of the disturbance, Miles<sup>59</sup> solution can be used. Handa provides a detailed analysis of the integration procedure once the dispersion relation is solved.

Such detail in carrying out the integrations is not warranted in this analysis. Experiments by Wagner<sup>49</sup> and Anderson<sup>51</sup> demonstrate that the perturbations



of subsonic jets "roll up" to form ring vortices that propagate down the jet column. It is these vortices that are essential to screech. The process of formation of these vortices is not contained in linear analyses such as this one.

The argument is that such vortices can form only if there is an amplifying disturbance of the shear layer. The hydrodynamic analogue is the formation of droplets by the amplifying oscillations of a water jet, first described by Rayleigh<sup>61</sup>. The key is to identify the amplifying roots of the dispersion relation. This is done analytically by the asymptotic procedure used by Tam<sup>57</sup>.

#### A.5 Removing the Duct Wall

Handa<sup>54</sup> and Sedel'nikov<sup>58</sup> have analyzed the free oscillations of a circular jet. Their analysis can be recovered if one assumes the wall is infinitely far from the jet. To evaluate this limit, the following expansions are used

$$\lim_{x \rightarrow \infty} I_n(x) = \frac{e^x}{\sqrt{2\pi x}} \quad |\arg(x)| < \frac{\pi}{2}$$

$$\lim_{x \rightarrow \infty} \frac{K_n(x)}{\pi} = \frac{e^{-x}}{\sqrt{2\pi x}} \quad |\arg(x)| < \frac{3\pi}{2}$$

$$\lim_{x \rightarrow \infty} I_n'(x) = \frac{e^x}{\sqrt{2\pi x}} \quad |\arg(x)| < \frac{\pi}{2}$$

$$\lim_{x \rightarrow \infty} \frac{K_n'(x)}{\pi} = \frac{-e^{-x}}{\sqrt{2\pi x}} \quad |\arg(x)| < \frac{3\pi}{2}$$

A30

These limits are used with  $x = \mu_+ R_0$ . By definition,  $R_0$  is a real number. This implies that the restriction on the argument  $x$  becomes a restriction on  $\mu_+$ . The restriction is then  $|\arg \mu_+| < \frac{\pi}{2}$  or  $\text{Re}(\mu_+) \geq 0$ . The only place that the wall diameter enters into the dispersion relation A29 is in the parameter  $\beta$  defined in Eq. A22. Thus

$$\begin{aligned} \lim_{R_0 \rightarrow \infty} \beta &= \lim_{x \rightarrow \infty} -\frac{1}{\pi} \frac{K_n'(x)}{I_n'(x)} \\ &= \lim_{x \rightarrow \infty} e^{-2x} \\ &= 0 \end{aligned}$$

A31

To make this notation coincide with Handa's, introduce his parameters

$$k_0 = \sqrt{\left(\frac{\Omega}{C_+}\right)^2 - k^2} = i\mu_+ \quad \text{A32}$$

$$k_1 = \sqrt{\left(\frac{\Omega - kV}{C_-}\right)^2 - k^2} = i\mu_-$$

and note

$$I_n(x) = e^{-\frac{i n \pi}{2}} J_n(ix) \quad -\pi < \arg(x) < \frac{\pi}{2}$$

A33

$$K_n(x) = \frac{i\pi}{2} e^{\frac{i n \pi}{2}} H_n'(ix) \quad -\pi < \arg(x) < \frac{\pi}{2}$$

Hence

$$I_n(\mu_- R_j) = I_n\left(\frac{k_1 R_j}{i}\right) = e^{-\frac{i n \pi}{2}} J_n(k_1 R_j)$$

A34

$$K_n(\mu_+ R_j) = K_n\left(\frac{k_0 R_j}{i}\right) = \frac{i\pi}{2} e^{\frac{i n \pi}{2}} H_n'(k_0 R_j)$$

Substituting Eqs. A31, A32 and A34 into Eq. A26 and setting  $\Delta(k, \omega) = 0$  gives

$$\frac{k_0 H_n'(k_0 R_j)}{\rho_+ \omega^2 H_n'(k_0 R_j)} = \frac{k_1 J_n'(k_1 R_j)}{\rho_- (\omega - kV)^2 J_n'(k_1 R_j)} \quad \text{A35}$$

which is identical to Handa's<sup>54</sup> Eq. 4.39, page 84, and Sedel'nikov's<sup>58</sup>, Eq. 6, page 73.

#### A.6 Simplification to Two Dimensions

The two-dimensional dispersion relation for a shear layer near a wall can also be recovered. This was first solved by Bilanin and Covert<sup>52</sup> and applied to the study of screech from air flow past rectangular cutouts. To do the expansions properly, one must specify the duct radius  $R_0 = R_j + D$ , where  $D$  is the distance between the jet and the wall. This distance is kept finite while  $R_j$  tends toward infinity. The expansions needed are

$$\lim_{R_j \rightarrow \infty} \beta = e^{-2\mu_+(R_j + D)} \quad \text{A36}$$

$$\begin{aligned} \lim_{R_j \rightarrow \infty} \frac{\beta I_n(x) + \frac{1}{\pi} K_n(x)}{\beta I_n'(x) + \frac{1}{\pi} K_n'(x)} \Big|_{x=\mu_+ R_j} &= \\ &= \lim_{R_j \rightarrow \infty} \frac{\beta e^{\mu_+ R_j} + e^{-\mu_+ R_j}}{\beta e^{\mu_+ R_j} - e^{-\mu_+ R_j}} \quad \text{A37} \\ &= -\coth(\mu_+ D) \end{aligned}$$

$$\lim_{R_j \rightarrow \infty} \frac{I_\eta(x)}{I_\eta'(x)} \Big|_{x=\mu_- R_j} = 1 \quad \text{A38}$$

Substituting Eqs. A36, A37 and A38 into Eq. A28 gives

$$\lim_{R_j \rightarrow \infty} \Delta(k, \Omega) = \rho_+ C_+^2 \left[ \frac{\mu_+^2 - k^2}{\mu_+} \coth(\mu_+ D) + \frac{\mu_-^2 - k^2}{\mu_-} \right] \quad \text{A39}$$

which is identical to Bilanin's<sup>55</sup> Eq. 3.30, page 23, and Bilanin and Covert's<sup>52</sup> Eq. 16, page 349. Note, however, that subscripts + and - are opposite those used here.

This stems from the difference in subscript used to define which region is moving.

To get Miles<sup>59</sup> dispersion relation for the free oscillations of a two-dimensional shear layer, let the distance D tend towards infinity. In this limit

$$\lim_{\substack{R_j \rightarrow \infty \\ D \rightarrow \infty}} \Delta(k, \Omega) = \rho_+ C_+^2 \left[ \frac{\mu_+^2 - k^2}{\mu_+} + \frac{\mu_-^2 - k^2}{\mu_-} \right] \quad \text{A40}$$

To recover Miles' solution exactly, introduce the transform

$$\beta_+ = \frac{i\mu_+}{k} = \sqrt{\left(\frac{-\Omega}{kC_+}\right)^2 - 1} = \sqrt{\bar{C}^2 - 1}$$

$$\beta_- = \frac{i\mu_-}{k} = \sqrt{\left(\frac{\Omega}{kC_-}\right)^2 - 1} = \sqrt{\left(\frac{C_+}{C_-}\right)^2 (\bar{C} - M)^2 - 1}$$

where  $\bar{c} = \frac{\Omega}{Kc_+}$  is the phase speed normalized to the speed of sound in the quiescent media. Thus

$$\lim_{\substack{R_j \rightarrow \infty \\ D \rightarrow \infty}} \Delta(k, \Omega) = \frac{-iK (\beta_+ + \beta_-) (\beta_+ \beta_- + 1)}{\beta_+ \beta_-} \quad \text{A42}$$

which is equal to  $\frac{-iK}{\beta_+ \beta_-}$  times Miles'<sup>59</sup> Eq. 5.3a, page 545.

The mathematical theory of vortex sheet instability was rigorously solved by Miles. In his analysis, he rejects spurious roots found by previous authors. Hence most modern authors use his paper as a reference for exact analysis of the shear layer instability. The zeros of Eq. A42 have been extensively studied by Miles, who concludes that: a) the vortex sheet is unstable if  $V < (c_+^{2/3} + c_-^{2/3})^{3/2}$ , b) the function  $\beta_+ + \beta_-$  has no complex zeros and hence does not give rise to unstable poles, c) in the unstable case the zeros of the function  $(\beta_+ (\bar{c}) \beta_- (\bar{c}) + 1)$  are the two complex conjugate roots of  $(\beta_+^2 \beta_-^2 - 1)$ .

For subsonic velocities one can approximate  $c_+ \approx c_-$ . In this limit

$$\Delta(k, \omega) = 0$$

gives

$$(\beta_+ \beta_- + 1) = 0$$

$$[\bar{c}^2 - 1]^{1/2} [(\bar{c} - M)^2 - 1]^{1/2} + 1 = 0 \quad \text{A43}$$

Take advantage of the symmetry, and let  $\bar{x} = \bar{c} - \frac{M}{2}$  and  $\bar{y} = \frac{M}{2}$ . Substituting into Eq. A43 gives

$$[(\bar{x} + \bar{y})^2 - 1][(\bar{x} - \bar{y})^2 - 1] = 1$$

which is quadratic in the quantity  $\bar{x}^2$ . Thus

$$\bar{x}^2 = \bar{y}^2 + 1 \pm \sqrt{4\bar{y}^2 + 1}$$

Substituting for  $\bar{x}$  and  $\bar{y}$  gives

$$\frac{\omega}{kc_+} = \bar{c} = \left\{ \begin{array}{l} \frac{M}{2} + \sqrt{\sqrt{1+M^2} - \left(1 + \frac{M^2}{4}\right)} \\ \frac{M}{2} - \sqrt{\sqrt{1+M^2} - \left(1 + \frac{M^2}{4}\right)} \\ \frac{M}{2} + \sqrt{\sqrt{1+M^2} + \left(1 + \frac{M^2}{4}\right)} \\ \frac{M}{2} - \sqrt{\sqrt{1+M^2} + \left(1 + \frac{M^2}{4}\right)} \end{array} \right.$$

A44

which is the solution of the dispersion relation Eq. A28 in the limit  $\lambda \ll R_j$ ,  $\lambda \ll R_o$ , and  $c_+ \approx c_-$ , where  $\lambda$  is the wavelength of the disturbance. Some comment can be made on the approximation  $c_+ \approx c_-$ , where  $c_-$  is the speed of sound in the jet. Assume the jet accelerates isentropically through an orifice. Then the speed of sound in the jet is<sup>61</sup>

$$c_-^2 = c_+^2 - \frac{1}{2} (\gamma - 1) V^2$$

A45

when the orifice is choked  $c_-$  is minimum and equal to  $.913 c_+$ , where  $c_+$  is the sound speed in the surrounding air (see Landau<sup>61</sup> Eq. 80.18). Thus the approximation is good for subsonic flow.

The dispersion relation yields complex roots for all Mach numbers less than  $\sqrt{8} \approx 2.83$ . The imaginary part of  $c$  is maximum at  $M = \sqrt{3} \approx 1.73$  and has a numerical value of  $.5$ . The imaginary portion increases monotonically from zero to the maximum as the flow speed increases from Mach 0 to Mach 1.73, then it decreases monotonically to zero as the flow speed increases to Mach 2.83.

#### A.7 Comments on the Application of the Theory to Screech

The most important point of the analysis is that the shear layer is unstable at subsonic speeds. Some ambiguity is inherent in further interpretation. This is because only the ratio of  $\omega$  to  $k$  is specified in Eq. A44 and not the absolute values. To interpret the relation, consider the limiting cases of  $\omega$  real and then  $k$  real. Recall that the shear displacement  $\eta$  is given by



$$\eta \propto e^{i(kz - \omega t)}$$

For  $\omega$  real one has

$$\eta \propto e^{i(k_r z - \omega t)} e^{-k_i z}$$

A46

For  $k$  real one has

$$\eta \propto e^{i(kz - \omega t)} e^{+\omega_i t}$$

A47

Specify that the acoustic pressure perturbation is harmonic in time at frequency  $\omega$ , where  $\omega$  is a real number. From Eq. A46 it is clear that the wave grows spatially in the downstream direction. This interpretation is used by Tam in his study of supersonic jets.

Given  $\omega$ , it follows that

$$k_r = \frac{\omega}{c_+} \operatorname{Re} \left\{ \frac{1}{\bar{c}} \right\} = \frac{\omega}{c_+} \frac{\frac{M}{2}}{\sqrt{1+M^2} - 1}$$

$$k_i = \frac{\omega}{c_+} \operatorname{Im} \left\{ \frac{1}{\bar{c}} \right\} = -\frac{\omega}{c_+} \frac{\sqrt{\sqrt{1+M^2} - \left(1 + \frac{M^2}{4}\right)}}{\sqrt{1+M^2} - 1}$$

$$V_{\text{phase}} = \left| \frac{\omega}{k_r} \right| = c_+ \frac{\sqrt{1+M^2} - 1}{\frac{M}{2}} \underset{M \rightarrow 0}{=} V \quad \text{A48}$$

where the second root of Eq. A44 was chosen so that  $k_i < 0$ , and the wave amplifies downstream.

Assume, on the other hand, that the acoustic perturbation grows in time, at a rate to be determined. Let the spatial perturbations be dominated by the spatial variation of the adjacent acoustic resonator. For an orifice one would require the wave number  $k$  to be real and equal to that of the axial acoustic mode. Given  $k$ , it follows that

$$\omega_r = k c_+ \operatorname{Re}|\bar{c}| = k c_+ \frac{M}{2}$$

$$\omega_i = k c_+ \operatorname{Im}|\bar{c}| = k c_+ \sqrt{\sqrt{1+M^2} - \left(1 + \frac{M^2}{4}\right)}$$

$$V_{\text{phase}} = \frac{\omega_r}{k} = \frac{c_+ M}{2} = \frac{V}{2}$$

A49

where the first root of Eq. A44 was chosen so that  $\omega_i > 0$  and the wave grows in time.

Concentrate on the phase speeds for each limit. If the forcing acoustic perturbation does not grow in time, the phase speed of the shear layer disturbances is approximately  $V$ . If, however, the coupling is through the spatial gradients, the phase speed of the shear layer disturbances is  $\frac{V}{2}$ . Recall that the orifice data was fit with a phase speed equal to  $.6 V$ . This suggests coupling through the wave number

Also recall the experiment on the coupling of impingement screech to the axial acoustic modes (section 4.3.5). There the screech frequency shifted down by about 2 kHz when the plate forming the acoustic cavity was fitted to the end of the pipe. One interpretation of this shift is that the phase speed of the disturbances on the jet was lowered.

These observations suggest that the influence of an acoustic resonator on shear layer instabilities is to determine the spatial gradients and thereby alter the phase speed of such instabilities. Before proceeding with such studies, the theoretical phase speed must be derived in greater detail. For orifice screech the acoustic wavelength is approximately the same length as the jet diameter and the two-dimensional approximation  $\lambda \ll R_j$  is no longer valid. It is therefore necessary to solve Eq. A28 numerically.

The interpretation is only preliminary. Physically, it is clear that the formation of ring vortices play an essential role in screech. If these are formed close to the inlet, the time of transit down the jet is determined by the propagation speed of such vortices. This speed may or may not be close to that given in Eqs. A48 and A49. One cannot reach a conclusion based on the linear analysis. If the vortex speed is independent of

the initial perturbation that forms such vortices, then the only important point is that the shear layer is unstable at low flow speeds.

## REFERENCES

1. Lighthill, M. J.: "On Sound Generated Aerodynamically: I. General Theory", Proc. Roy. Soc. (London) Ser. A, Vol. 211, No. 1107 (March, 1952) pp. 564-587.
2. Lighthill, M. J.: "On Sound Generated Aerodynamically: II. Turbulence as a Source of Sound", Proc. Roy. Soc. (London) Ser. A, Vol. 222, No. 1148 (February, 1954) pp. 1-32.
3. Ribner, H. S.: "New Theory of Jet-Noise Generation, Directionality and Spectra", J. Acoust. Soc. Amer., Vol. 31, No. 2 (February, 1959) p. 245.
4. Ribner, H. S.: "The Generation of Sound by Turbulent Jets" in Advances in Applied Mechanics, Vol. 8, New York: Academic Press (1964), pp. 103-182.
5. Curle, S. N.: "General Theory of Aerodynamic Sound" in Noise and Acoustic Fatigue in Aeronautics, edited by E. J. Richards and D. J. Mead, New York: Wiley Press (1968) pp. 111-134.
6. Goldstein, M. E.: Aerocoustics, NASA, SP-346 (1974).
7. Lighthill, M. J.: "On Sound Generated Aerodynamically", Proc. Roy. Soc. (London), <sup>Ser. A</sup> Vol. 267, No. 11329 (May, 1962) pp. 147-181.
8. Lilley, G. M.: "On the Noise from Air Jets", ARC-20, 376; N40: FM-2724, British Aeronautical Research Council (September, 1958).

9. Ffowcs Williams, J. E. and Hawkings, D. L.: "Sound Generation by Turbulence and Surfaces in Arbitrary Motion", Phil. Trans. Roy. Soc. (London), Ser. A, Vol. 264 (May, 1969) pp. 321-342.
10. Curle, S. N.: "The Influence of Solid Boundaries on Aerodynamical Sound", Proc. Roy. Soc. (London), Ser. A., Vol. 231, No. 1187 (September, 1955) pp. 505-514.
11. Kraichnan, R. H.: "The Scattering of Sound in a Turbulent Medium", J. Acoust. Soc. Amer., Vol. 25, No. 6 (November, 1953) pp. 1096-1104.
12. Mawardi, O. K.: "On the Spectrum of Noise from Turbulence", J. Acoust. Soc. Amer., Vol. 27, No. 3 (May, 1955) pp. 442-445.
13. Blokhintsev, D. I.: Acoustics of a Nonhomogeneous Moving Medium, in Russian (1946), translated as NACA T.M. 1399 (February, 1956).
14. Morse, P. M. and Ingard, K. U.: Theoretical Acoustics, New York: McGraw-Hill (1958).
15. Davies, P. O. A. L., Fisher, M. J. and Barratt, M. J.: "The Characteristics of Turbulence in the Mixing Region on a Round Jet", J. Fluid Mech. Vol. 15, Pt. 3 (March, 1963) pp. 337-367.
16. Ribner, H. S.: "Quadrupole Correlations Governing the Pattern of Jet Noise", J. Fluid Mech., Vol. 38, Pt. 1 (August, 1969) pp. 1-29.

17. Goldstein, M. E. and Rosenbaum, B.: "Effect of Anisotropic Turbulence on Aerodynamic Noise", J. Acoust. Soc. Amer., Vol. 54, No. 3 (September, 1973) pp. 630-645.
18. Atvars, J., Schubert, T. K. and Ribner, H. S.: "Refraction of Sound from a Point Source Placed in an Air Jet", J. Acoust. Soc. Amer., Vol. 37, No. 1 (January, 1965) pp. 168-170.
19. Grande, E.: "Refraction of Sound by Jet Flow and Jet Temperature", NASA CR-840 (August, 1967).
20. Gottlieb, P.: "Acoustics in Moving Media", Ph.D. Thesis, Physics Dept., M.I.T. (June, 1959); also: "Sound Source Near a Velocity Discontinuity", J. Acoust. Soc. Amer., Vol. 82, No. 9 (September, 1960) pp. 1117-1122.
21. Grahm, E. W. and Grahm, B. B.: "The Acoustical Source in a Two-Dimensional Jet", Boeing Scientific Research Laboratories, DI-82-0909 (1969).
22. Townsend, A. A.: "The Measurement of Double and Triple Correlation Derivatives in Isotropic Turbulence", Proc. Camb. Phil. Soc., Vol. 43 (1947) p. 560.
23. Batchelor, G. G.: The Theory of Homogeneous Turbulence, Cambridge: Cambridge University Press (1953).

24. Uberoi, M. S. and Singh, P. I.: "Turbulent Mixing in a Two-Dimensional Jet" in The Physics of Fluids, Vol. 18, No. 7 (July, 1975) pp. 764-769.
25. Lassiter, L. W.; "Turbulence in Small Air Jet at Exit Velocities Up to 705 Feet Per Second", J. Appl. Mech., Vol. 24, No. 3 (September, 1957) pp. 349-354.
26. Meecham, W. C.: "Acoustic Spectra from Turbulent Jets" in Basic Aerodynamic Noise Research, edited by I. R. Schwartz, NASA SP-207 (July, 1969) pp. 177-185.
27. Olsen, W. A., Guturrry, O. A. and Dorsch, R. G.: "The Effect of Nozzle Inlet Shape, Lip Thickness and Exit Shape on Subsonic Jet Noise", NASA T.M. X-68182 (1973).
28. von Gierke, H.: "Types of Pressure Fields of Interest in Acoustical Fatigue Problems" in University of Minnesota Conference on Acoustical Fatigue, edited by W. J. Trapp and D. M. Forney, W.A.D.C. Tech. Rep., pp. 59-676.
29. Ffowcs Williams, J. E.: "The Noise from Turbulence Convected at High Speed", Phil. Trans. Roy. Soc. (London), Ser. A, Vol. 255, No. 1061 (April, 1963) pp. 469-503.
30. Ingard, K. U. and Singhal, V. K.: "Effect of Flow on the Acoustic Resonance of an Open-Ended Duct",



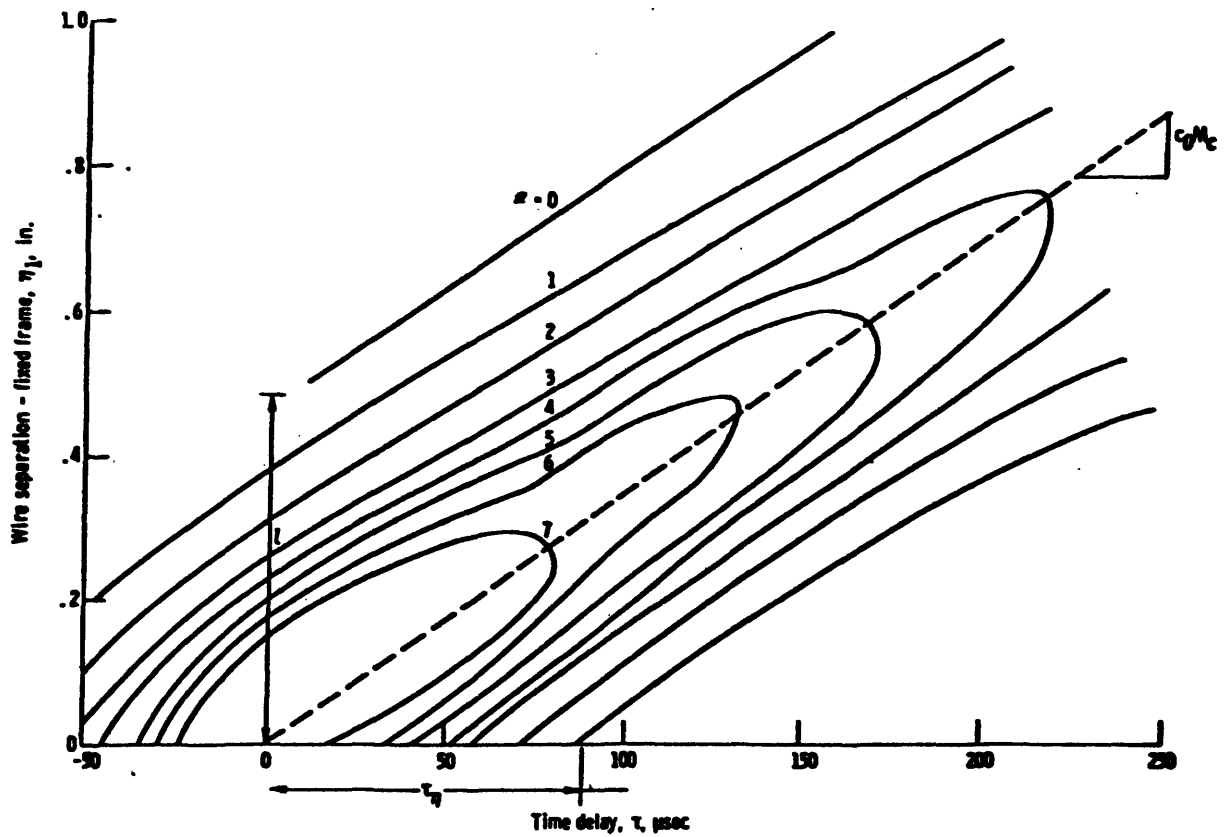
- J. Acoust. Soc. Amer., Vol. 58, No. 4 (October, 1975) pp. 788-793.
31. Ingard, K. U.: lecture notes in "Noise Control Engineering", M.I.T. course 16.56 (Fall semester, 1976).
  32. Marble, F. E.: "Acoustic Disturbance from Gas Non-uniformities Convected through a Nozzle" in Vol. II, Proceedings, Interagency Symposium on University Research in Transportation Noise, Stanford University (March 28-30, 1973) pp. 547-560.
  33. Bohn, M. S. and Zukoski, E. E.: "Effect of Flow on the Acoustic Reflection Coefficient at a Duct Inlet", J. Acoust. Soc. Amer., Vol. 59, No. 6 (June, 1976) pp. 1497-1499.
  34. Cummings, A.: "Sound Transmission at a Sudden Area Expansions in Circular Ducts with Superimposed Mean Flow", J. Sound and Vib., Vol. 38, No. 1 (January, 1975) pp. 149-155.
  35. Morse, P. M.: Vibration and Sound, New York: McGraw-Hill (1948).
  36. Abramowitz, M. and Stegun, I.: Handbook of Mathematical Functions with Formulas, Graphs and Mathematical Tables, N.B.S. Applied Math, Ser. 55 (1964).
  37. Lee, J. F. and Sears, F. W.: Thermodynamics, Reading, Mass.: Addison-Wesley (1963) Chap. 8.

38. von Gierke, H. E., Parrach, H. O., Gannon, W. J. and Hansen, R. G.: "The Noise Field of a Turbo-Jet Engine", J. Acoust. Soc. Amer., Vol. 24, No. 1 (March, 1952) pp. 169-174.
39. Mungar, P. and Gladwell, G. M. L.: "Acoustic Wave Propagation in a Sheared Fluid Contained in a Duct", J. Sound and Vib., Vol. 9, No. 1 (January, 1969) pp. 28-48.
40. Ingard, K. U.: lecture notes in "Noise Control Engineering", M.I.T. course 16.56 (Fall semester, 1975).
41. Roe, G. M.: "Frequency Distribution of Normal Modes", J. Acoust. Soc. Amer., Vol. 13, No. 1 (July, 1941) pp. 1-7.
42. Doak, P. E.: "Elements of Sound Propagation" in Noise and Acoustic Fatigue in Aeronautics, edited by E. J. Richards and D. J. Mead, New York: Wiley Press (1968) pp. 43-72.
43. Chanaud, R. C. and Powell, A.: "Some Experiments Concerning the Hole and Ring Tone", J. Acoust. Soc. Amer., Vol. 37, No. 5 (May, 1965) pp. 902-911.
44. Anderson, A. B. C.: "A Jet Tone Orifice Study for Orifices of Small Thickness - Diameter Ratio", J. Acoust. Soc. Amer., Vol. 26, No. 1 (January, 1954) pp. 21-25.

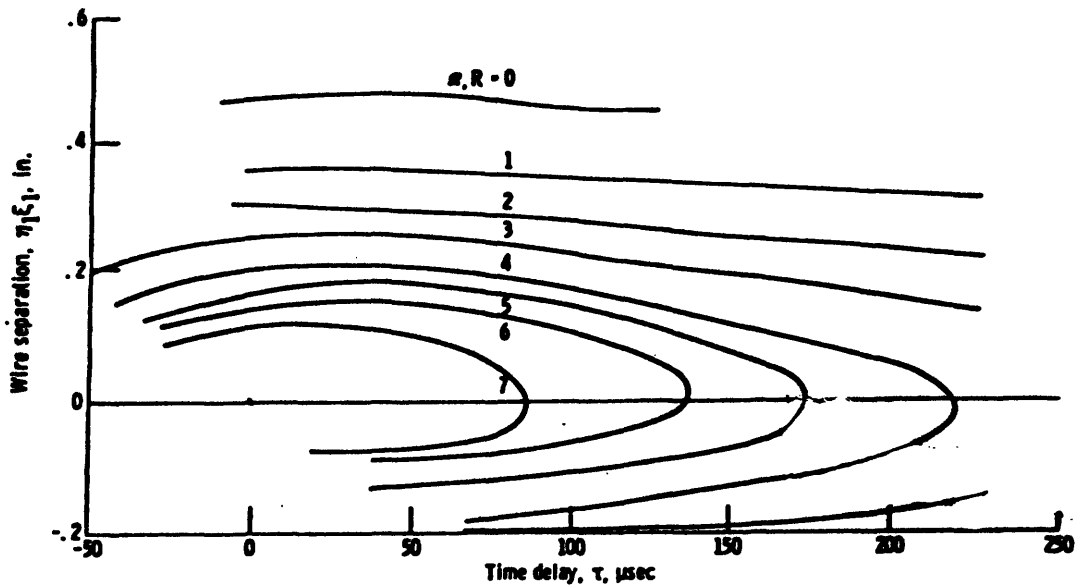
45. Heller, H. H.: "Tone Generation by Subsonic Flow Through Sharp-Edged Circular Nozzles", '73 meeting of Acoust. Soc. Amer. (April 21, 1967) paper N/EF3 (abstract only) p. 1615.
46. Thomas, N.: "On the Production of Sound by Jets", J. Acoust. Soc. Amer., Vol. 27, No. 3 (May, 1955) pp. 446-448.
47. Powell, A. and Unfreid, H. H.: "An Experimental Study of Edgetones", U.C.L.A. Rept. 64-49 (1964).
48. Powell, A.: "On the Edgetone", J. Acoust. Soc. Amer., Vol. 33, No. 4 (April, 1961) pp. 395-409.
49. Wagner, F. R.: "Zum Schall-und Strömungsfeld eines Axialsymmetrischen Freistralls beim Auftreffen auf eine Wund", in German, English abstract, Z. Flugwiss 19 (1971) Heft. 1, pp. 30-44.
50. Neuwerth, G.: "Acoustic Feedback Phenomena of the Subsonic and Hypersonic Free Jet Impinging on a Foreign Body", NASA TT-F-15719 (July, 1974).
51. Anderson, A. B. C.: "Vortex Ring Structures in a Jet Emitting Discrete Acoustic Frequencies", J. Acoust. Soc. Amer., Vol. 28, No. 5 (September, 1956) pp. 914-921.
52. Bilanin, A. J. and Covert, E. E.: "Estimation of Possible Excitation Frequencies for Shallow Rectangular Cavities", AIAA Jour., Vol. 11, No. 3 (March, 1973) pp. 347-351.

53. Rossiter, J. E.: "Wind Tunnel Experiments in the Flow over Rectangular Cavities at Subsonic and Transonic Speeds", R and M 3438 (1966), Aeronautical Research Council, Brittain.
54. Handa, H.: "Jet Instabilities and Noise", Ph.D. Thesis, Mechanical Engineering Dept., M.I.T. (February, 1974).
55. Bilanin, A. J.: "Flow-Induced Oscillations in Rectangular Cavities", M. S. Thesis, Aeronautics Dept., M.I.T. (September, 1970).
56. Ingard, K. U., Cho, Y. C., Singhal, V. K., Succi, G. P. and Patric, W. P.: "Studies of Sound Absorption Materials and Attenuation of Sound in Ducts", Proc. 2nd Interagency Symp. on Research in Transportation Noise, Vol. 2, N. Carolina State Univ. (June, 1974) p. 816.
57. Tam, C. K. W.: "Directional Acoustic Radiation from a Supersonic Jet Generated by Shear Layer Instabilities", J. F. Mech., Vol. 46, Pt. 4 (April, 1974) pp. 757-768.
58. Sedel'nikov, T. Kh.: "The Frequency Spectrum of the Noise in a Supersonic Jet" in Physics of Aerodynamic Noise, edited by Rimskey-Korsakov, translated in NASA TT-F-538 (November, 1969) pp. 71-75.

59. Miles, J. W.: "On the Disturbed Motion of a Plane Vortex Sheet", J. Fluid Mech., Vol. 4, Pt. 5 (September, 1958) pp. 538-552.
60. Rayleigh, Theory of Sound, Dover Reprint (1945).
61. Landau, L. D. and Lifshitz, E. M.: Fluid Mechanics, Reading, Mass.: Addison Wesley (1959).
62. Olsen, W. A., Miles, J. H. and Dorsch, R. G.: "Noise Generated by the Impingement of a Jet on a Jet on a Large Flat Plate", NASA TN D-7075 (December, 1972).
63. Lee, H. K., and Ribner, H. S.: "Direct Correlation of Noise and Flow of a Jet", J. Acoust. Soc. Amer., Vol. 52, No. 5, Pt. 1 (1972), pp. 1280-1290.



Isocorrelation contours for fixed observer (measurements in center of mixing region  $1\frac{1}{2}$  diameters downstream).



- Isocorrelation contours in moving frame (measurements in mixing region  $1\frac{1}{2}$  diameters downstream).

FIGURE 1.1 -- Correlation contours for a free jet. (Ref. 15)

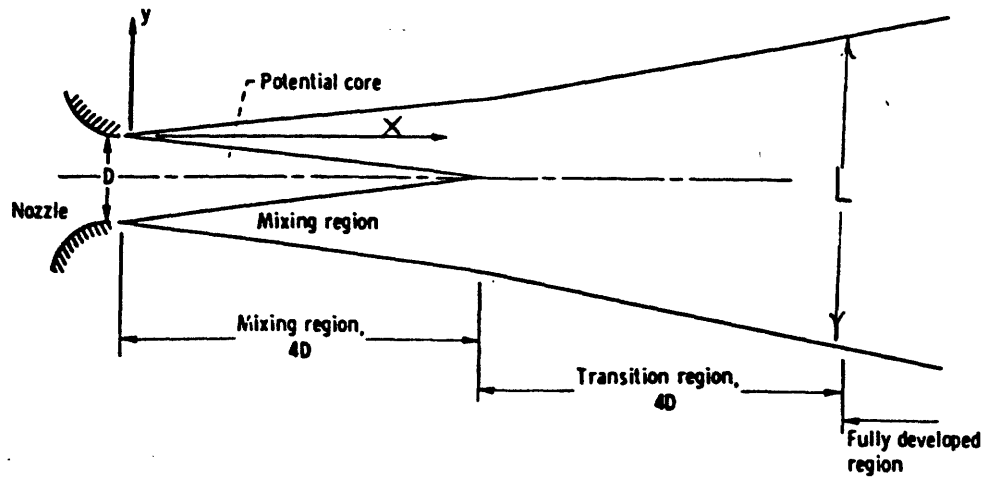
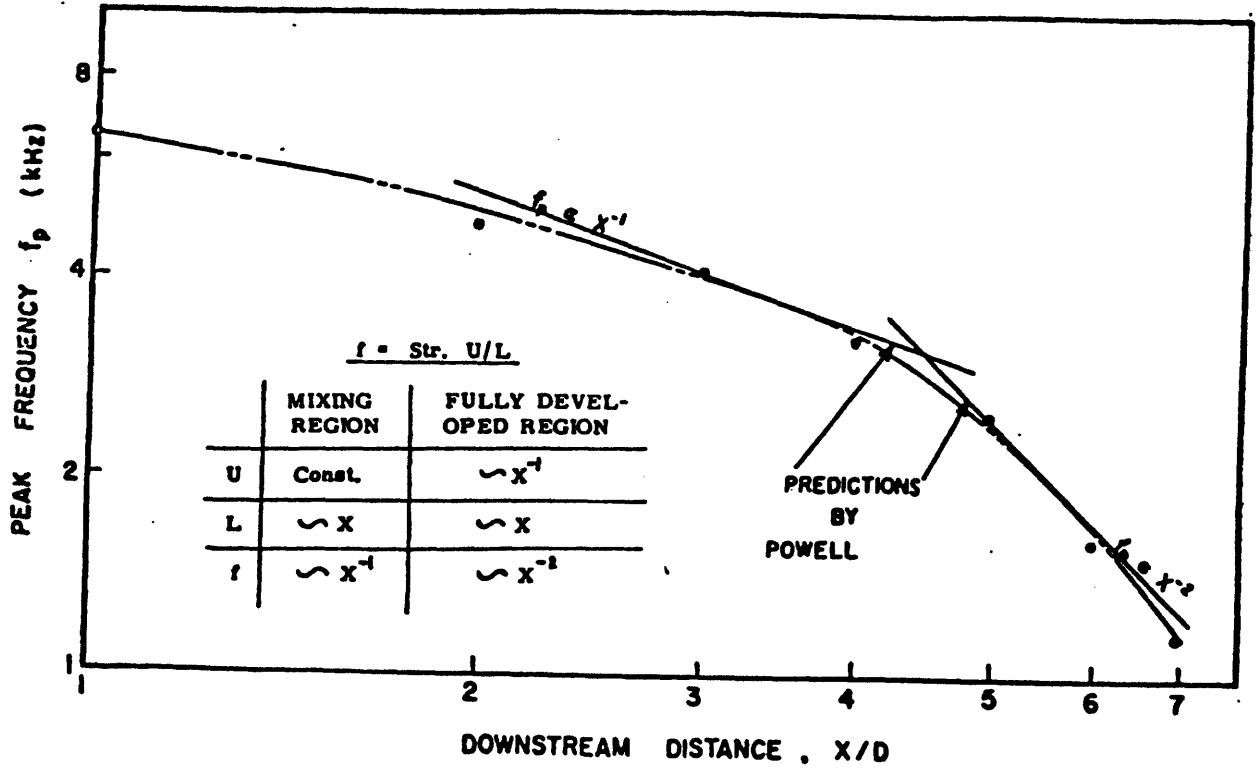


FIGURE 1.2 -- Peak frequency of acoustic power versus downstream distance in a free jet. (Ref.63 )

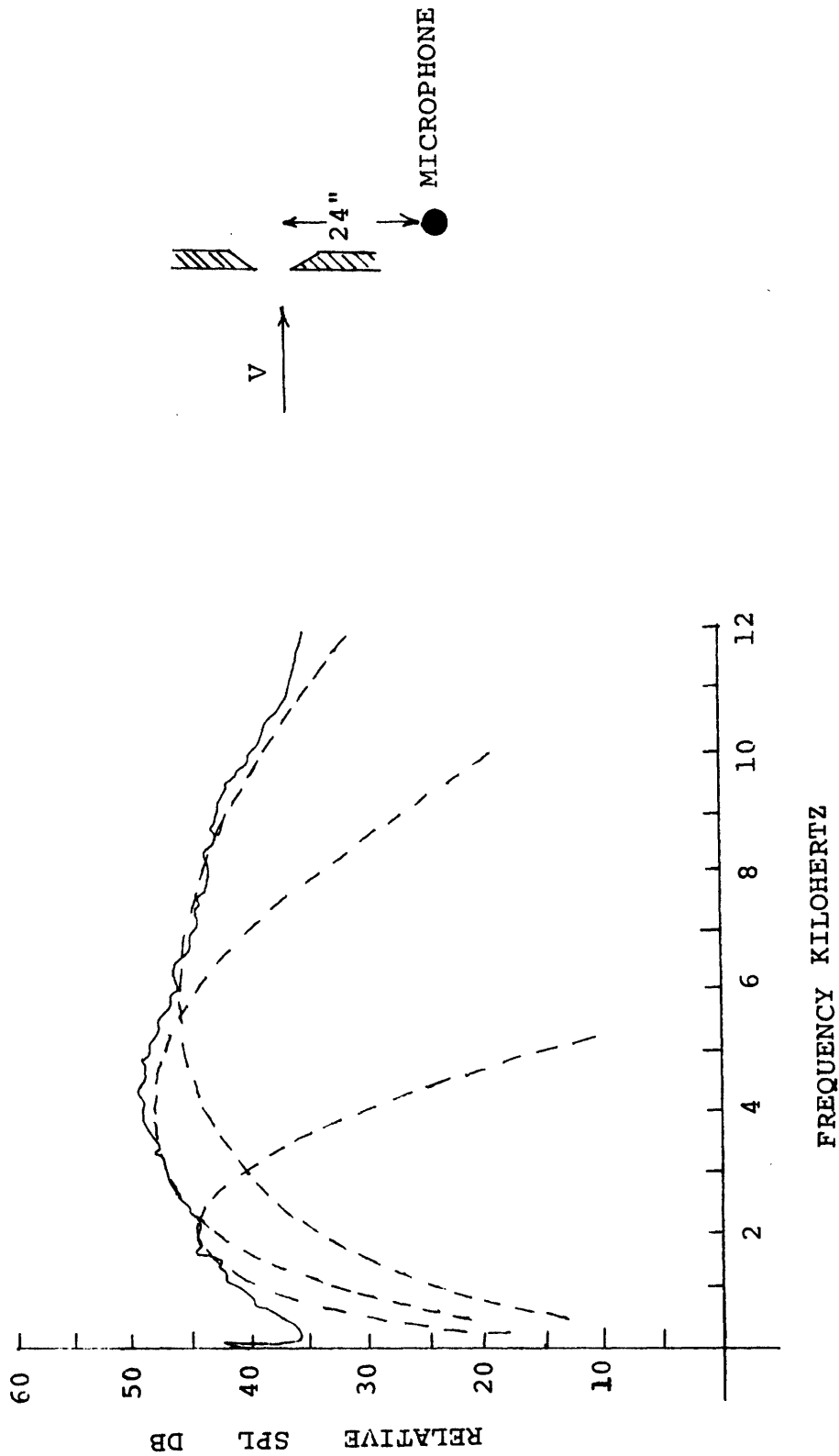


FIGURE 1.3 -- Free space spectra fit by three independent isotropic correlation functions. Solid line is the experimental spectra for an air jet from a 1/2" diameter orifice. Dotted lines are predictions based on Eq. 1.66



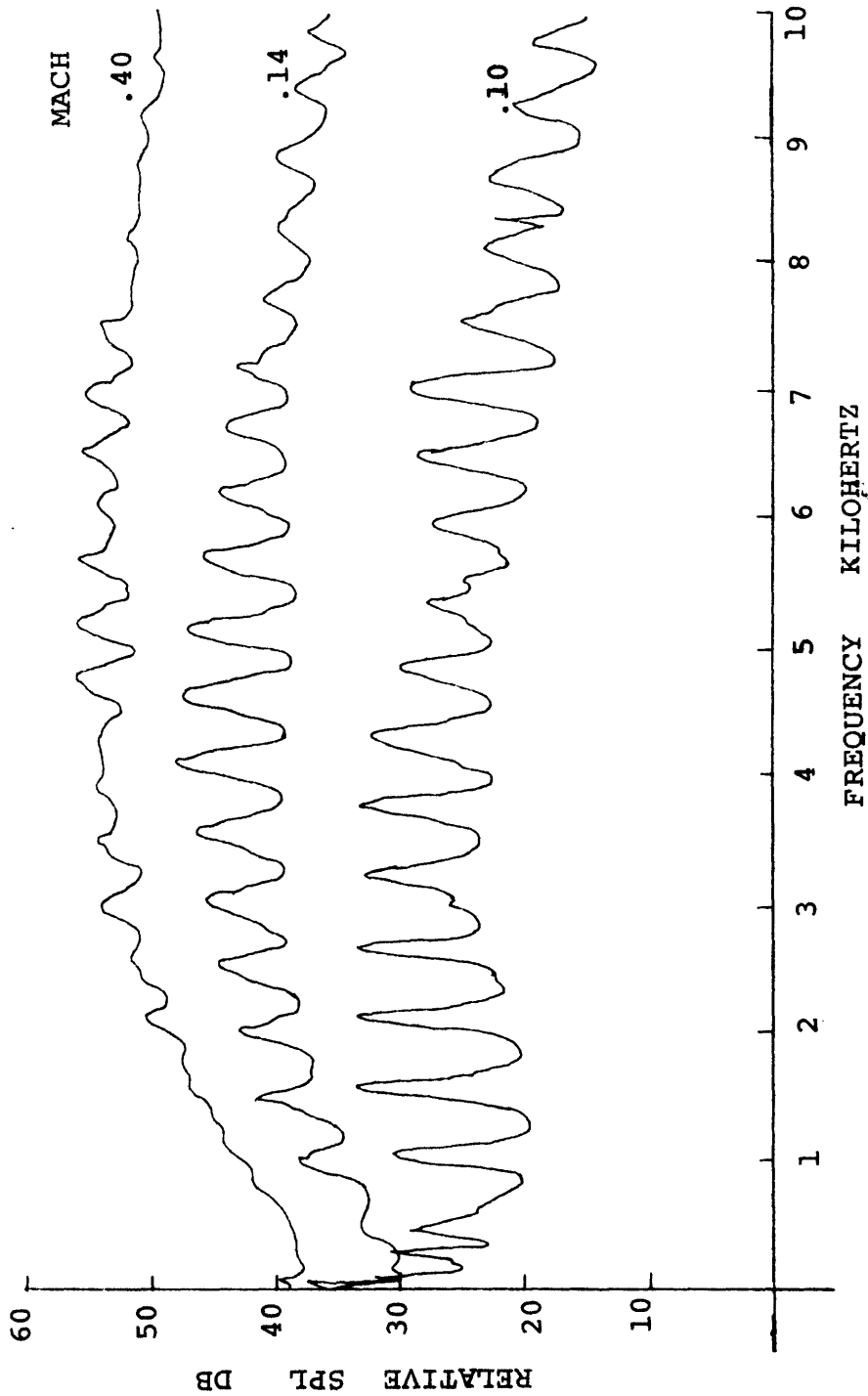


FIGURE 2.1 -- Acoustic spectra versus mean flow. At high flow rates the axial modes are damped by radiation losses, (L = 12", D = 1/2",  $\theta = 0^\circ$ , R = 2").

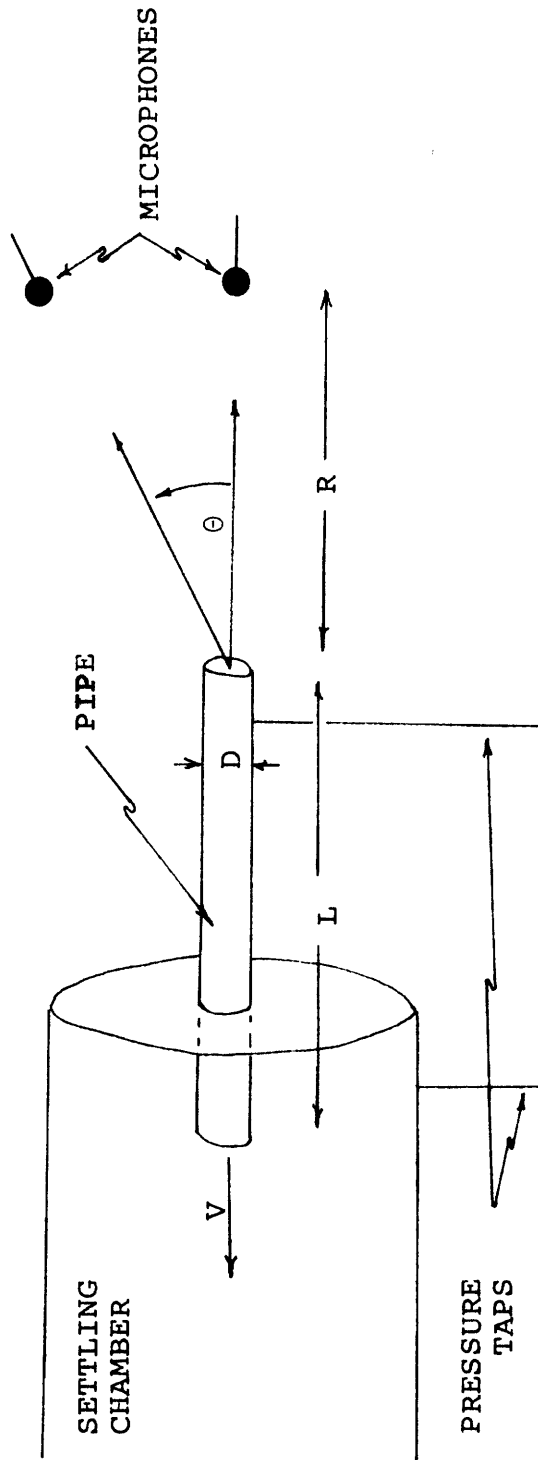


FIGURE 2.2 -- Apparatus used for axial mode study Cylindrical pipes are attached to a settling chamber. Air is drawn through the pipe into the chamber.

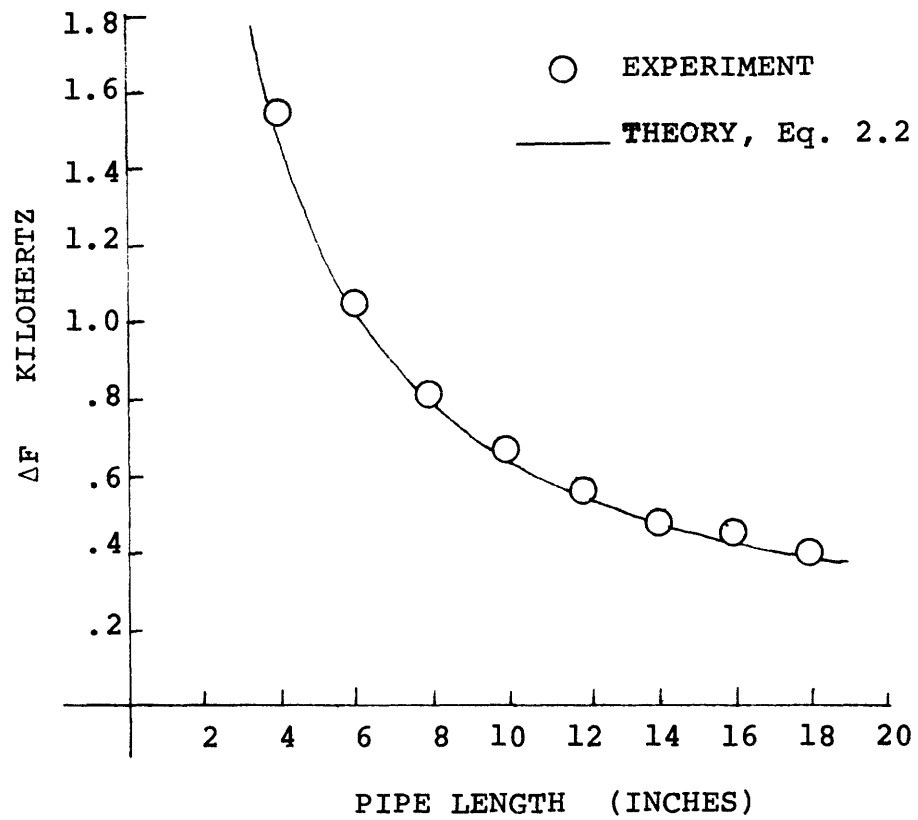


FIGURE 2.3 -- Frequency interval between axial acoustic modes versus pipe length.  
 (L as indicated; D=1";  $\theta=0^\circ, 45^\circ, 90^\circ$ ; R=12")

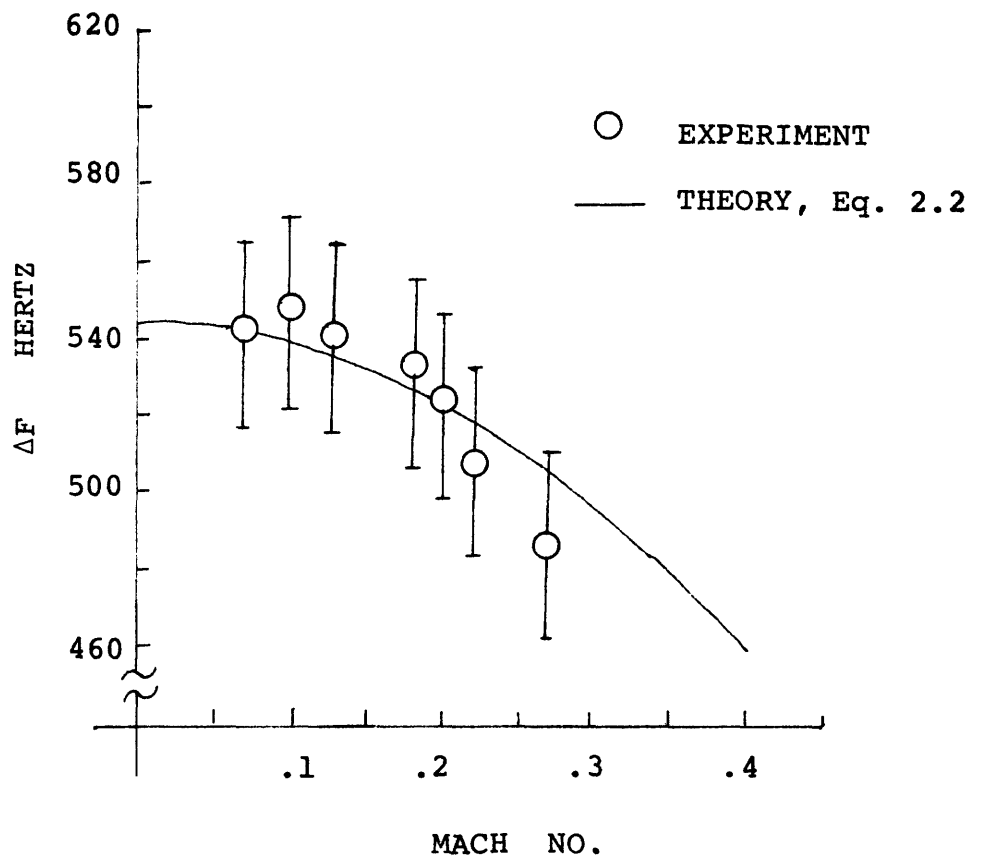


FIGURE 2.4 -- Frequency interval between axial acoustic modes versus mean flow speed.  
 (L = 12", D = 1/2",  $\theta = 0^\circ$ , R = 2")

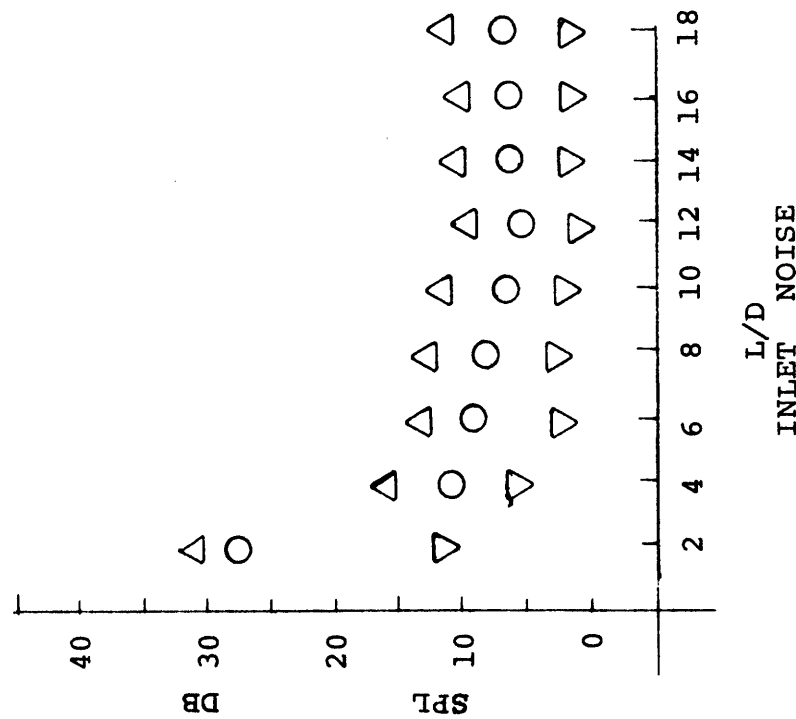
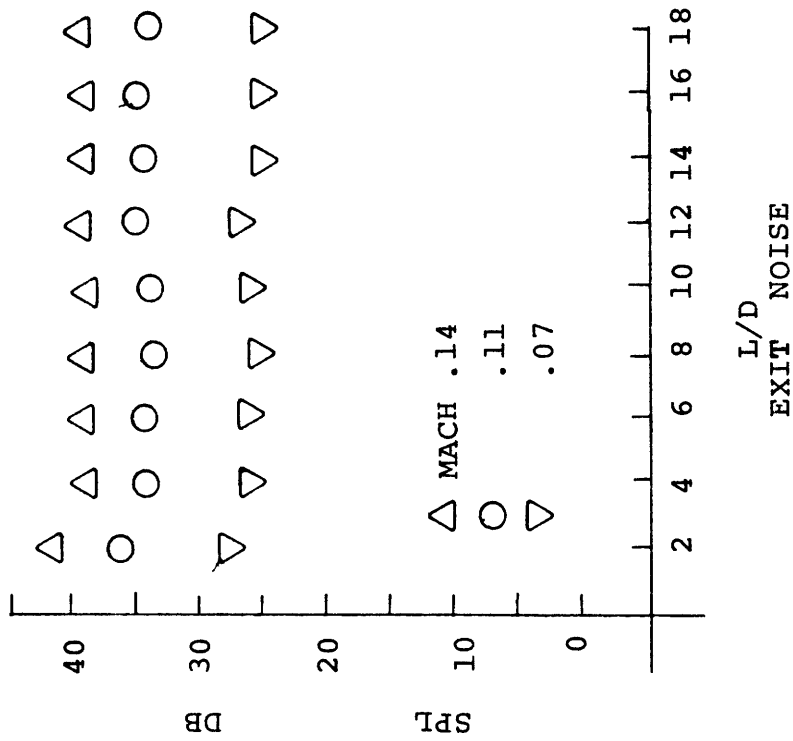


FIGURE 2.5 -- Comparison of inlet and exit pipe noise. The inlet noise is measured in free space, the exit noise is measured in the settling chamber. The increase in level due to reverberation in the chamber is approximately 10 DB. Zero DB corresponds to ambient lab noise which is approximately 65 DB C weight. (L as indicated; D = 1";  $\theta = 0^\circ, 180^\circ, R = 12"$ )

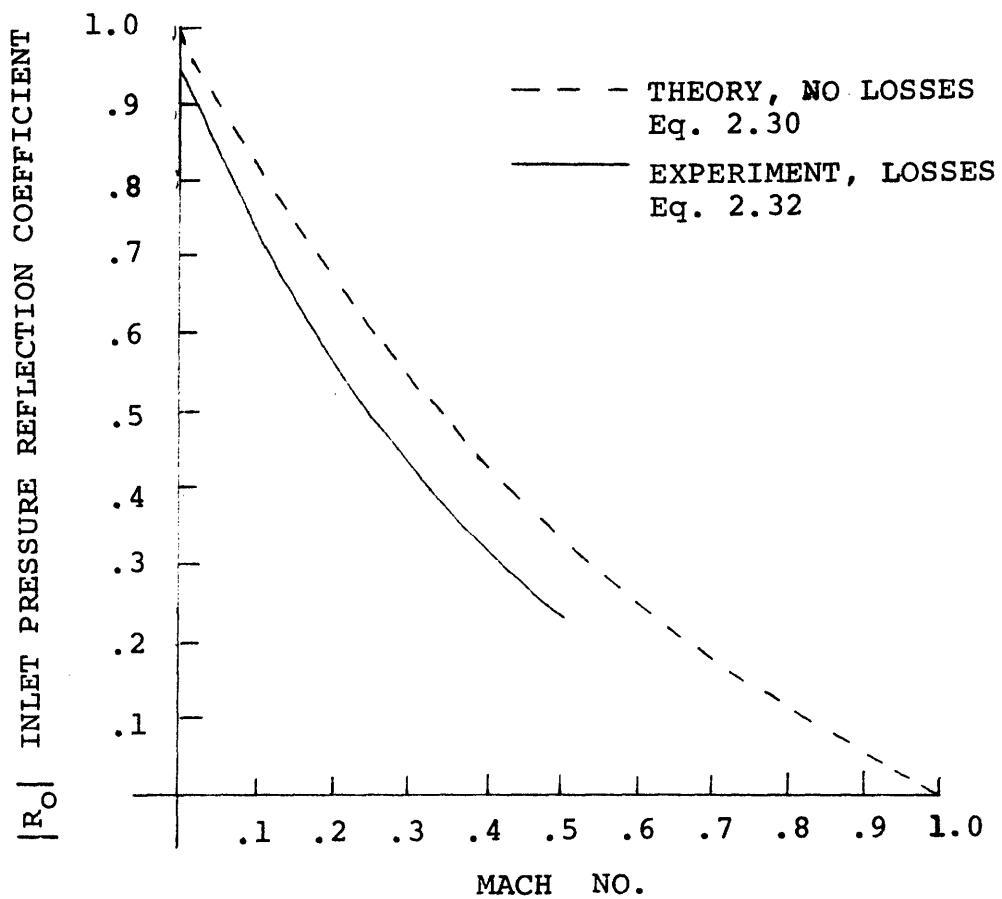


FIGURE 2.6 -- Inlet pressure reflection coefficient.  
Experiment from Ref. 30.

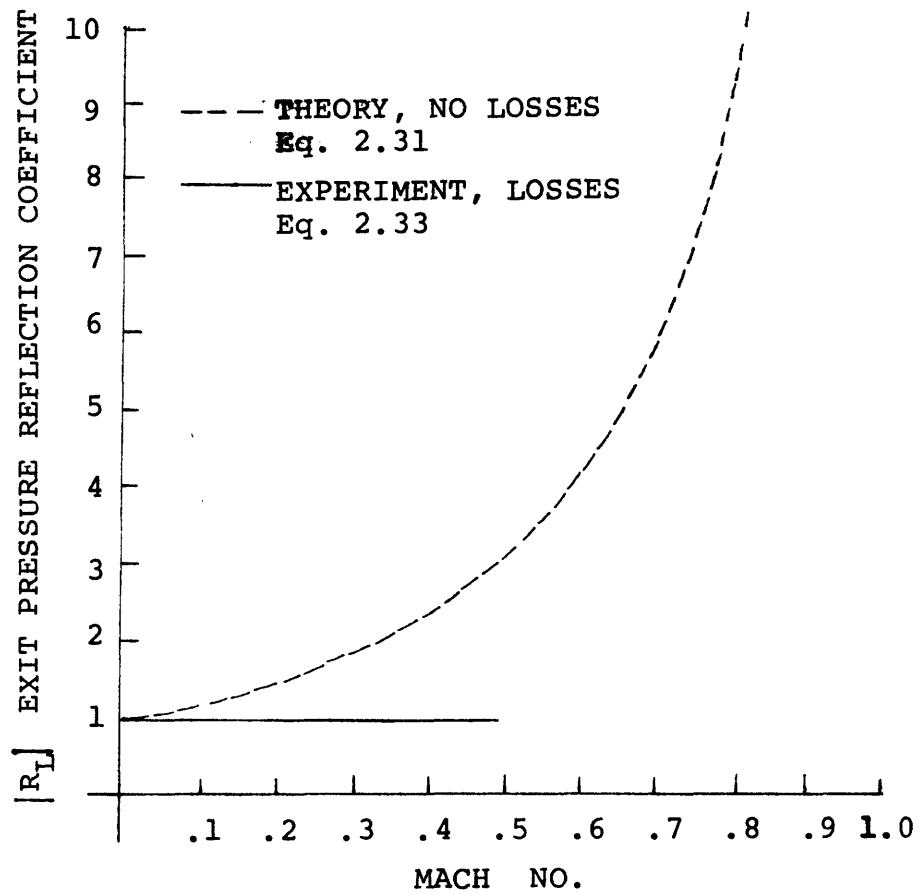


FIGURE 2.7 -- Exit pressure reflection coefficient.  
Experiment from Ref. 30

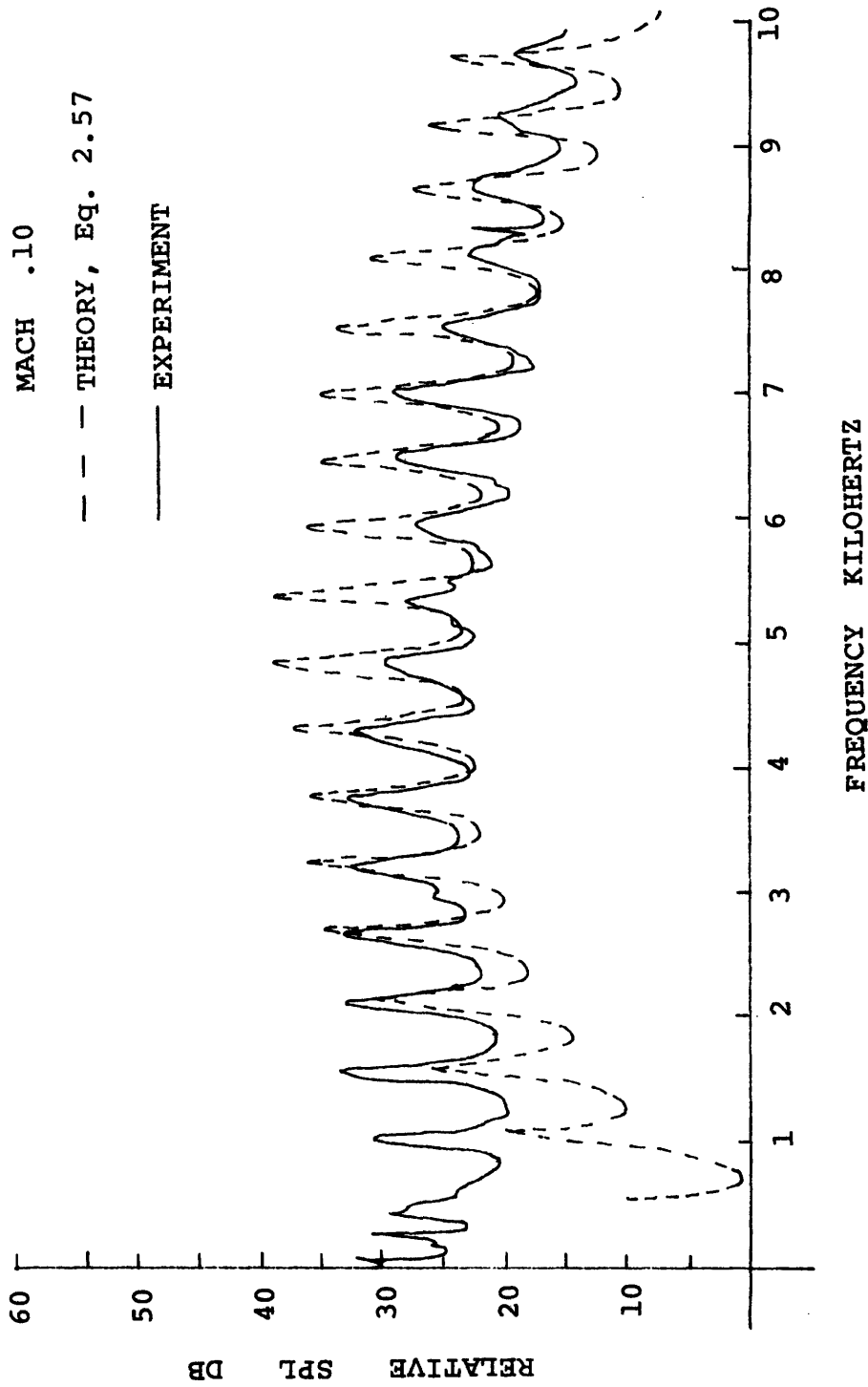


FIGURE 2.8 -- Comparison of experimental and theoretical spectra at Mach .10.  
 (L = 12", D = 1/2",  $\theta = 0^\circ$ , R = 2")



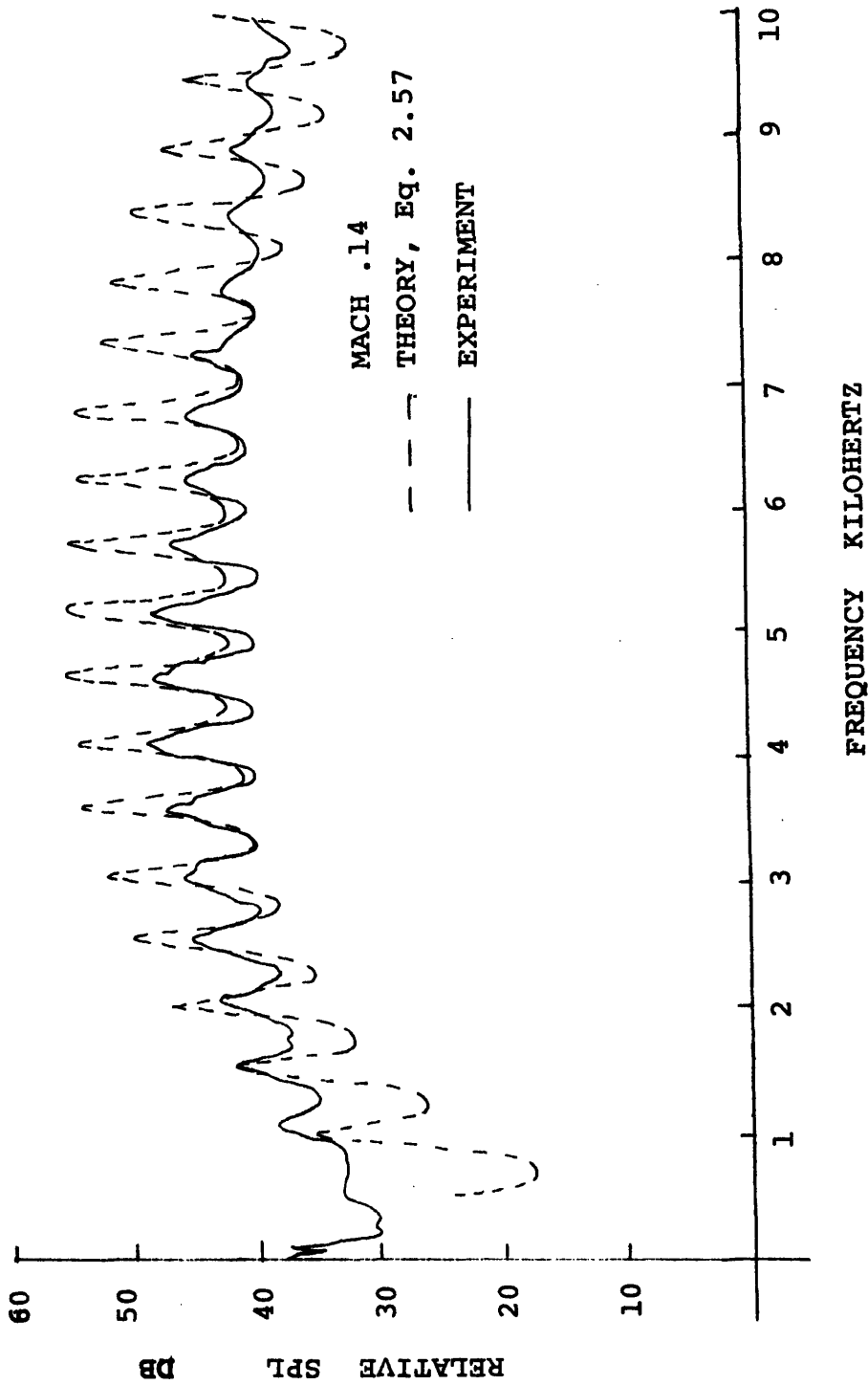


FIGURE 2.9 -- Comparison of experimental and theoretical spectra at Mach .14.  
 (L = 12", D = 1/2",  $\theta = 0^\circ$ , R = 2")

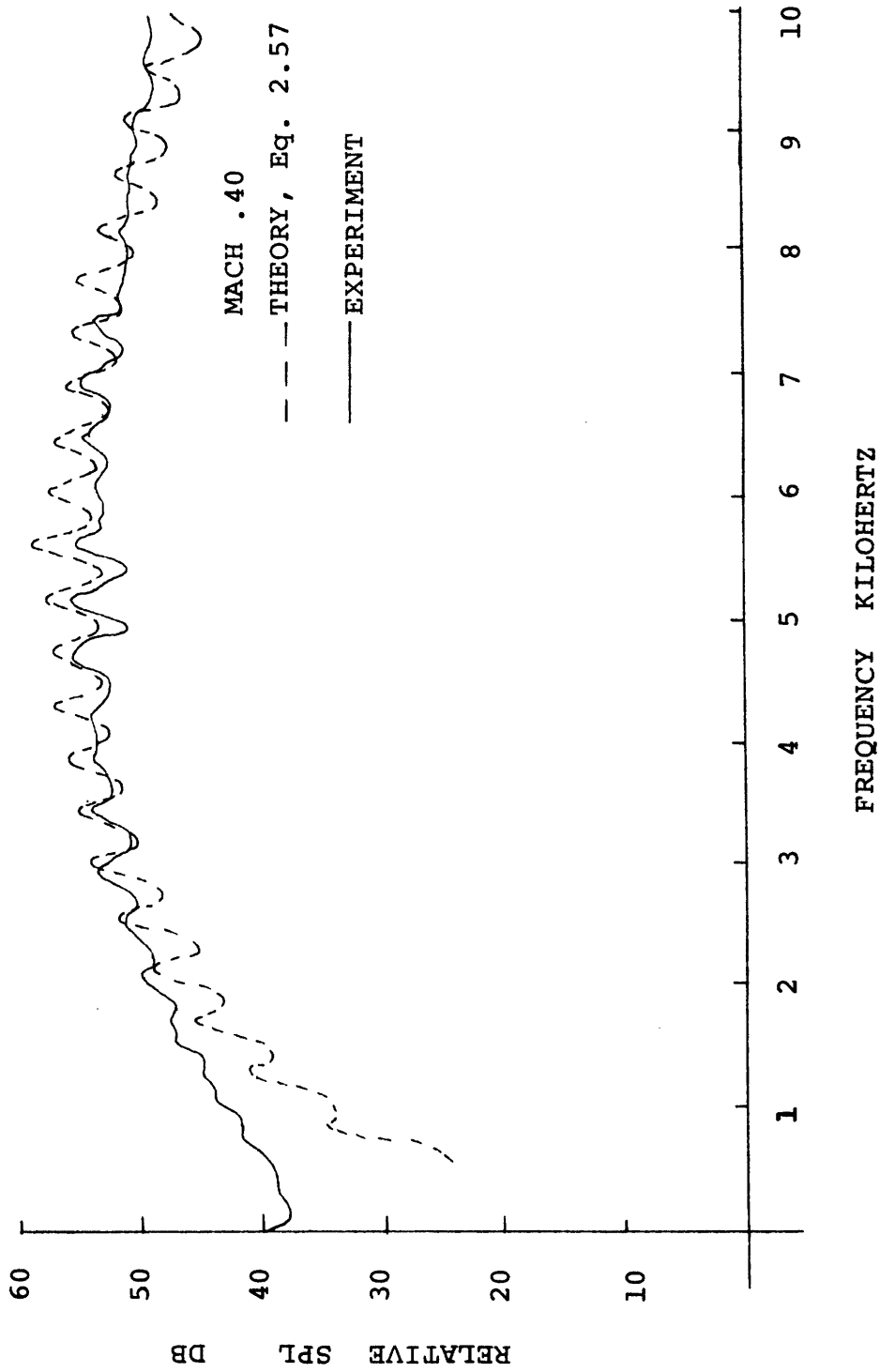


FIGURE 2.10 -- Comparison of experimental and theoretical spectra at Mach .40.  
 (L = 12", D = 1/2",  $\theta = 0^\circ$ , R = 2")

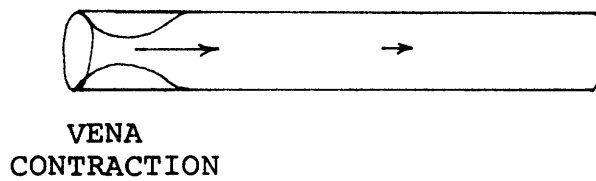
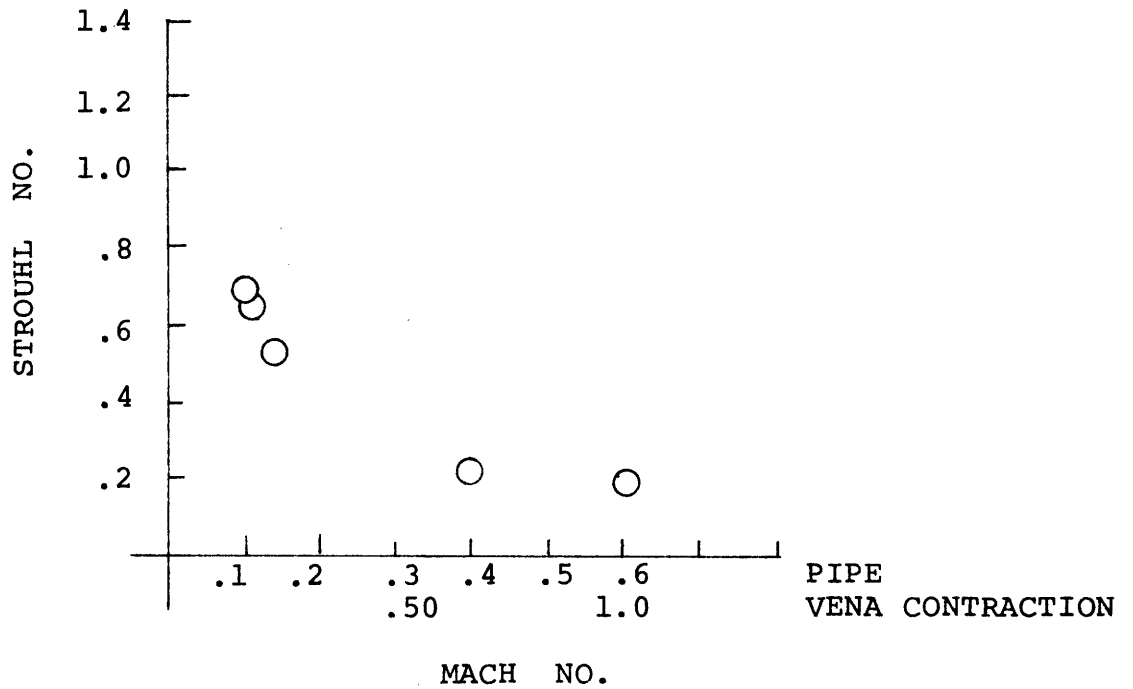


FIGURE 2.11 -- Strouhl numbers used to compute the spectra. The data points are determined by a least squares fit of the theory to the experimental spectra. The velocity and diameter at the narrowest point of the inlet contraction are used to compute the Strouhl number.

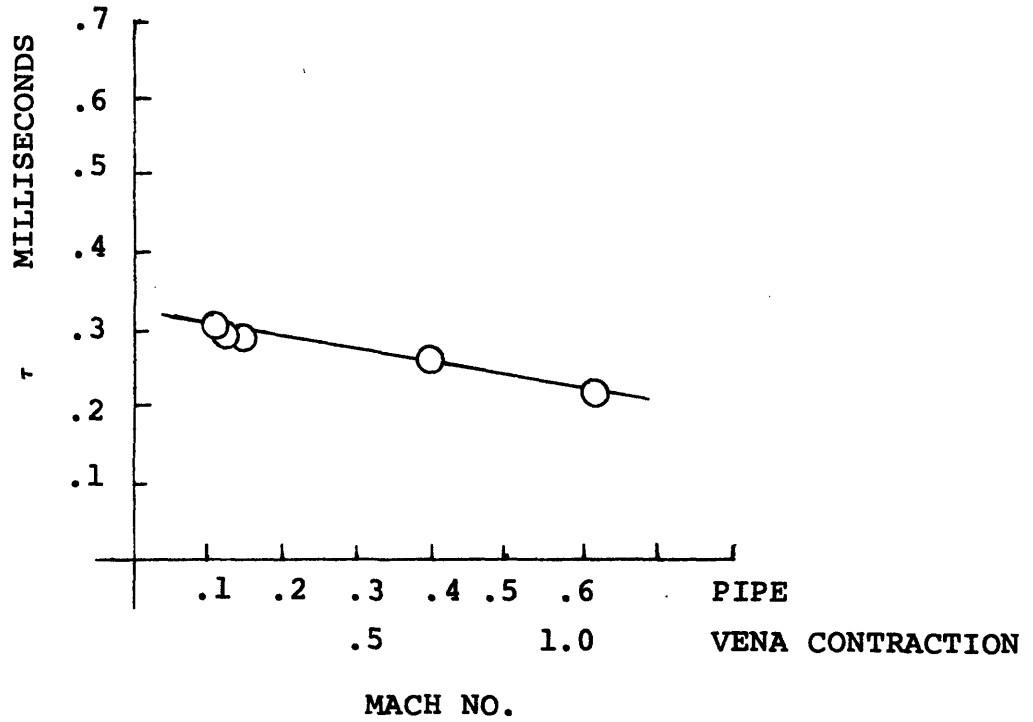


FIGURE 2.12 -- Correlation time based on the Strouhl numbers. The data in Figure 2.11 is used to compute the correlation time by Eq. 2.63.

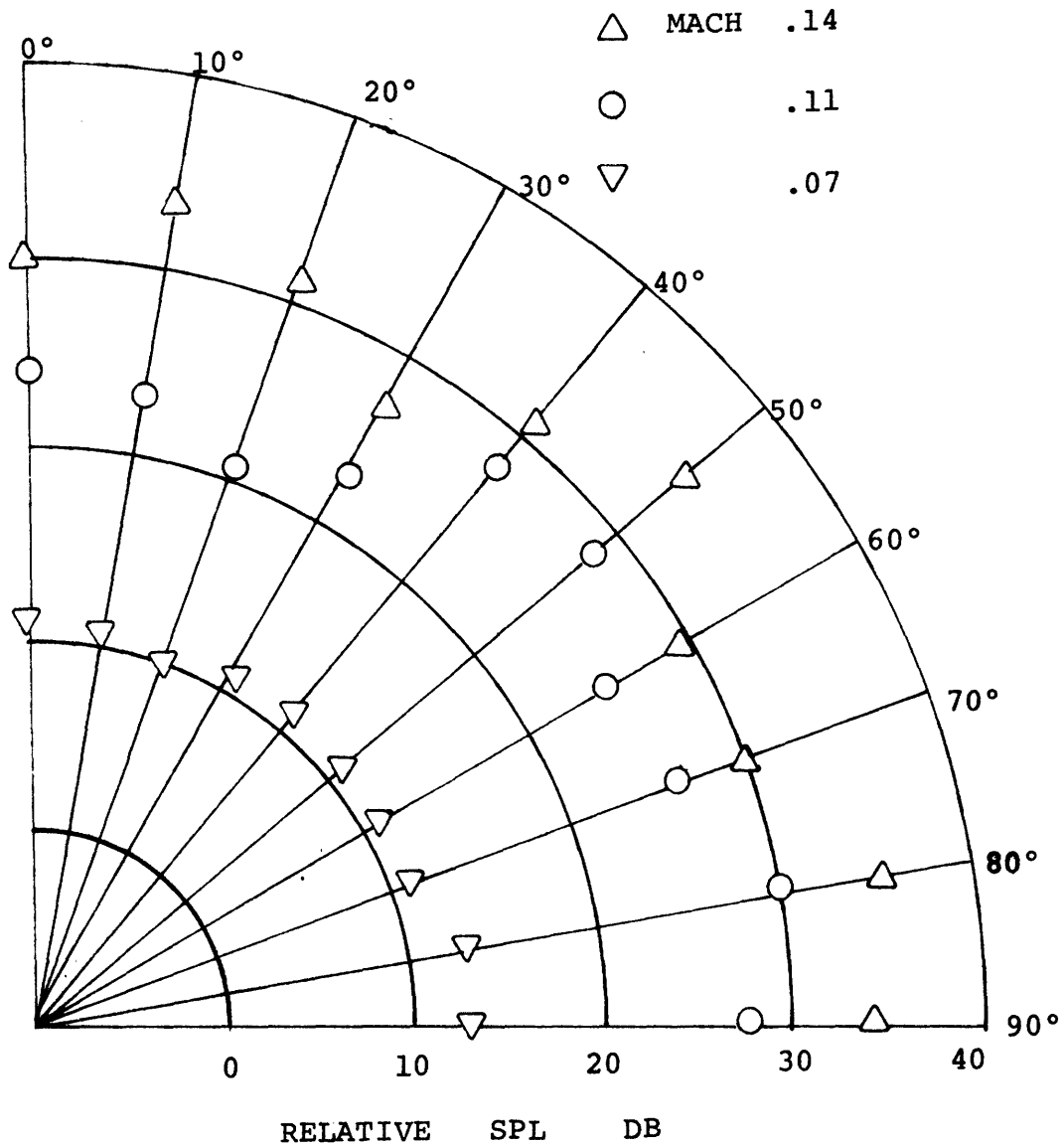


FIGURE 2.13 -- Polar intensity plot for a 2" pipe. Pipes that screech, such as this one, have variations in the intensity with angle. This is to be compared to the uniform distribution of intensity for longer pipes. Zero DB corresponds to ambient lab noise which is approximately 65 DB C weight. . (L=2", D=1",  $\theta$  as indicated, R=12")

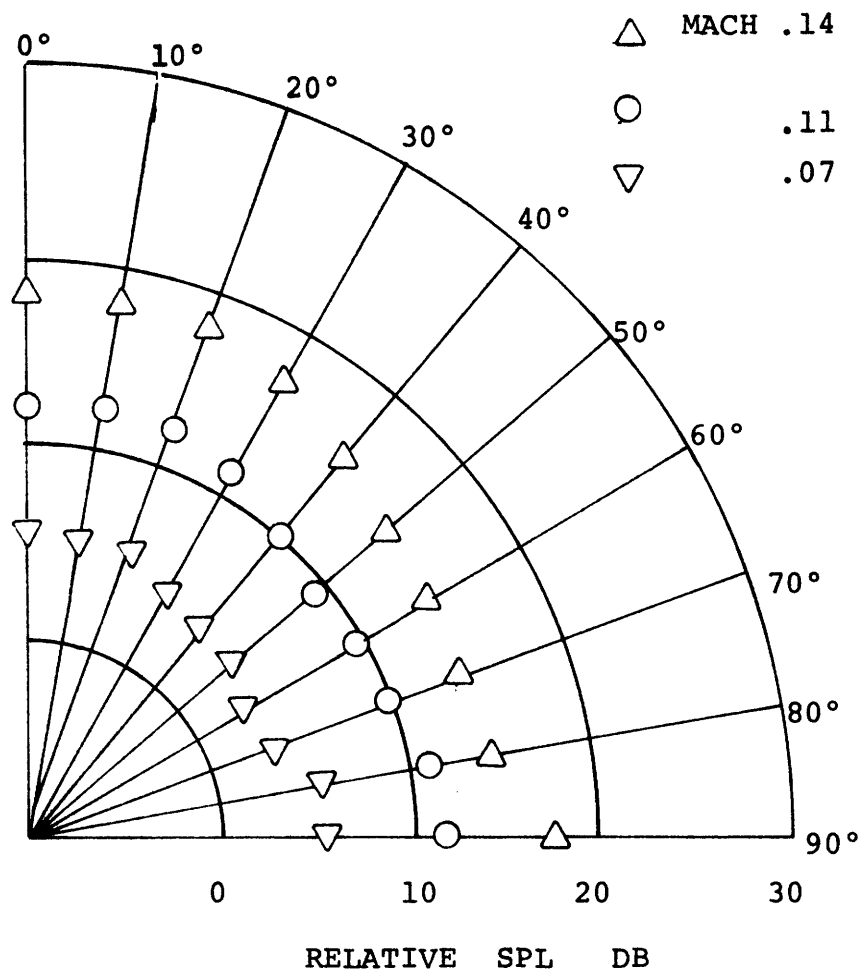


FIGURE 2.14 -- Polar intensity plot for a 4" pipe.  
 (L = 4", D = 1", R = 12")

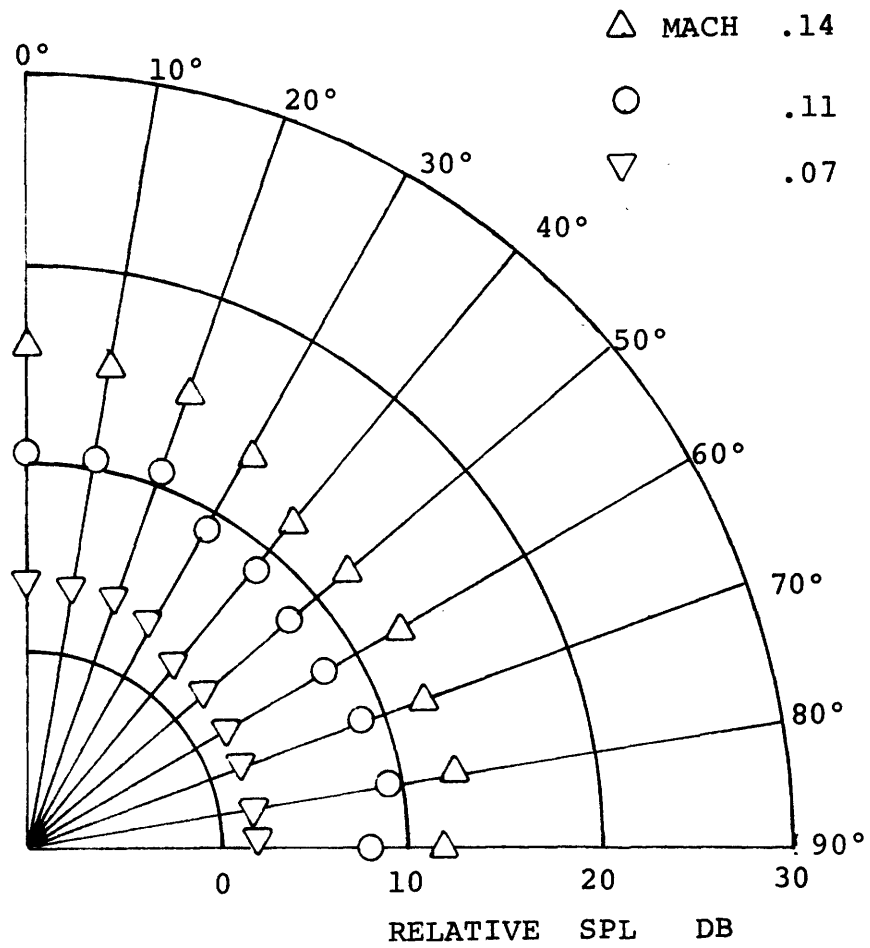


FIGURE 2.15 -- Polar intensity plot for a 6" pipe.  
 (L = 6", D = 1", R = 12")

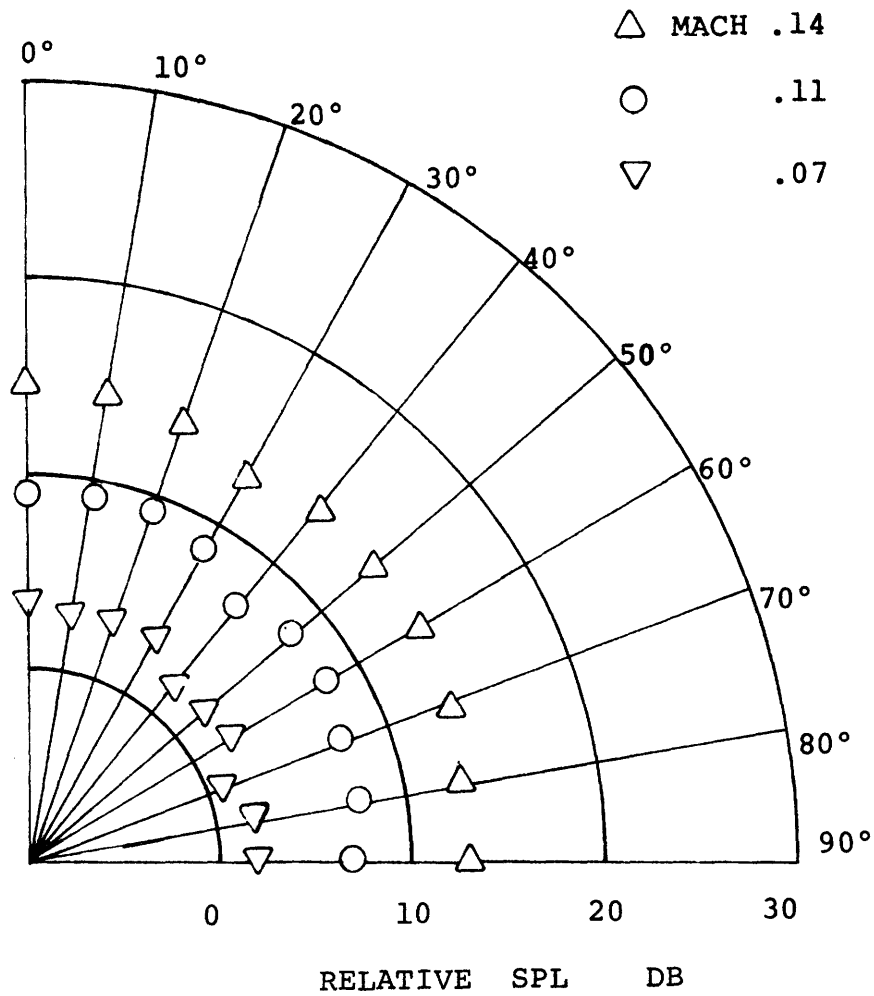


FIGURE 2.16 -- Polar intensity plot for an 8" pipe.  
 (L = 8", D = 1", R = 12")



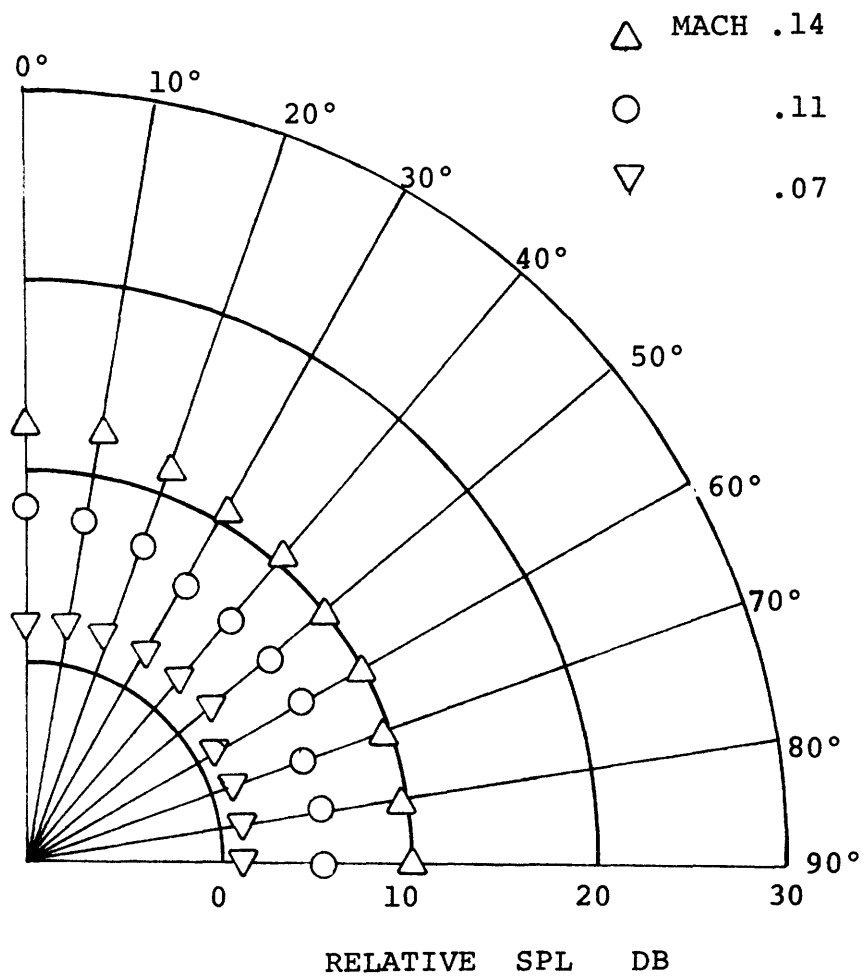


FIGURE 2.17 -- Polar intensity plot for a 10" pipe.  
 (L = 10", D = 1", R = 12")

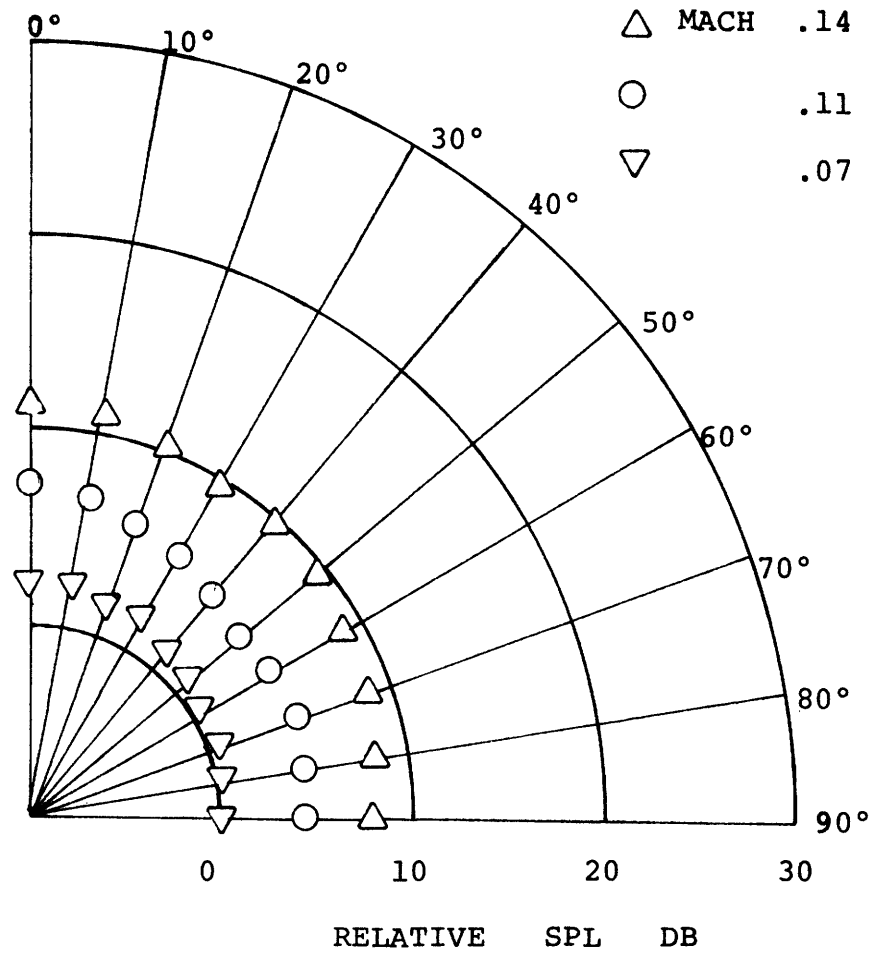


FIGURE 2.18 -- Polar intensity plot for a 12" pipe.  
 (L = 12", D = 1", R = 12")

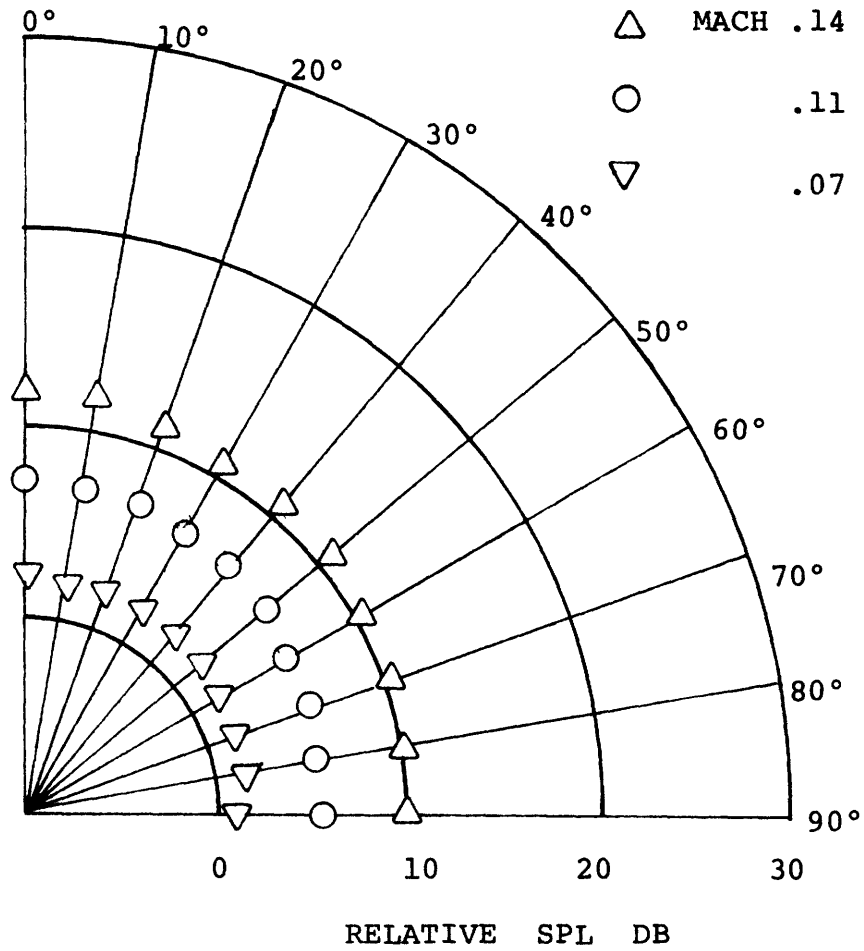


FIGURE 2.19 -- Polar intensity plot for a 14" pipe.  
 (L = 14", D = 1", R = 12")

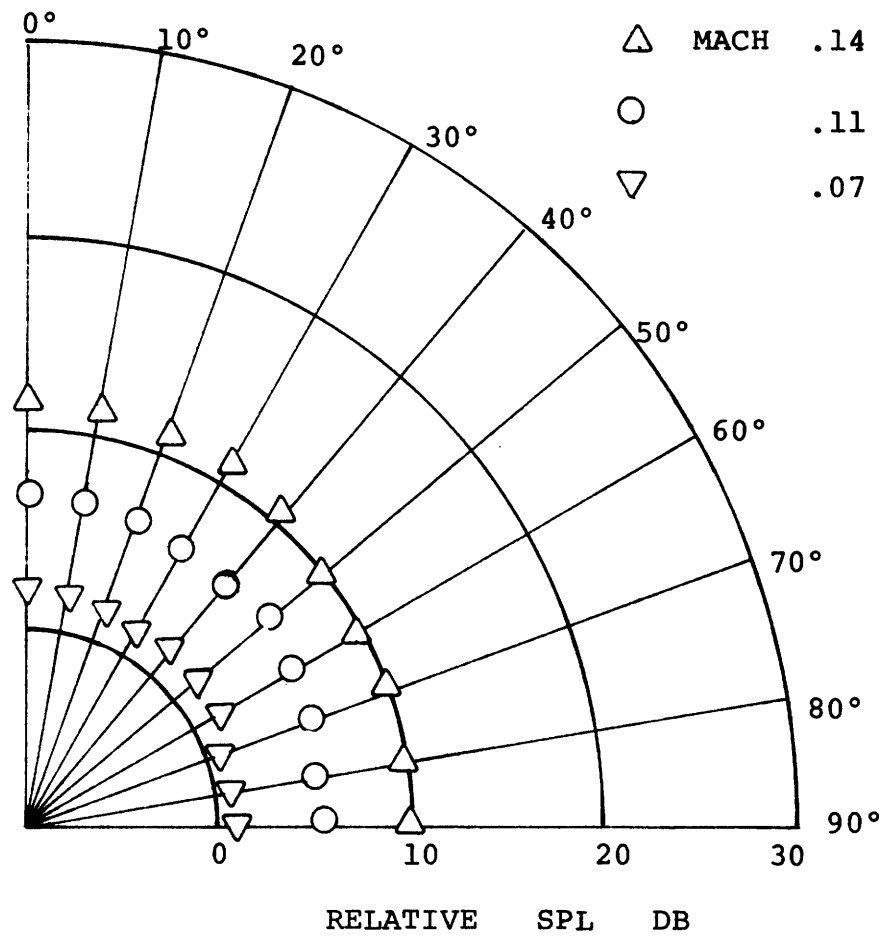


FIGURE 2.20 -- Polar intensity plot for a 16" pipe.  
 (L = 16", D = 1", R = 12")

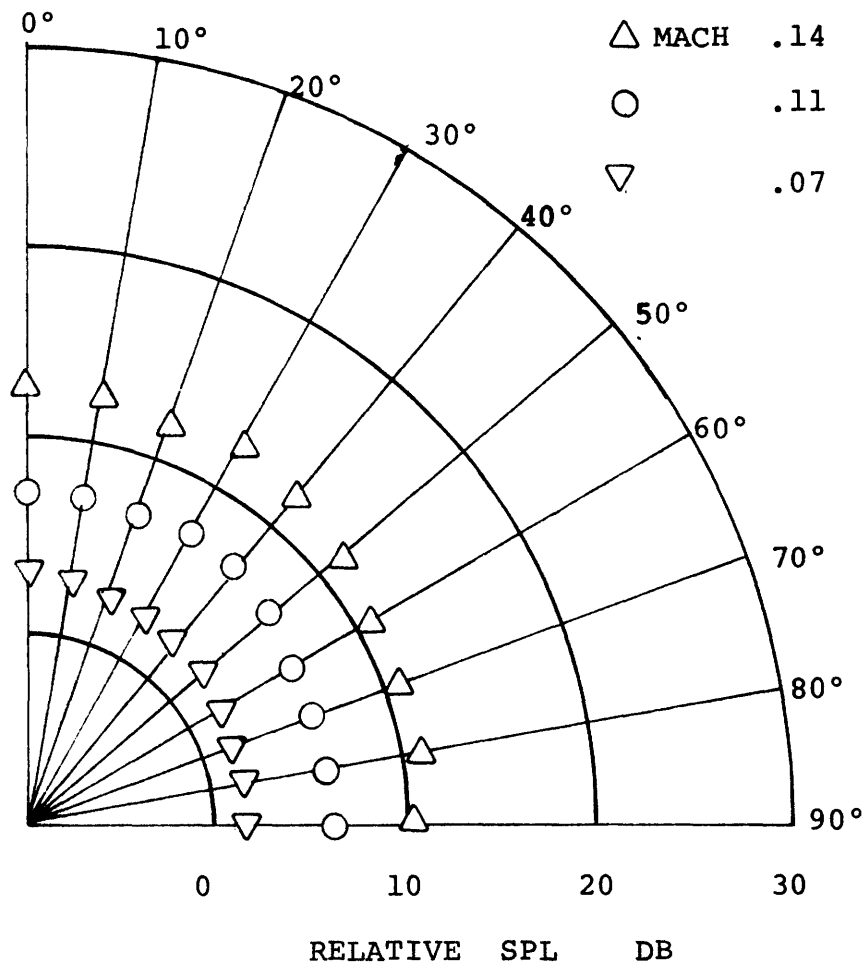


FIGURE 2.21 -- Polar intensity plot for an 18" pipe.  
 (L = 18", D = 1", R = 12")



FIGURE 3.1

Photo of the experimental apparatus used to study the turbulent excitation of transverse modes in ducts.

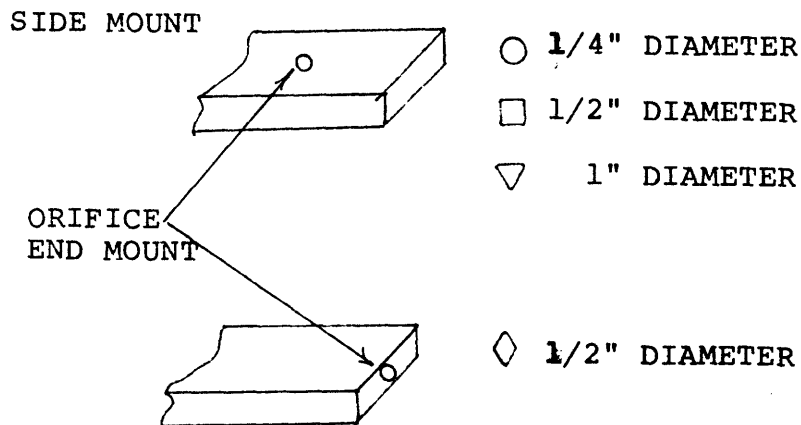
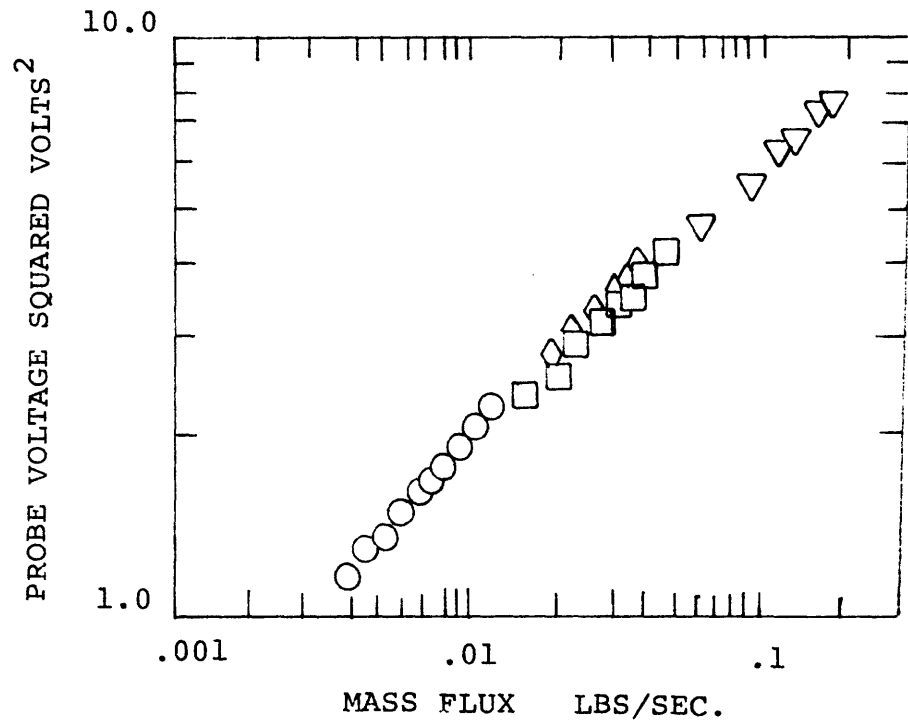


FIGURE 3.2 -- Hot wire velocity calibration. The mass flux is calculated from the pressure drop across the orifice assuming there is isentropic flow. This is compared to the mass flux in the duct measured with the hot wire. Note the coincidence of standard end mount data points with measurements for side mounted orifices. This shows that the jet velocity can be calculated from the pressure drop across the orifice (Eq. 4.1).

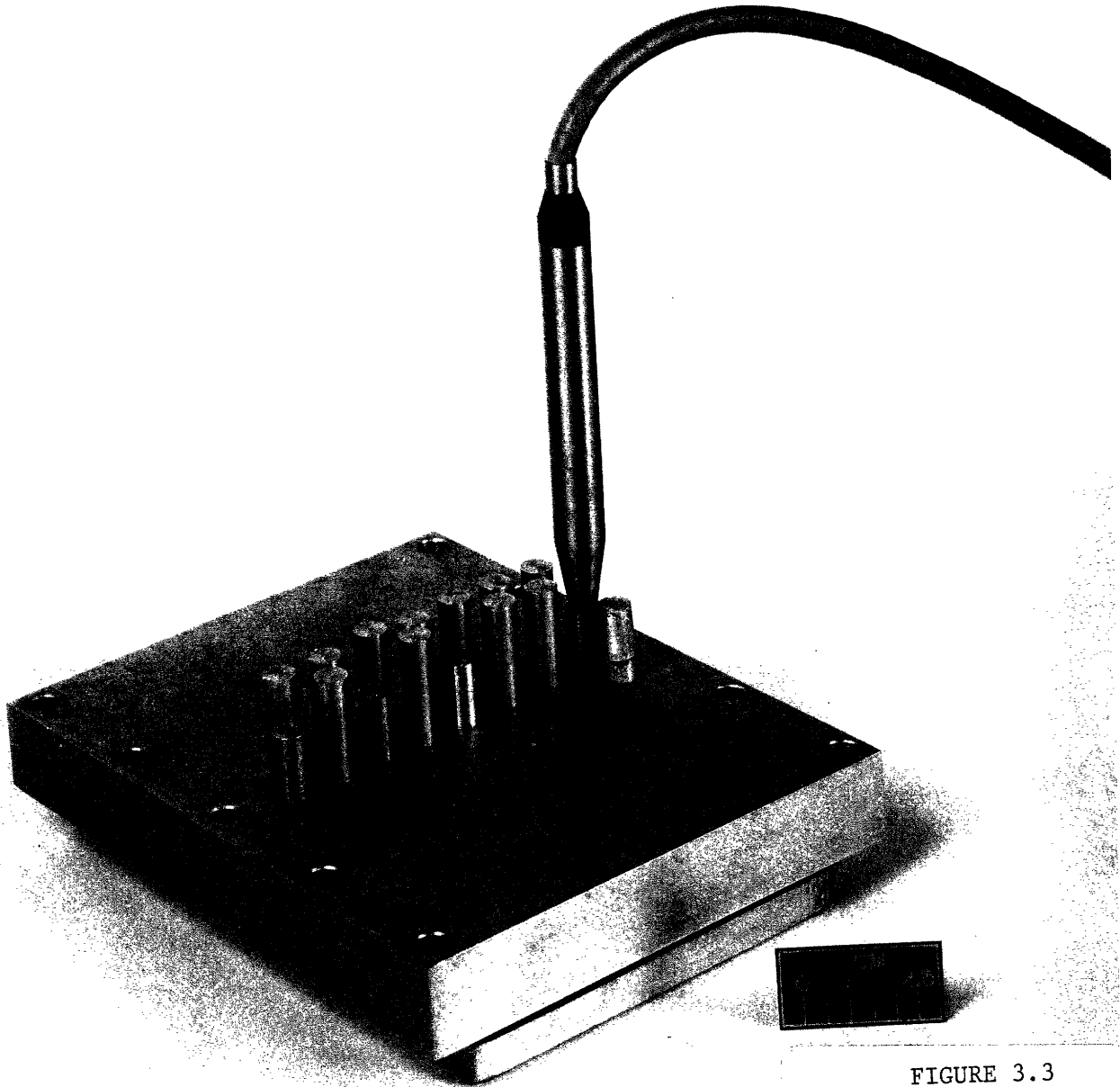


FIGURE 3.3  
Photo of the micro-  
phone holder used to  
detect the mode shape  
of the radiated  
sound.



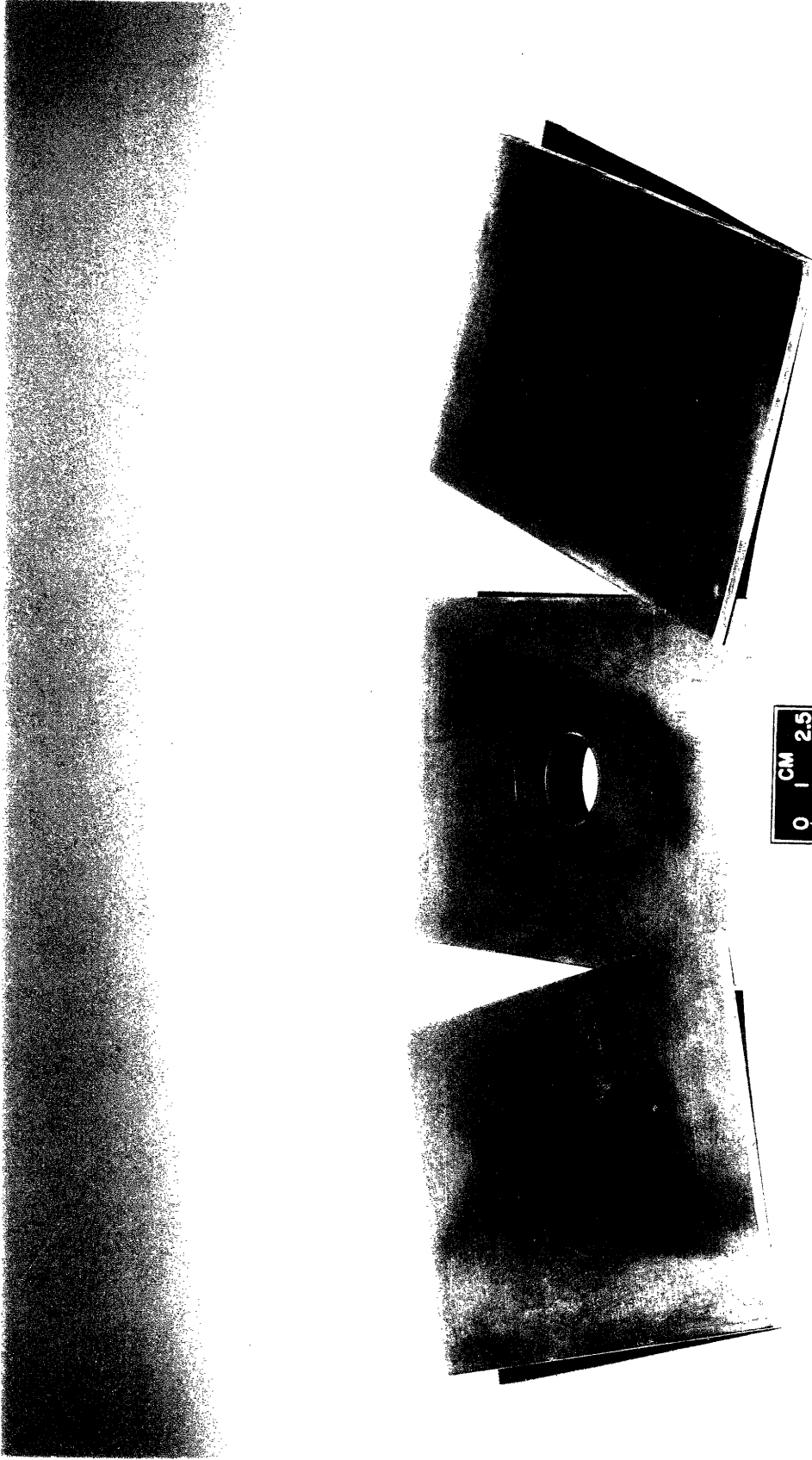


FIGURE 3.4

Photo of orifice plates used to form air jets ( $1/4''$ ,  $1/2''$ , and  $1''$  diameters).

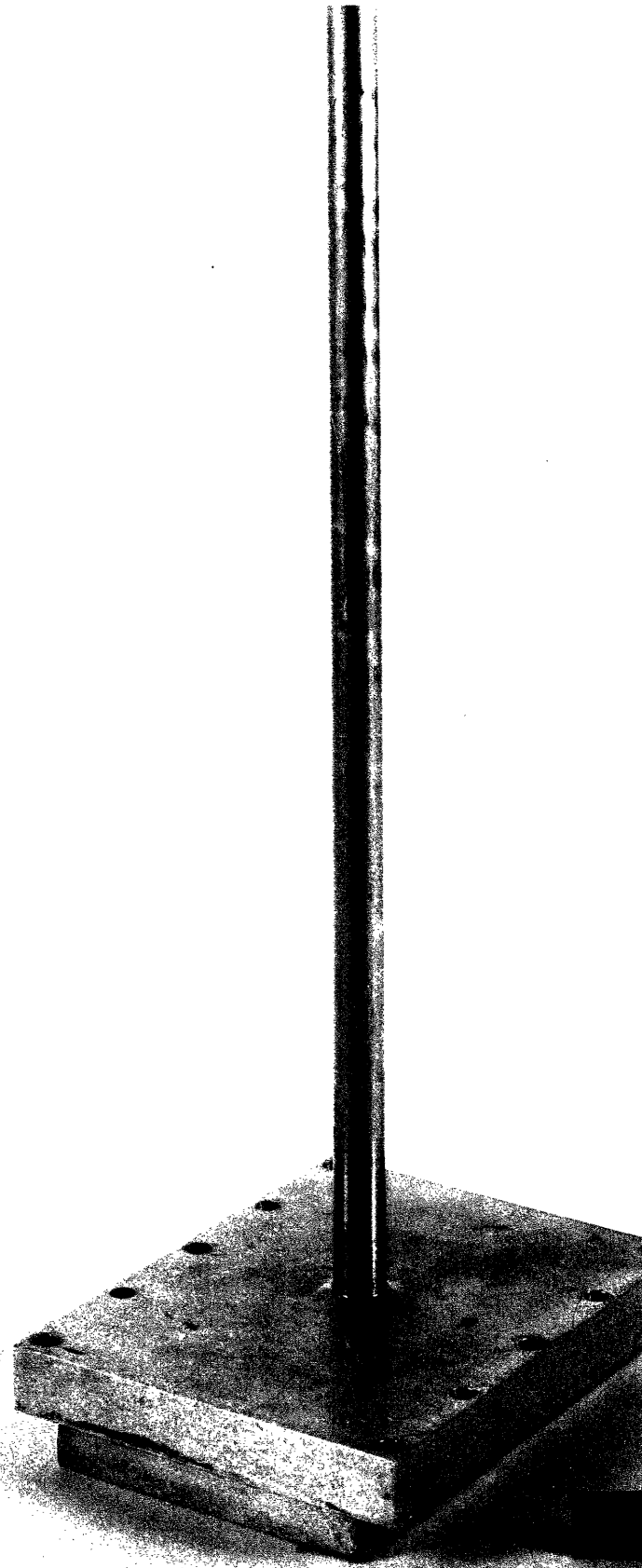
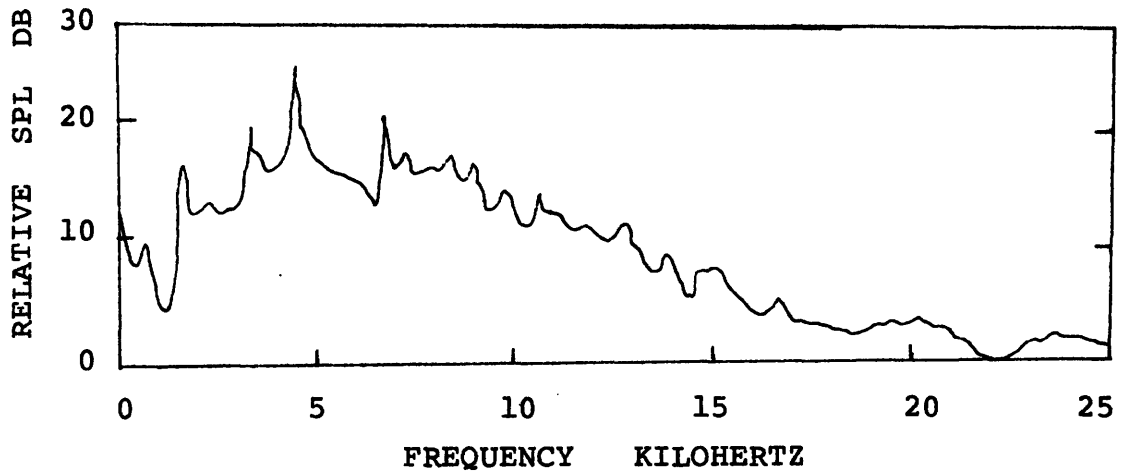
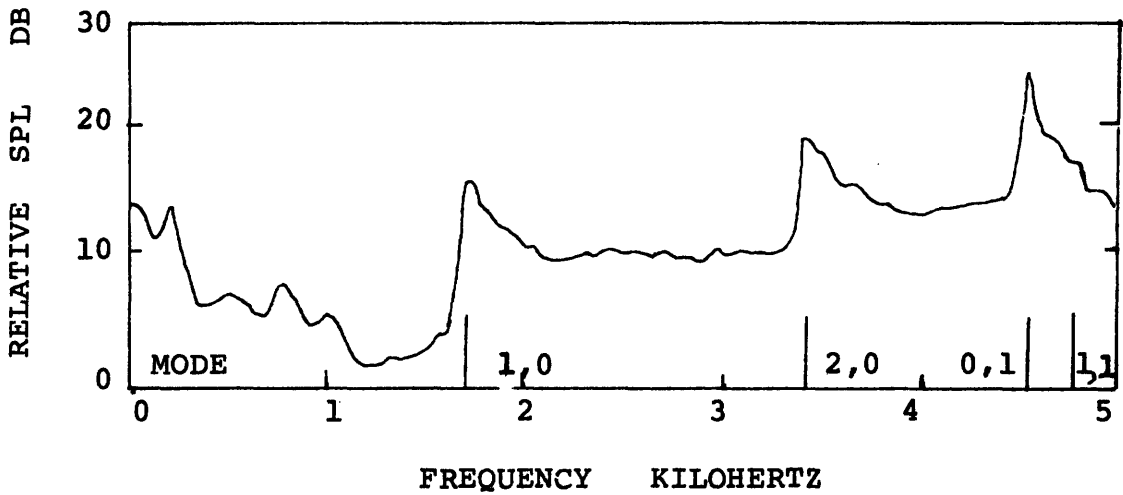


FIGURE 3.5  
Photo of 60" pipe  
with 1/2" inside  
diameter used to  
form air jet.



In the high frequency range the smooth duct spectra resembles the free space jet spectra.



In the low frequency range asymmetric peaks at the cutoff frequencies are evident.

FIGURE 3.6 -- Comparison of low and high frequency spectra in a rectangular duct. The air jet generating the sound is from a 1/2" orifice mounted on the 4" side of a 1-1/2" by 4" duct. The flow speed in the jet is Mach .44.

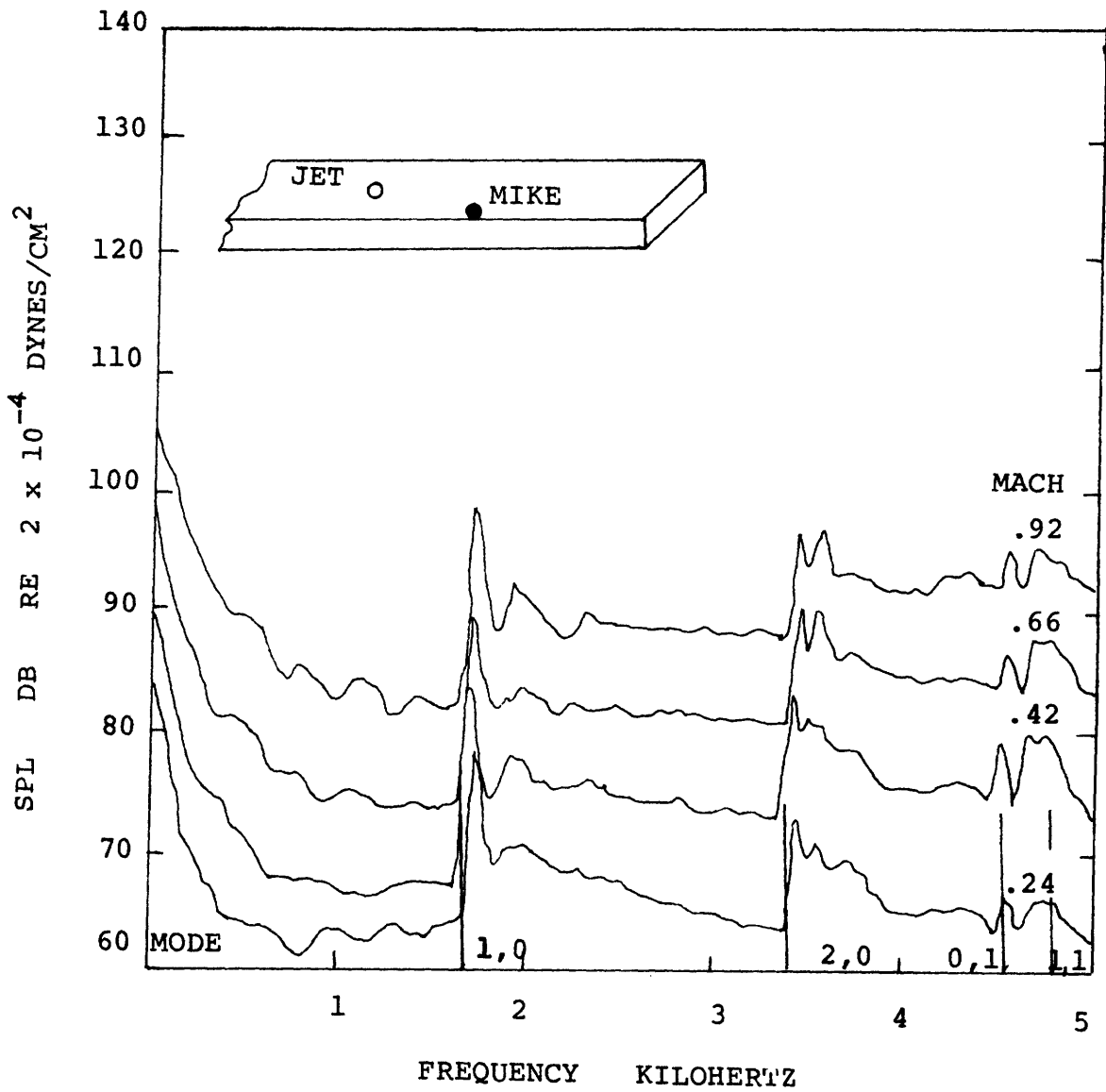


FIGURE 3.7 -- Low frequency spectra using a 1/4" diameter orifice.

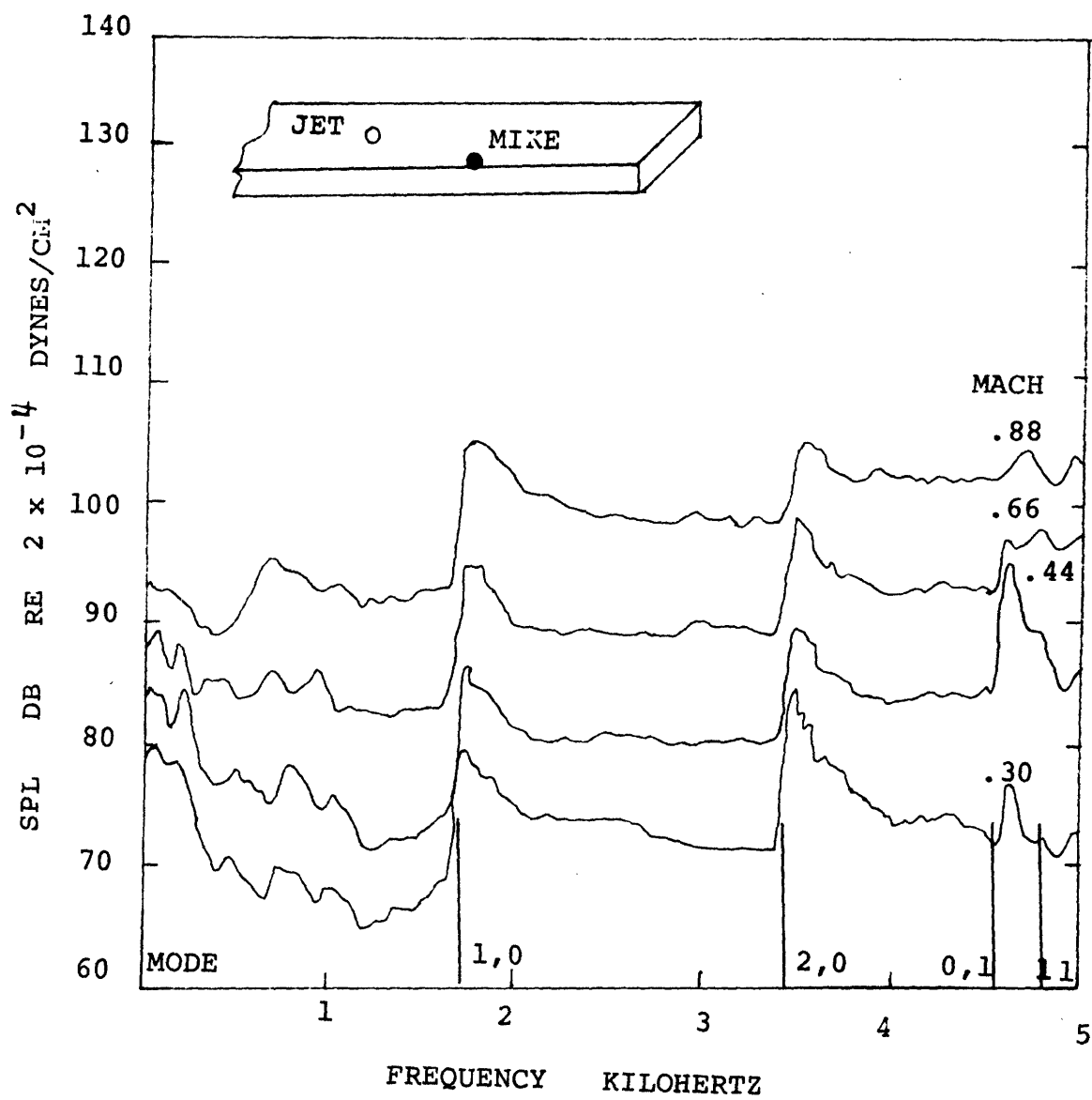


FIGURE 3.8 -- Low frequency spectra using a 1/2" diameter orifice plate.

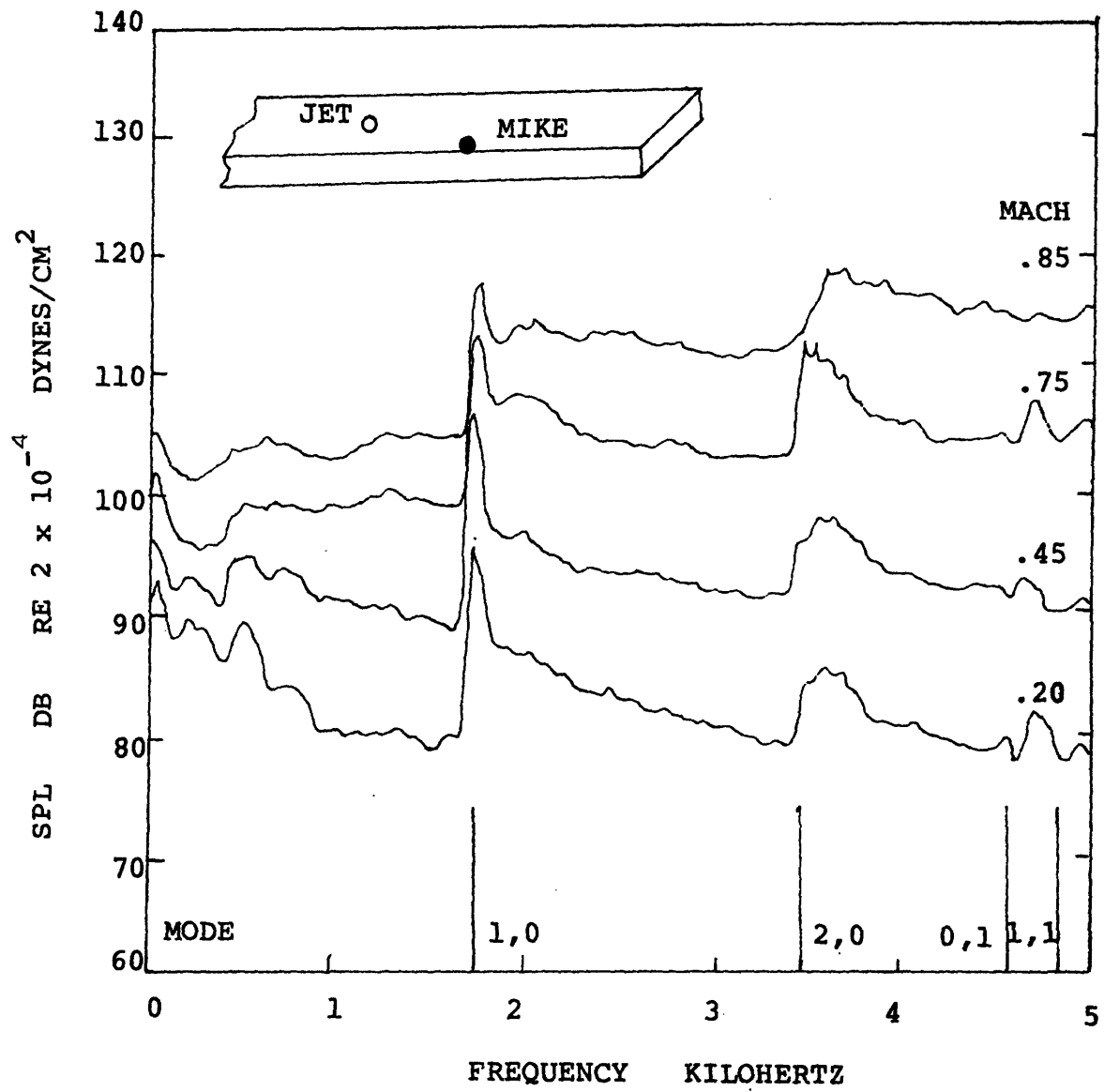
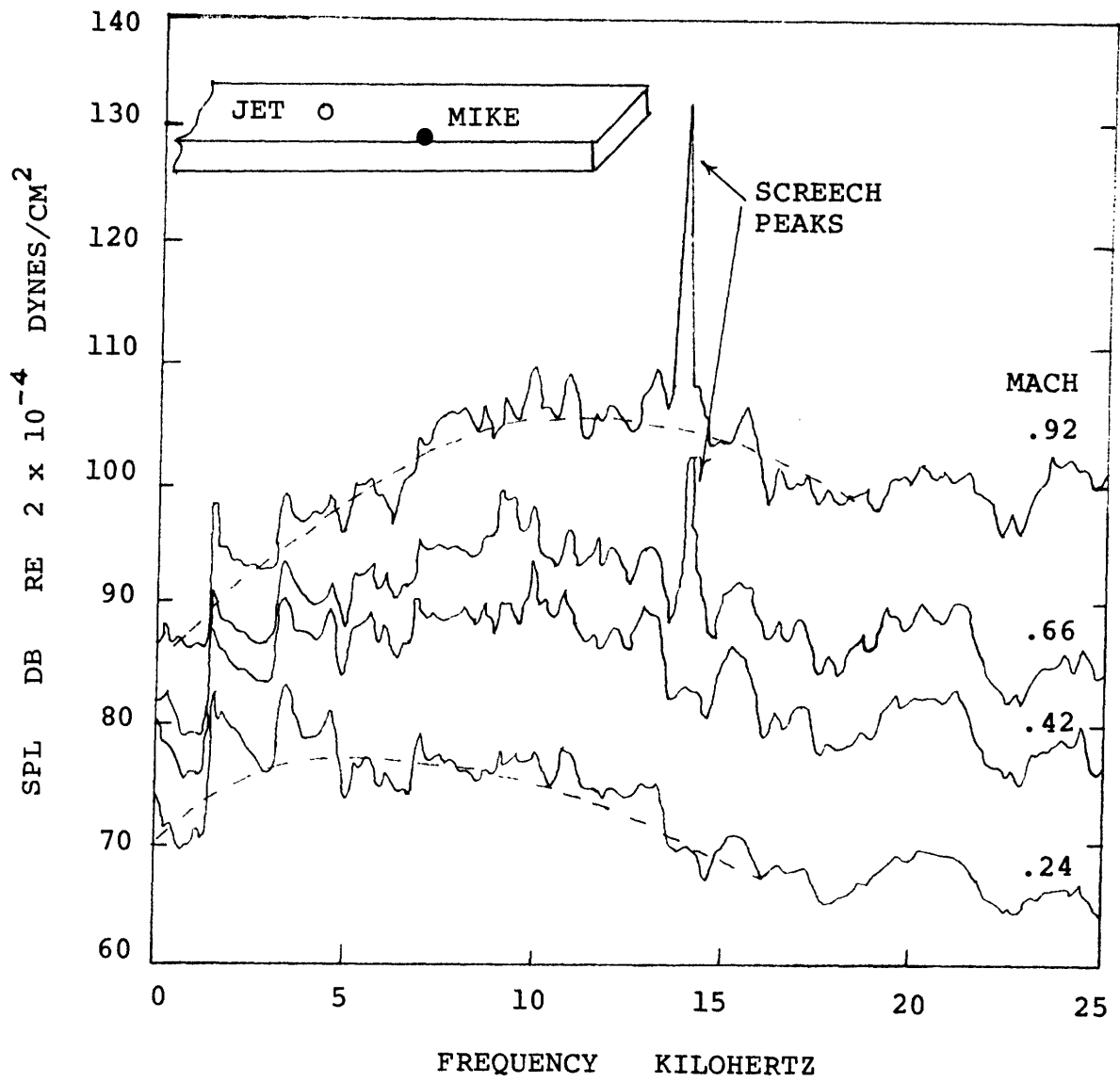


FIGURE 3.9 -- Low frequency spectra using a 1" diameter orifice plate.



FIGUER 3.10 -- High frequency spectra using a 1/4" diameter orifice plate.

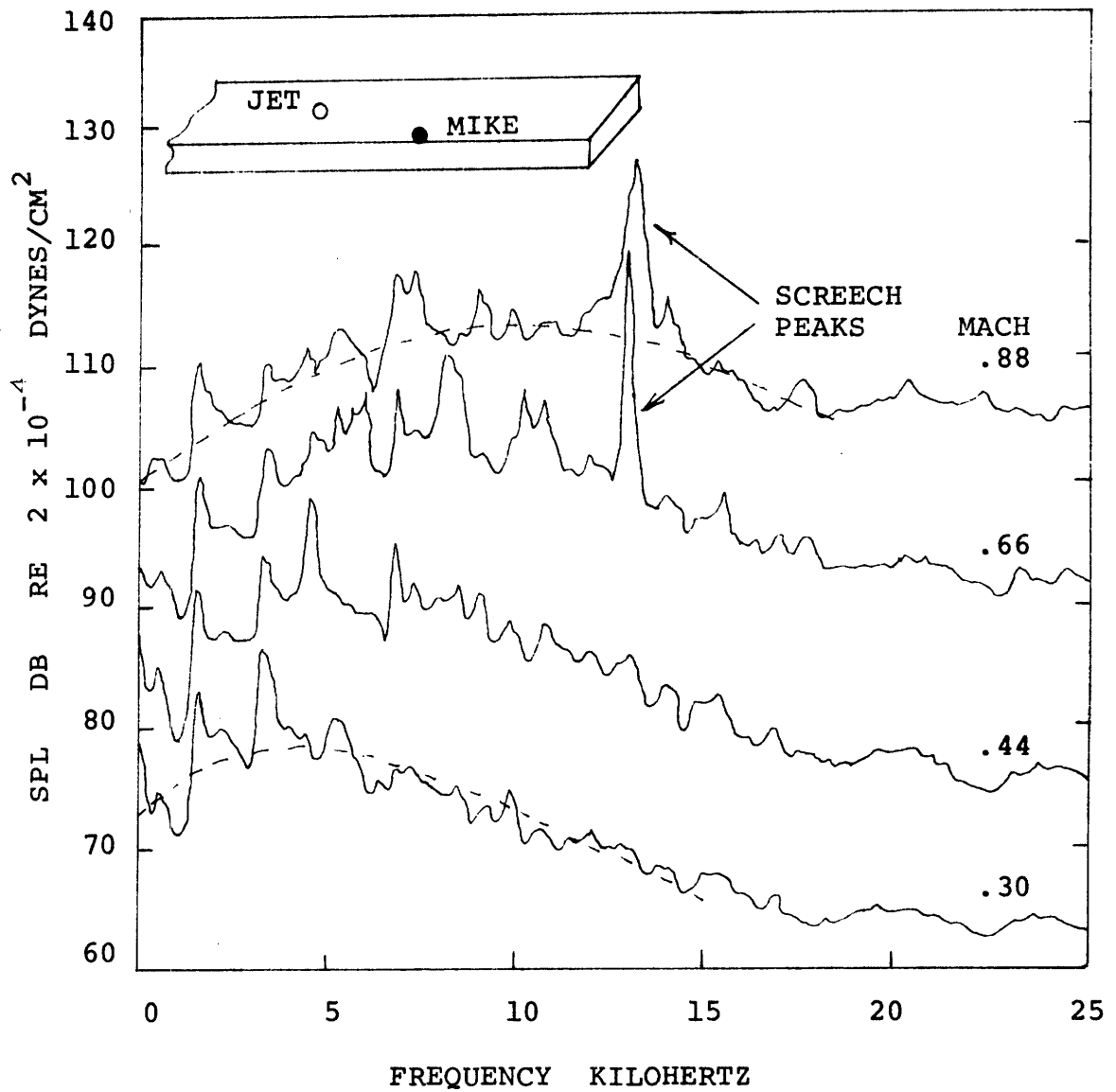


FIGURE 3.11 -- High frequency spectra using a 1/2" diameter orifice plate.



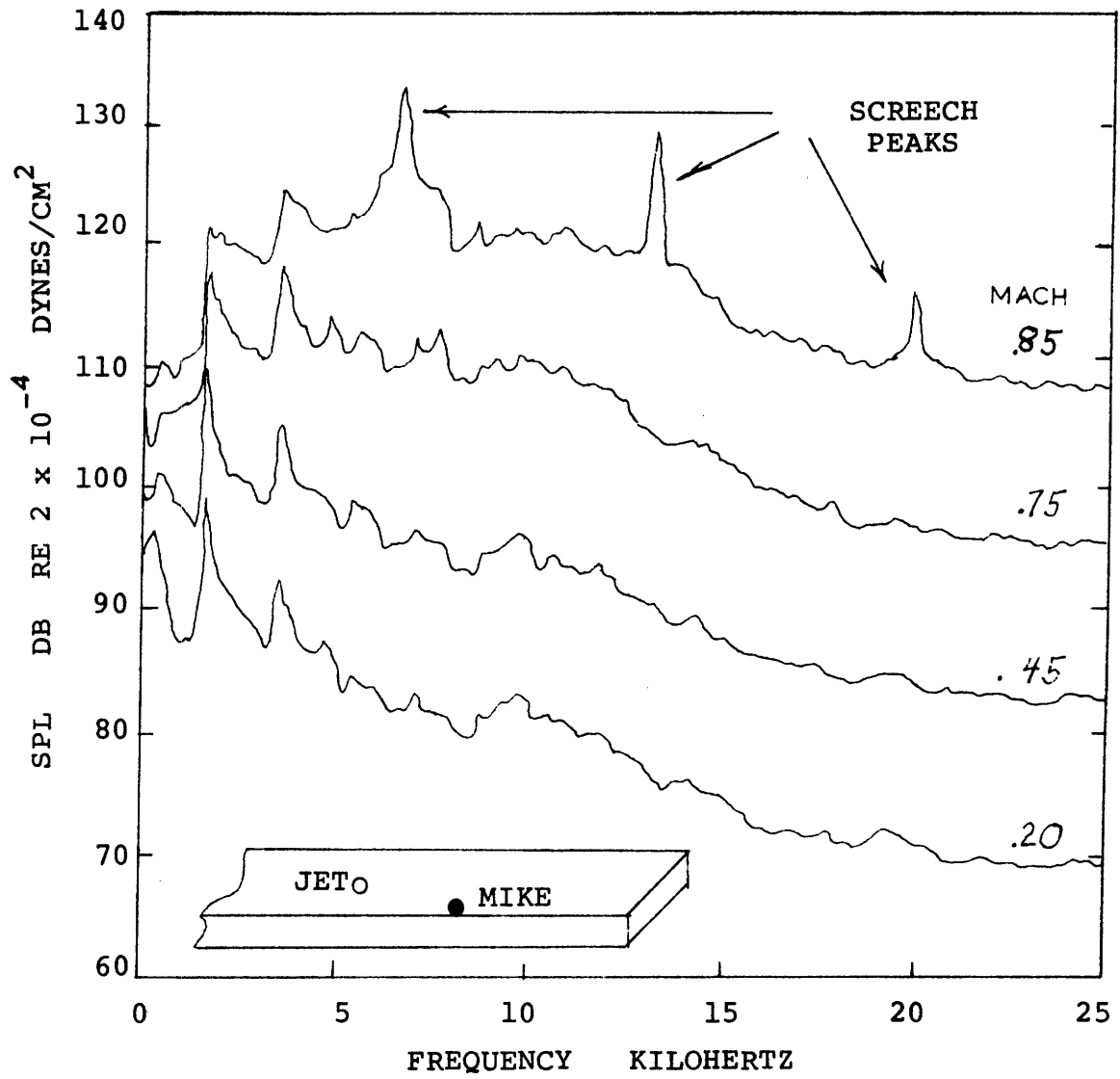


FIGURE 3.12 -- High frequency spectra using a 1" diameter orifice plate.

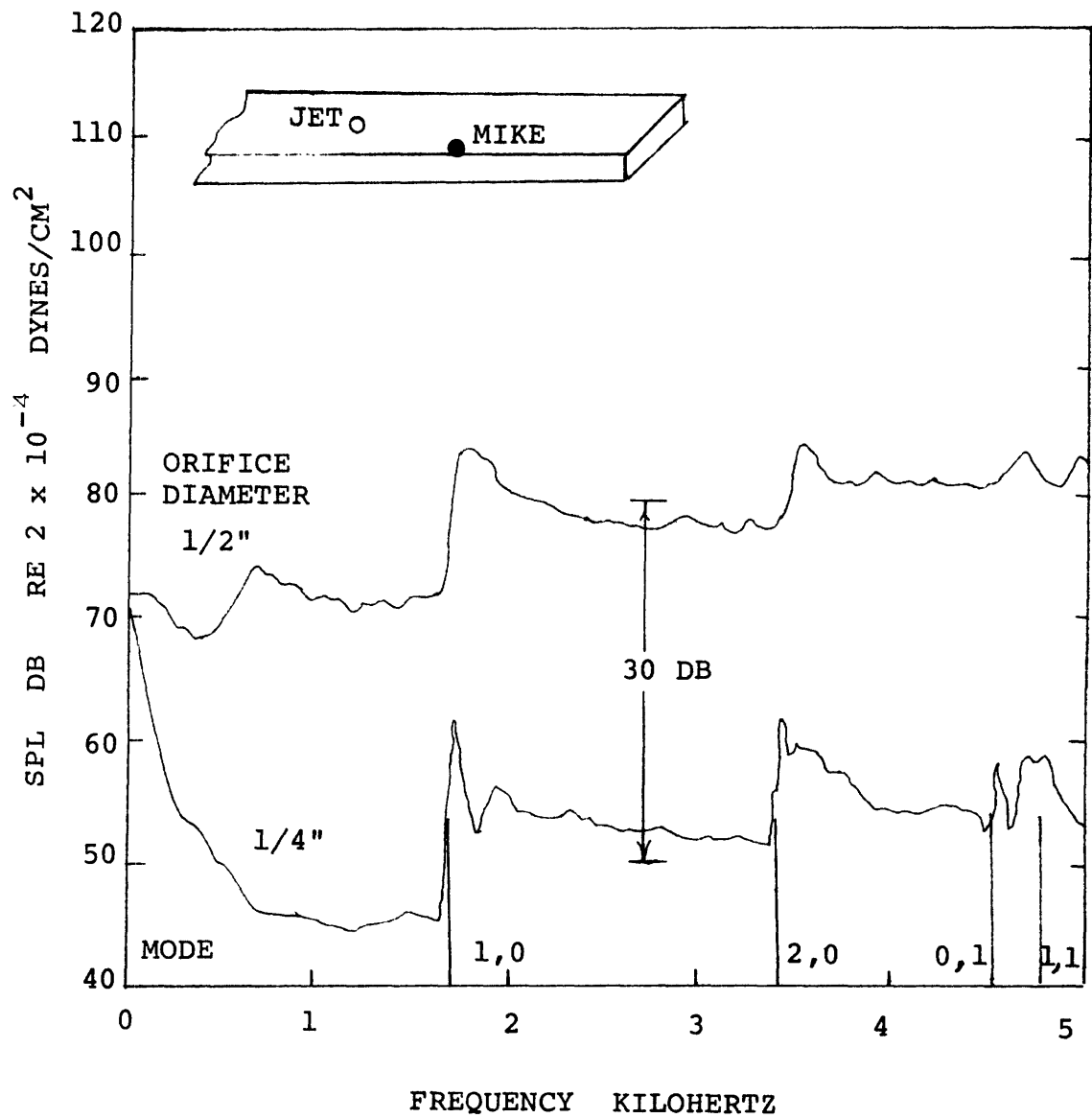


FIGURE 3.13 -- Reduction of low frequency spectra by Strouhal frequency. Here

$$f_s = .2 \frac{V}{D} \approx 5.7 \text{ kHz.}$$

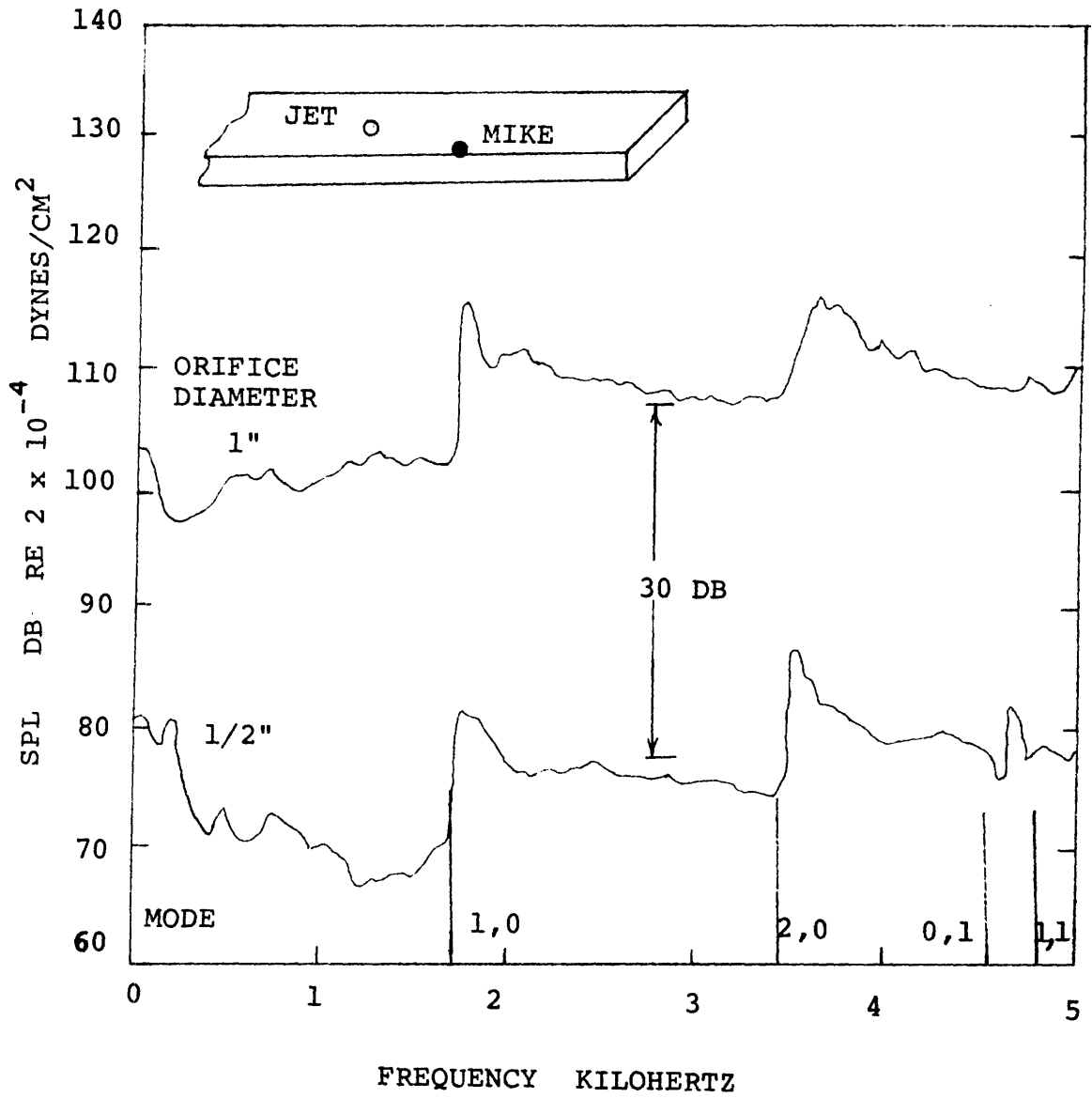


FIGURE 3.14 -- Reduction of low frequency spectra by Strouhal frequency. Here  $f_s = .2 \frac{V}{D} \approx 2.5$  kHz.

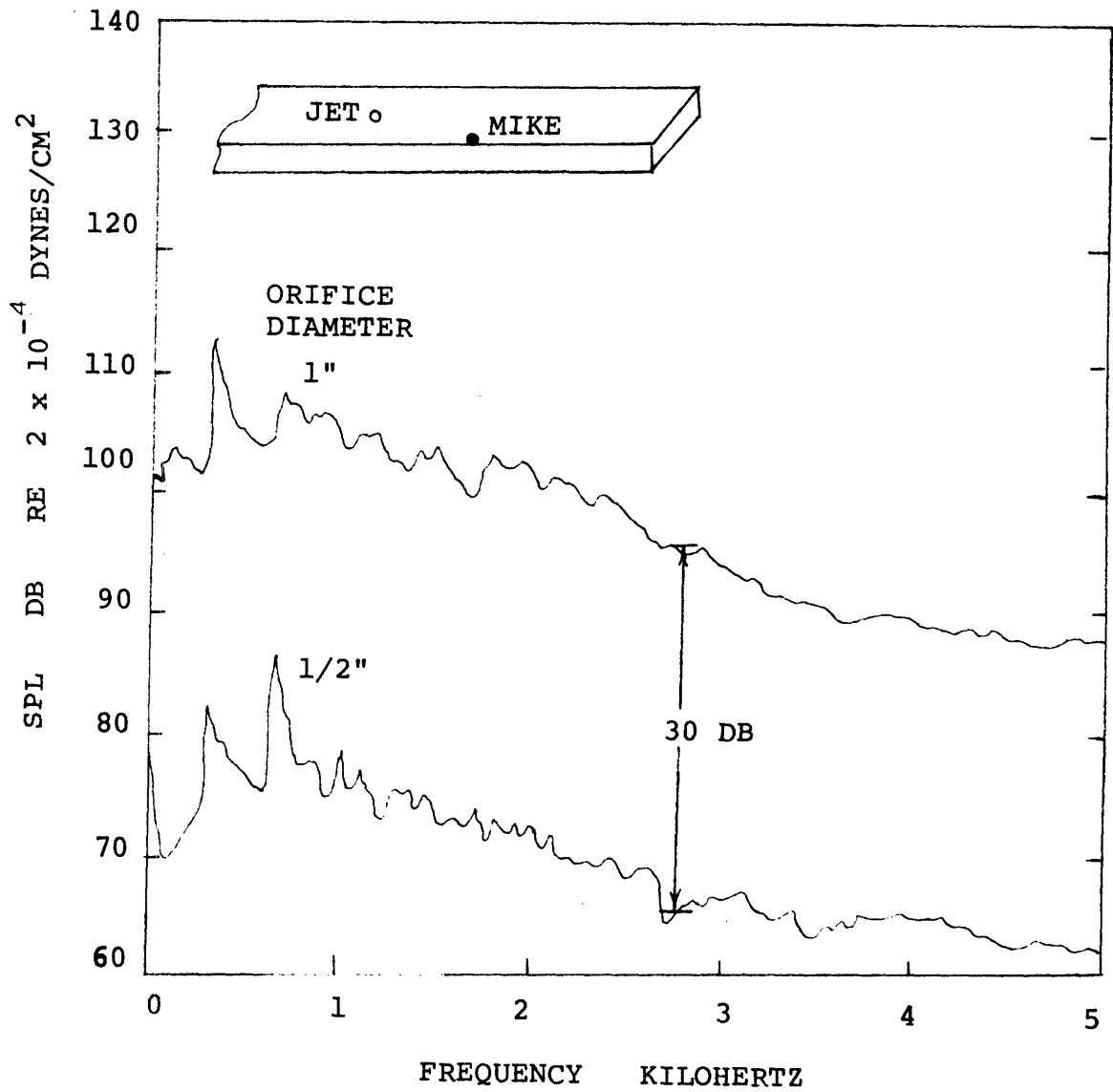


FIGURE 3.15 -- Reduction of high frequency spectra by Strouhl frequency. Here  $f_s = .2 \frac{V}{D} \approx 1.9 \text{ kHz}$ .

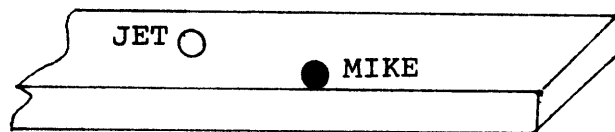
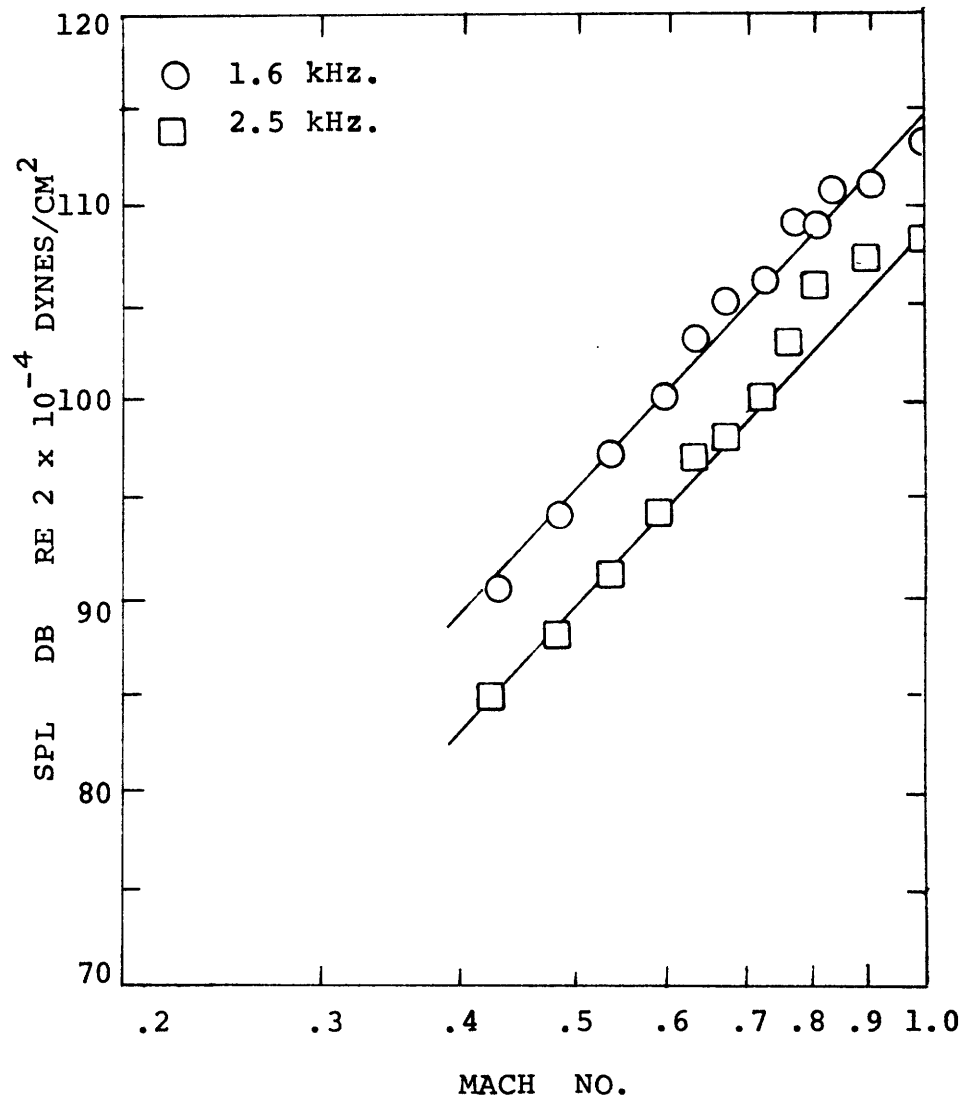


FIGURE 3.16 -- Sound level versus mean flow for a 1/2" diameter orifice plate. Levels at first cutoff frequency (1.6 kHz) are compared to those at a frequency between the first and second cutoff (2.5 kHz).

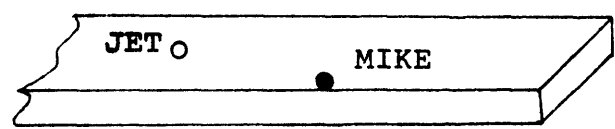
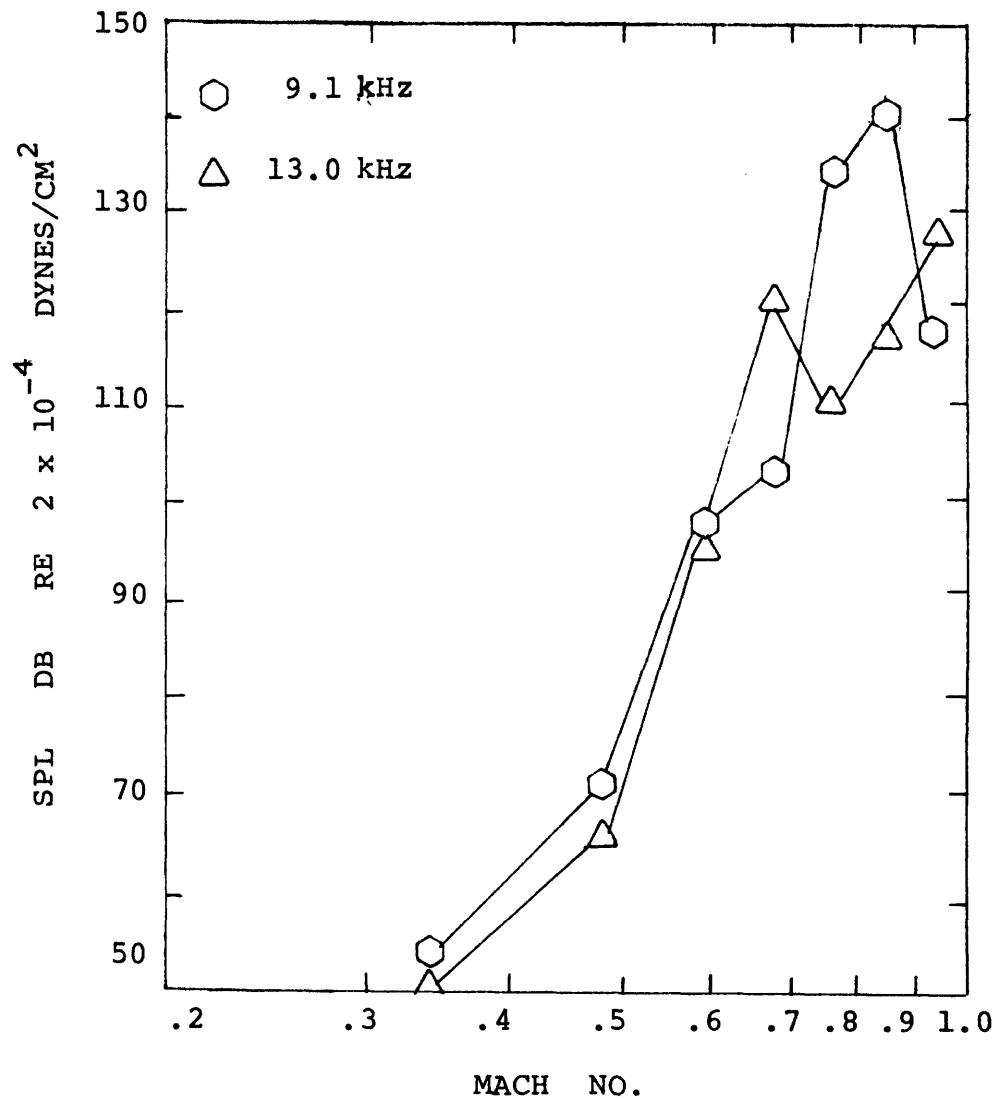


FIGURE 3.17 -- Sound level versus mean flow for a 1/2" diameter orifice plate. Two frequencies at which screech occurs are shown.

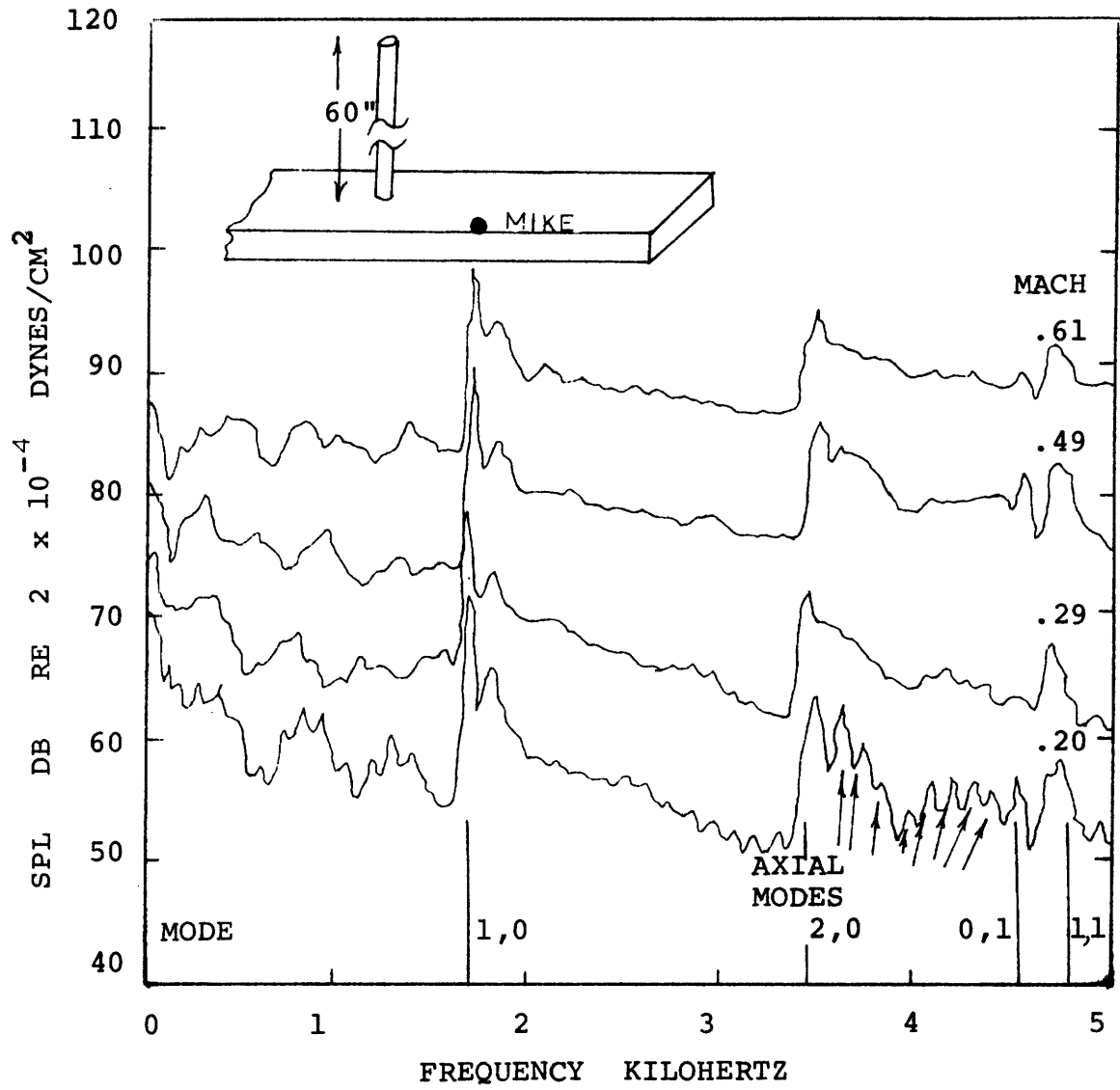


FIGURE 3.18 -- Low frequency spectra from an initially turbulent jet. The jet is from a 60" pipe of 1/2" inside diameter.

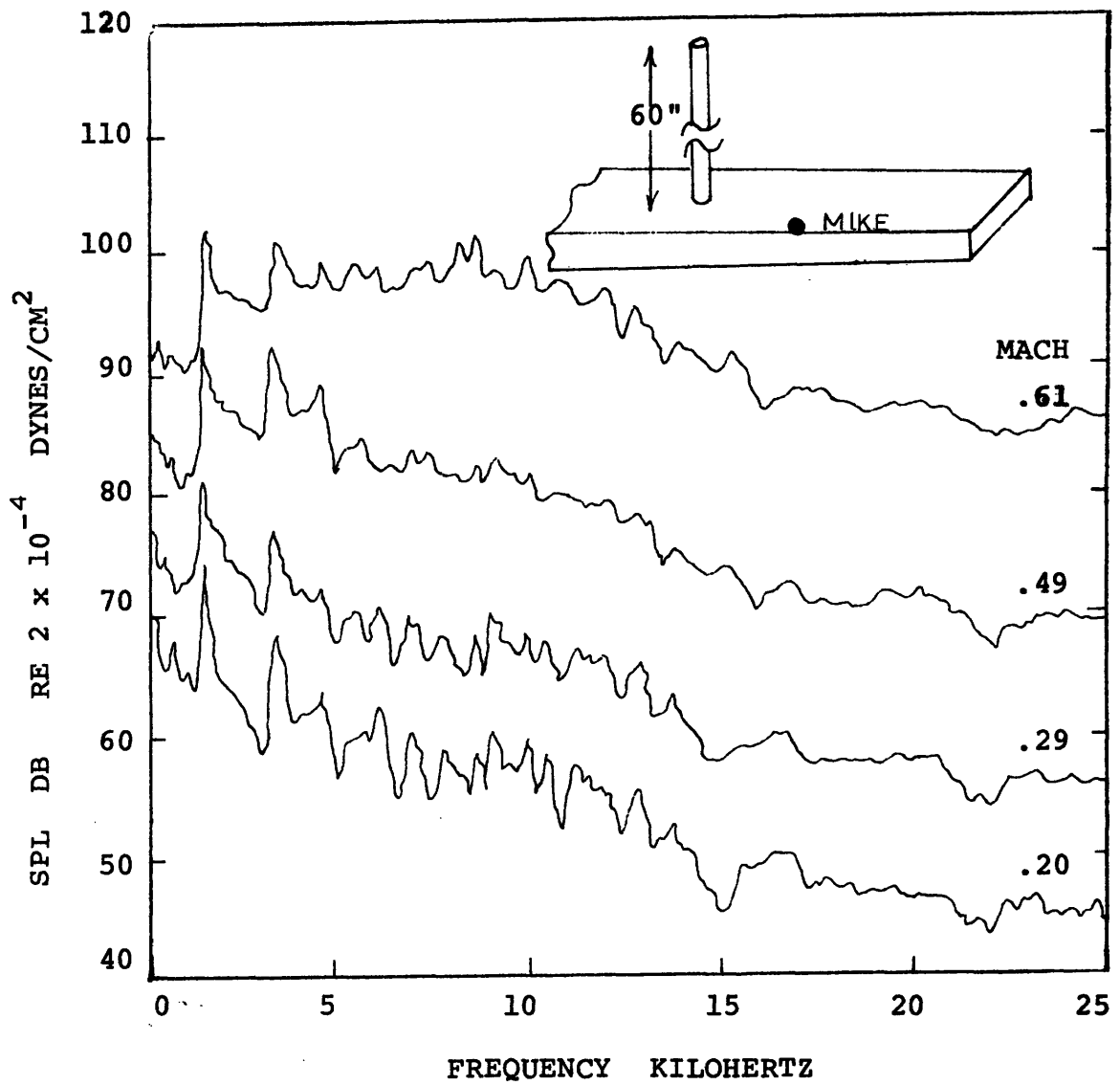


FIGURE 3.19 -- High frequency spectra from an initially turbulent jet. The jet is from a 60" pipe of 1/2" inside diameter.



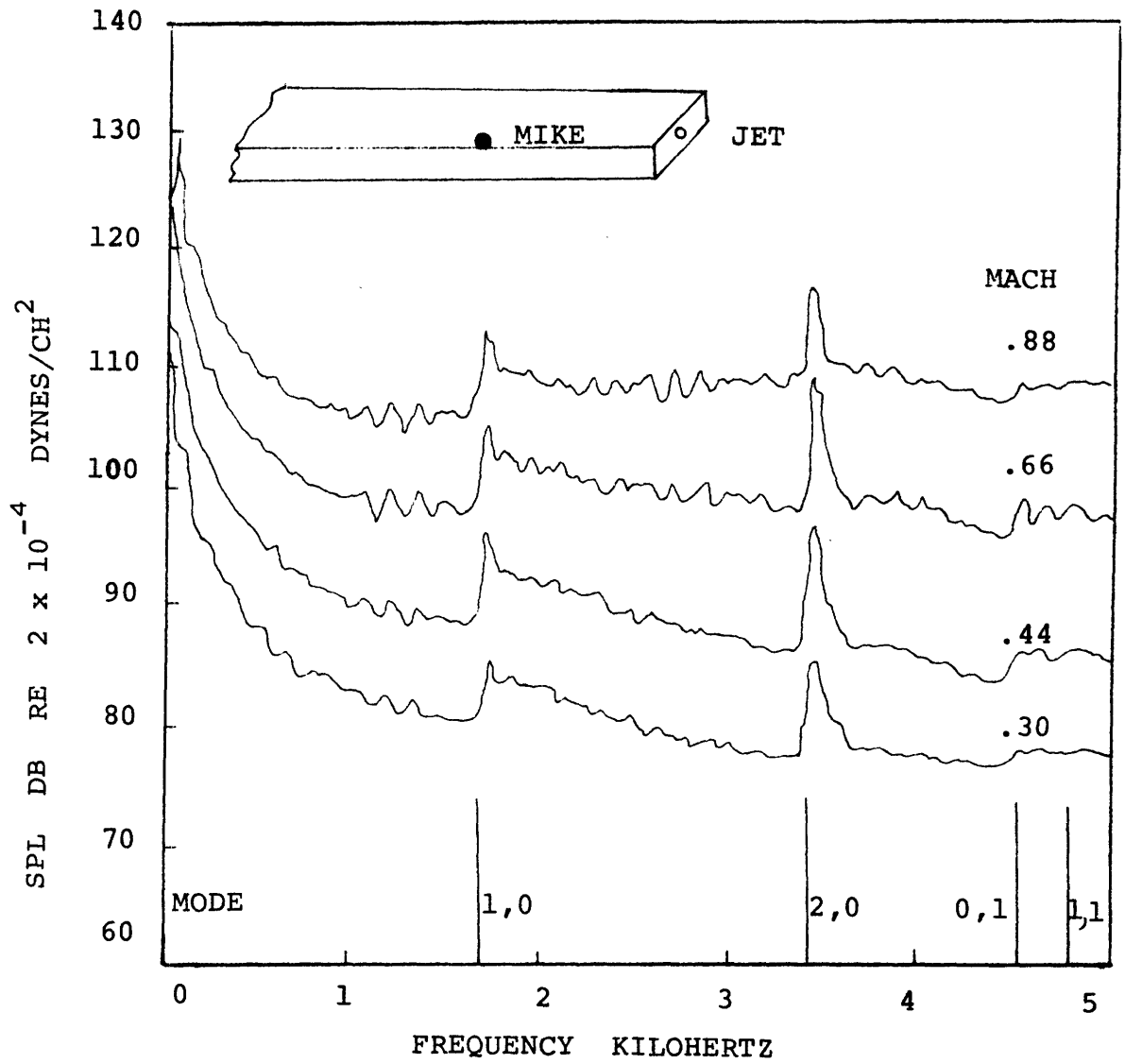


FIGURE 3.20 -- Low frequency spectra observed when jet and duct axis are parallel.

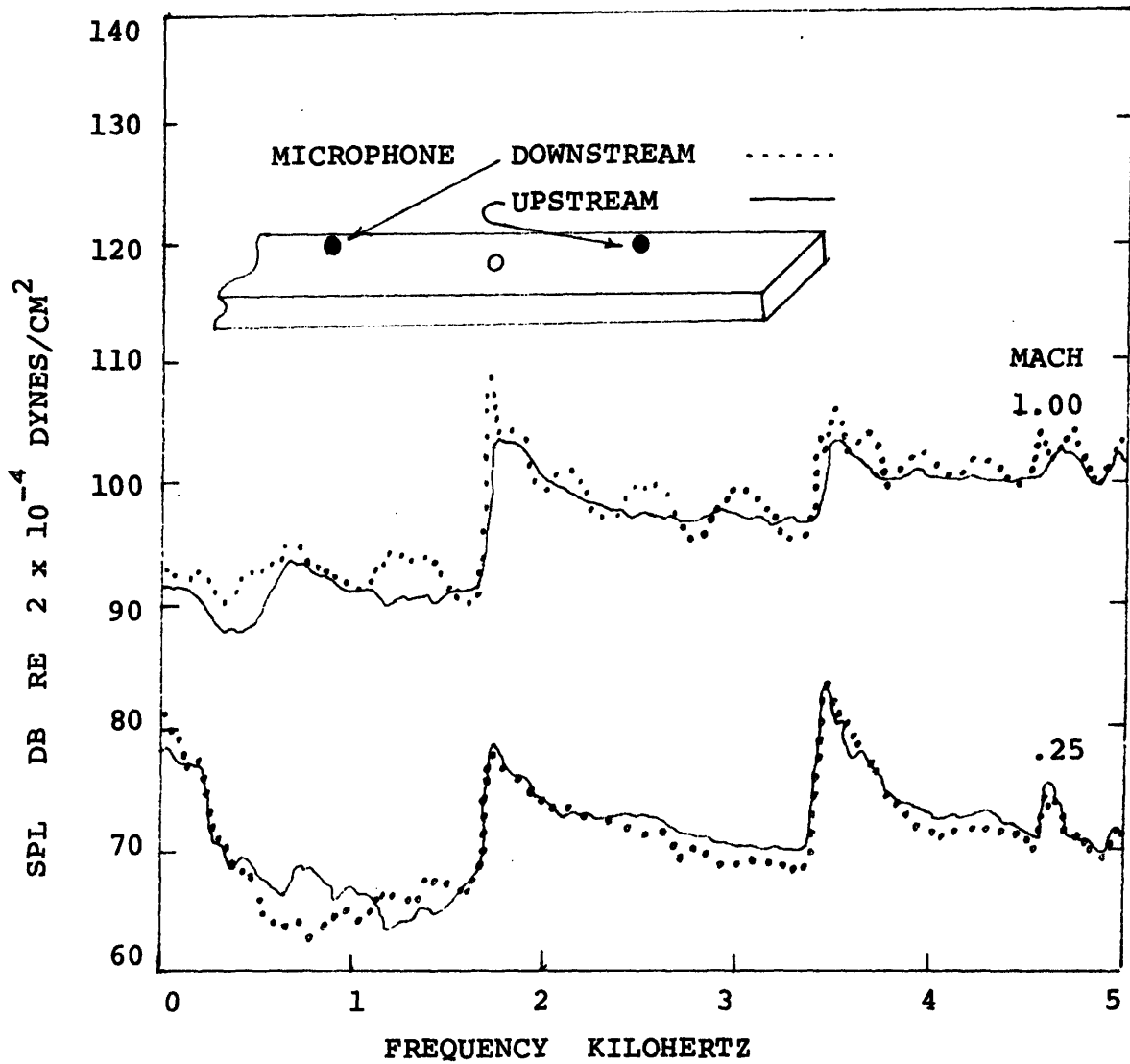


FIGURE 3.21 -- Comparison of upstream and downstream radiated acoustic spectra.

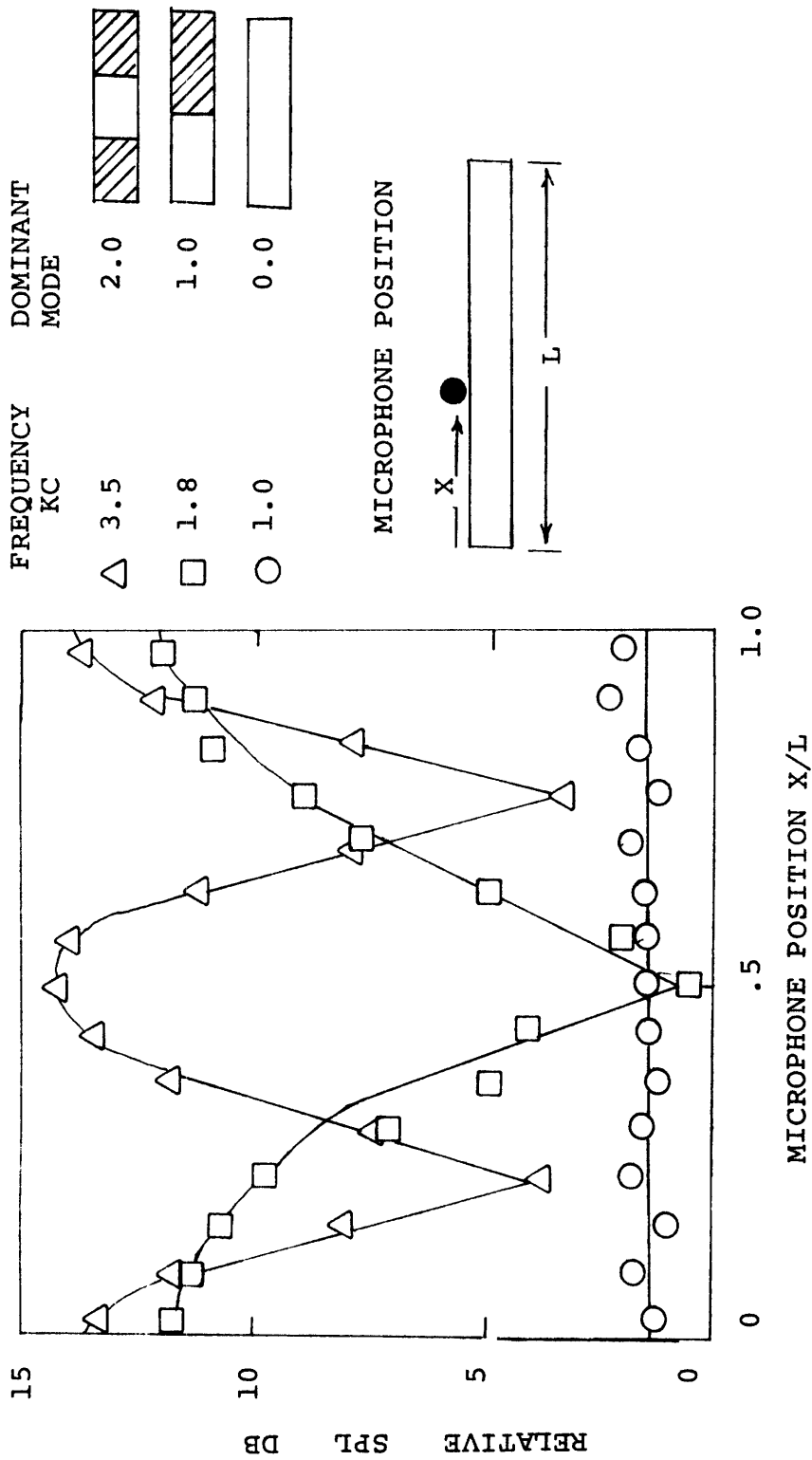


FIGURE 3.22 -- Transverse variation of radiated sound levels at frequencies selected to show the mode shape.

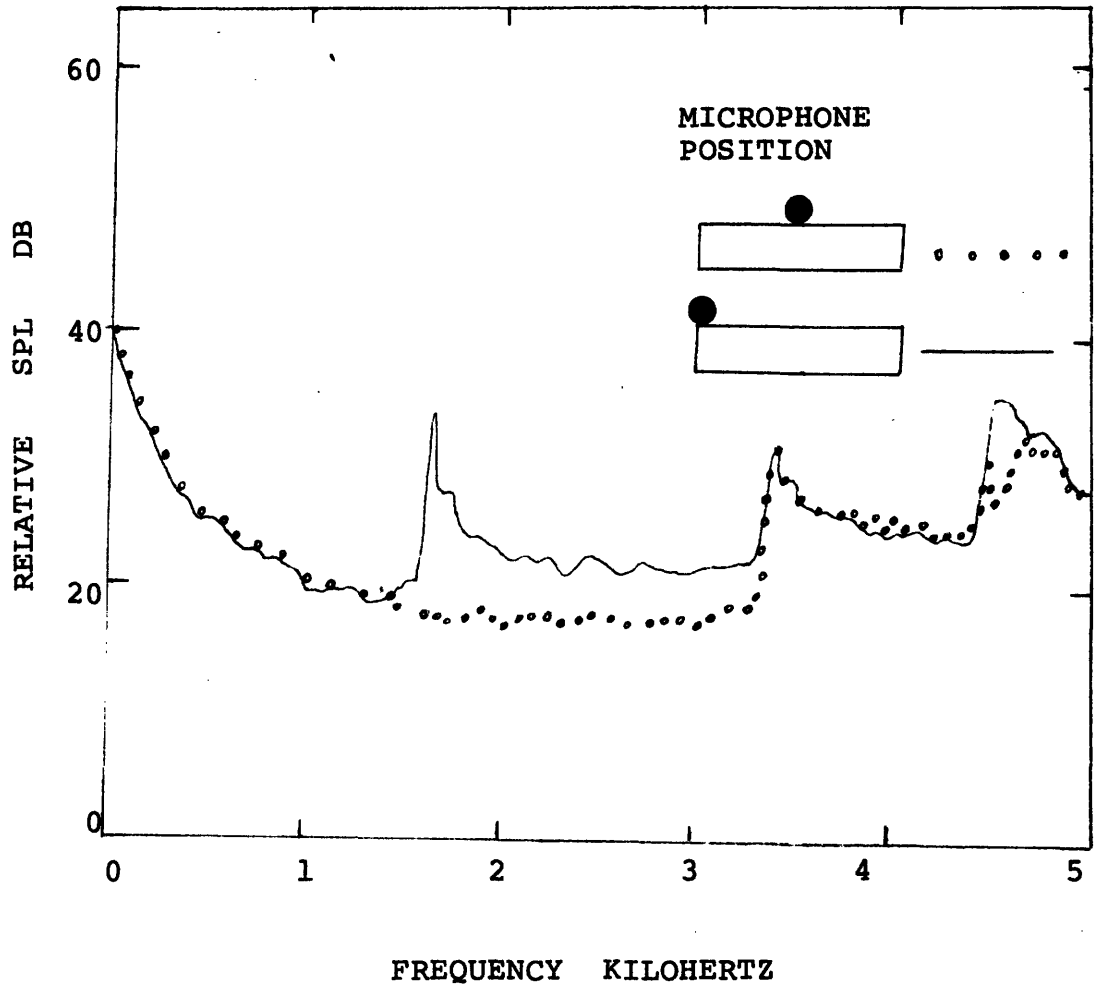


FIGURE 3.23 -- Influence of mode shape on detected spectra. At the duct center, the microphone does not detect sound radiated in the 1,0 mode.

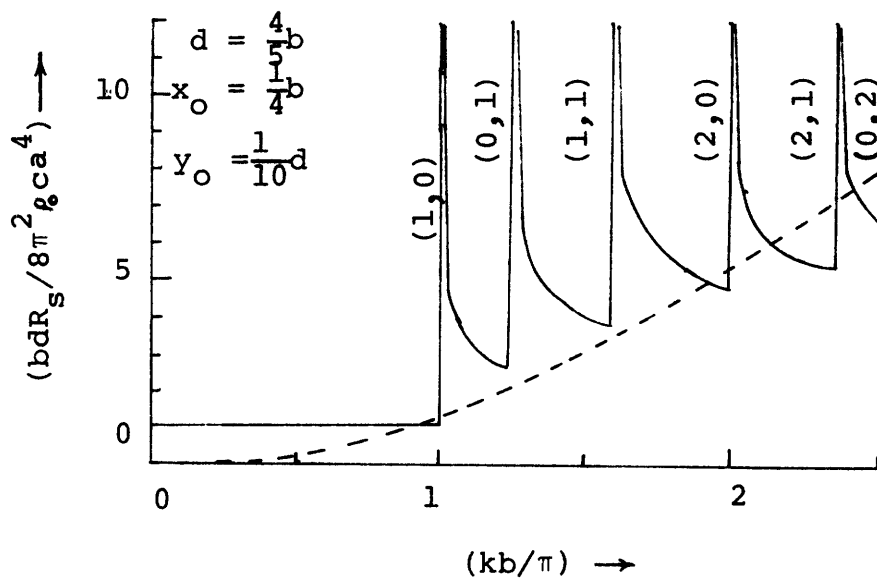


FIGURE 3.24 -- Radiation resistance  $R_s$  of a simple source of radius  $a$  at point  $x_0, y_0, 0$  in a rectangular duct of sides  $b, d$ . Numbers by each peak indicate the  $m, n$  of the mode resonating. Dashed curve is radiation resistance from same source in free space. (Ref. 14)

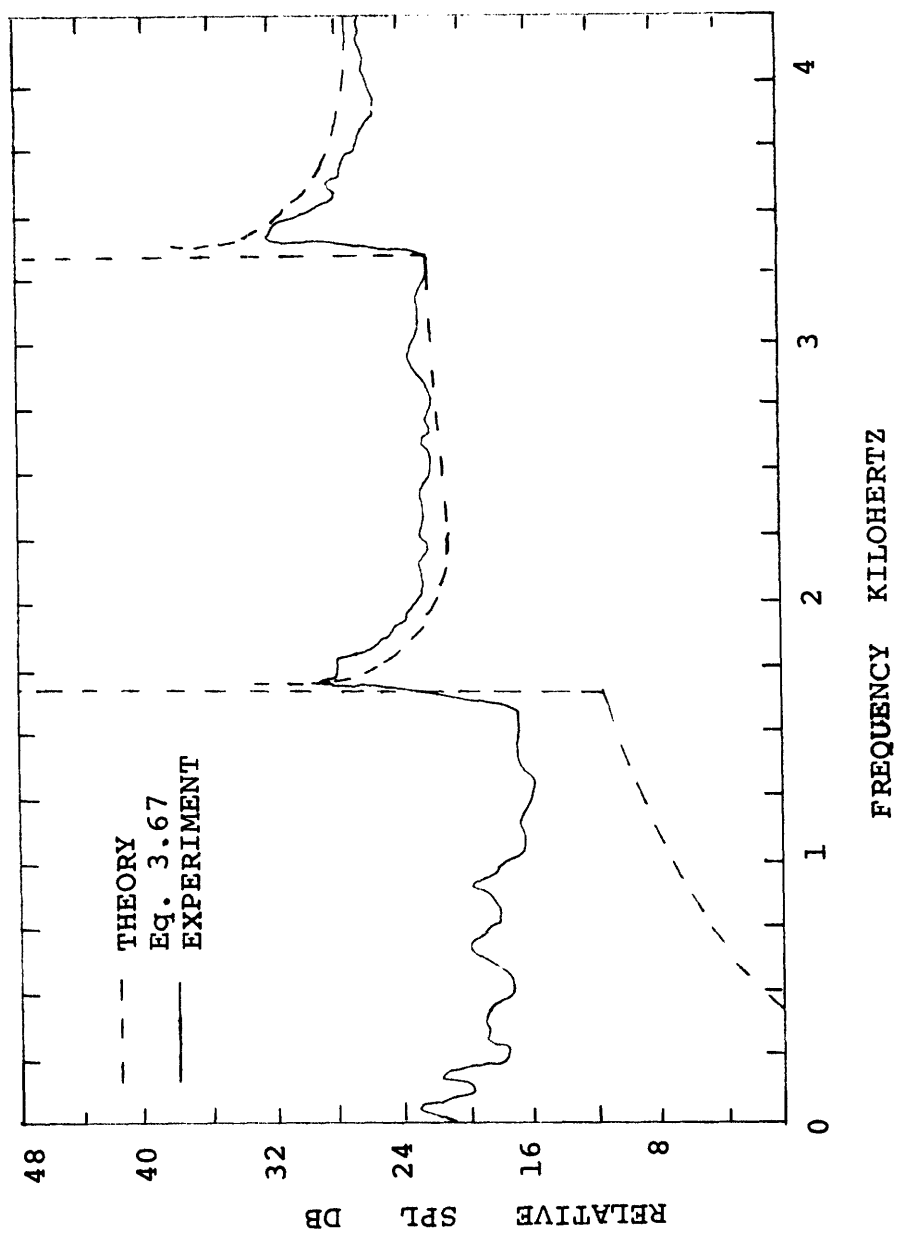


FIGURE 3.25 -- Comparison of theoretical and experimental spectra at Mach .6 for a 1/2" diameter orifice plate.

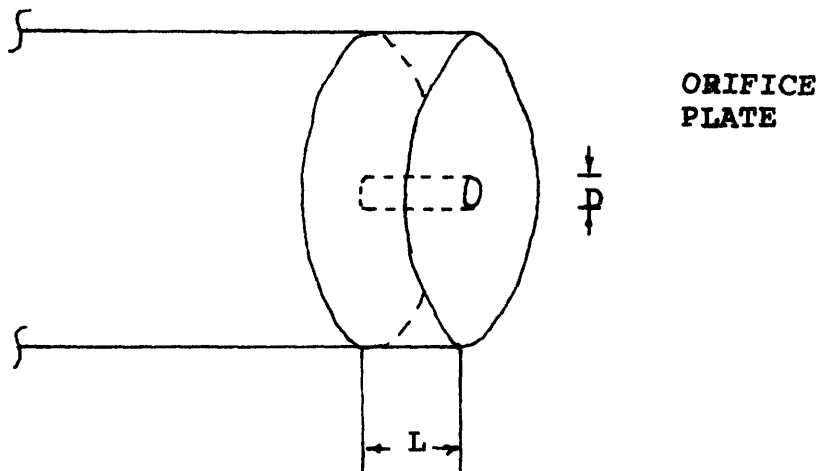
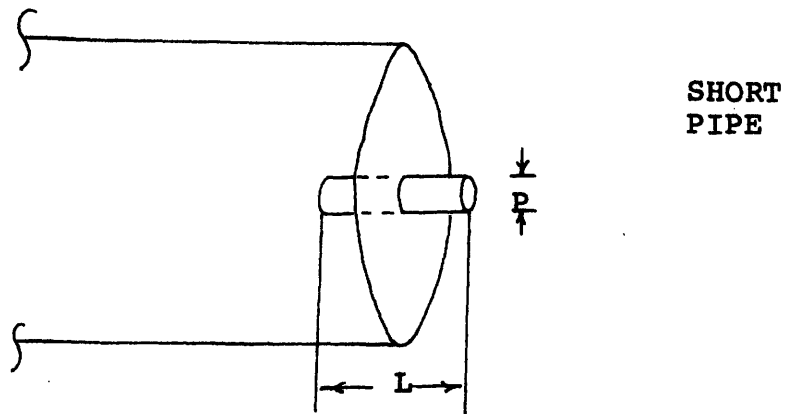


FIGURE 4.1 -- Experimental apparatus used to generate screech. For screech the length to diameter ratio must be less than two. In these experiments the orifice plate is used.

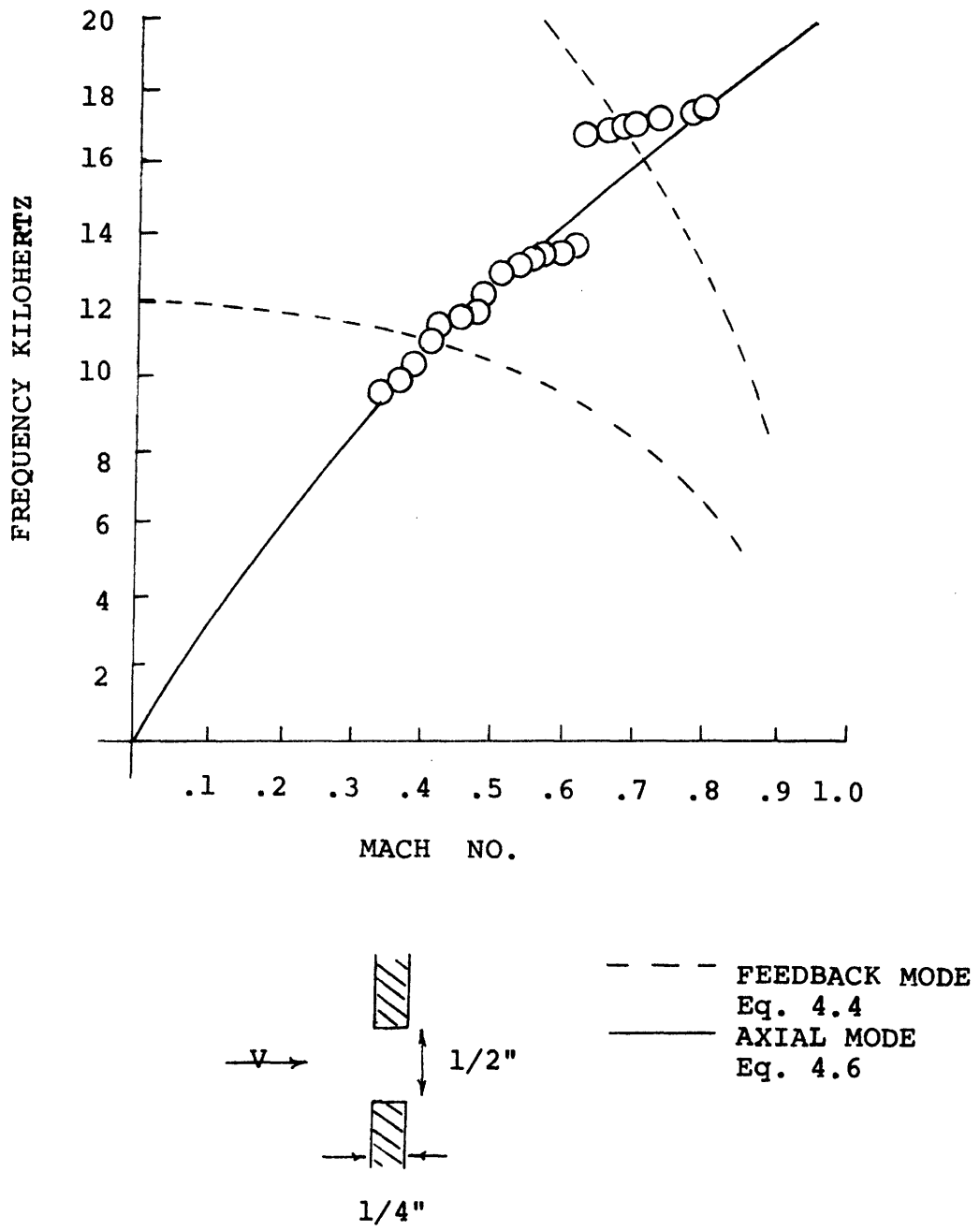


FIGURE 4.2 -- Screech frequency versus flow speed for a 1/4" long orifice plate.



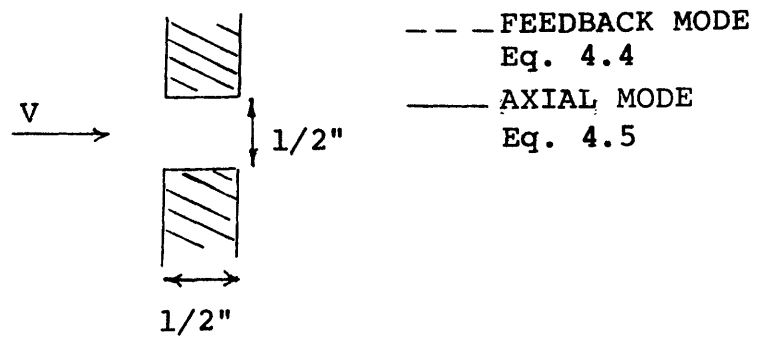
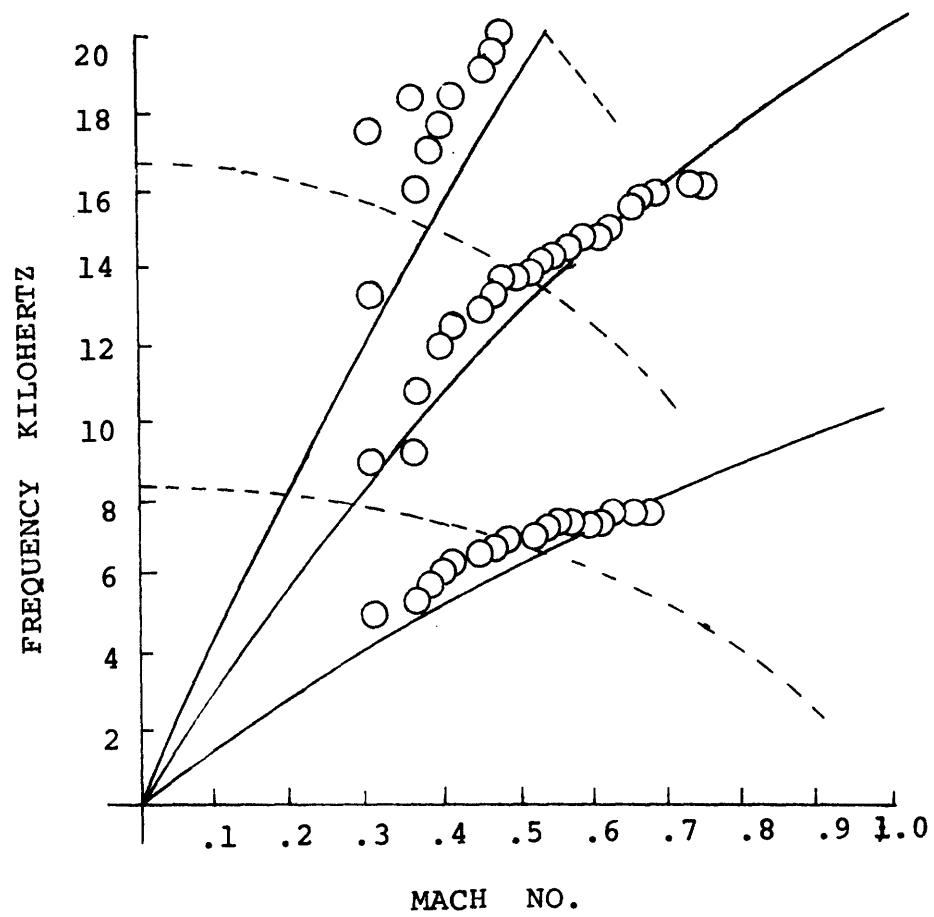


FIGURE 4.3 -- Screech frequency versus flow speed for a 1/2" long orifice plate.

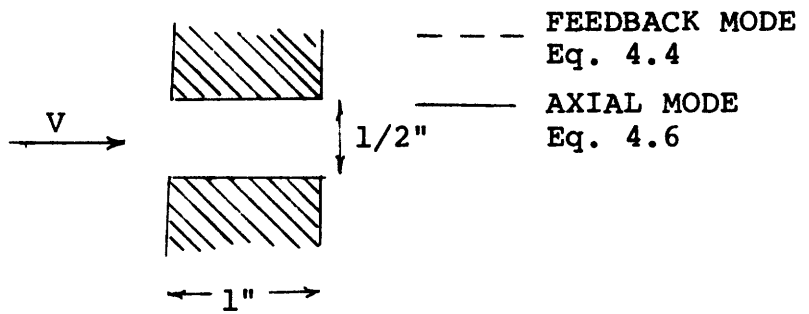
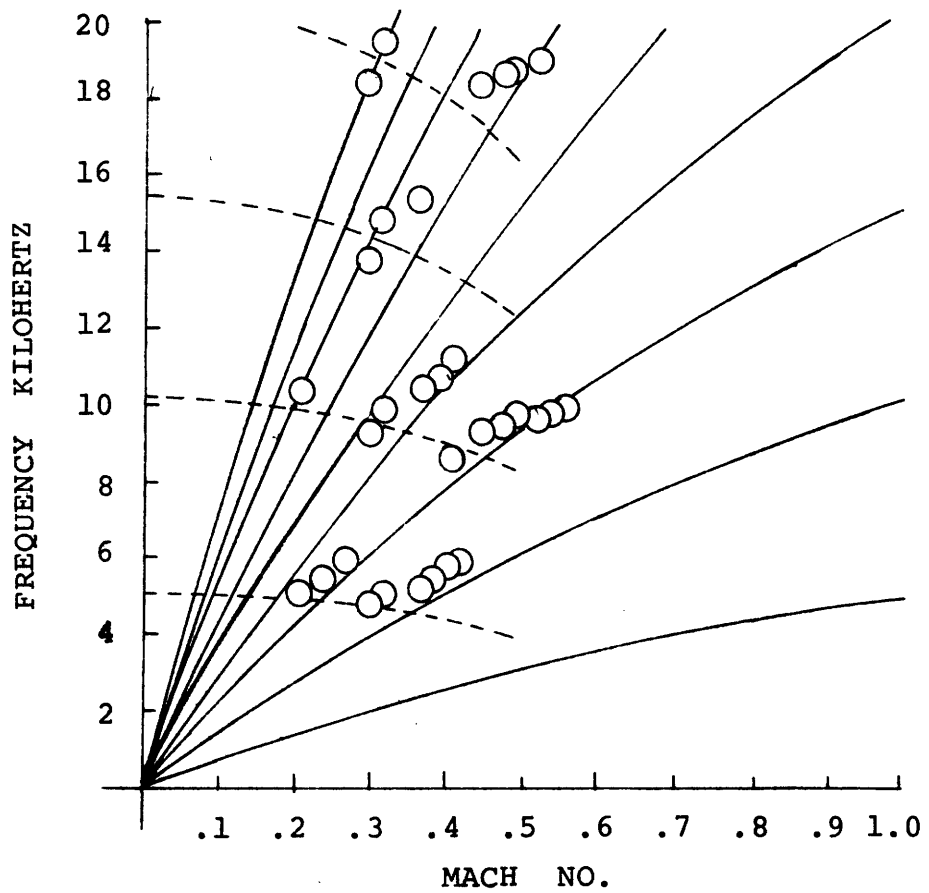
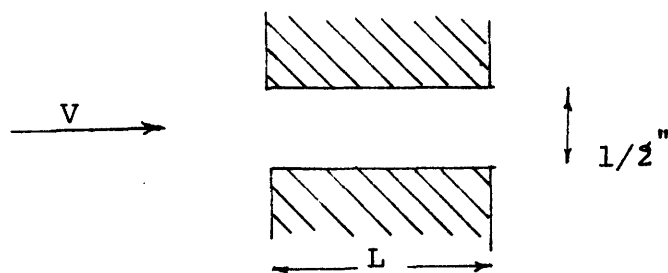
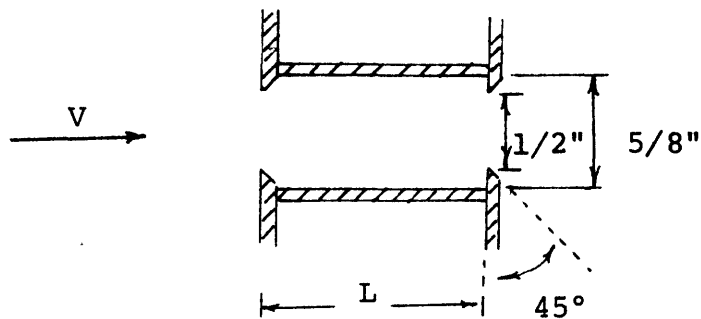


FIGURE 4.4 -- Screech frequency versus flow speed for a 1" long orifice plate.



LENGTH	SCREECH OBSERVED	SCREECH NOT OBSERVED
1/8"		✓
1/4"	✓	
1/2"	✓	
1"	✓	
2"		✓

FIGURE 4.5 -- Summary of tests made to determine the length to diameter ratio necessary for screech.



LENGTH	SCREECH OBSERVED	SCREECH NOT OBSERVED
SINGLE PLATE		✓
1/4"	✓	
1/2"	✓	
1"	✓	
2"		✓

FIGURE 4.6 -- Summary of tests made to determine the length to diameter ratio necessary for the modified hole tone.

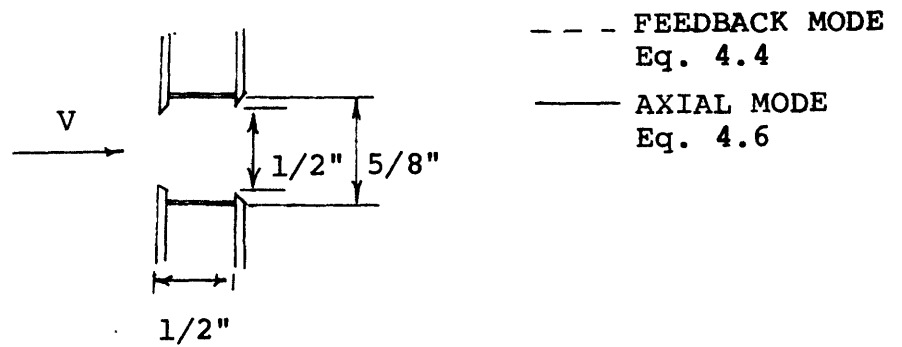
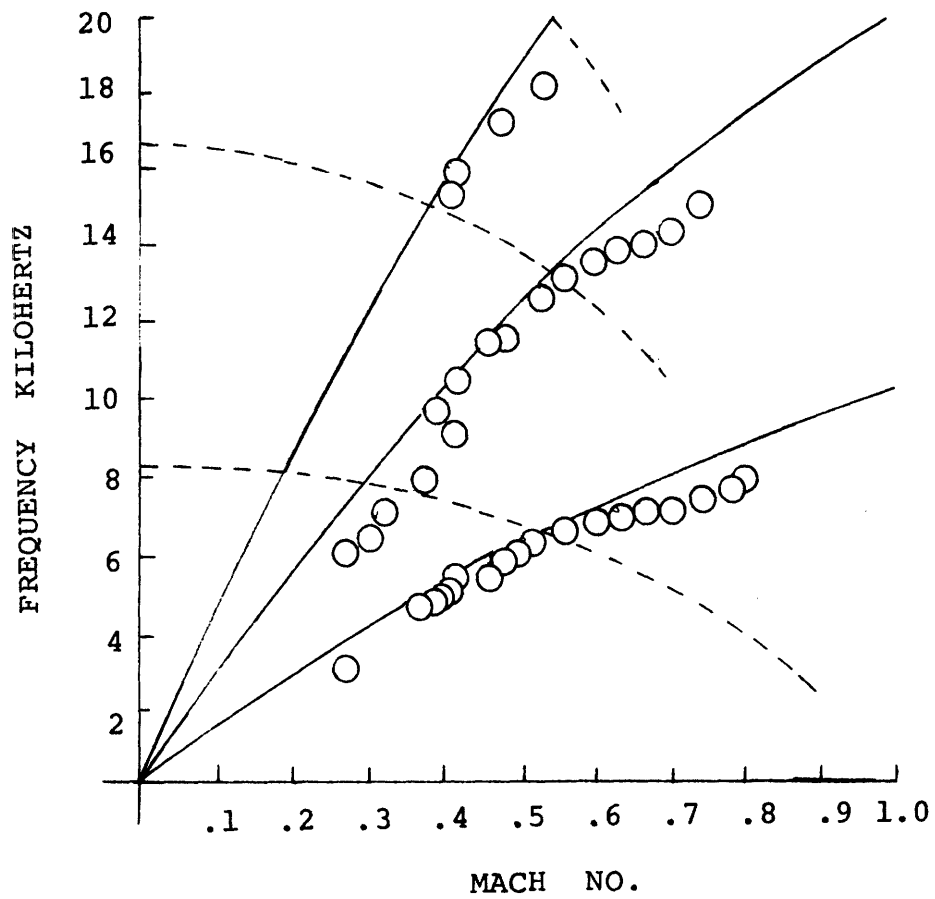


FIGURE 4.7 -- Screech frequency versus flow speed for the modified hole tone with a 5/8" inside diameter.

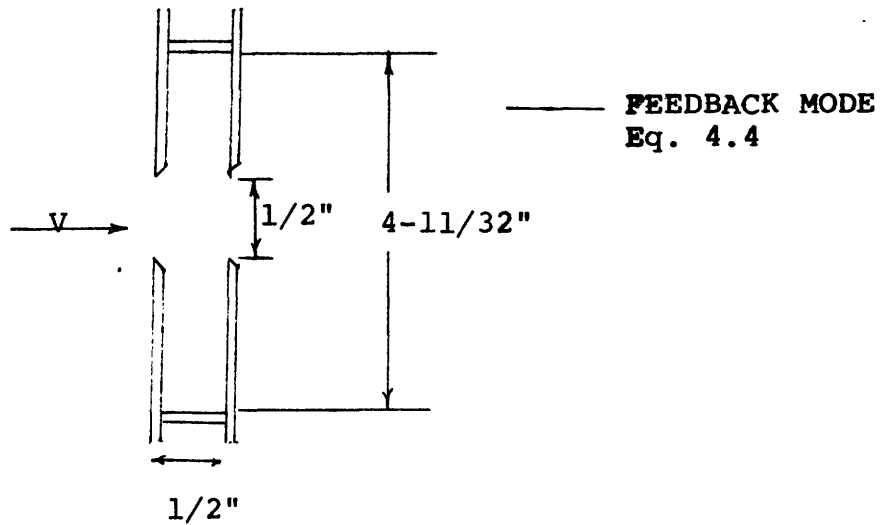
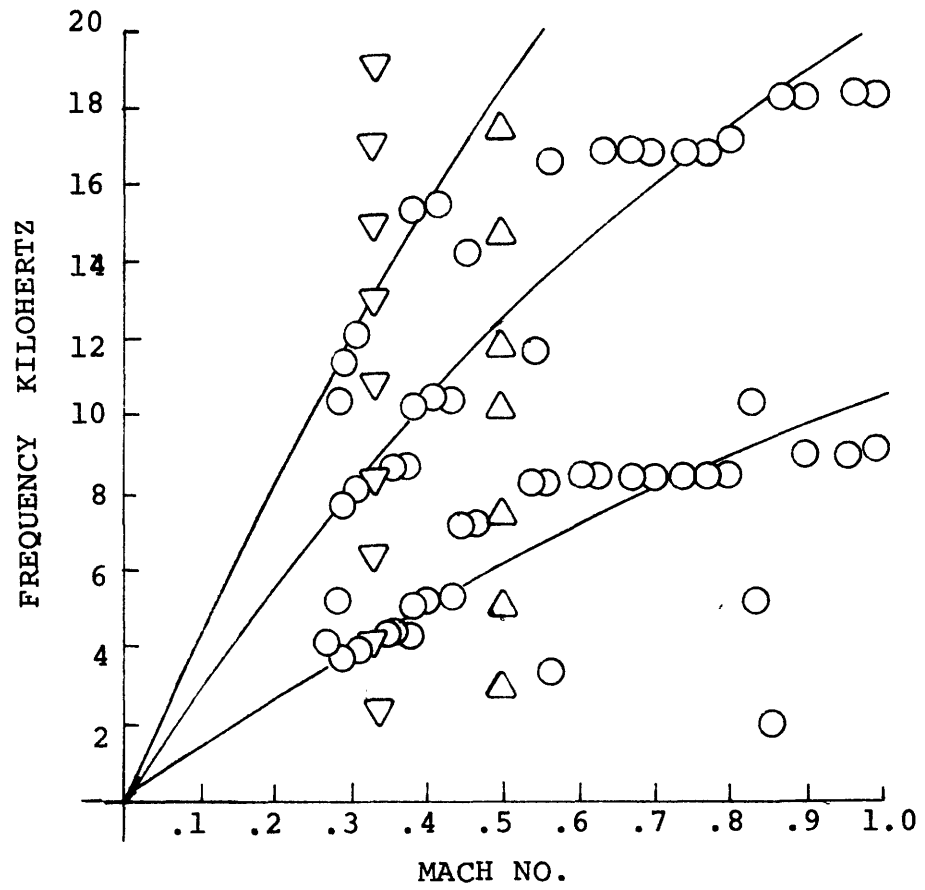


FIGURE 4.8 -- Screech frequency versus flow speed for the modified hole tone with a 4-11/32" inside diameter.

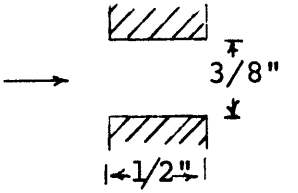
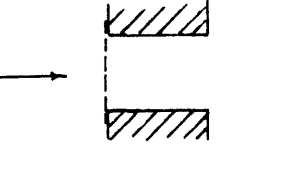
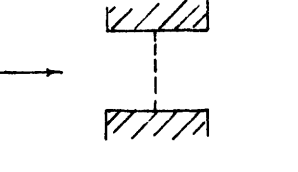
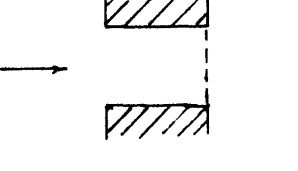
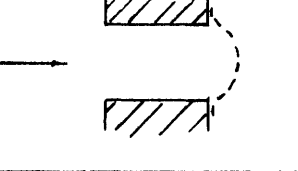
POSITION OF SCREEN (DOTTED LINE)	SCREECH OBSERVED	SCREECH NOT OBSERVED
	✓	
		✓
		✓
		✓
	✓	

FIGURE 4.9 -- The suppression of the orifice screech by screens.

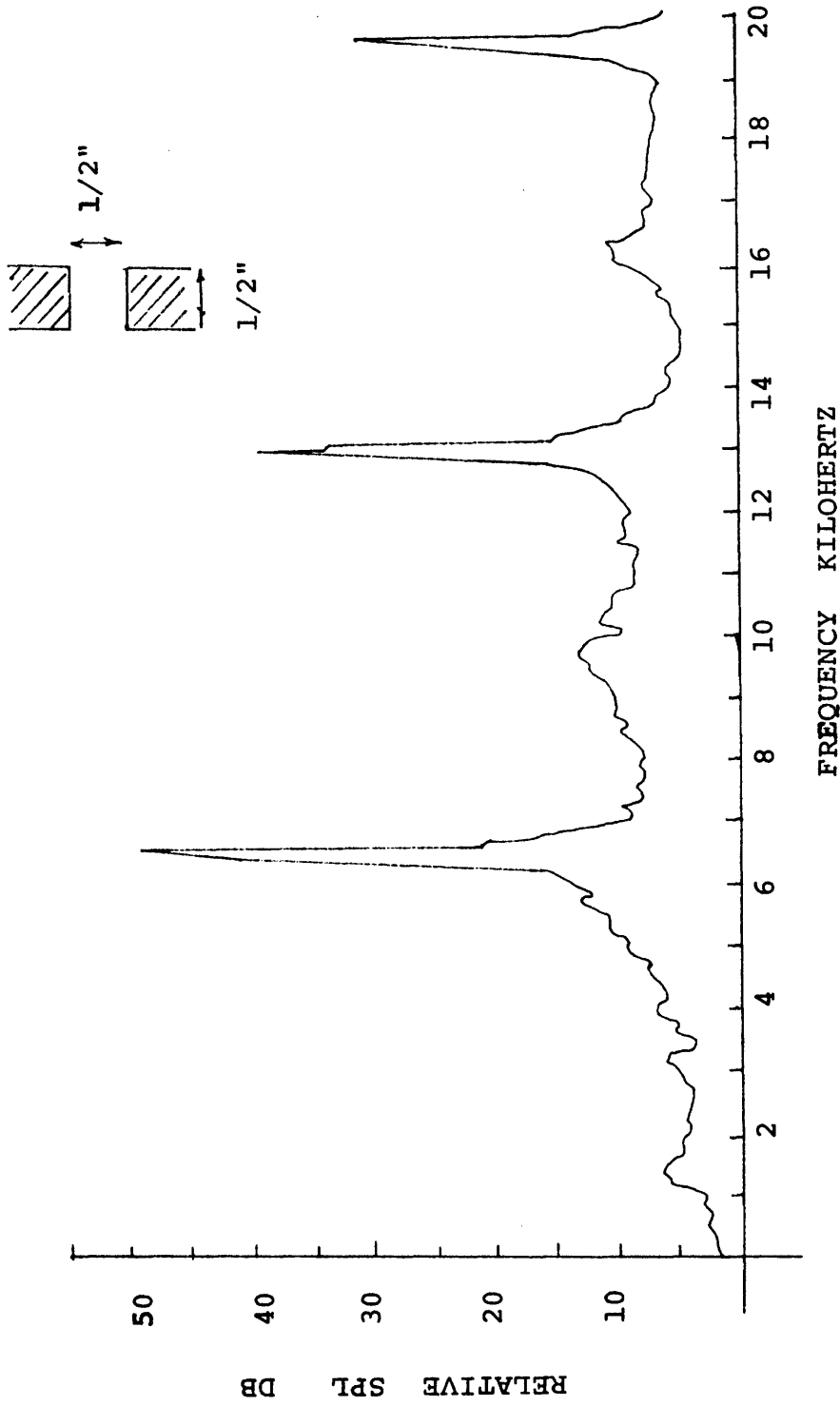


FIGURE 4.10 -- Typical orifice screech spectra (Mach .48).



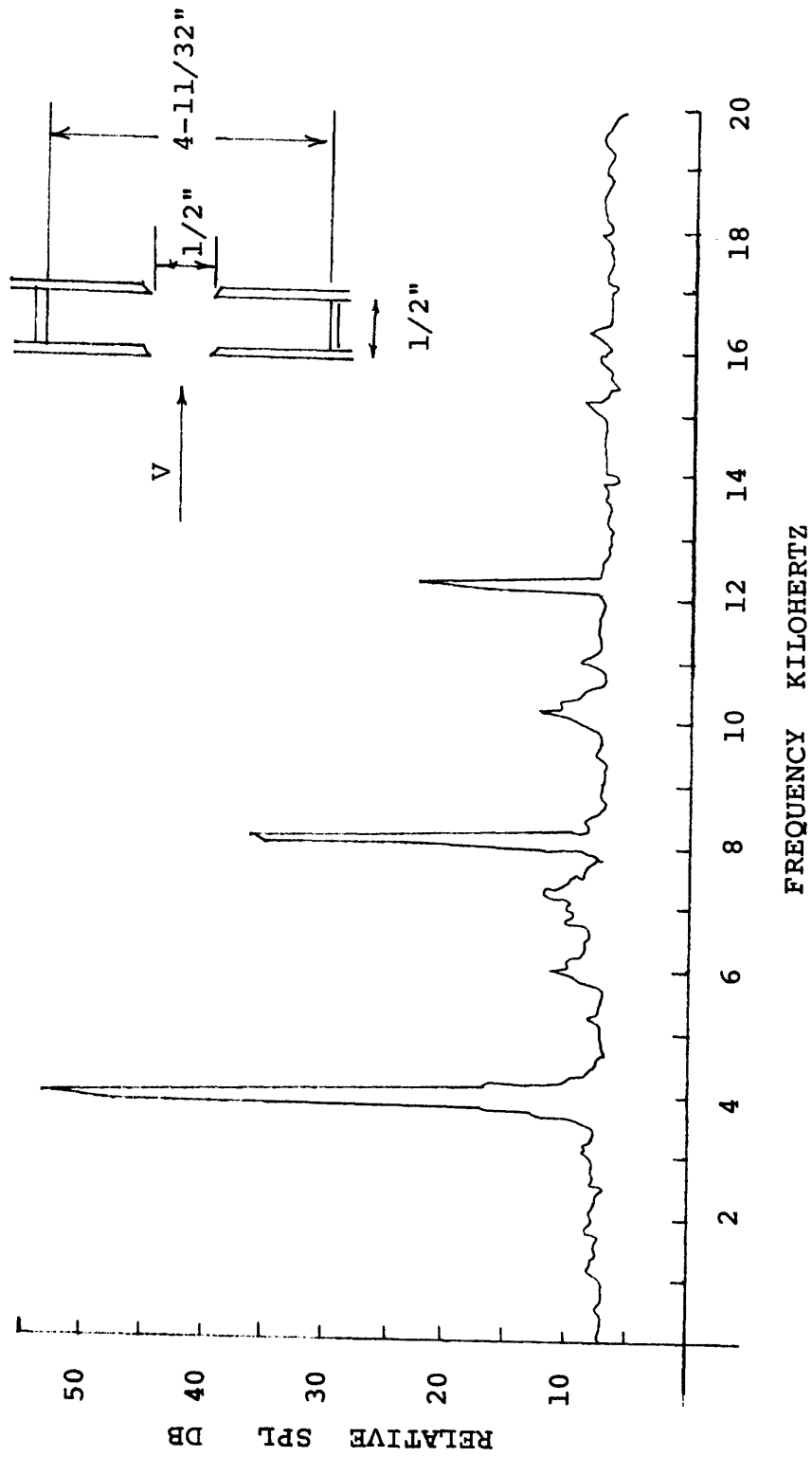


FIGURE 4.11 -- Screech spectra for the modified hole tone at Mach .33.

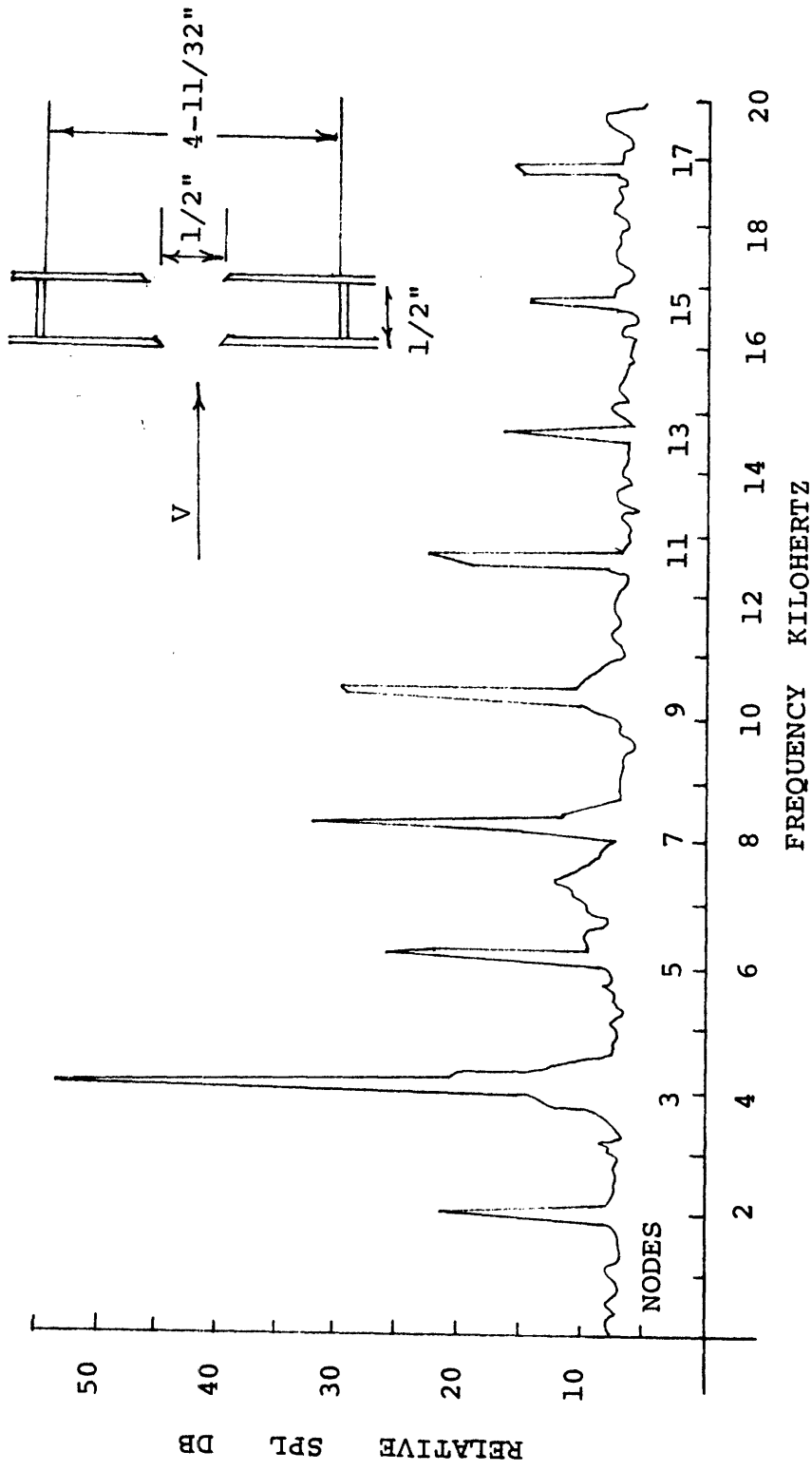


FIGURE 4.12 -- Screech spectra for the modified hole tone at Mach .34. All but the first peak are shown to coincide with cavity modes which have the indicated number of nodal diameters.

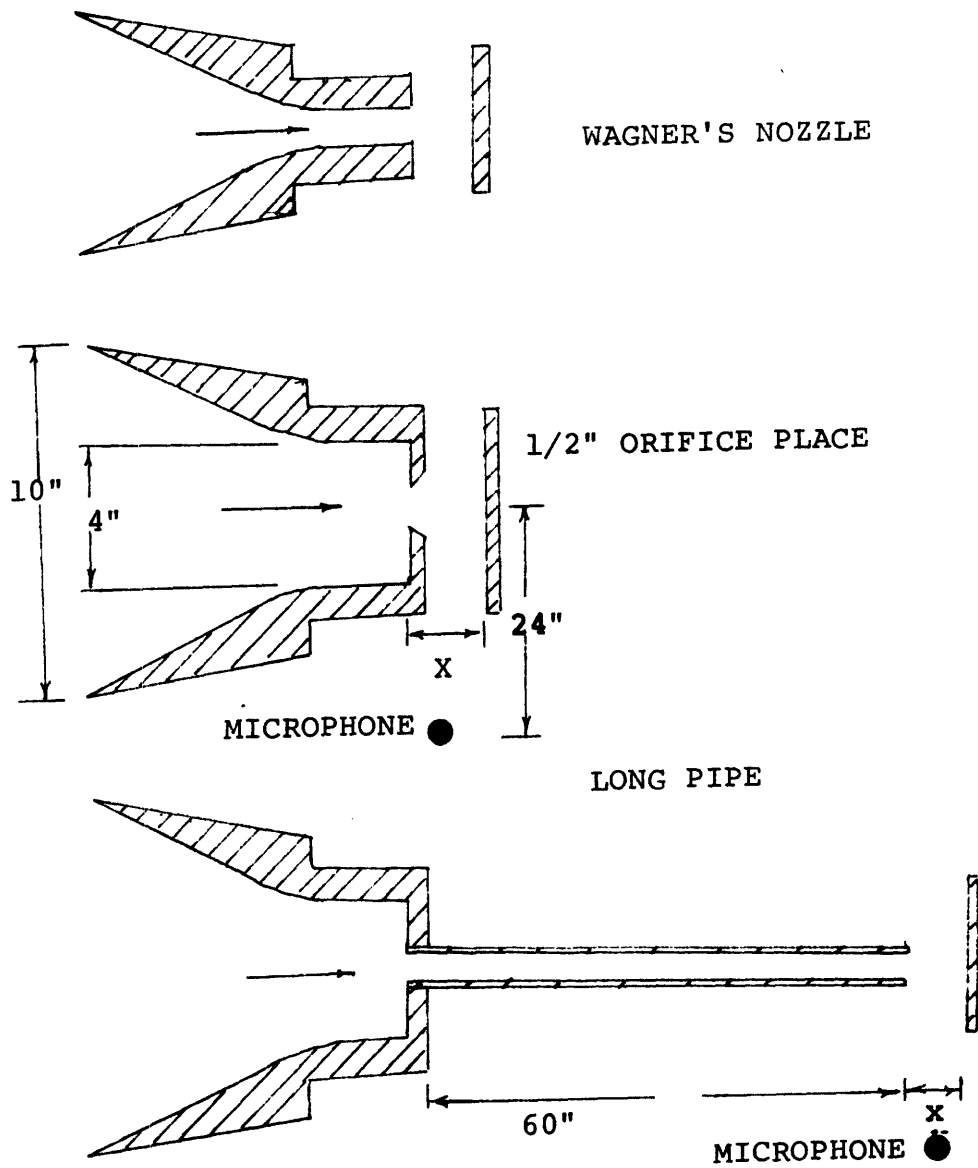


FIGURE 4.13 -- Experimental apparatus used to generate impingement screech.

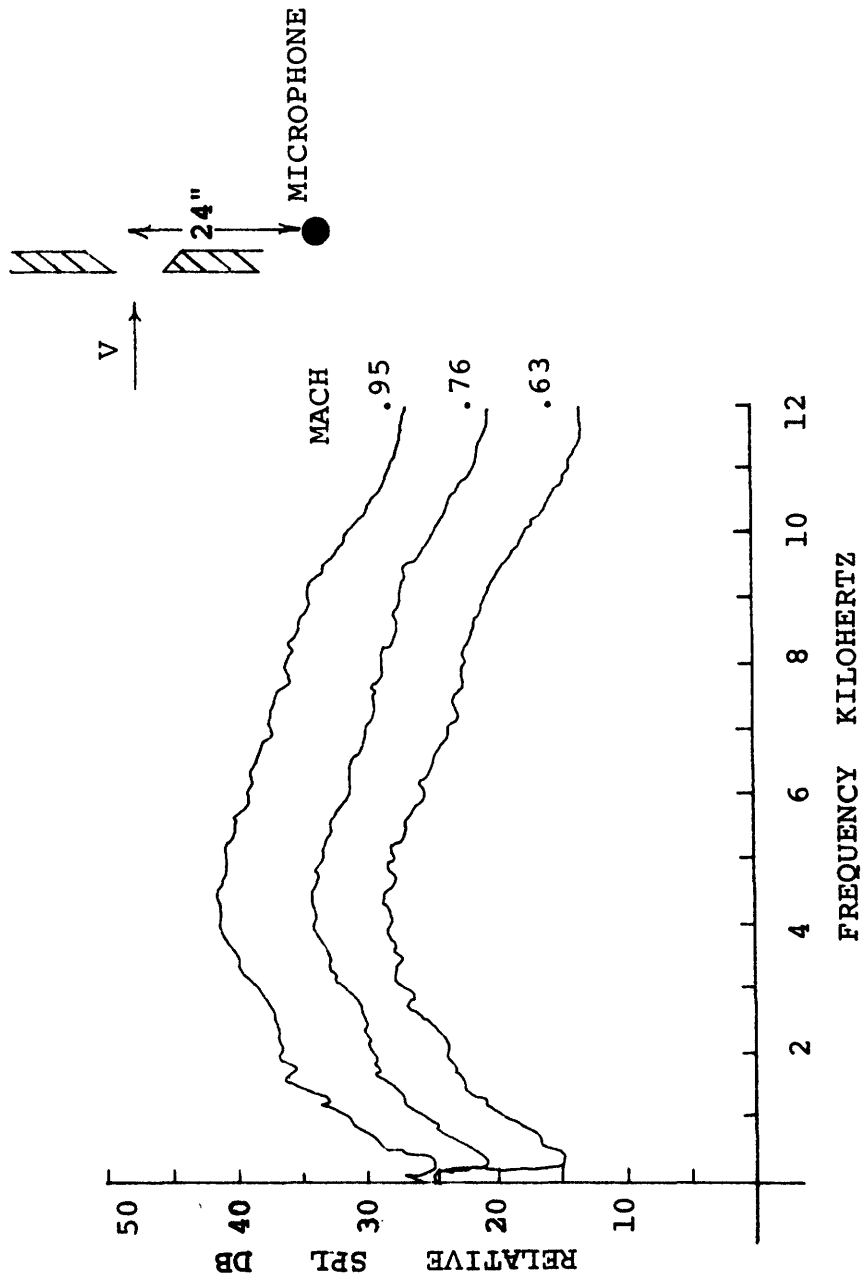


FIGURE 4.14 -- Free space spectra from a 1/2" diameter orifice plate.

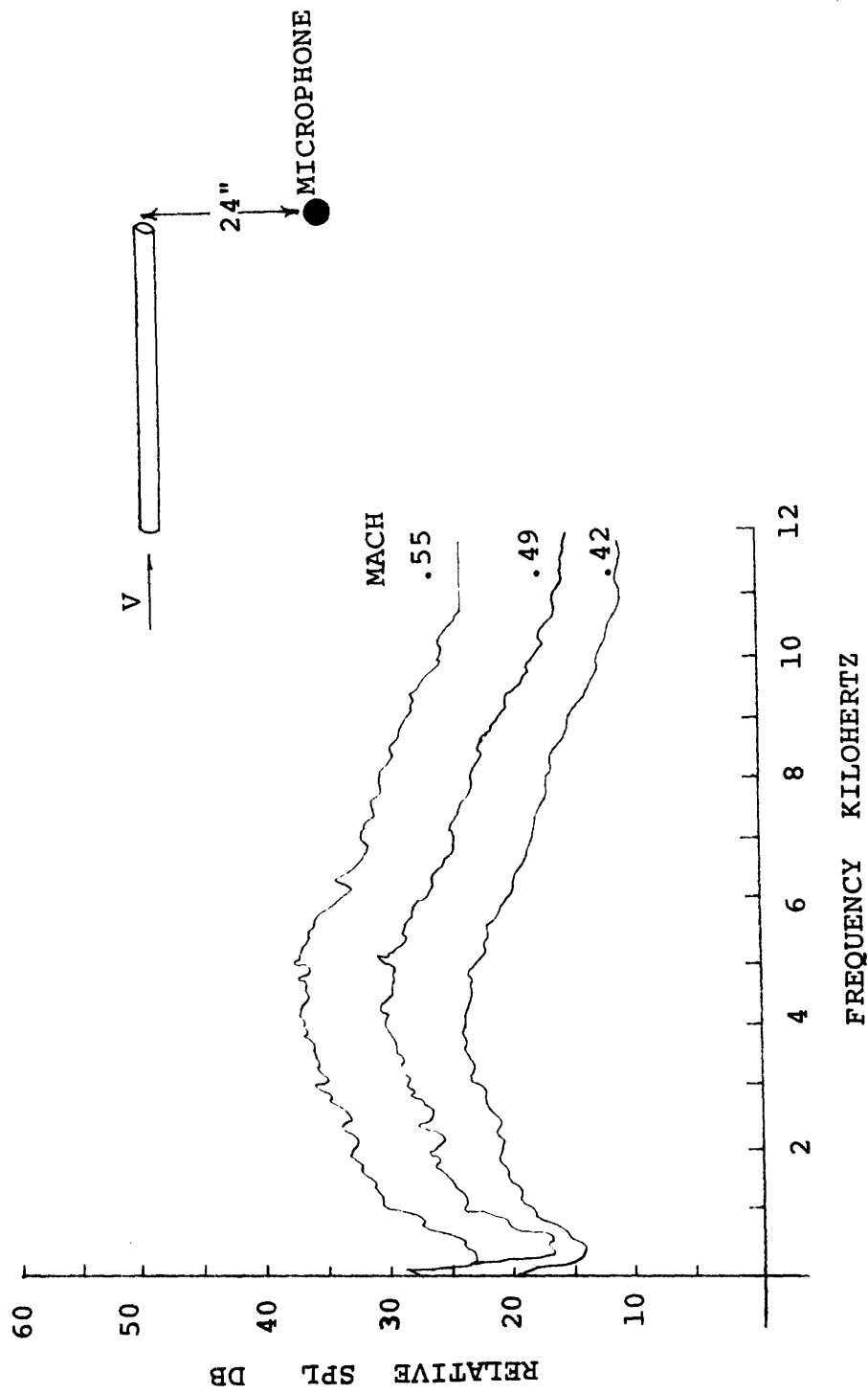


FIGURE 4.15 -- Free space spectra from a 60" long pipe with a 1/2" inside diameter.

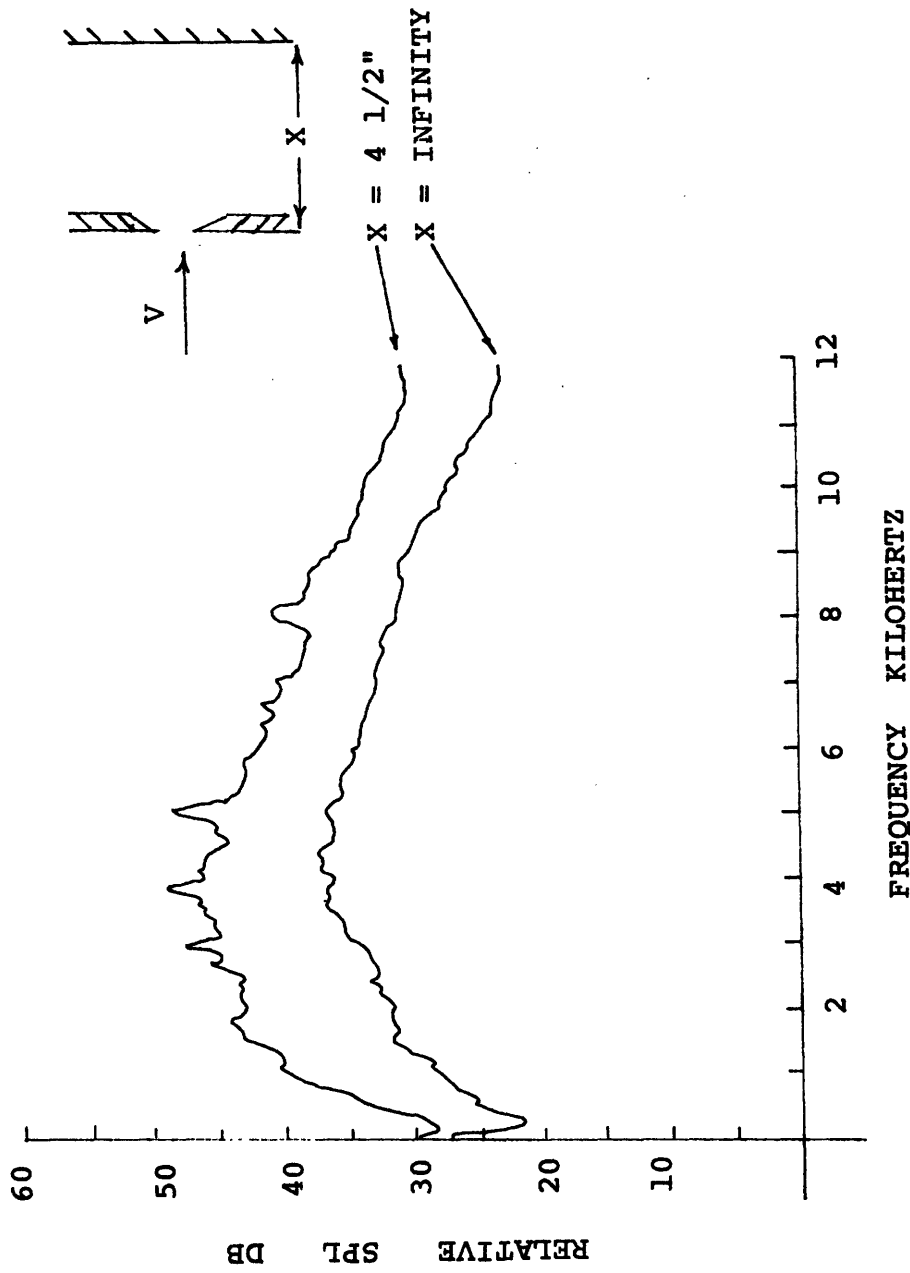


FIGURE 4.16 -- Increased sound level due to obstruction of flow by a flat plate. The orifice has a 1/2" diameter, the flow speed is Mach .8.

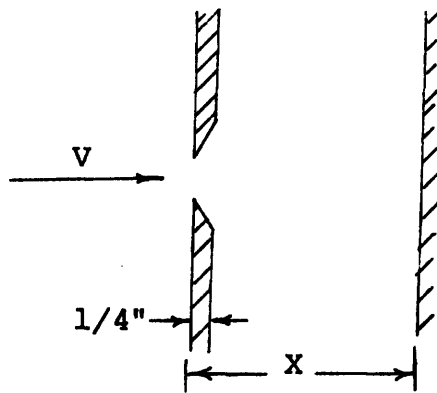
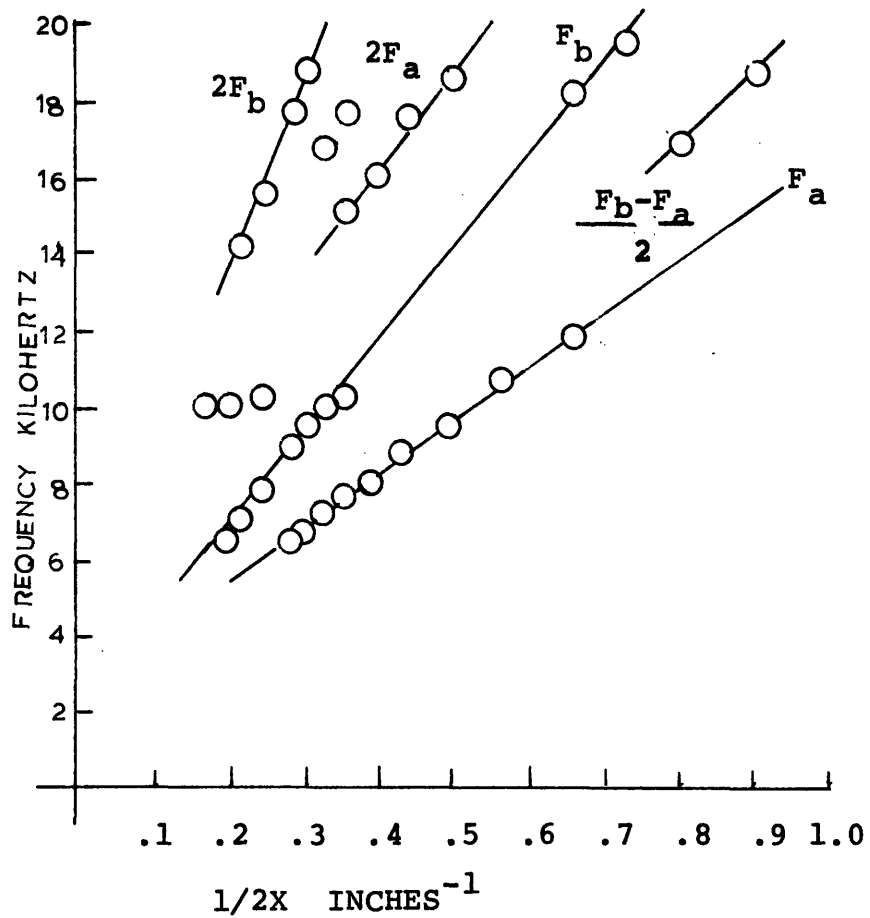
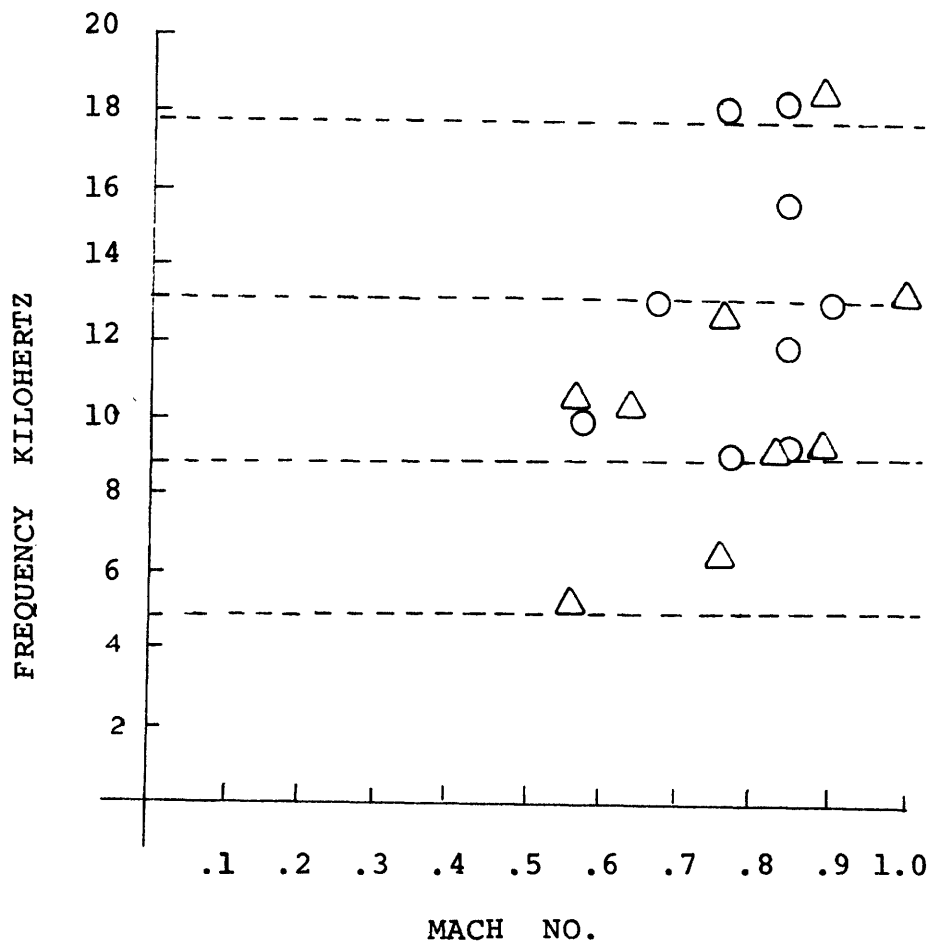


FIGURE 4.17 -- Impingement screech frequency versus distance to plate. The orifice has a  $1/2$ " diameter, the flow speed is Mach .8. The two dominant lines are labeled  $F_a$  and  $F_b$  arbitrarily. All other tones are interpreted as the sum or difference of these two modes.



- IMPINGEMENT SCREECH IN DUCT
- △ IMPINGEMENT SCREECH IN FREE SPACE

FIGURE 4.18 -- Direct comparison of impingement screech to screech observed in a rectangular duct. The dotted lines are the acoustic cavity mode frequencies for two plates separated by 1 1/2".



### BIOGRAPHICAL NOTE

George Succi was born in Stamford, Connecticut, on May 8, 1951. He attended St. Mary's Grammar School and Stamford Catholic High School in the same town.

From September, 1969, his studies were continued at the Massachusetts Institute of Technology in the Department of Physics, leading to a S.B. Degree in June, 1973. He attended M.I.T. under a grant from the Engineering Education Foundation. He was employed as a mathematician at Data Control Systems, in 1969, and as a research assistant at Trans-Sonics, in 1972. After finishing his undergraduate studies he headed for the mountains and eventually hiked 900 miles in the Southern Appalachian Wilderness.

In September, 1973, he returned to M.I.T. for his doctoral program in the Department of Physics under the direction of Dr. Uno Ingard. During this time he was employed as an acoustic consultant for Sonotech, in 1974, and in the aero-acoustics group at NASA Lewis Research Center, in 1976.